MEASUREMENT OF THE TOP ANTI-TOP QUARK PAIR PRODUCTION CROSS SECTION IN THE DILEPTON DECAY CHANNEL USING LEPTON+TRACK SELECTION IN 7 TeV $p-p$ COLLISIONS WITH $\mathcal{L} = 698$ PB^{-1}

BY

HOVHANNES KHANDANYAN

DISSERTATION

Submitted in partial fulfillment of the requirements
for the degree of Doctor of Philosophy in Physics
in the Graduate College of the
University of Illinois at Urbana-Champaign, 2012

Urbana, Illinois

Doctoral Committee:

Professor J. E. Wiss, Chair
Professor S. M. Errede, Director of Research
Professor L. S. Cooper
Professor J. D. Stack

Abstract

We present measurements of the $t\bar{t}$ production cross section obtained using the ATLAS detector at the LHC with pp collisions at $\sqrt{s} = 7$ TeV in dilepton final states, from a data sample of $\mathcal{L}$=698 pb^{-1} taken in 2011. For dilepton pair selection we have used a 'Lepton+Track' approach, where selection requirements on one lepton leg are reduced to a requirement of only a high quality Inner Detector track. This procedure, while allowing more background in the selected sample, enhances the sensitivity to τ-leptonic decays of the $W^{\pm}$ and increases the $t\bar{t}$ acceptance by 20% over the conventional dilepton analysis (where each lepton is identified as an electron or muon). Two modes of the l+track analysis were studied: the inclusive and the exclusive mode. The measured $t\bar{t}$ cross sections in the inclusive eTL and μTL channels are 182.9±9.3 (stat.)$^{+21.9}_{-16.7}$ (syst.)$^{+8.2}_{-7.3}$ (lum.) pb and 171.0±8.5 (stat.)$^{+20.6}_{-17.5}$ (syst.)$^{+7.8}_{-7.0}$ (lum.) pb, respectively. The inclusive eTL and μTL combined $t\bar{t}$ cross section is 177.4 ± 6.3 (stat.)$^{+18.4}_{-15.2}$ (syst.) ± 7.6 (lum.) pb. The measured $t\bar{t}$ cross sections in the exclusive eTL and μTL channels are 160.8 ±22.6 (syst.)$^{+45.1}_{-33.1}$ (syst.)$^{+8.3}_{-6.8}$ (lum.) pb and 168.3 $\pm$ 23.9 (syst.)$^{+45.8}_{-39.0}$ (syst.)$^{+9.0}_{-7.5}$ (lum.) pb, respectively. The exclusive eTL and μTL combined $t\bar{t}$ cross section is 164.5 $\pm$ 16.4 (syst.)$^{+39.0}_{-30.5}$ (syst.)$^{+8.6}_{-7.1}$ (lum.) pb. These $t\bar{t}$ cross section measurements are consistent with each other and are in good agreement with the Standard Model prediction of $164.6^{+11.5}_{-15.8}$ pb.

To Father and Mother,

To Grandfather, Uncle and Elder Brother

Acknowledgments

I would first like to thank my wonderful family for their abundant love and support which made it possible for me to go this far. I am very grateful to them for their substantial support, as if they were next to me all the time - despite the thousands of miles separation.

I would also like to emphasize the prominent role of two professors who deserve a special thanks since they have had the most impact on my graduate career. Thanks much to my advisor Steven Errede for inviting me to join the UIUC ATLAS group, for all his help dedicated to ensure the success of my ATLAS detector related effort: starting from detailed understanding of the TileCal system and finishing with the individual tile surface uniformity and pulse shape studies. Thanks much to my co-advisor Tony Liss for his support and suggestions with the top quark analysis. It was due to Tony's eagerness and support in taking an unknown path, that some 'raw' ideas were turned into mature solutions providing desired results.

Special thanks goes to Debbie Errede for her time and help in getting up to speed with ATLAS analysis tools and techniques and the opportunity to attend the very useful analysis jamboree at ANL. I cannot imagine how I would have handled the initial stages of my stay at CERN without the support of UIUC visiting professor Eirini Vichou, whose support was invaluable research wise and in terms of integration into the Swiss pace of life. Along with Eirini's support I would like to also mention the help that I received from Evgeny Starchenko and Ana Henriques that was important to successfully complete the tile uniformity studies.

I must also thank my fellow graduate students that I have become friends with over the years. Thanks guys for being such an amazing team to work with and sharing those numerous all-nighters doing homeworks or preparing for the qual. Special thanks goes to the UIUC ATLAS team (Nektarios, Allison, Arely, Austin, James and Kie) for the opportunity to share with and get answers to many technical questions that sometimes may be rather frustrating. In addition, I would like to thank the whole TileCal crew and the entire ATLAS collaboration for being such great example of outstanding collaborative effort. I must thank all the other friends of mine for their support while at Graduate School both in Champaign-Urbana and in Geneva. Thanks much each and everyone for being such an awesome crew to work and party with.

This theis was supported in part by the United States Department of Energy under the grant DE-FG02-91ER40677.

Table of Contents

List of Tables

List of Figures

Chapter 1

Introduction: The Standard Model and Top Quarks

1.1 Introduction

The main quest of particle physics is to answer the following three questions:

- What are the elementary constituents of matter ?
- What are the laws governing the interactions of the elementary constituents ?
- What is the true nature of the microscopic vacuum?

The answer to these questions has evolved throughout the whole history of mankind. Ancient Greeks knew that matter was made up of atomos (atoms). The electron was discovered in 1897. Immediately after the discovery of the neutron in 1932, the elementary constituents of matter were identified as protons, neutrons and electrons. Point-like protons and neutrons were the building blocks for nuclei, which combined with electrons, formed the atoms. Atoms bind together to form molecules. Nonetheless, this neat model for elementary particles failed to describe several new particles that were discovered shortly after the neutron. In addition, the proton and the neutron were subsequently found to contain internal structure representing compound states of yet more elementary objects.

The current understanding of particle physics claims that all matter consists of leptons and quarks, which interact via the strong, electromagnetic, weak and gravitational forces. The characteristics of fundamental interactions (e.g. relative strength, range, etc.) and masses for leptons and quarks vary in a wide range with the top quark (t) being the most massive known fundamental particle $m_t = 172.6 \pm 1.4$ GeV [1].

This dissertation is dedicated to the measurement of the top anti-top pair production cross section measurement using experimental data collected with the ATLAS detector [2]. The ATLAS detector is located at one interaction region of the Large Hadron Collider (LHC) at CERN in Geneva, Switzerland [2]. The dissertation is organized as follows:

- Chapter 1 presents an introduction to the Standard Model of particle physics with an emphasis on the

top quark sector. A brief description of the role of the top quark in the so-called Beyond the Standard Model theories is also provided.

- Chapter 2 discusses the general definition of a process cross section, and provides the physics motivation for the $t\bar{t}$ cross section measurement. It also lists earlier $t\bar{t}$ pair production cross section measurements by Tevatron experiments.
- Chapter 3 describes the LHC and ATLAS detector.
- Chapter 4 discusses the pp instantaneous luminosity measurement at the ATLAS detector and describes the data sample used in the scope of this dissertation.
- Chapter 5 describes the Monte Carlo simulations we used to model the physics processes under study.
- Chapter 6 describes the analysis objects used in this study: electrons, muons, jets and $E_{\mathrm{T}}^{\mathrm{miss}}$. It also provides the definition of the track-lepton object used for dilepton event selection. This includes the discussion of track-lepton efficiency and Scale Factor measurements performed by UIUC graduate student Austin Basye and special treatment of the transverse missing energy studies by James Coggeshall.
- Chapter 7 provides the detailed description of the Lepton+Track approach to dilepton event selection. It also discusses the methods used to calculate the Standard Model background contamination to $t\bar{t}$ production. This chapter presents the data-driven technique for fake track lepton background estimation done by Arely Cortes.
- Chapter 8 discusses the systematic uncertainties associated with the $t\bar{t}$ cross section measurements.
- Chapter 9 presents the $t\bar{t}$ cross section measurement per analysis channel and the combination technique used to merge information from orthogonal channels.
- Chapter 10 summarizes our conclusions and outlook for future measurements of the $t\bar{t}$ cross section at the LHC.

1.2 The Standard Model

The Standard Model (SM) of particle physics is the most successful theory that describes the fundamental particles and the nature of the interactions between them. According to the SM, the fundamental matter particles are spin-$\frac{1}{2}$ fermions - the leptons and the quarks, and spin-1 bosons which mediate the interactions

between the fundamental fermions. While most of the particles in the lepton family were discovered long before the SM was formulated, the experimental evidence for the existence of quarks was achieved later giving a great deal of credence to the quark model, which subsequently was incorporated into the SM. Recall the discovery of the J/Ψ particle in 1974 [3–5], the discovery of the τ-lepton in 1975 [6] followed by the discovery of the heavy $b\bar{b}$ meson Υ in 1977 [7], the top quark in 1995 by CDF [8] and D0 collaborations [9] and the tau neutrino in 2000 [10]. Table 1.1 summarizes some of the fundamental properties of leptons and quarks. For each fermion, the SM predicts the existence of an anti-fermion with the same mass but opposite charge. The existence of anti-fermions with properties in compliance with the SM predictions is well tested experimentally, adding to the credence of the theory. Currently, active research efforts are on-going to investigate the problem of neutrino mass and whether the neutrino and anti-neutrino are indeed different particles (Dirac scenario) or the same (Majorana scenario). We note that recent measurements of solar, atmospheric, reactor and accelerator neutrino oscillations provide compelling evidence that the neutrinos are massive.

The SM is remarkably successful in describing the the strong, electromagnetic and weak interactions[1] where the gauge theory for each is derived from a local gauge invariance principle. The field quanta are the spin-1 gauge bosons that mediate the interaction. Table 1.2 summarizes some of the features of the fundamental interactions. It is important to note that while leptons participate only in electromagnetic and weak interactions by virtue of possessing electromagnetic and weak charge, quarks also have color charge[2] and hence interact via the strong interaction as well. Similarly, due to the lack of electric charge, neutrinos do not participate in the electromagnetic interaction. The quoted values for coupling constants are those measured at low energies ($\sim$ 1 GeV). The following sections provide more details of the SM gauge theories describing these fundamental interactions.

Table 1.1: The leptons and quarks in the Standard Model.

		1st Generation		2nd Generation		3rd Generation	
	Charge		Mass [MeV/c^2]		Mass [MeV/c^2]		Mass [MeV/c^2]
Quarks	$\frac{+2}{3}$	u	1.7-3.1	c	(1.17 - 1.34)$\cdot 10^3$	t	(172.9 $\pm$1.5)$\cdot 10^3$
	$\frac{-1}{3}$	d	4.1 - 5.7	s	80 - 130	b	(4.13- 4.37)$\cdot 10^3$
Leptons	-1	e^-	0.51	μ^-	105.7	τ^-	1776.8
	0	ν_e	$< 3 \cdot 10^{-6}$	ν_μ	< 0.19	ν_τ	< 18.2

[1] One of the shortcomings of the SM is that it does not incorporate gravity as described in the theory of General Relativity. Nonetheless, gravity is extremely weak compared to the other forces (see Table 1.2) and can be neglected at the energy scales currently probed by particle physics experiments.

[2] The color charge was introduced to explain how 3 spin-$\frac{1}{2}$ quarks coexist in baryons in otherwise identical quantum states without violating the Pauli exclusion principle.

Table 1.2: The gauge bosons in the Standard Model.

Interaction	Mediator	Coupling Strength (α)	Range (fm)	Mass [GeV/c^2]
Strong	gluon (g)	~ 1	~ 1	0
Electromagnetic	photon (γ)	$\sim 10^{-2}$	∞	0
Weak	$W^{\pm}$, Z^0	$\sim 10{-}6$	10^{-2}	$m_W = 80.4$, $m_Z = 91.2$

1.3 Quantum Electrodynamics

Quantum Electrodynamics (QED) is the quantum field theory of electromagnetic interactions derived using gauge or phase invariance of the electromagnetic interactions [11]. In this section, we will take a closer look at how local gauge invariance necessitates the introduction of a massless gauge field and restricts the possible interactions of electromagnetic radiation with matter.

Let us start the discussion by looking at the Dirac Lagrangian density describing free spin-$\frac{1}{2}$ particles.

$$\mathcal{L}_{free} = i\bar{\psi}\gamma^{\mu}\partial_{\mu}\psi - m\bar{\psi}\psi \tag{1.1}$$

Note that $\mathcal{L}_{free}$ is invariant under a global gauge transformation $\psi(x) \rightarrow e^{iq\alpha}\psi(x)$. Noether's theorem then states a conservation law corresponding to global gauge invariance. Using the Euler-Lagrange equations one can readily show the conservation of the charged current:

$$j^{\mu} = q\bar{\psi}\gamma^{\mu}\psi. \tag{1.2}$$

Under a local gauge transformation[3] the matter field will transform as:

$$\psi(x) = e^{iq\alpha(x)}\psi(x) \tag{1.3}$$

$$\bar{\psi}(x) = e^{-iq\alpha(x)}\bar{\psi}(x) \tag{1.4}$$

The second term in the above Lagrangian density, known as a mass term is apparently invariant under the local gauge transformation. Let's examine how the first term behaves under this transformation. Start by looking at :

$$\partial_{\mu}\psi(x) = e^{iq\alpha(x)}[\partial_{\mu}\psi(x) + iq(\partial_{\mu}\alpha)\psi(x)] \tag{1.5}$$

[3]Gauge transformations 1.3 and 1.4 define transformations of the U(1) group.

As expression 1.5 suggests the first term is not invariant under a local phase transformation. Impose the invariance by substituting the partial derivative with the gauge-covariant derivative

$$\mathcal{D}_\mu \equiv \partial_\mu + iqA_\mu(x) \tag{1.6}$$

Provided that the vector field $A_\mu(x)$ transforms as:

$$A_\mu(x) \rightarrow A_\mu(x) - \partial_\mu \alpha(x) \tag{1.7}$$

the covariant derivative then simply undergoes the same phase rotation as the matter field $\psi(x)$:

$$\mathcal{D}_\mu \psi = e^{iq\alpha(x)} \mathcal{D}_\mu \psi \tag{1.8}$$

Expression 1.8 then implies local gauge invariance for the Dirac Lagrangian 1.1. Hence, we see how the local gauge invariance requirement necessitates the introduction of a massless gauge field − the photon field $A_\mu(x)$ and restricts the possible interactions of radiation with matter.

In order to arrive at the complete Lagrangian for QED one only needs to add a kinetic term for the photon field. This term describes the propagation of free photons and must respect the local U(1) gauge invariance of QED. Define:

$$F_{\mu\nu} = \partial_\mu A_\nu - \partial_\nu A_\mu \equiv [D_\mu, D_\nu] \tag{1.9}$$

One can readily show that the kinetic term of the form $F_{\mu\nu}F^{\mu\nu}$ is gauge invariant under transformation 1.7. Hence, one arrives at the following expression for the QED Lagrangian:

$$\mathcal{L}_{QED} = i\bar{\psi}\gamma^\mu \mathcal{D}_\mu \psi - m\bar{\psi}\psi - \frac{1}{4} F_{\mu\nu}F^{\mu\nu} \tag{1.10}$$

Note that the photon mass term $\mathcal{L}_\gamma \sim A^\mu A_\mu$ is not allowed by local U(1) gauge invariance, implying massless photons.

In classical electrodynamics, a test charge placed in a dielectric substance polarizes the medium which results in a reduction of the magnitude of the effective charge as seen from a distance greater than the molecular size of the dielectric. This effect is known as charge screening. A similar effect is present in QED where the vacuum acts as a polarizable medium in which virtual charged fermion-anti-fermion and W^+W^- pairs are polarized by the test charge. The associated lowest-order corrections occur in one-loop corrections to Coulomb scattering. A convenient way to account for these corrections is to introduce a so-called *running*

coupling constant, which is to say an effective coupling strength of the interaction. The Coulomb coupling constant $\alpha = \frac{q^2}{4\pi}$ will be modified as in expression 1.11 to account for one-loop corrections in QED:

$$\alpha_R(q^2) = \alpha_R(m^2)[1 + \frac{\alpha_R(m^2)}{3\pi} log(\frac{-q^2}{m^2}) + O(\alpha_R^2)] \tag{1.11}$$

We see that to this approximation, the effective electric charge increases logarithmically with increasing $-q^2$ or equivalently, decreasing distance.

1.4 Quantum Chromodynamics

Quantum Chromodynamics (QCD) is the quantum field theory that describes the strong interactions of quarks [11]. As for the case of QED, the theory for the strong interactions is derived by imposing local gauge invariance that both requires the introduction of massless vector gauge bosons and prescribes the form of the interactions of these gauge bosons with quarks[4], hence the theory of QCD shares many structural similarities with QED. Nonetheless, there are several significant differences. First, consider the quantum number responsible for the strong interactions of quarks − *the color charge*. Three types of color charge (say Red, Blue, Green) are introduced to describe the spectrum of baryons as bound states of three quarks that coexist inside baryons in otherwise identical quantum states without violating the Pauli exclusion principle. Other experimental pieces of evidence include the magnitude of the cross section for electron-positron annihilation into hadrons, the branching ratios for $\tau-$decays, and the π^0 lifetime [11]. Hence, for the strong interactions, the U(1) symmetry group of QED is replaced by the $SU(3)_C$ color gauge symmetry group. Under $SU(3)_C$ the matter field transformations will take the form:

$$\psi \rightarrow U\psi \tag{1.12}$$

$$\bar{\psi} \rightarrow U^\dagger\psi \tag{1.13}$$

where

$$U(x) = exp[i\Theta^A(x)T^A] \tag{1.14}$$

[4]As will be shown in this section, local gauge invariance also defines the interactions among the gauge bosons that arise due to the non-Abelian nature of the imposed gauge symmetry group.

and $T^A = \frac{1}{2}\lambda^A$ are the non-commuting, Hermitian Gell-Man matrices with A = 1,...,8. Following the same prescription as for the case of QED, one can construct the $SU(3)_C$ local color gauge invariant Lagrangian density for QCD of the form:

$$\mathcal{L}_{QCD} = i\bar{\psi}\gamma^\mu(\partial_\mu + ig_s T^A G^A_\mu)\psi - m\bar{\psi}\psi - \frac{1}{2}Tr(F^{\mu\nu}F_{\mu\nu}) \tag{1.15}$$

Similar to the case of QED, the local $SU(3)_C$ gauge invariance requirement necessitates the introduction of the massless gauge field – *the gluon field* $G^A_\mu(x)$, and restricts the possible interactions of gluons with matter. It also imposes the following transformation rule for the gluon field:

$$T^A G^A_\mu \rightarrow U T^A G^A_\mu U^\dagger + \frac{i}{g_s}(\partial_\mu U)U^\dagger \tag{1.16}$$

In analogy with the expression 1.9 the gluon field-strength tensor is defined as:

$$F_{\mu\nu} = \frac{1}{ig_s}[\mathcal{D}_\mu, \mathcal{D}_\nu] \tag{1.17}$$

$$= T^A(\partial_\mu G^A_\nu - \partial_\nu G^A_\mu) + ig_s[T^B, T^C]G^B_\mu G^C_\nu \tag{1.18}$$

While the first term of 1.18 is similar to its QED counterpart 1.9, the second term arises due to the non-Abelian nature of the $SU(3)_C$ symmetry group. The important consequence of this is the emergence of the three-gluon and four-gluon interaction vertices.

The expression for the running coupling constant for QCD takes the form:

$$\alpha_s(q^2) = \alpha(\mu^2)[1 + 2n_f\frac{\alpha(\mu^2)}{12\pi}log(\frac{-q^2}{\mu^2}) - 33\frac{\alpha(\mu^2)}{12\pi}log(\frac{-q^2}{\mu^2}) + O(\alpha_s^2)] \tag{1.19}$$

with n_f being the number of quark flavors appearing in the loop and $-\mu^2$ being a spacelike renormalization point.

It is important to note that the second term in 1.19 arises due to gluon-quark interactions and tends to decrease the effective coupling constant at longer distances (i.e. smaller values of $-q^2$) thus screening the color charge, while the third term emerges due to the gluon-gluon interaction and has the opposite effect

i.e. it tends to increase the effective $\alpha_s(q^2)$ with increasing distance or equivalently decreasing energy hence anti-screening the color charge. Thus, as long as $2n_f < 33$, the anti-screening contribution dominates and the running strong coupling constant becomes larger at larger distances resulting in the so called effect of *Strong Color Confinement* due to which quarks can never be observed in a free state, and can only exist in colorless bound states − *the hadrons*. On the other hand, the expression 1.19 implies the existence of a high energy regime[5] when $\alpha_s(q^2) \ll 1$ allowing the application of QCD perturbation theory. This property of non-Abelian gauge theories is known as *asymptotic freedom*. Figure 1.1 shows the measured value of α_S as a function of energy.

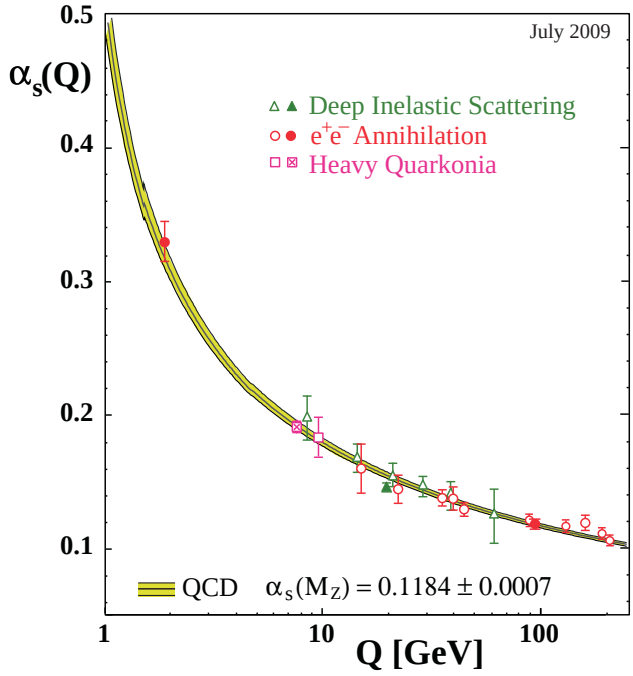

Figure 1.1: Summary of measurements of α_S as a function of the respective energy scale Q [12].

1.5 The Weak Interactions

The strong, the electromagnetic and the weak[6] interactions are all renormalizable gauge theories and as such share a number of structural similarities. Nonetheless, there are remarkable differences as well, some of which are summarized in Table 1.2, indicating that at low energies ($\sim$ 1 GeV), the weak interactions are much weaker than the other two fundamental types of interactions. A nice illustration of the latter is readily available from a comparison of the π^0 lifetime $\tau_{\pi^0} = (8.4 \pm 0.6) \cdot 10^{-17}$ sec to that of the much longer living

[5] The scale of QCD is set by $\Lambda_{QCD} \sim 200$ MeV .
[6] As we will see below, the latter two interactions are unified in the theory of electroweak interactions.

$\pi^{\pm}$, $\tau_{\pi^{\pm}} = (2.6033 \pm 0.0005) \cdot 10^{-8}$ sec. The reason for this substantial difference is that π^0 decays into a pair of photons via the electromagnetic interaction, while the $\pi^{\pm}$ cannot undergo a similar decay due to charge conservation and decays predominantly to a l-ν pair via the weak charged current interaction. Table 1.2 also indicates that the range of the weak interactions is only $\sim 10^{-17}$m due to massive mediators of the weak force - the $W^{\pm}, Z^0$ bosons (which were discovered in 1983 at CERN by UA1 and UA2 collaborations [13,14]). Hence, the theory of the weak interactions should provide a mechanism that endows the gauge bosons of the weak interactions with non-zero masses. We will discuss this mechanism in more detail in the next section(s).

Another fundamental difference of the weak interactions from QED and QCD has to do with the fact that the weak interactions maximally violate parity, and only left handed fermions (i.e. $\Psi_L = (1 - \gamma^5)\Psi$) participate in weak interactions. In other words, the left and right handed components of the fermion fields have different 'weak charges' . Based on this latter fact, as well as several other experimental observations Marshak and Sudarshan proposed the so-called V−A (vector minus axial vector) form for the weak interactions [11].

A few important remarks regarding the weak interaction are in order:

- $W^{\pm}$ bosons only couple to leptons within the same generation e.g. $\nu_\mu e^- \rightarrow \mu^- \nu_e$
- $W^{\pm}$ bosons couple to same generation and different generation quarks. However, inter-generational coupling is suppressed compared to intra-generational decays (see CKM matrix in section 1.5.5). For example, the decay $D^0 \rightarrow K^- X$ occurs 53% of the time, while $D^0 \rightarrow K^+ X$ occurs only 3% of the time. The decays $D^0 \rightarrow K^{\pm}\pi^{\mp}$ are shown in Figure 1.2. In the case $D^0 \rightarrow K^-\pi^+$ the c quark decays to an s quark (same generation) while for the case of $D^0 \rightarrow K^+\pi^-$ the c quark decays to a d quark (different generation).
- The neutral Z^0 boson couples to all leptons and quarks. The flavor of the leptons and quarks is conserved, i.e. no evidence of flavor-changing neutral currents has been observed.

1.5.1 Spontaneous Symmetry Breaking

As previously discussed, the local gauge invariance requirement for QED and QCD theories restricts the possible interactions of radiation with matter and necessitates the introduction of massless gauge boson(s) in agreement with respective experimental measurements. However, the mediators of the weak interactions are observed to have mass. Hence, the gauge theory of the weak interactions should answer that fundamental

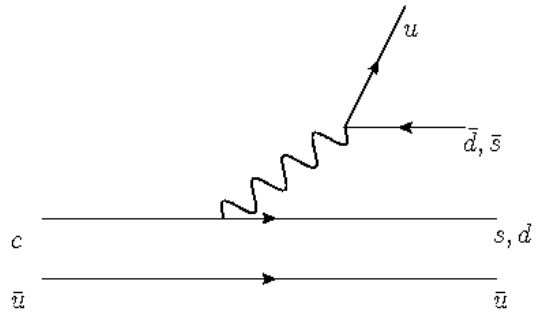

Figure 1.2: The Feynman diagram for the decays $D^0 \to K^{\pm}\pi^{\pm}$.

question, i.e. what endows the weak bosons ($W^{\pm}, Z^0$) with mass? The answer (in the context of the SM) is the mechanism of *spontaneous symmetry breaking*.

Before diving into the details of how spontaneous symmetry breaking enables the existence of massive weak bosons, let us make a detour and discuss various types of symmetries in nature that are associated with conservation laws and their implications on the construction of interacting field theories. The physical world manifests a number of apparently exact conservations laws, which reflect the operation of exact symmetries of Nature. The Lagrangian $\mathcal{L}$ is invariant under the symmetry in question if

1. $\delta\mathcal{L} = 0$ under the appropriate transformation

2. the unique physical vacuum is invariant under the symmetry transformation

While some of the fundamental symmetries of nature are exact and result in fundamental laws, such as conservation of energy, momentum, angular momentum etc., many symmetries hold only approximately. This can happen if the Lagrangian is exactly invariant under some symmetry (i.e. $\delta\mathcal{L} = 0$ holds). However, the dynamics determined by $\mathcal{L}$ implies a degenerate set of vacuum states, which are not invariant under the symmetry.

Let us now turn to the discussion of the Spontaneous Symmetry Breaking mechanism for a simple example of a complex scalar field Lagrangian density:

$$\mathcal{L} = \partial_\mu\phi^*\partial^\mu\phi - V(\phi) = \partial_\mu\phi^*\partial^\mu\phi - m^2\phi^*\phi - \lambda(\phi^*\phi)^2 \tag{1.20}$$

which is invariant under a global gauge transformation:

$$\phi \rightarrow e^{iQ\theta}\phi \tag{1.21}$$

In order to identify the vacuum state of the field most easily, let us construct the Hamiltonian for the field ϕ and determine its minimum. The Hamiltonian (density) is given by:

$$\mathcal{H} = \pi\dot{\phi} - \mathcal{L} \tag{1.22}$$

where

$$\dot{\phi} = \partial_0\phi \tag{1.23}$$

and the canonical momentum is

$$\pi \equiv \partial\mathcal{L}/\partial\dot{\phi} = \dot{\phi}^* \tag{1.24}$$

$$\pi^* \equiv \partial\mathcal{L}/\partial\dot{\phi}^* = \dot{\phi} \tag{1.25}$$

We therefore have:

$$\mathcal{H} = \pi\dot{\phi} + \pi^*\dot{\phi}^* - \mathcal{L} \tag{1.26}$$

$$= 2\dot{\phi}^*\dot{\phi} - [\dot{\phi}^*\phi^* - \vec{\nabla}\phi^* \cdot \vec{\nabla}\phi - m^2\phi^*\phi - \lambda(\phi^*\phi)^2] \tag{1.27}$$

$$= \dot{\phi}^*\dot{\phi} + \vec{\nabla}\phi^* \cdot \vec{\nabla}\phi + m^2\phi^*\phi + \lambda(\phi^*\phi)^2] \tag{1.28}$$

The state of lowest energy (the ground state) would thus be one for which the value of the field ϕ is a constant $< \phi >_0$, the value of which is determined by requiring that the potential energy $V(\phi)$ is at its minimum. If the parameter $m^2 > 0$ then $< \phi >_0 = 0$, whereas for the case $m^2 < 0$ the potential $V(\phi)$ takes the form of the 'Mexican Hat' potential as depicted in Figure 1.3 and the ground state is described by:

$$|\phi| = \pm\sqrt{\frac{-m^2}{2\lambda}} \equiv \pm\frac{v}{\sqrt{2}} \tag{1.29}$$

which corresponds to degenerate lowest-energy states, either of which may be chosen to be the ground state. We arbitrarily choose:

$$Re(\phi) = \frac{|m|}{\sqrt{2\lambda}} \tag{1.30}$$

$$Im(\phi) = 0 \tag{1.31}$$

Hence, the ground state takes the form:

$$< \phi >_0 = \frac{|m|}{\sqrt{2\lambda}} \tag{1.32}$$

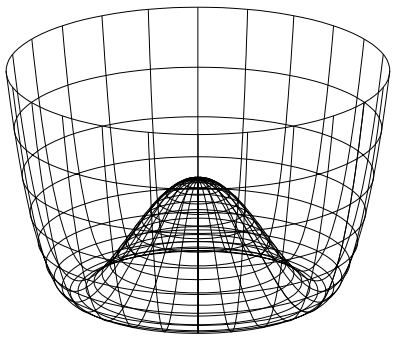

Figure 1.3: The Higgs potential. The neutral component of the Higgs field acquires a vacuum-expectation value $\langle\phi^0\rangle = v/\sqrt{2} = 174$ GeV on the circle of minima in Higgs-field space.

Consider oscillations about the ground state:

$$\phi = \frac{1}{\sqrt{2}}(h(x) + v)e^{i\pi(x)/v} \tag{1.33}$$

where $h(x)$ and $\pi(x)$ are fields with:

$$< h >_0 \;=\; 0 \tag{1.34}$$

$$< \pi >_0 \;=\; 0 \tag{1.35}$$

Substituting the expression 1.33 for ϕ into 1.20 one obtains:

$$\begin{aligned}
\mathcal{L} &= \frac{1}{2}(\partial_\mu h \partial^\mu h + (h+v)^2 \frac{1}{v^2}\partial_\mu \pi \partial^\mu \pi) - m^2 \frac{1}{2}(h+v)^2 - \lambda \frac{1}{4}(h+v)^4 && (1.36)\\
&= \frac{1}{2}(\partial_\mu h \partial^\mu h + \partial_\mu \pi \partial^\mu \pi) + \frac{1}{v^2}(h^2+2hv)\partial_\mu \pi \partial^\mu \pi - \frac{1}{2}m^2(h^2+2hv+v^2) \\
&- \frac{1}{4}\lambda(h^4 + 4h^3 v + 6h^2 v^2 + 4hv^3 + v^4) && (1.37)
\end{aligned}$$

Noting that $v^2 = |m|/\sqrt{\lambda}$, expression 1.37 can be simplified to:

$$\mathcal{L} = \frac{1}{2}(\partial_\mu h \partial^\mu h + \partial_\mu \pi \partial^\mu \pi) + \frac{1}{v^2}(h^2+2hv)\partial_\mu \pi \partial^\mu \pi - \lambda v^2 h^2 - \frac{1}{4}\lambda(h^4 + 4h^3 v) + \underbrace{\frac{1}{4}\lambda v^4}_{\text{Vacuum energy}} \tag{1.38}$$

The result 1.38 tells us that due to spontaneous symmetry breaking, there are 2 particle fields in the spectrum; the h(x)-particle associated with radial oscillations has a mass $m_h^2 = 2\lambda v^2$ and the massless π(x) particle. The massive h(x) particle may be viewed as a consequence of the restoring force of the potential against radial oscillations. In contrast, the masslessness of the π(x) particle may be viewed as a consequence of the U(1) invariance of the Lagrangian, meaning that there is no restoring force against angular oscillations. The appearance of the massless particle is known as the Goldstone phenomenon. The massless particles (called Goldstone bosons) are the zero-energy excitations that connect possible vacua. More generally, *The Goldstone Theorem* claims: Every broken generator[7] of the original symmetry group has a corresponding massless spin-zero boson. In this example, the symmetry group is the U(1) transformation $e^{iQ\theta}$ with the generator Q. Let us explicitly show that the generator Q is broken, i.e. it does not annihilate the vacuum:

$$Q < \phi >_0 \neq\; 0 \tag{1.39}$$

Indeed, for a small angle θ one would have:

[7] A broken generator is the one that does not annihilate the vacuum.

$$e^{iQ\theta} < \phi >_0 \quad \cong \quad (1 + iQ\theta) < \phi >_0 \neq < \phi >_0 \tag{1.40}$$

$$Q < \phi >_0 \neq \ 0 \tag{1.41}$$

Hence, indeed the generator Q does not annihilate the vacuum.

1.5.2 The Higgs Mechanism

The questions to address now is how the Goldstone boson endows gauge bosons with mass. As we will see the answer to this is provided by the *Higgs Mechanism*, due to which an unexpected cooperation between massless gauge fields and the massless Goldstone bosons arises.

Let us promote the Lagrangian 1.20 to possess local gauge invariance:

$$\mathcal{L} = \mathcal{D}_\mu \phi^* \mathcal{D}^\mu \phi - V(\phi) = \mathcal{D}_\mu \phi^* \mathcal{D}^\mu \phi - m^2 \phi^* \phi - \lambda (\phi^* \phi)^2 \tag{1.42}$$

Since the Lagrangian 1.42 is locally gauge invariant we can set the phase to:

$$\theta(x) = -\frac{\pi(x)}{v} \tag{1.43}$$

due to which the expression 1.33 then takes the form:

$$\phi = \frac{1}{\sqrt{2}}(h(x) + v) \tag{1.44}$$

On the one hand, fixing the gauge eliminates the π(x) particle. On the other hand, the kinetic term for the h(x) particle takes the following form:

$$
\begin{aligned}
(\mathcal{D}_\mu\phi)^*(\mathcal{D}^\mu\phi) &= \frac{1}{2}(\partial_\mu - ieQA_\mu)(h(x)+v)(\partial^\mu + ieQA^\mu)(h(x)+v) && (1.45)\\
&= \frac{1}{2}(\partial_\mu h\partial^\mu h + e^2Q^2A_\mu A^\mu(h+v)^2) && (1.46)\\
&= \frac{1}{2}\partial_\mu h\partial^\mu h + \underbrace{\frac{1}{2}e^2Q^2v^2}_{\equiv M_A^2}A_\mu A^\mu + \frac{1}{2}e^2Q^2(h^2+2hv)A_\mu A^\mu && (1.47)
\end{aligned}
$$

Thus, the gauge field A(x) has acquired a mass $M_A = eQv$, suggesting that the Goldstone boson π(x) was 'eaten' by the gauge field A(x) in order to acquire mass. Also note that the number of degrees of freedom of the system is preserved. Before the spontaneous symmetry breaking, the system had 2 scalar fields (ϕ and ϕ^*) and the 2 helicity states of the massless gauge field A(x). After the spontaneous symmetry breaking, a scalar field h(x) and 3 helicity states of the massive gauge boson A(x) exist.

1.5.3 Electroweak Interactions

The theory of electroweak interactions with the simplest scalar sector was developed by Glashow, Weinberg and Salam. Firstly, let us define the spectrum of fundamental fermions of the theory. In order to account for the fact that the weak interaction couples only to left-handed fermions, these are grouped into doublets under the gauge group $SU(2)_L$:

$$
L_i = \begin{pmatrix}\nu_e\\ e\end{pmatrix}_L, \begin{pmatrix}\nu_\mu\\ \mu\end{pmatrix}_L, \begin{pmatrix}\nu_\tau\\ \tau\end{pmatrix}_L, \begin{pmatrix}u\\ d\end{pmatrix}_L, \begin{pmatrix}c\\ s\end{pmatrix}_L, \begin{pmatrix}t\\ b\end{pmatrix}_L \tag{1.48}
$$

While right-handed fermions are represented by $SU(2)_R$ singlets:

$$
R_i = \nu_R^e, e, \nu_R^\mu, \mu, \nu_R^\tau, \tau, u_R, d_R, c_R, s_R, t_R, b_R \tag{1.49}
$$

In order to incorporate electromagnetic interactions, we must introduce a $U(1)_Y$ symmetry group with the generator hypercharge Y defined as follows:

$$
Q = T^3 + Y \tag{1.50}
$$

Here, Q is the electric charge, $T^3 = \frac{1}{2}\sigma^3$ is the third generator of the $SU(2)_L$ group with σ representing the

usual Pauli matrices. Knowing the values of the electric charge of fundamental fermions, one may deduce their hypercharge assignments.

Table 1.3: First generation fermion representation under $SU(2)_L$ and their hypercharge. The same hypercharge assignment holds for the second and the third generations.

$SU(2)_L$ Representation	Hypercharge
$\binom{\nu_e}{e}_L$	$-\frac{1}{2}$
ν_R	0
e_R	-1
$\binom{u}{d}_L$	$+\frac{1}{6}$
u_R	$+\frac{2}{3}$
d_R	$-\frac{1}{3}$

The gauge group $SU(2)_L \otimes U(1)_Y$ is adopted as the group of transformations for the gauge theory of electroweak interactions. Introducing gauge bosons as follows:

$$A^1_\mu,\ A^2_\mu,\ A^3_\mu \qquad \text{for } SU(2)_L \text{ group}$$

$$B_\mu \qquad \text{for } U(1)_Y \text{ group}$$

The Lagrangian of the theory will be:

$$\underbrace{\sum_i \bar{L}_i i\gamma^\mu(\partial_\mu + igT^a A^a_\mu + ig'YB_\mu)L_i + \sum_i \bar{R}_i i\gamma^\mu(\partial_\mu + ig'YB_\mu)R_i}_{\mathcal{L}_{fermions}}$$
$$+ \quad \underbrace{-\frac{1}{4}F^l_{\mu\nu}F^{l\mu\nu} - \frac{1}{4}f_{\mu\nu}f^{\mu\nu}}_{\mathcal{L}_{gauge}} \tag{1.51}$$

Here, g is the coupling constant for the so-called weak isospin group $SU(2)_L$ and g' is the coupling for the weak hypercharge group $U(1)_Y$. In analogy with the expressions 1.9 and 1.18, the field-strength tensor takes the form:

$$f_{\mu\nu} = \partial_\mu B_\nu - \partial_\nu B_\mu \tag{1.52}$$

$$F^l_{\mu\nu} = \partial_\mu A^l_\nu - \partial_\nu A^l_\mu + g\epsilon_{jkl} A^j_\mu A^k_\nu \tag{1.53}$$

So far the theory contains 4 massless gauge bosons whereas Nature has only one massless mediator for the electroweak interactions − the photon. In addition, the global $SU(2)_L$ invariance forbids mass terms for fermions which again disagrees with the experimental observations. Therefore, the theory needs a modification that retains only one massless gauge boson associated with the conserved electric charge ($Q = T^3 + Y$), and also endows fermions with mass.

Introducing a complex doublet of scalar fields:

$$\begin{pmatrix} \phi^+ \\ \phi^0 \end{pmatrix} \tag{1.54}$$

which transforms as a $SU(2)_L$ doublet and must therefore have $Y_\phi = +\frac{1}{2}$.

Add to the Lagrangian 1.51 a term:

$$\mathcal{L}_{scalar} = [(\partial_\mu + igT^a A^a_\mu + ig'Y B_\mu)\phi]^\dagger [(\partial_\mu + igT^a A^a_\mu + ig'Y B_\mu)\phi] - V(\phi^\dagger \phi) \tag{1.55}$$

where the potential energy is defined as in 1.20. Following the procedure of spontaneous symmetry breaking as described in Section 1.5.1; the continuum of vacuum states is described by $\langle \phi^\dagger \phi \rangle = \frac{-m^2}{2\lambda} = \frac{v^2}{2}$. Choose as the vacuum state:

$$\langle \phi \rangle_0 = \begin{pmatrix} 0 \\ \frac{v}{\sqrt{2}} \end{pmatrix} \tag{1.56}$$

The expression 1.56 for the vacuum state readily suggests that the symmetries associated with all 4 generators of the $SU(2)_L \otimes U(1)_Y$ group (i.e. T^1, T^2, T^3, Y) are broken. However, one can see that the combined generator $T^3 + Y$ is not broken, which according to 1.50 corresponds to conserved electric charge. Expanding the field ϕ about the chosen vacuum state, one gets:

$$\phi = \frac{1}{\sqrt{2}}(h+v)\exp\left[iT^1\pi^1 + iT^2\pi^2 + i(T^3 - Y)\pi^3\right]\begin{pmatrix}0\\1\end{pmatrix} \tag{1.57}$$

Here π^1, π^2, π^3 are the Goldstone bosons corresponding to the broken generators mentioned above. Following the Higgs mechanism and gauging away the Goldstone bosons, one may readily convince oneself that the gauge boson spectrum contains A^1_μ, A^2_μ fields that have acquired mass $m_A = \frac{1}{4}g^2v^2$ by 'eating up' the Goldstone bosons. The linear combinations:

$$W^\pm_\mu = \frac{1}{\sqrt{2}}(A^1_\mu \mp iA^2_\mu) \tag{1.58}$$

with the mass:

$$m^2_W = \frac{1}{4}g^2v^2 \tag{1.59}$$

are identified with the $W^\pm$ bosons, the mediators of the weak charged current. Using the weak decay $\mu \to \nu_\mu e\bar{\nu_e}$ one can determine $v = 246$ GeV. The third massive gauge boson is:

$$Z^0_\mu = \frac{1}{\sqrt{g^2 + g'^2}}(gA^3_\mu - g'B_\mu) \tag{1.60}$$

with the mass:

$$m^2_{Z^0} = \frac{1}{4}(g^2 + g'^2)v^2 \tag{1.61}$$

which is the carrier of the weak neutral current Z^0. The massless gauge boson representing the photon field is orthogonal to Z^0:

$$A_\mu = \frac{1}{\sqrt{g^2 + g'^2}}(gA^3_\mu + g'B_\mu) \tag{1.62}$$

Hence, due to spontaneous symmetry breaking, the initial symmetry group $SU(2)_L \otimes U(1)_Y$ is reduced to $U(1)_{EM}$. The associated Goldstone bosons π^i were 'eaten' by $W^{\pm}$, Z^0 fields to acquire mass.

One can alternately express the equations 1.60 and 1.62 in matrix form as:

$$\begin{pmatrix} Z^0_\mu \\ A_\mu \end{pmatrix} = \begin{bmatrix} \cos\theta_w & -\sin\theta_w \\ \sin\theta_w & \cos\theta_w \end{bmatrix} \times \begin{pmatrix} A^3_\mu \\ B_\mu \end{pmatrix} \tag{1.63}$$

where:

$$\cos^2\theta_w = \frac{g^2}{g^2+g'^2}, \quad \sin^2\theta_w = \frac{g'^2}{g^2+g'^2}, \tag{1.64}$$

The angle θ_w is known as the weak mixing angle, which at tree level relates the masses of the weak charged current carrier $W^{\pm}$ to the neutral one Z^0:

$$M_W^2 = M_Z^2 \cos^2\theta_w \tag{1.65}$$

We also note the relation between the weak and electromagnetic coupling strengths:

$$\alpha_w = \frac{\alpha_{EM}}{sin^2\theta_w} = \frac{e^2}{4\pi sin^2\theta_w} \tag{1.66}$$

Experimental measurements of the masses of weak interaction carriers are $M_W = 80.4$ GeV and $M_Z = 91.2$ GeV. The weak mixing angle is measured to be $\sin^2\theta_w \simeq 0.24$. Lastly, the field $h(x)$ is the remnant of the Higgs doublet field - the radial oscillations about the minimum. The particle associated with it is the Higgs boson. As we have seen, experimentally the W and Z are massive, hence there must be a field to which the longitudinal components of W, Z bosons couple. Whether it is the Higgs field or not is currently under intensive experimental investigation.

1.5.4 Yukawa Interactions

As mentioned earlier, $SU(2)_L$ invariance forbids a mass term for the fermions $m\bar{\psi}\psi = m\left(\bar{\psi}_L\psi_R - \bar{\psi}_R\psi_L\right)$. In order to overcome this and also generate fermion masses, we introduce the *Yukawa Interaction* which

couples the Higgs field to the fermion fields. For simplicity, let us consider the first generation of quarks and express the Yukawa Lagrangian as follows:

$$\mathcal{L}_{Yukawa} = -y_u \left(\bar{q}_L \phi^\dagger\right) u_R - y_d \left(q_L \phi\right) d_R + H.C. \tag{1.67}$$

where y_u, y_d are the Yukawa coupling constants for u and d quarks. Appealing to the Higgs mechanism, the scalar doublet ϕ will take the form:

$$\phi = \begin{pmatrix} 0 \\ \frac{H(x)+v}{\sqrt{2}} \end{pmatrix} \tag{1.68}$$

Upon substitution of 1.68 into 1.67, one deduces that $m_u = \frac{1}{\sqrt{2}} y_u v$ and $m_d = \frac{1}{\sqrt{2}} y_d v$. It is instructive to estimate the value for $y_{u,d}$. As we know $g \sim \frac{2}{3}$, $M_W \sim 80$ GeV and $v = 246$ GeV. But $m_{u,d} \sim 1$ MeV, so $y_{u,d} \sim 10^{-5}$ and only for the top quark $y_t \sim 1$ implying that due to its strong coupling to the $H(x)$ field, the top quark could be a good probe of the Higgs sector of the SM electroweak theory.

1.5.5 The Cabibbo Kobayashi Maskawa (CKM) Matrix

We now generalize the Yukawa Lagrangian 1.67 to include all three generations of quarks. Note that along with intra-generational terms, this Lagrangian may include inter-generational terms as well. The most general expression for the Lagrangian would be:

$$\mathcal{L} = -\Gamma^u_{ij} \left(\bar{q}^i_L \phi^\dagger\right) u^j_R - \Gamma^d_{ij} \left(\bar{q}^i_L \phi\right) d^j_R + H.C. \tag{1.69}$$

where the Yukawa couplings $\Gamma^{u,d,\cdots}$ are in general complex numbers.

After symmetry breaking the Lagrangian 1.69 takes the form:

$$\mathcal{L} = -M^u_{ij} \bar{u}^i_L u^j_R - M^d_{ij} \bar{d}^i_L d^j_R + H.C. \tag{1.70}$$

where:

$$M^u_{ij} = \Gamma^u_{ij}\frac{v}{\sqrt{2}} \quad (1.71)$$

$$M^d_{ij} = \Gamma^d_{ij}\frac{v}{\sqrt{2}} \quad (1.72)$$

The mass matrices M^u, M^d in the basis of weak flavor eigenstates $u_{L,R}, d_{L,R}$ are not real and are non-diagonal, suggesting that the quark flavor eigenstates are different from real particle mass eigenstates (we denote those as $u'_{L,R}, d'_{L,R}$). However, the two bases are related to each other via a unitary transformation. One may readily show that these transformations do not affect the electromagnetic and weak neutral currents. The weak charged currents are affected by this change of basis. The 'strength' of the change is described by the *Cabibbo Kobayashi Maskawa (CKM) Matrix*:

$$\begin{pmatrix} d' \\ s' \\ b' \end{pmatrix} = \begin{bmatrix} V_{ud} & V_{us} & V_{ub} \\ V_{cd} & V_{cs} & V_{cb} \\ V_{td} & V_{ts} & V_{tb} \end{bmatrix} \times \begin{pmatrix} d \\ s \\ b \end{pmatrix} \quad (1.73)$$

The CKM matrix is a unitary matrix with 4 free parameters. To 90% confidence level, the experimentally measured values of the magnitudes of the CKM matrix elements V_{ij} are the following:

$$\begin{bmatrix} 0.9739 \text{ to } 0.9751 & 0.221 \text{ to } 0.227 & 0.0029 \text{ to } 0.0045 \\ 0.221 \text{ to } 0.227 & 0.9730 \text{ to } 0.9744 & 0.039 \text{ to } 0.044 \\ 0.0048 \text{ to } 0.014 & 0.037 \text{ to } 0.043 & 0.9990 \text{ to } 0.9992 \end{bmatrix} \quad (1.74)$$

The quasi-diagonal structure of the CKM matrix explains the dominance of the same generation charged-current decays over different generation charged-current decays.

1.6 Top Quark Production and Decay

1.6.1 Top Production

In hadron colliders, most of the top quarks are produced in pairs via light quark-antiquark annihilation - $q\bar{q} \rightarrow t\bar{t}$ and guon-gluon fusion - $gg \rightarrow t\bar{t}$ processes. Tree level Feynman diagrams for these processes are shown in Figure 1.4. At the Tevatron, $t\bar{t}$ pairs are predominantly produced via light quark-antiquark

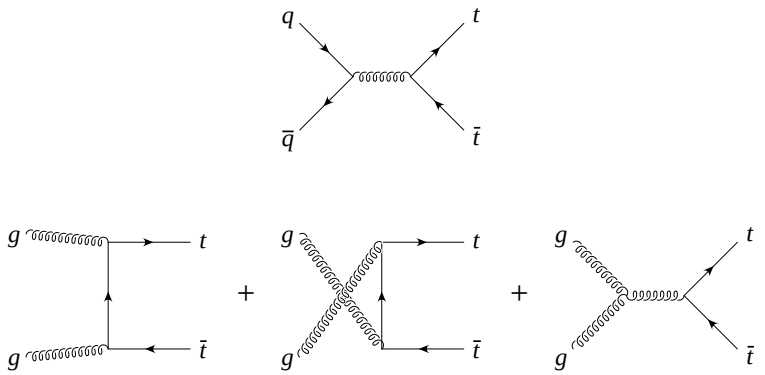

Figure 1.4: Top-quark production via the strong interaction at hadron colliders proceeds through quark-antiquark annihilation (upper diagram) and gluon fusion (lower diagrams).

annihilation ($\sim 85\%$ of the time), while at the LHC the main production mechanism is gluon-gluon fusion ($\sim 90\%$ of the time). In order to understand the reason behind this let us recall the parton[8] model of the proton. Figure 1.5 shows schematically $t\bar{t}$ production in pp collisions at the LHC via the quark annihilation sub-process where each of the quarks carries a fraction x of the proton momentum. Interacting partons at a minimum must have total momentum $\sqrt{\hat{s}}$ such that:

$$\hat{s} = (x_1 P_1 + x_2 P_2)^2 \approx 2 x_1 x_2 P_1 P_2 = x_1 x_2 S \geq 4 m_t^2 \tag{1.75}$$

where $\sqrt{S}$ is the center-of-mass energy of the collider.

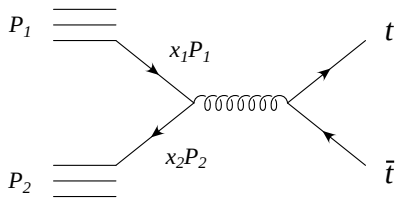

Figure 1.5: The parton-model description of top-quark pair production. A quark carrying fraction x_1 of the proton's momentum P_1 annihilates with an antiquark carrying fraction x_2 of the antiproton's momentum P_2.

Assuming for simplicity that the typical value for $x_1 x_2$ is near the threshold of $t\bar{t}$ production and that $x_1 \approx x_2$, one can deduce that the threshold value for the parton momentum fraction is $x \approx \frac{2m_t}{\sqrt{S}}$. This implies that for the Tevatron ($\sqrt{S} = 1.96$ TeV), typically the momentum fraction is $x = 0.18$, while for the LHC

[8]Parton is the collective name for quarks and gluons.

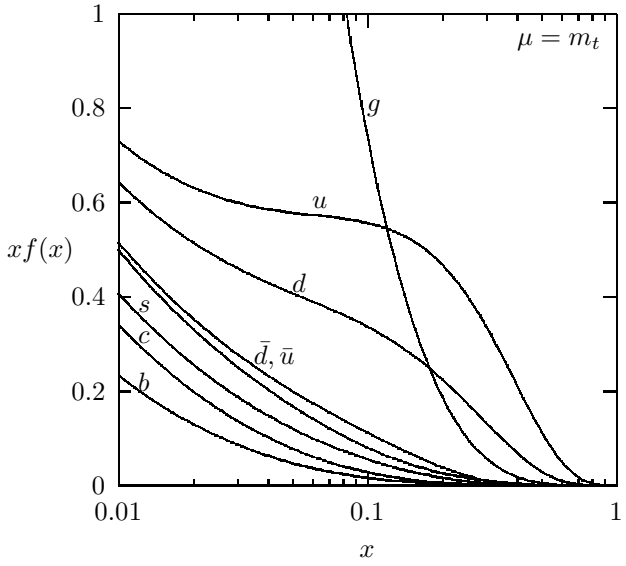

Figure 1.6: Proton parton distribution functions at the scale $\mu = m_t$, relevant for top-quark production.

($\sqrt{S} = 7$ TeV) typically $x = 0.05$. The distribution of proton momentum among the constituent partons inside the proton is given by the parton distribution functions (PDFs), which are shown in Figure 1.6 as a function of momentum fraction x, for the scale $\mu = m_t$. One can clearly see that the $u(x)$-distribution function is larger than the $g(x)$-distribution and that the $d(x)$-distribution is comparable to $u(x)$ for $x = 0.18$. On the other hand, for $x = 0.05$ where partons are energetic enough for top pair production at the LHC, the gluon distribution function dominates that of quarks and therefore $t\bar{t}$ pairs are mostly produced through gg fusion at the LHC.

Another source for top quark production is the electroweak single-top production mechanism, tree level Feynman diagrams of which are shown in Figure 1.7. Single-top production suffers both a smaller production rate (compared to that for $t\bar{t}$ pair production) and also has significantly larger backgrounds. Because of this, the experimental observation of this production mechanism was reported only recently by the CDF [15] and D0 [16] collaborations at the Tevatron and the ATLAS [17] and CMS [18] collaborations at the LHC. Within this dissertation, I will focus solely on the $t\bar{t}$ pair production processes.

1.6.2 Top Decay

As discussed earlier, the CKM matrix in Equations 1.73 and 1.74 has a quasi-diagonal structure, hence the heavy top quark almost exclusively decays via the $t \to Wb$ channel. The SM prediction for the decay width of the top quark at next-to-leading order is:

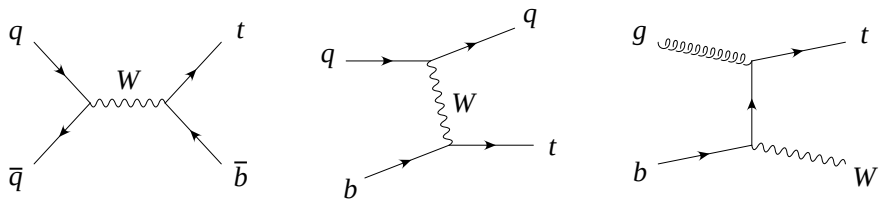

Figure 1.7: Single-top-quark production via the weak interaction. The first diagram corresponds to the s-channel subprocess, the second to the t-channel subprocess, and the third to Wt associated production (only one of the two contributing diagrams is shown).

$$\Gamma_t = \frac{G_F m_t^3}{8\pi\sqrt{2}} \left(1 - \frac{M_W^2}{m_t^2}\right)^2 \left(1 + 2\frac{M_W^2}{m_t^2}\right) \left[1 - \frac{2\alpha_s}{3\pi}\left(\frac{2\pi^2}{3} - \frac{5}{3}\right)\right] \tag{1.76}$$

where terms of the order $m_b^2/m_t^2, \alpha_s^2$ and $(\alpha_s/\pi)^2 M_W^2/m_t^2$ have been neglected. Assuming $m_t = 171$ GeV/c^2, the top decay width is $\Gamma_t = 1.29$ GeV/c^2 implying that $\tau_t = 0.5 \times 10^{-24}$ sec. The latter is much shorter than the minimal time of $\sim 10^{-22}$ sec needed for hadron production, which is the reason behind non-observation of top-flavored bound-state hadrons. On the contrary, due to its very short life time, top is the only quark that can be measured in a 'bare' state.

Following the $t \to Wb$ decay, the b quarks then hadronize to B mesons or hadrons inside jets. The $W^\pm$ boson in turn decays into a quark pair 2/3 of the time and into a charged lepton and its associated neutrino 1/3 of the time. Thus, depending on the W decay mode, the following final state categorization for $t\bar{t}$ pair production process emerges:

1. $t\bar{t} \to W^+ b W^- \bar{b} \to q\bar{q'}b\ q''\bar{q'''}\bar{b}$ (all-hadronic 46.2%)
2. $t\bar{t} \to W^+ b W^- \bar{b} \to q\bar{q'}bl\bar{\nu}_l\bar{b} + \bar{l}\nu_l b q\bar{q'}\bar{b}$ (semi-leptonic 43.5%)
3. $t\bar{t} \to W^+ b W^- \bar{b} \to \bar{l}\nu_l b\ l\bar{\nu}_l\bar{b}$ (dilepton 10.3%)

A detailed description of $t\bar{t}$ pair decay final states and corresponding branching ratios is shown in Figure 1.8.

In the scope of this dissertation I will focus on the dilepton final state of the $t\bar{t}$ pair decays, which although it suffers from a relatively low branching ratio of 10.3%, represents a rather clean signature due to two charged lepton identification requirements that experimentally enables keeping backgrounds well under control. The $t\bar{t}$ dilepton analyses with stringent lepton identification requirements are most sensitive to $e^\pm$ and $\mu^\pm$ decays of the $W^\pm$ and less so for $W \to \tau\nu_\tau$ decays. In contrast to a $t\bar{t}$ dilepton analysis that requires

2 identified charged leptons (2ID analysis) and in order to enhance analysis sensitivity to τ-leptonic decays of $W^{\pm}$ and restore $t\bar{t}$ signal events lost due to charged lepton identification inefficiencies, I utilized a so-called lepton+track (l+track analysis) selection in dilepton events, where the selection requirements on one charged lepton leg are relaxed to require only a high quality inner detector track. I will describe two types of l+track analysis; the *Inclusive* analysis, where the l+track selection is applied on the totality of the accumulated data sample, and the *Exclusive* analysis, where $t\bar{t}$ candidate events selected by the conventional dilepton analysis are explicitly discarded, facilitating the combination of the exclusive l+track and 2ID analysis. It is also important to note that the analysis using the l+track approach is exposed to a different set of systematic uncertainties than that using the 2ID analysis.

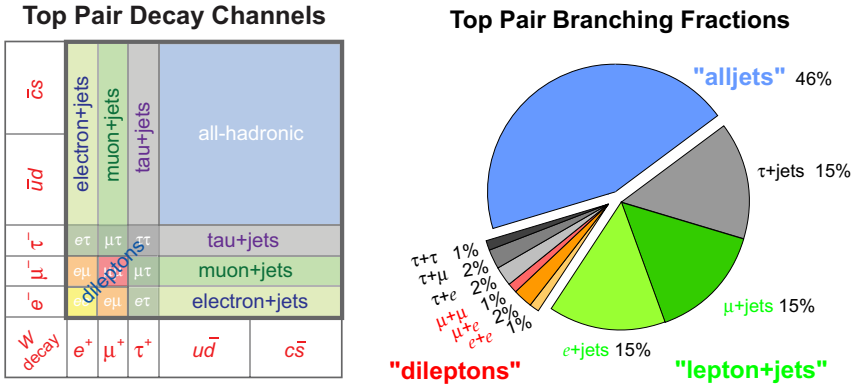

Figure 1.8: The $t\bar{t}$ decay channels (left) and the branching ratios (right).

1.7 The Top quark as a Window to Physics Beyond the Standard Model

We start with the disclaimer stating that the Standard Model of particle physics is a theory which reflects our best current theoretical explanation of observed experimental phenomena and as such it continuously undergoes refinements to account for the 'new physics' processes as soon as the underlying theory behind it is understood.

Let us make a detour on the empirical and philosophical reasons that argue the need for theories beyond the current SM. In the past few decades, various experiments have obtained results that are not possible to explain within the scope of the SM [19]. A brief listing of these includes:

- Dark matter

- Dark energy
- Neutrino masses
- Matter anti-matter asymmetry of the universe

In addition to the above empirical reasons, there are several philosophical aesthetic desires that demand physics beyond the SM. Some of these include:

- The Hierarchy problem, i.e. the non-applicability of the SM beyond the scale $r_H \leq 10^{-19}$m.
- Why there are apparently exactly 3 generations of quarks and leptons
- Why the Yukawa coupling for the top quark (and hence the top quark mass) is so much larger than that of the other fundamental fermions, and the pattern of fermion masses, in general.
- The Higgs sector of the SM Lagrangian does not arise from a first principle theory but rather is introduced 'by hand' to generate the fermion masses.

Another aspect that is presently in the focus of the high energy physics community is the search for the Higgs boson, where the SM prefers a relatively light mass Higgs boson. In December 2011, the ATLAS collaboration presented updated results on the Higgs search using up to 4.9 fb^{-1} of LHC data, where a statistically insignificant excess of events around $m_H \sim 126$ GeV was observed [20]. The excess was characterized by local significance of 3.6σ with contributions from $H \rightarrow \gamma\gamma$, $H \rightarrow ZZ^* \rightarrow 4l$ and $H \rightarrow WW^* \rightarrow l\nu l\nu$ analyses. The measured global significance, taking into account the Look-Elsewhere-Effect (LEE) was $\sim 2.3\ \sigma$. The updated CMS results using the same final states also claimed an observation of an event excess around ~124 GeV with 2.6 σ local significance and 1.9 σ global after correcting for the LEE in the low mass region [21]. Figure 1.9 (a) and (b) summarize the most recent results on the limits of σ/σ_{SM} obtained by the ATLAS and CMS collaborations. In addition, the new W mass measurement by CDF and the latest precision determination of the mass of the top quark from Fermilab triangulate the location of the Higgs particle and restrict its mass to less than 145 GeV. Moreover, as Figure 1.11 illustrates the updated Tevatron result on direct searches for the SM Higgs boson in $p\bar{p}$ collisions reported an excess of data events with respect to background estimation in the mass range $115 < m_H < 135$ GeV. At $m_H = 125$ GeV, the local significance of the event excess is 2.7σ, while the global significance corrected for the LEE is 2.2σ [22]. This is in excellent agreement with the latest direct Higgs boson searches at the LHC as shown in Figure 1.10 [23]. The entire high energy physics community is looking forward to 2012 when a definitive answer to the existence/non-existence of the SM Higgs boson is expected.

Let us now discuss the top quark in the context of BSM physics. We showed in section 1.5.4 that the top quark has the largest Yukawa coupling to the Higgs sector ($y_t \sim 1$) making it the most massive fundamental particle. Due to its large mass, top has been exploited in a number of BSM theories. Examples include the top color model, where top is responsible for triggering electroweak symmetry breaking (EWSB) or the MSSM model where top allows the Higgs mass to survive the LEP bound [24]. Several models rely on top as a facilitator for an alternative EWSB mechanism, where the top quark is responsible for the generation of boson and/or fermion masses. Examples of such theories are Topcolor [25–28], and top see-saw [29–31]. More recent models use the top as means to compensate for the large radiative corrections to the Higgs mass. In SUSY such a mechanism entails the existence of top scalar partners; the Little Higgs theory introduces fermion partners instead. Hence, many rich and theoretically motivated BSM theories predict new physics in connection with the top quark, which motivates in-depth studies of top quark production and decay properties [32–39].

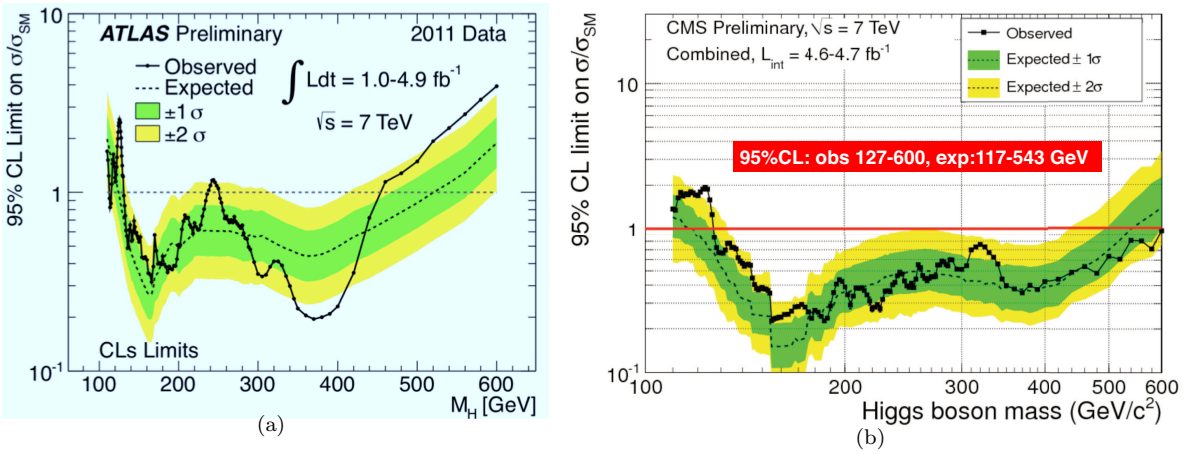

(a) (b)

Figure 1.9: The combined 95% C.L. upper limits on the signal strength parameter $\mu = \sigma/\sigma_{SM}$, as a function of the SM Higgs boson mass in the range $110 - 600$ GeV/c^2 obtained by ATLAS (left) [20] and CMS (right) [21] collaborations. The observed limits are shown by solid symbols. The dashed line indicates the median expected 95% CL value for the background-only hypothesis, while the green (yellow) band indicates the range expected to contain 68% (95%) of all observed limit excursions from the median, respectively.

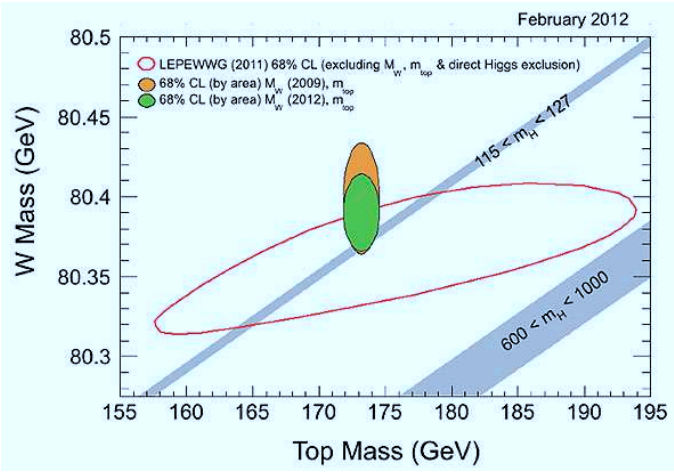

Figure 1.10: The new CDF result for the W boson mass, combined with the world's best value for the top quark mass, restricts the Higgs mass to the green area, requiring it to be less than 145 GeV.

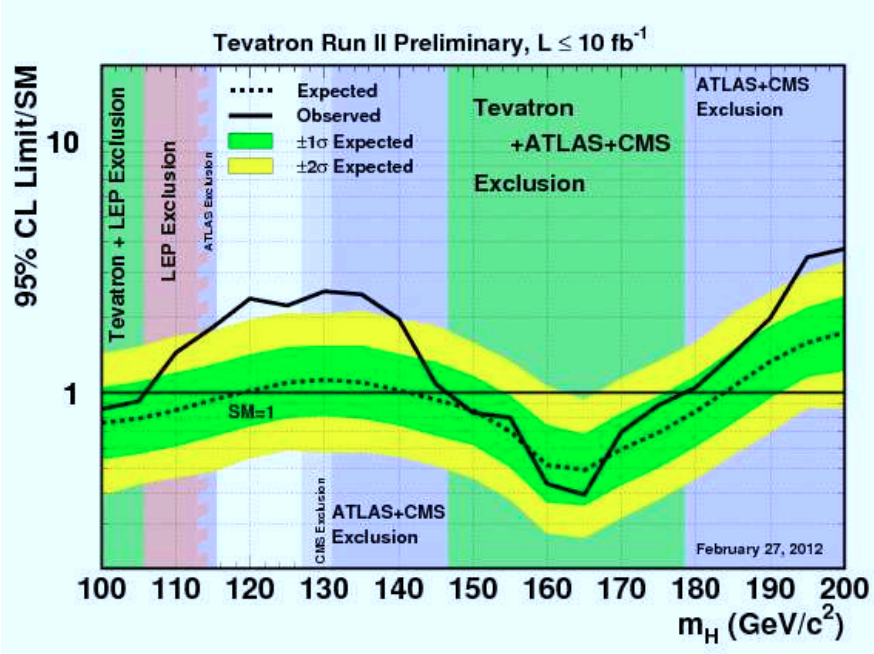

Figure 1.11: Observed and expected (median, for the background-only hypothesis) 95% C.L. upper limits on the ratios to the SM cross section, as a function of the Higgs boson mass for the combined CDF and D0 analyses. The limits are expressed as a multiple of the SM prediction for test masses (every 5 GeV) for which both experiments have performed dedicated searches in different channels. The points are joined by straight lines for better readability. The bands indicate the 68% and 95% probability regions where the limits can fluctuate, in the absence of a signal. The limits displayed in this figure are obtained with Bayesian calculation.

Chapter 2

$t\bar{t}$ Cross Section Measurement

2.1 Introduction

One needs to work with a quantitative measure of $t\bar{t}$ pair production that both has a sound theoretical prediction and can be measured experimentally with reasonable precision. Such a quantitative measure is the $t\bar{t}$ pair production cross section that, as we will see has an interpretation of the production probability[1] for a $t\bar{t}$ pair in a pp collision event. The $t\bar{t}$ cross section is measured in barns and has units of a cross sectional area ($1\text{b} = 10^{-24}\text{cm}^2$). Hence, the $t\bar{t}$ cross section can also be intuitively interpreted as the effective cross sectional area over which two protons interact to produce a $t\bar{t}$ pair.

The cross section for top pair production is related to the invariant amplitude $\mathcal{M}$ of the $pp \to t\bar{t}$ process via the expression:

$$d\sigma_{t\bar{t}} = \frac{|\mathcal{M}|^2}{F} d\mathcal{Q}, \tag{2.1}$$

where $d\mathcal{Q}$ is the Lorentz invariant phase space factor and F is the incident flux, which measures the number of protons per beam passing through unit area of overlapping beams per unit time (for more details see [41]).

As discussed in Section 1.6.1, in pp collision events most of the top quarks are produced in pairs through quark annihilation - $q\bar{q} \to t\bar{t}$ and guon-gluon fusion - $gg \to t\bar{t}$ parton subprocesses. Hence, the total cross section for the $t\bar{t}$ pair production cross section can be expressed as the convolution of these sub-processes with the corresponding parton distribution functions of the proton:

$$\sigma_{t\bar{t}} = \sum_{ij} \int dx_i dx_j f_{i,p}(x, Q^2) f_{j,p}(x_j, Q^2) \hat{\sigma}_{ij}(ij \to t\bar{t}) \tag{2.2}$$

[1] Strictly speaking one needs to normalize the $t\bar{t}$ cross section by the one for total pp interaction to get the top pair production probability. For pp LHC collisions at $\sqrt{s} = 7$ TeV the total cross section is $\sigma_{\text{total}} = 98$ mb [40]. Hence, the probability for $t\bar{t}$ pair production at LHC is 1.68×10^{-9}.

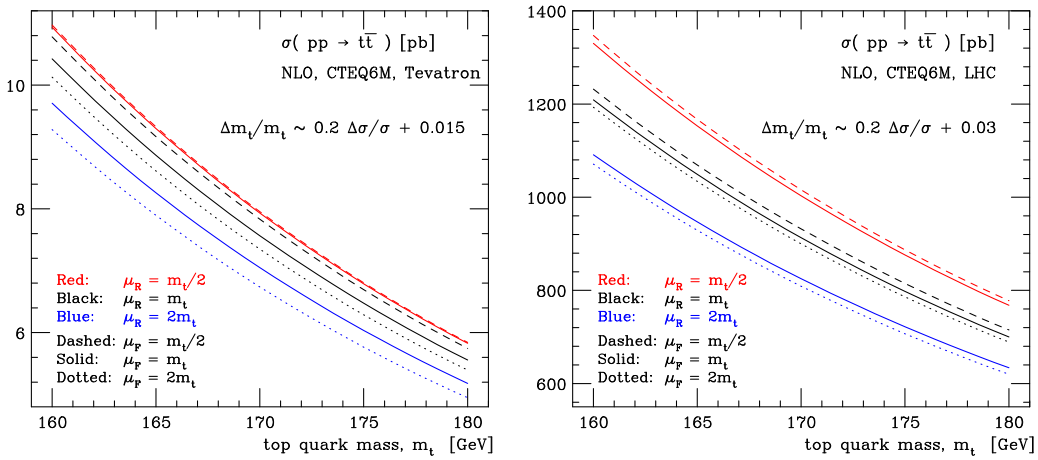

(a) (b)

Figure 2.1: The NLO $t\bar{t}$ production cross section as a function of the top quark mass m_t including scale dependence at the Tevatron (a) and the LHC (b) [42].

where $x_i(x_j)$ is the momentum fraction carried by the parton i (j) in the proton that belongs to the first (second) beam, respectively.

One also expects the top pair production cross section to be dependent on the top quark mass, since the heavier the t-quark, the harder it is to produce it. Figure 2.1 shows the $t\bar{t}$ production cross section dependence on the top quark mass. The bottom line is that a 1 GeV increase in m_t corresponds to a 0.25 pb (25 pb) decrease in the $t\bar{t}$ cross section at the Tevatron (LHC), respectively. Note that Figure 2.1(b) shows the $t\bar{t}$ cross section dependence on m_t for the case of nominal $\sqrt{s} = 14$ TeV center-of-mass energy of the LHC.

The most recent calculation of the $t\bar{t}$ pair production cross section at NLO (next-to-leading-log soft gluon resummation), for the case of $\sqrt{s} = 1.96$ TeV center of mass collision at the Tevatron assuming $m_t = 171$ GeV/c^2 with CTEQ6.5 PDFs, predicts a value of $7.61^{+0.30}_{-0.53}$ (scales) $^{+0.53}_{-0.36}$ (PDFs) pb [43–46]. Experimental measurements of this quantity by CDF and D0 collaborations are: $\sigma_{CDF} = 7.5 \pm 0.31$ (stat) $\pm$ 0.34 (syst) $\pm$ 0.15 (theory) pb [47], and $\sigma_{D0} = 7.56^{+0.63}_{-0.56}$ (stat + syst + lumi) pb [48], both of which are in good agreement with the SM prediction. Figure 2.2 summarizes the most recent results of $t\bar{t}$ pair production cross section measurements from Tevatron experiments.

For the case of the center of mass energy of $\sqrt{s} = 7$ TeV, characteristic for present day LHC pp collisions, the SM prediction for the $t\bar{t}$ cross section production at approximate NNLO, using CTEQ6.6 PDFs and assuming $m_t = 172.5$ GeV is $\sigma_{SM} = 164.57^{+11.45}_{-15.78}$ pb [43–46], approximately 20 times larger than that for the Tevatron collider. In this dissertation, I will present the result of the top pair production cross section measurement using 7 TeV, $\mathcal{L} = \int Ldt = 698$ pb^{-1} of pp collision data collected with the ATLAS detector.

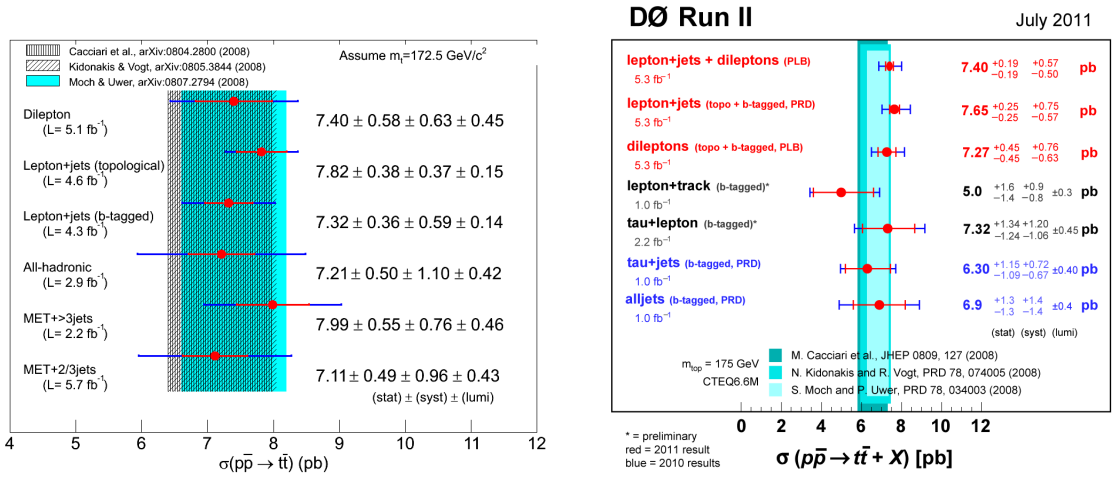

(a) (b)

Figure 2.2: The $t\bar{t}$ production cross section measurement results for Tevatron experiment: CDF (a) [47] and D0 (b) [48].

One can express the total number of produced $t\bar{t}$ pairs over some period of time T as:

$$N_{t\bar{t}} = \sigma_{t\bar{t}} \cdot \int_T Ldt \tag{2.3}$$

where $\mathcal{L} = \int Ldt$ is the integrated luminosity associated with the colliding beams and is proportional to the number of pp collisions over the time period T. Since there are detector geometrical acceptance limitations and signal selection requirement inefficiencies, some of the $t\bar{t}$ events are not detected. The fraction of detected signal events is determined using Monte Carlo simulation and is introduced into the Equation 2.3 as a factor A. Further, the fraction A is corrected by a factor ϵ to account for the mis-modeling of lepton reconstruction, finite lepton identification and lepton trigger efficiency in data and Monte Carlo simulation, thus yielding the following expression that we used to measure the $t\bar{t}$ pair production cross section:

$$\sigma_{t\bar{t}} = \frac{N_{t\bar{t}}^{\text{obs}}}{A \cdot \epsilon \int Ldt} \tag{2.4}$$

2.2 Physics Motivation for $t\bar{t}$ Pair Production Cross Section Measurement

In this section, I summarize the reasons that motivate the significance of the measurement of the top quark pair production cross section in the dilepton channel using the l+track approach, especially noting that the ATLAS detector as of December 2011 has completed its first year of operation and both the detector commissioning program and establishing 'benchmark' SM signals in the new 7 TeV center-of-mass energy regime are the primary focus of the ATLAS collaboration. Although some of the incentives to perform this measurement were already mentioned in this text, I will repeat those in the compilation below:

- Due to its very short lifetime of $\tau_t = 0.5 \times 10^{-24}$ sec, the top quark decays before top-flavored hadron formation, thus enabling direct measurements of the properties of an otherwise strong color confined quark.
- Uncertainties on the theoretical $t\bar{t}$ cross section prediction are currently at the 10% level and a comparison with experimental measurement is an excellent test for perturbative QCD predictions.
- The top quark has the largest Yukawa coupling $y_t \sim 1$, hence top is characterized as the strongest coupling to the Higgs sector, and as such serves as source of inspiration for many alternative BSM theories.
- A significant excess of the measured $t\bar{t}$ cross section from the predicted SM value would imply a BSM top production mechanism, while a significant deficit suggests alternative top decay channels (e.g. $t \to H^+ b$), different from $t \to Wb$ which according to the CKM matrix must occur very nearly 100% of the time.
- An abundant $t\bar{t}$ data sample is well-suited for the use as in-situ calibration tool for jet, lepton, b-tagging algorithms.
- $t\bar{t}$ pair production is a major background for many new BSM physics scenarios.
- The $t\bar{t}$ dilepton final state represents a rather clean signature due to two lepton identification requirements that enables backgrounds to be kept well under control.
- The $t\bar{t}$ cross section measurement in dilepton channel enables performing an explicit check of the lepton universality principle.

- The l+track approach to dilepton event selection enhances the analysis sensitivity to τ-leptonic decays of the $W^{\pm}$ boson and restores signal events lost due to lepton identification inefficiencies.

All of the above items motivate the importance of an in-depth understanding and thorough research of the top quark sector, where a precise measurement of the top quark pair production cross section is a key descriptive quantity.

Chapter 3

CERN: The Large Hadron Collider and the ATLAS Detector

3.1 Introduction

The European Organization for Nuclear Research (CERN) is an international laboratory for particle physics research operating the world's largest accelerator facility. Founded in September of 1954, CERN was the cradle for the number of fundamental discoveries that shaped, changed and expanded the knowledge of mankind about Nature and the Universe. Some of those include: the discovery of neutral weak currents in 1973, the discovery of $W^{\pm}$ and Z^0 bosons in 1983, the discovery of direct CP-violation in 1999 and the invention of the World Wide Web in 1990. More than 10,000 scientists and engineers from all over the world rely on CERN facilities in their quest for an understanding of the fundamental laws of Nature.

3.2 The Large Hadron Collider

The Large Hadron Collider (LHC) is a two-ring-superconducting-hadron accelerator and is the largest and highest-energy collider in the world. The collider is located ~ 100 m underground in a 27 km circular tunnel initially built for the Large Electron-Positron Collider (LEP) [49]. The LHC was designed to provide pp collisions at a 14 TeV[1] center-of-mass energy with an instantaneous luminosity of 10^{34} cm^{-2}s^{-2} [2]. The LHC is part of the CERN accelerator complex system that prepares the protons (or heavy ions) for injection into the LHC. More specifically:

1. The protons are obtained by stripping off electrons from hydrogen atoms, accelerated to 50 MeV by the LINAC (linear particle accelerator) and fed to the Proton Synchrotron Booster (PSB).

2. The PSB accelerates protons to 1.4 GeV and injects them into the Proton Synchrotron (PS).

3. The PS further accelerates protons to 26 GeV and injects them into the Super Proton Synchrotron (SPS).

[1] At the initial stage (i.e. 2009 - 2012) of the LHC operations it was decided to limit the center-of-mass energy for the pp collisions to 7 TeV.

4. The SPS brings the proton energy to 450 GeV and prepares them for the injection into the LHC.

Figure 3.1 gives the schematic view of CERN accelerator facility complex.

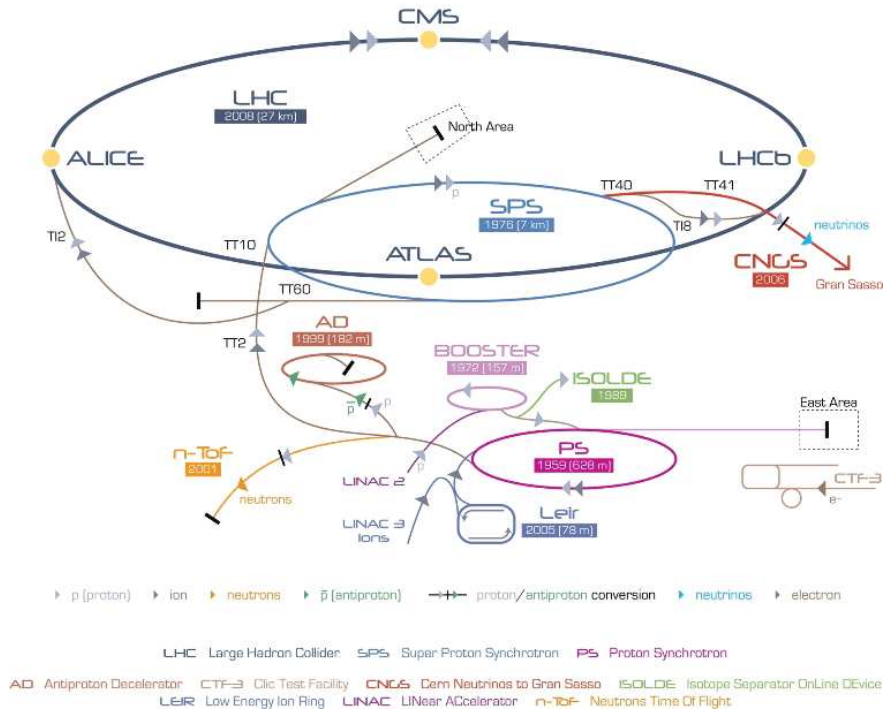

Figure 3.1: The schematic view on accelerator facility complex at CERN.

Proton beams at the LHC are organized as a train of 2808 proton bunches, where each bunch contains 1.15×10^{11} protons at nominal proton fill, is a few cm in length and has ~ 1 mm transverse dimension. At the collision point, bunches receive an extra squeeze from quadrupole magnet pairs and become ~ 16 μm transversely. At the entrance into the LHC, the protons are split into two beams that are brought to collision at four points around the LHC ring. At each of the collision points large detectors have been constructed to study various phenomena. The detectors and corresponding collaborations are: ALICE, LHCb, CMS and ATLAS. Details of the ATLAS detector are provided in the next section.

3.3 The ATLAS Detector

ATLAS is a general-purpose experiment designed to exploit the full extent of the exciting particle physics opportunities for fundamental discoveries at LHC [2]. A schematic view of the ATLAS detector is shown in Figure 3.2. Some of the aspects of the rich physics potential of the LHC include:

- Precision measurement of QCD, electroweak and flavour physics processes due to high luminosity and

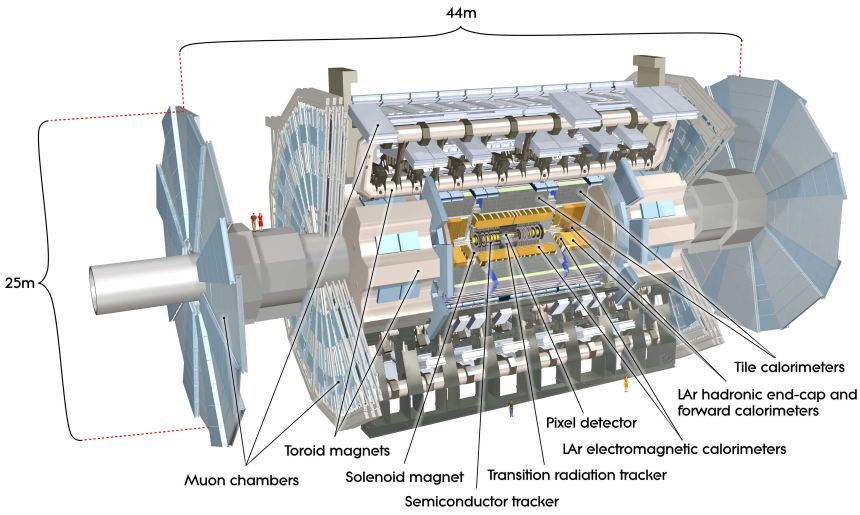

Figure 3.2: Cut-away view of the ATLAS detector. The dimensions of the detector are 25 m in height and 44 m in length. The overall weight of the detector is approximately 7000 tonnes.

large cross section values at the LHC.

- A vast physics program in the top sector (cross section, mass, spin, couplings etc.) due to the remarkable top production rate at the LHC.

- Searches for the Higgs boson. The ATLAS detector subsystems were designed to maximize the performance characteristics of the detector in searches for the Higgs boson, which remains the only undiscovered mediator of interactions as predicted by the SM. The excellent characteristics of the ATLAS detector enable successful Higgs searches in a number of decay scenarios.

- Searches for heavy W' and Z' bosons with masses up to $\sim$ 6 TeV. In order to study their leptonic decays, high-resolution lepton P_T measurement and charge identification are needed in the p_T- range of a few TeV.

- Quark compositeness, as probed through high p_T jet cross section measurements.

- Searches for supersymmetric particles (squarks, gluinos) and low to intermediate scale gravity/higher dimensions through reliable E_T^{miss} measurement.

The above mentioned physics research goals define those requirements that the ATLAS detector system must meet in order to successfully carry out these physics programs. Table 3.1 summarizes the general performance goals for each of the ATLAS detector subsystems.

Table 3.1: General performance goals of the ATLAS detector. Note that for high p_T muons, the muon spectrometer performance is independent of the inner-detector system. The units for E and p_T are in GeV.

Detector Subsystem	Required resolution	η coverage	
		Measurement	Trigger
Tracking	$\sigma_{p_T}/p_T = 0.05\%\ p_T \oplus 1\ \%$	± 2.5	-
EM Calorimetry	$\sigma_E/E = 10\%\ /\sqrt{E} \oplus 0.7\ \%$	± 3.2	± 2.5
Hadronic calorimetry (jets)			
barrel and end-cap	$\sigma_E/E = 50\%\ /\sqrt{E} \oplus 3\ \%$	± 3.2	± 3.2
forward	$\sigma_E/E = 100\%\ /\sqrt{E} \oplus 10\ \%$	$3.1 < \lvert\eta\rvert < 4.9$	$3.1 < \lvert\eta\rvert < 4.9$
Muon spectrometer	$\sigma_{p_T}/p_T = 10\%$ at $p_T = 1$ TeV	± 2.7	± 2.4

A right-handed coordinate system is used to describe the ATLAS detector and the particles emerging from pp collisions, and is defined as follows: the nominal interaction point is taken as the origin, the beam direction defines the z-axis, the positive x-axis is defined as pointing from the interaction point to the center of the LHC ring, and the positive y-axis is defined as pointing upwards. The azimuthal angle ϕ is measured around the beam axis, and the polar angle θ is the angle from the beam axis. The pseudorapidity $\eta = -\ln(\tan(\theta/2))$ is frequently used instead of the polar angle θ. In this thesis I will refer to the transverse momentum $p_T \equiv \sqrt{p_x^2 + p_y^2}$, transverse energy $E_T \equiv E \sin\theta$, and missing transverse energy E_T^{miss} which are defined as projections of corresponding variables in the transverse plane.

The magnet configuration of the ATLAS detector consists of a thin superconducting solenoid surrounding the tracker cavity, and three large superconducting toroids (one barrel and two end-caps) arranged with an eight-fold azimuthal symmetry around the calorimeters. This fundamental choice has dictated the design of the rest of the detector.

3.3.1 The Inner Detector

The Inner Detector (ID) is the innermost part of the ATLAS detector. The ID is immersed in a solenoidal magnetic field of 2.0 T. It consists of independent, yet complementary charged particle tracking sub-detectors. At the inner-most radii, high-resolution charged track pattern recognition capabilities are available using discrete space-points from silicon pixel layers (typically three pixel layers are traversed by a charged particle) and stereo pairs of silicon microstrip (SCT) layers. For the SCT, eight strip layers are traversed by each track. The precision tracking sub-detectors (Pixel and SCT) cover the pseudorapidity region $|\eta| < 2.5$. In the barrel region, they are arranged in concentric cylinders around the beam axis, while in the end-cap regions they consist of disks perpendicular to the beam axis. The total number of pixel detector read out channels is 80.4 million and for the SCT the tracking information has 6.3 million read out channels. At larger radii,

the transition radiation tracker (TRT) consists of many layers of gaseous straw tube elements interleaved with transition radiation material. The typical TRT yield per track is approximately 36 hits, which enables continuous tracking to enhance the pattern recognition and improve charged particle momentum resolution over $|\eta| < 2.0$ and electron identification complementary to that of the calorimeter over a wide range of energies. In the barrel region, the 144 cm long TRT straws are parallel to the beam axis. In the end-cap region the TRT straws are arranged radially and are 37 cm long. The total number of TRT readout channels is $\sim 350,000$. The tracker accounts for $0.5X_0$ to $2X_0$ of the material in front of the calorimeters up to $|\eta| = 2.5$. A cut-away view of the ATLAS Inner Detector is shown in Figure 3.3.

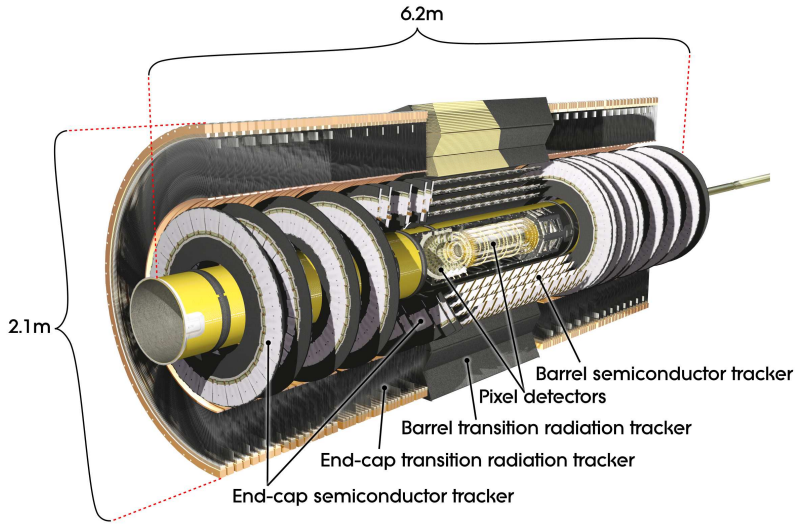

Figure 3.3: Cut-away view of the ATLAS Inner Detector.

3.3.2 Calorimetry

Calorimeters cover the range $|\eta| < 4.9$, using different techniques suited to the widely varying requirements of the physics processes of interest. Over the η-region matched to the ID, the fine granularity of the EM calorimeter is ideally suited for precision measurement of electrons and photons. The coarser granularity of the rest of the calorimeter is sufficient to satisfy the physics requirements for jet reconstruction and E_T^{miss} measurements. It is also important to note that the calorimeter depth is designed and constructed such that the calorimeter provides good containment of electromagnetic and hadronic showers, ensuring the precision measurement requirements summarized in Table 3.1. Figure 3.4 depicts ATLAS subdetectors that constitute the ATLAS calorimetry.

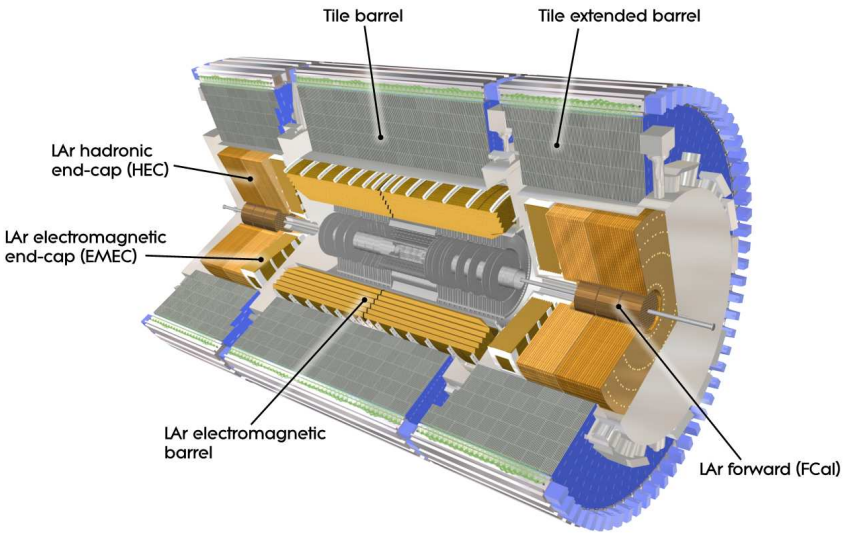

Figure 3.4: Cut-away view of the ATLAS calorimeter system.

Liquid Argon Electromagnetic Calorimeter

The EM calorimeter is divided into a barrel part ($|\eta| < 1.475$) and two end-cap components ($1.375 < |\eta| < 3.2$), each located in individual cryostats. The EM calorimeter is lead-LAr detector with accordion-shaped kapton electrodes and lead absorber plates over its full coverage. The accordion geometry for the absorbers and electrodes is chosen as such in order to provide full ϕ-coverage without any cracks and fast extraction of the EM shower signal at the rear and at the front of the electrodes. This enables a very uniform performance in terms of linearity and resolution as a function of ϕ.

Tile Hadronic Calorimeter

The Scintillating Tile Hadronic Calorimeter (TileCal) is composed of a Long Barrel (LB) and two Extended Barrel (EB) cylindrical structures spanning the pseudorapidity region $|\eta| \leq 1.7$. Azimuthally, the barrel and extended barrels are divided into 64 modules, each spanning $2\pi/64$ azimuthal angle. In the radial direction, the TileCal extends from an inner radius of 2280 mm to an outer radius of 4230 mm. Each of the TileCal modules is composed of a grid of alternating layers of steel plates (absorber) and scintillator tiles (active material) with period of 18 mm (Fig. 3.5(a)). Tiles are oriented perpendicular to the colliding beams and are radially staggered in depth. The Tile calorimeter contains 11 different sizes of trapezoidal shaped tiles, ranging from about 200 mm to 350 mm in length and 97 mm to 187 mm in radial width. All tiles are 3 mm thick. Fig. 3.5(b) and Table 3.2 give details on the tile characteristics. Each tile has two holes 9 mm in

diameter always placed 13.5 mm away from the tile extremity (Fig. 3.5(b)). Typically, the tile inner radius hole is used for metal fixing rods and the tile outer radius hole is used for the ^{137}Cs calibration tubes. In tile row 7 of EB modules both holes serve for $Cs^{137}\gamma$-source passage purposes. The scintillating tiles are read out via wavelength shifting (WLS) fibers on both sides of the tile into two separate PMTs. In the LB eight WLS fibers of different lengths are used per period per side to achieve the 3 longitudinal (i.e. depth) samplings, while in the EB six WLS fibers of different lengths are used, as summarized in Table 3.2. The TileCal is segmented longitudinally into three depth layers, which are about 1.4 (sampling A), 4.0 (sampling BC) and 1.8 (sampling D) interaction lengths thick at η=0 for Long Barrel modules. In the Extended Barrel, the second depth layer is thinner, whereas the third depth layer is thicker compared to LB modules as shown in Fig. 3.6. The quasiprojective read out cells are formed by grouping the WLS fibers into different PMTs. Cells are organized in pseudo-projective towers oriented towards the interaction point. The cell division of the 3 samplings of the Tile Calorimeter is shown in Fig. 3.6. The resulting cell granularity is: $\Delta\eta \times \Delta\phi = 0.1 \times 0.1$ (0.2×0.1 in the last longitudinal layer). A schematic drawing is given in Fig. 3.6.

Table 3.2: Tile Dimensions and Cell Structure. The labeling of the dimensions corresponds to the drawing of the tile shown in Fig. 3.5(b)

Tile Size	A mm	B mm	H mm	E mm	Sampling		Fiber	
					LB	EB	LB	EB
1	231.0	221.3	97	70	A	A	1	1
2	240.8	231.3	97	70	A	A	2	2
3	250.6	241.0	97	70	A	A	1	1
4	262.0	249.5	127	100	B	B	3	3
5	274.8	262.3	127	100	B	B	4	4
6	287.5	275.0	127	100	B	B	3	3
7	302.3	287.8	147	120	C	B	5	4
8	317.0	302.6	147	120	C	D	6	5
9	331.7	317.3	147	120	C	D	5	6
10	350.4	332.0	187	160	D	D	7	5
11	369.0	350.7	187	160	D	D	8	6

LAr Hadronic End-cap Calorimeter

The Hadronic End-Cap Calorimeter (HEC) consists of two independent wheels per end-cap. Each of the wheels is located behind the end-cap electromagnetic calorimeter and share the same LAr cryostat. Each wheel is built from 32 identical wedge-shaped modules, assembled with fixtures at the periphery and at the central bore. Each wheel is divided into two segments in depth, for a total of four layers per end-cap. Copper plates are interleaved with 8.5 mm LAr gaps, providing the active medium for this sampling calorimeter.

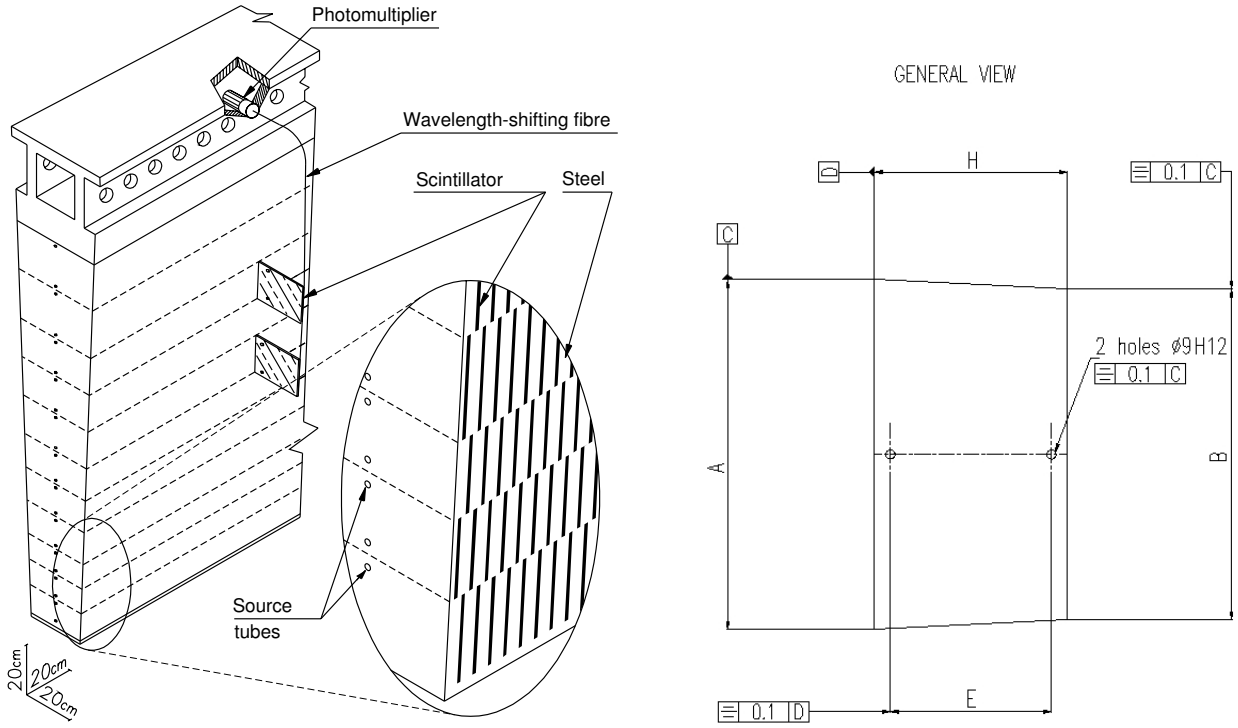

(a) Calorimeter Structure

(b) Scintillating Tile

Figure 3.5: A blowup of the Tile calorimeter structure (a) and drawing of a scintillating tile with the tile outer and inner radius holes for the passage of the Cs^{137} source (b).

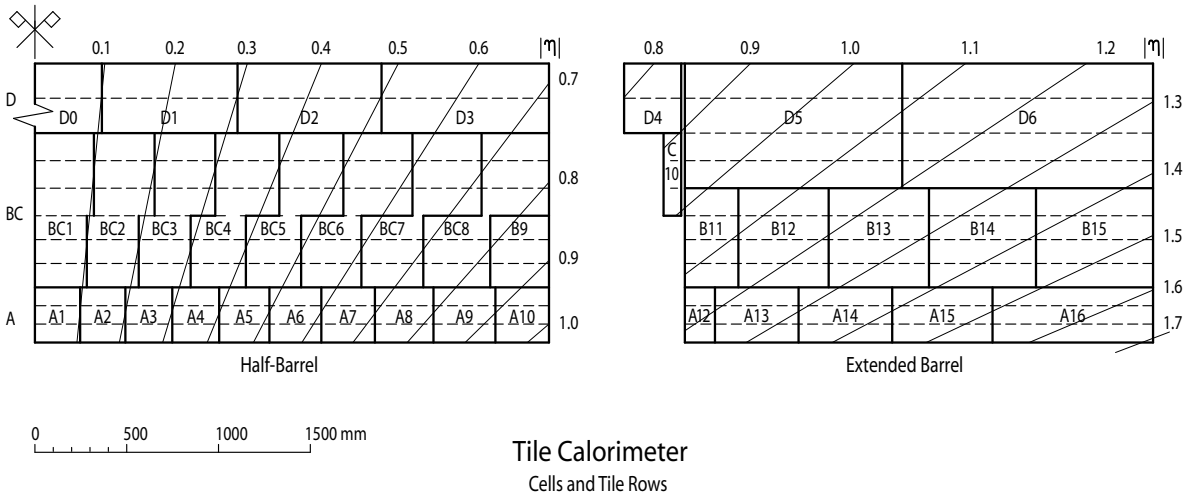

Figure 3.6: Layout of cells (solid lines) and tilerows (dashed lines) in the Barrel and Extended Barrel Tile calorimeter sections. The lines defining different η regions are also shown.

LAr Forward Calorimeter

The Forward Calorimeter (FCAL) is integrated into the end-cap cryostats, as this facilitates uniform calorimetric coverage and reduced radiation background levels in the muon spectrometer. The FCal is ~ 10 interaction lengths deep, and consists of three modules in each end-cap; the first module is made of copper and is optimized for electromagnetic measurements, the second and the third are made of tungsten and measure predominantly the energy of hadronic interactions. Each module consists of a metal matrix, with regularly spaced longitudinal channels filled with an electrode structure consisting of concentric rods and tubes parallel to the beam axis. The LAr in the gap between the rod and the tube is the sensitive ionaziation medium.

3.3.3 Muon Spectrometer

Muons are minimum ionizing particles and will typically pass through the ATLAS detector without depositing a substantial portion of their kinetic energy in the calorimeter. The muon spectrometer (MS) is used for muon momentum reconstruction. The muon system identifies tracks in the region $|\eta| < 2.7$ with precision measurements up to $|\eta| = 2.5$. Special transition regions in the MS lie in $|\eta| < 0.1$ and $1.0 < |\eta| < 1.3$. The MS comprises four main components: Muon Drift Tubes (MDT), Cathode Strip Chambers (CSC), Resistive Plate Chambers (RPC), and Thin Gap Chambers (TGC)[2]. Over most of the η-range, a precision measurement of the track coordinate in the principal bend direction of the magnetic field is provided by MDTs. In order to ensure reliable operation of the MDTs, the sense wires are mechanically isolated in each drift tube. In the larger η-region, track coordinates are measured with the Cathode Strip Chambers (CSCs' are multi-wire proportional chambers with their cathodes segmented into strips). The MS trigger system covers the region up to $|\eta| < 2.4$. Resistive Plate Chambers (RPC) are used in the barrel region, while Thin Gap Chambers (TGC) in the end-cap regions. The MS trigger system has three main functions: pp bunch-crossing identification, provide well-defined muon P_T thresholds, and independent measurement the of muon coordinate in the direction orthogonal to that determined by the ID precision-tracking chambers.

3.3.4 Luminosity Detectors

The Beam Condition Monitor (BCM) detector is used to monitor beam losses and to provide fast feedback to the accelerator operations team. It is a core component of the detector protection system, in that it provides a fast accelerator abort signal in the event of substantial beam loss. The BCM consists of two arms of diamond sensors located at $z = \pm 184$ cm and $r = 5.5$ cm and uses programable front-end electronics to

[2]Chambers are also used for triggering.

histogram the single-sided and coincidence rates as a function of Bunch Crossing Identifier (BCID). Thus, bunch-by-bunch rates are available for luminosity determination and monitoring.

At ±17 m from the interaction point lies the LUCID (LUminosity measurement using Cerenkov Integrating Detector) is specifically designed for measuring the *pp* instantaneous luminosity at ATLAS. It consists of 16 optically reflecting aluminum tubes filled with C_4F_{10} (perfluorobutane) gas surrounding the beam pipe on each side of the interaction point. Cerenkov photons created by charged particles in the gas are reflected by the tube walls until they reach PMTs situated at the back end of the tubes. The PMT signal further amplified and digitized with 80 samplings. If the pulse height of the signal is larger than the discriminator threshold a tube counts a 'hit'.

3.3.5 Magnet System

The ATLAS magnet system consists of four large superconducting magnets. The schematic view of the magnet system is shown in Figure 3.7 and includes:

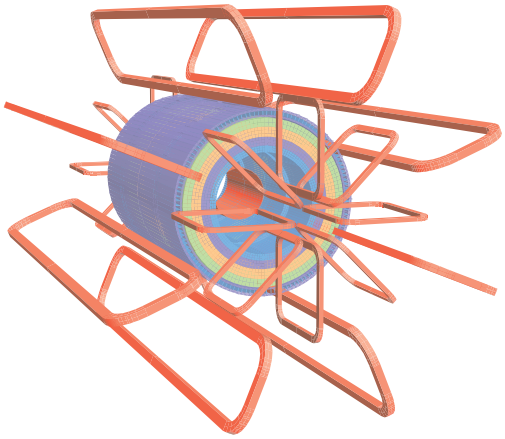

Figure 3.7: Geometry of magnet windings and tile calorimeter steel. The eight barrel toroid coils, with the end-cap coils interleaved are visible. The solenoid winding lies inside the calorimeter volume. For the sake of clarity the forward shielding disk is not displayed.

- a solenoid aligned on the beam axis that provides a 2.0 T axial magnetic field for the ID. It also minimizes the radiation thickness in front of the barrel EM calorimeter
- a barrel and two end-cap toroid magnets, which produce magnetic fields of $\sim$ 0.5 T and 1 T respectively for the muon trajectory bending and subsequent momentum measurement.

Due to the above described structure of the ATLAS magnets, charged particle tracks are bent in the $r-\phi$ plane while traversing the ID immersed in the solenoidal magnetic field and bent in the $r-z$ plane in

the MS. The bend parameters are further used to measure particle descriptive parameters such as charge, momentum, mass, etc.

3.3.6 Trigger

At the design luminosity of 10^{34} cm^{-2} s^{-1} the pp collision rate at LHC is ~ 1 GHz, while the overall ATLAS event data recording rate is limited to 200 Hz, due to technology and resource limitations. Hence, the ATLAS detector needs a robust trigger system that provides an overall rejection factor of 5×10^6 against minimum-bias processes and maintains maximum efficiency for the new physics. The ATLAS trigger system is organized in three levels LEVEL 1 (L1), LEVEL 2 (L2), and Event Filter (EF).

The L1 trigger searches for events with high p_T muons, electrons, photons, jets, 3-prong τ decays, substantial missing and high total transverse energy. The L1 trigger decision is based only on a subset of detector information, reducing the L1 trigger rate to 75 kHz, limited by the current bandwidth of the readout system (upgradable to 100 kHz). High p_T muons are identified using TGCs and CSCs as described above. Reduced-granularity information from all calorimeters provides the input for the L1 trigger calorimeter information. In each event, the L1 trigger also defines one or more Regions-of-Interest (RoI), i.e. the η and ϕ coordinates of those regions of the detector where the selection process has identified interesting features.

RoI information provided by the L1 trigger is further used to seed the L2 trigger which uses full granularity and precision detector data within the RoI in its selection process. The L2 trigger reduces the rate to $\sim$ 3.5 kHz with an event processing time of about 40 ms averaged over all events. The last stage of the event selection is carried out by the Event Filter, which reduces the trigger rate to 200 Hz. The EF selection requirements are implemented using a computer farm with offline analysis procedures, with an average event processing time of the order of a few seconds. Figure 3.8 shows the schematic summary view of the ATLAS trigger system.

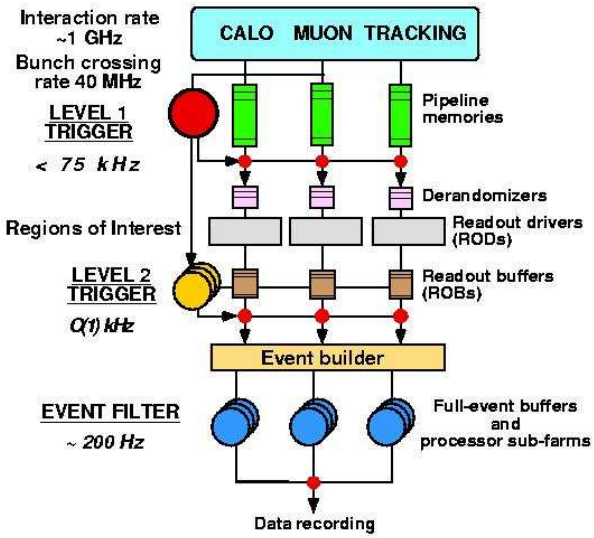

Figure 3.8: Schematic diagram of ATLAS trigger system.

Chapter 4

Luminosity Measurement and Data Sample

4.1 Introduction

As discussed earlier in Section 2.1, we use Equation 2.4 to measure the $t\bar{t}$ pair production cross section. Hence, an accurate determination of the integrated luminosity $\int Ldt$ is of central importance for the precision of the measurement. Below, we briefly discuss the ATLAS strategy for measuring and calibrating the instantaneous luminosity as well as describe the detectors used for instantaneous luminosity determination.

The instantaneous luminosity for pp collisions can be expressed as:

$$L = \frac{R_{inel}}{\sigma_{inel}} \quad \text{cm}^{-2}\text{s}^{-1} \tag{4.1}$$

where R_{inel} is the instantaneous rate of inelastic pp collisions and σ_{inel} is the pp inelastic cross section. If the beam revolution frequency is f_r, the number of proton bunches per beam (assuming that all bunches cross at the interaction point) is n_b, and the average number of inelastic interactions per bunch crossing (BC) is μ, then the instantaneous interaction rate can be equivalently expressed as $R_{inel} = \mu n_b f_r$. Hence:

$$L = \frac{\mu n_b f_r}{\sigma_{inel}} \tag{4.2}$$

In order to determine the average number of interactions per BC μ, ATLAS utilizes the so-called *Event Counting* method, where one determines the fraction of bunch crossings that contain events satisfying some selection requirements. The events are selected with efficiency $\epsilon < 1$, hence what one measures experimentally is $\mu_{vis} = \epsilon\mu$ and $\sigma_{vis} = \epsilon\sigma_{inel}$. Hence, the instantaneous luminosity expressed in terms of measurable μ_{vis} takes the form:

$$L = \frac{\mu n_b f_r}{\sigma_{inel}} = \frac{\epsilon \mu n_b f_r}{\epsilon \sigma_{inel}} = \frac{\mu_{vis} n_b f_r}{\sigma_{vis}} \tag{4.3}$$

4.2 Absolute Luminosity Measurement

As follows from Equation 4.3, the problem of absolute instantaneous luminosity determination boils down to measurement of μ_{vis} and σ_{vis}, where the visible cross section σ_{vis} is essentially the calibration constant that relates the measurable quantity μ_{vis} to the instantaneous luminosity $\mathcal{L}$. One should also note that the above mentioned calibration constant σ_{inel} is specific to event selection requirements (or equivalently the event selection algorithm) and the detector system, the information of which is used by the event selection algorithms.

Determination of Visible Average Number of Inelastic Interactions per BC μ^{vis}

In order to determine the quantity μ^i_{vis} for a given BC i, ATLAS makes use of two types of event counting algorithms, where the raw number of selected events N_i and the number of bunch crossings N_B are measured.

1. EventOR algorithm, where an event is counted if the sum of all hits in both the forward ('A') and backward ('C') sides is at least one. Assuming that the number of interactions in a BC are described by a Poisson distribution, the probability of observing an inclusive (EventOR) type of event can be computed as [50]:

$$P_{Event\_OR}(\mu^{OR}_{vis}) = \frac{N_{OR}}{N_{BC}} = 1 - e^{-\mu^{OR}_{vis}} \tag{4.4}$$

   Hence, μ_{vis} can be expressed in terms of the event-counting rate yields as:

$$\mu^{OR}_{vis} = -ln\left(1 - \frac{N_{OR}}{N_{BC}}\right) \tag{4.5}$$

2. EventAND algorithm, where an event is selected if there is at least one hit on each side of the detector. Here, the probability to record a coincidence event is P_{Event_AND} which one minus the probability $P_0^{Zero\_OR}$ of there being no hit on at least one side. The latter in turn equals the probability that there be no hit on at least side A ($P_{0A} = e^{-\mu\epsilon^A}$), plus the probability that there is no hit on at least side

C ($P_{0C} = e^{-\mu}\epsilon^C$), minus the probability that there be no hit on either side ($P_0 = 1 - P_{Event\_OR} = e^{-\mu\epsilon^{OR}}$) [50]. Combining terms, one arrives at:

$$\begin{aligned} P_{Event\_AND} &= \frac{N_{AND}}{N_{BC}} = 1 - P_0^{Zero\_OR}(\mu) && (4.6)\\ &= 1 - \left(e^{-\mu\epsilon^A} + e^{-\mu\epsilon^B} - e^{-\mu\epsilon^{OR}}\right) && (4.7)\\ &= 1 - \left(e^{-\mu\epsilon^A} + e^{-\mu\epsilon^B} - e^{-\mu(\epsilon^A+\epsilon^C+\epsilon^{AND})}\right) && (4.8) \end{aligned}$$

Recall that $\epsilon^{AND} \equiv \sigma_{vis}^{AND}/\sigma_{inel}$ and $\epsilon^{OR} \equiv \sigma_{vis}^{OR}/\sigma_{inel}$, also the relation between efficiencies: $\epsilon^{OR} = \epsilon^A + \epsilon^C - \epsilon^{AND}$. For the ATLAS experiment, one can assume $\epsilon^{AND} << \epsilon^{A,C}$ and $\epsilon^A \approx \epsilon^B$, hence the final expression for P_{Event_AND} is:

$$P_{Event\_AND}\left(\mu_{vis}^{AND}\right) = \frac{N_{AND}}{N_{BC}} = 1 - 2e^{-(1+\sigma_{vis}^{OR}/\sigma_{vis}^{AND})\mu_{vis}^{AND}} + e^{-(\sigma_{vis}^{OR}/\sigma_{vis}^{AND})\mu_{vis}^{AND}} \quad (4.9)$$

It is not possible to invert this relation analytically to obtain an expression for μ_{vis}^{AND} in terms of the number of selected coincidence events N_{vis}^{AND} and the total number of bunch crossings N_{BC}. Typically, the inversion is performed numerically using a look-up table, or the function is inverted for a specific value of μ using an iterative technique, such as the Newton-Raphson method [51].

Determination of the calibration constant σ^{vis}

Determination of the calibration constant σ^{vis} in ATLAS is achieved in two steps. The first step is to infer the instantaneous luminosity from accelerator parameters, such as n_b number of bunches that cross at the interaction point, collider revolution frequency f_r, the number of particles in colliding bunches $n_{1,2}$ and the horizontal and vertical beam profile characteristics $\Sigma_{x,y}$:

$$L = \frac{n_b f_r n_1 n_2}{2\pi\Sigma_x\Sigma_y} \quad [\mathrm{cm}^{-2}\mathrm{s}^{-1}] \quad (4.10)$$

Typically, one measures the beam parameters $\Sigma_{x,y}$ using van der Meer (vdM) scans, where the event rate is recorded while scanning the two beams across each other first in the horizontal (x) and then in the vertical (y) direction. The beam conditions during the vdM scans are different from those in normal physics

operations, with fewer bunches colliding, no bunch trains, and lower bunch intensities. These conditions are chosen in order to reduce various systematic uncertainties in the scan procedure. As a result of the vdM scan a Gaussian curve is obtained per scan, with the maximum rate at zero separation from which one extracts the values of Σ_x and Σ_y [50].

The number of protons in colliding bunches $n_{1,2}$ or equivalently the bunch charge currents are measured with eight Bunch Current Transformers (BCTs). Each beam is monitored by two identical and redundant DC current transformers (DCCT), which are high accuracy devices but are not capable of separating individual bunch charges. Each beam is also monitored by two fast beam current transformers (FBCT) which have the ability to measure individual bunch currents. Combining the total current measured with DCCT with the relative fraction of the total current in each BCID determined with FBCT provides the needed bunch charge current values $n_{1,2}$. Combining expressions 4.3 and 4.10 one arrives at the following expression for the luminosity calibration constant:

$$\sigma_{vis} = \mu_{vis} \frac{2\pi \Sigma_x \Sigma_y}{n_1 n_2} \quad [\mathrm{cm}^2] \tag{4.11}$$

where μ_{vis} is the visible average number of inelastic interactions per bunch crossing.

Determining the calibration constant σ_{vis} per luminosity detector per luminosity algorithm, allows conversion of the measured value for μ^i_{vis} into the absolute luminosity value for each bunch crossing.

4.3 Instantaneous Luminosity Uncertainty Evaluation

The absolute instantaneous luminosity determination described in the previous section suffers from both systematic and statistical uncertainties, which in turn arise from the uncertainties on the measured average number of interactions per bunch crossing μ^{vis} and the luminosity calibration constant σ^{vis}. Table 4.1 summarizes the main sources of systematic uncertainty for the visible cross section σ^{vis} along with the relative systematic uncertainties $\delta\sigma^{vis}/\sigma^{vis}$ per uncertainty source [52]. The main uncertainty comes from 'Bunch charge product' measurement, where among other sources of systematic uncertainty, the DCCT scale variation ($\pm 2.7\%$) and bunch-to-bunch fraction measurement ($\pm 1.3\%$) are the dominant contributors.

Table 4.2 lists the main sources of the total uncertainty on the absolute instantaneous luminosity measurement of the data sample used for this analysis [52].

Table 4.1: Relative systematic uncertainties on the determination of the visible cross section σ^{vis}.

Source	Systematic Uncertainty [%]
Bunch charge product	3.0
Beam centering	0.1
Emittance growth	0.4
Beam-position jitter	0.3
Bunch-to-bunch σ_{vis} consistency	0.4
Length scale calibration	0.3
Absolute ID length scale	0.3
Fit model	0.8
Transverse correlations	0.5
μ dependence	0.5
BCM consistency	0.7
Total	3.4

Table 4.2: Relative uncertainty (in %) on the calibrated instantaneous luminosity broken down by the source.

Uncertainty Source	$\delta L/L$
vdM Scan Calibration	3.4 %
Afterglow Calibration	0.2 %
Long-term Consistency	1.9 %
μ Dependence	1.0 %
Total	3.7 %

4.4 Data Sample

In the scope of this dissertation we used *pp* collision data provided by the LHC accelerator at 7 TeV center-of-mass energy collected in the first half of 2011. The data taking was separated into data collection periods within which the trigger conditions and LHC operation mode remained stable. The data used here was collected in data-taking periods B-G5, during which the LHC provided stable colliding beams and ATLAS systems critical for the E_T^{miss} determination, muon, electron, jet identification were producing data of sufficient quality so as to be suitable for physics analysis. Proceeding from the absolute instantaneous luminosity determination prescription described in Section 4.2, one can then compute the integrated luminosity associated with data collection periods B-G5 to be $\mathcal{L} = \int Ldt = 698$ pb^{-1}. As discussed in Section 4.3 this integrated luminosity measurement has an overall uncertainty of 3.7 %.

Chapter 5

Monte Carlo Simulation for Signal and Background Processes

5.1 Introduction

In collider experiments, typically interesting physics events are those that contain collisions with *hard scattering* processes, characterized by large momentum transfer. Along with the hard scattering signal process, depending on colliding beam parameters, the same event may contain additional hard and/or soft scattering processes that comprise the so-called *underlying event*[1]. All of these processes are governed by strong interaction physics and, hence by its underlying field theory - QCD. According to QCD, the partons emitted from collisions radiate additional partons which in turn create more partons in a process similar to an electromagnetic shower. This process is known as the parton shower. Because of color confinement, quarks and anti-quarks created in parton showers cannot exit in a free state and must combine to form color-neutral hadrons. The latter process is known as *hadronization*. The tight cone of particles created by the hadronization of a single high p_T quark is called a *jet*. Hence, realistic Monte Carlo simulations of hard-scattering collision events must provide an accurate description of the hard scattering signal, underlying events, parton shower evolution and subsequent hadronization. Figure 5.1 shows a schematic drawing of a typical hadron collision hard scattering event.

As discussed earlier, we make use of perturbative QCD in order to calculate the probability (or equivalently the matrix element squared) for a given strong interaction processes; the calculation is more precise the more higher-order perturbative terms are included in that calculation. On the other hand, what one ultimately observes in the collider experiment is a final state containing some number of leptons and jets. In order to describe the latter to arbitrary order, typically one makes use of Parton Shower Modeling following the strategy described below:

1. Knowing the PDFs for the proton, calculate the parton-parton hard scattering subprocess matrix

[1]The underlying event should be distinguished from the concept of the *minimum bias event* which is an event that causes the detector trigger to fire with imposed minimal requirements. Frequently, these are soft pp scattering processes. At high luminosities, where there are multiple interactions per typical proton bunch crossing event, the hard scattering process would be overlaid with several minimum bias processes that are called *pile-up* events.

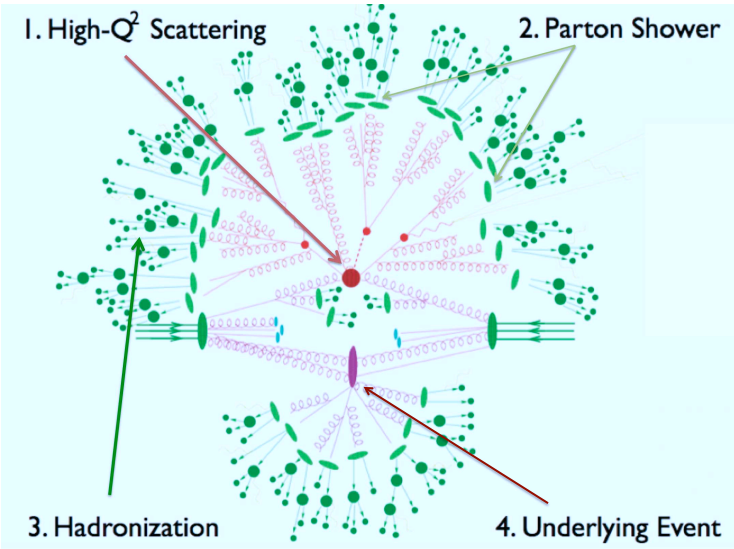

Figure 5.1: Schematic drawing of a hadronic collision hard scattering event.

element at the leading log order in QCD.

2. Add additional QCD and QED radiation in a shower approximation and subsequent hadronization.

Parton Shower modeling provides a reasonably good description of collision physics for soft scattering, collinear partons, whereas it performs poorly for the cases of hard scattering events with widely separated jets (such as those produced in $t\bar{t}$ pair decay). However, one can do better by replacing the first step with a higher-order perturbative calculation of the hard scattering matrix element and interfacing the hard scattering products to the parton shower simulation. At the interfacing step, one needs to combine different jet multiplicities from matrix elements without double counting with the parton shower emission. There are two widely used approaches to accomplish this: the CKKW scheme [53] and the MLM scheme [54].

At the final stage, following hadronization, the stable particles[2] are propagated through the full ATLAS detector simulation by Geant4 [55].

[2]In ATLAS, a particle is assumed to be stable if $c\tau \geq 10$ mm.

5.2 Monte Carlo Simulation for Signal and Background Processes

The Monte Carlo simulation samples, intended for the determination of signal acceptance and background contamination, as well as validation of analysis procedures of the ATLAS data collected in the first half of 2011, were produced in the scope of the MC10b production project by the ATLAS production group [56]. Event generation was followed by the propagation of events through the full Geant4 simulation of the ATLAS detector for all Monte Carlo samples. The reconstruction and digitization in the MC10b project was performed with the same ATLAS software release as the 2011 data reprocessing. Only one pile-up configuration corresponding to the LHC running with 50 ns bunch separation was used. The effect of pile-up was simulated using PYTHIA6 [57] Monte Carlo generated minimum bias events and assuming variable pile-up rates.

In the scope of the MC10b project, the individual MC sample event statistics generated was such that the statistical uncertainties associated with the Monte Carlo event samples were considerably smaller than the statistical uncertainties associated with the actual data sets. Therefore, MC samples with an integrated luminosity of at least $\sim$ 10-15 fb^{-1} were used for the main signal and background processes. For the signal and each of the main background processes several Monte Carlo models were used. A baseline model was selected for each of the MC samples; the baseline MC sample was used as the default MC sample by the ATLAS Top Working Group (TWG) analyses and had been generated with larger statistics than the MC samples generated using the alternative models. Below we summarize the main features of the MC10b production campaign MC sample.

Signal $t\bar{t}$ and single top events generated using the MC@NLO [58] generator v3.41 with the CTEQ66 [59] parton distribution function were chosen as baseline MC samples. The addition of parton shower and the underlying event was achieved by using HERWIG v6.510 [60] and JIMMY [61] MC event generators using the CTEQ66 HERWIG and JIMMY AUET1 PDF's tuned [62] to the ATLAS data. The MC $t\bar{t}$ cross section was normalized to the approximate next-to-next-to leading order prediction value of 164.6 pb obtained using the HATHOR tool [63]. For the single top MC samples, 300000 events were generated for each of the e, μ and τ t-channel and s-channel leptonic decay channels. For signal MC $t\bar{t}$ production, other Monte Carlo generators and generator parameter setups were used to provide simulation samples with statistics complying with the MC10b production guidelines. Alternative MC $t\bar{t}$ samples simulated using POWHEG [64] interfaced with PYTHIA as well as HERWIG [65] and JIMMY enabled the comparisons of two different parton shower and hadronization models against the baseline and also a comparison of the

POWHEG and MC@NLO generators. A set of twelve samples generated with AcerMC [66] and PYTHIA generators was made available for the MC $t\bar{t}$ initial and final state radiation studies. For these MC samples, the initial and final state parameters (or their combinations) were set to a range of values not excluded by the current experimental data.

The MC vector boson production was simulated using ALPGEN interfaced to HERWIG MC event generators while JIMMY [61] was used for underlying event simulation. The CTEQ6.1 parton distribution function was used for both the matrix element calculations and the parton shower evolution. The additional partons produced in the matrix element part of the MC event generation can be either light partons (W+jets and γ/Z+jets) or heavy quarks ($W + c$+jets, $W + c\bar{c}$+jets, $W + b\bar{b}$+jets, $Z + c\bar{c}$+jets and $Z + b\bar{b}$+jets).

The inclusive W and γ/Z MC samples were produced as a full set of the parton multiplicity sub-samples. For all of the MC vector boson production process samples requested and used by the Top Group, the ALPGEN parameters controlling the minimal transverse momentum and angular separation of the light quarks were set to `ptjmin`=15 GeV and `drjmin`=0.7. The clustering parameters used for the MLM matching were set to `RCLUS`=0.7 and `ETCLUS`=20 GeV. The MC vector boson production processes had integrated luminosities of $\sim$ 10 fb^{-1}, in order for the parton multiplicity sub-samples to have a reasonable probability of surviving the $t\bar{t}$ signal event selection cuts. The production cross sections of all of the ALPGEN and HERWIG samples were normalized to the corresponding next-to-next-to leading order cross section predictions [67].

ALPGEN was used for MC di-boson event (WW, WZ and ZZ) simulation. These samples were produced with up to three additional partons from the matrix element. They were therefore likely to represent a more credible background simulation than the other (e.g. HERWIG) samples when the event selection cuts included the multiplicity cuts on high-pt QCD jets. A list of all Monte Carlo simulated data samples used in this analysis is given in Appendix D.

Chapter 6

Analysis Object Reconstruction and Identification

6.1 Electrons

6.1.1 Trigger Chain

As discussed in Section 3.3.6, ATLAS employs a three-level trigger system. The first level trigger (L1) consists of special purpose hardware, while the second (L2) and third (EF) were software based and collectively referred to as the High Level Trigger (HLT). Triggers for the electron channel of top events were based on selecting high transverse momentum electrons. The trigger for the electron sample for the top pair production cross section measurements is as follows: at the first trigger level, electron candidate events are selected by requiring an electromagnetic object passing a certain high energy threshold. At the HLT level, calorimeter clusters are associated with tracks, the full granularity of the calorimeter becomes available and fast calorimeter and track reconstruction algorithms were deployed. For both the data and MC simulation we require the `EF_e20_medium` trigger path [68]. The efficiency of the trigger (ϵ_{trig}) and the ratio of efficiencies (SF_{trig}) obtained from data and MC were measured using the unbiased leg in $Z \to ee$ and $W \to e\nu$ in 18 bins of $|\eta|$ (cluster position) and were found to plateau for $E_T > 25$ GeV, with $\epsilon_{trig} \simeq 98\%$ and $SF_{trig}(\eta)$ within 1 ± 0.02 for all except forward ($|\eta| > 2$) regions.

6.1.2 Electron Reconstruction, Identification and Kinematical Selection

Electron candidate selection starts with the trigger requirement described above, followed by selection cuts imposed on the reconstructed offline candidate electrons (we use `ElectronAODCollection`). A set of quality requirements was applied in order to ensure that candidates were consistent with the energy deposition of an electron in the calorimeters and the presence of a well-measured high P_T track that spatially matched to the electromagnetic cluster was also required. Specifically, electron candidates were required to pass the egamma group definition of a 'tight' [1] electron selection [69], with an overall efficiency of ∼75%. Electron identification cuts also included a requirement to pass $E_T = E_{\text{cluster}}/\cosh(\eta_{\text{track}}) > 25$ GeV, where E_{cluster}

[1] This corresponds to 'egammaPIDs::ElectronTight' selection.

is the calorimeter cluster energy and η_{track} is the longitudinal direction of the electron track. Additionally, we require that $|\eta_{\text{cluster}}| < 2.47$, excluding the calorimeter crack region at $1.37 < |\eta_{\text{cluster}}| < 1.52$, where η_{cluster} is the pseudorapidity of the calorimeter energy cluster associated with the candidate. The value of E/p, the ratio of electron cluster energy measured in the calorimeter to momentum in the inner tracker, was required to be consistent with that expected for an electron[2]. In addition, the track was required to have an associated hit in the innermost pixel layer in order to suppress photon conversions, except when the track passed through modules known to be dead. Information about high-threshold TRT hits was also used to separate electrons from photons. In addition, a run-dependent quality map (OTX map) was used to reject electrons from detector regions with known problems, such as non-nominal high voltage or readout problems.

The efficiencies of the electron track and cluster reconstruction and the electron identification were measured within the egamma combined performance group using data and MC samples of $Z \rightarrow ee$ and $W \rightarrow e\nu$ [70]. MC simulations were reported to agree reasonably well with data, with a few exceptions - mainly regarding the lateral development of EM showers and the TRT data in the end-caps. Scale factors were applied to account for differences in efficiency values measured in MC versus data. The electron reconstruction efficiency, including track quality cuts, was measured in three $|\eta|$ regions and the scale factor was found to be consistent with 1 except for $|\eta| > 2.37$, where it was $\simeq 0.97$. The electron ID efficiencies and scale factors were measured in 18 η bins (plus 2 for the calorimeter gaps) and 6 E_T bins [71]. The η-dependent scale factors were corrected by the ratio of E_T-dependent scale factors to the overall scale factors to form a 2-dimensional matrix. Figure 6.1 shows the ID SF's as a function of the electron η and E_T.

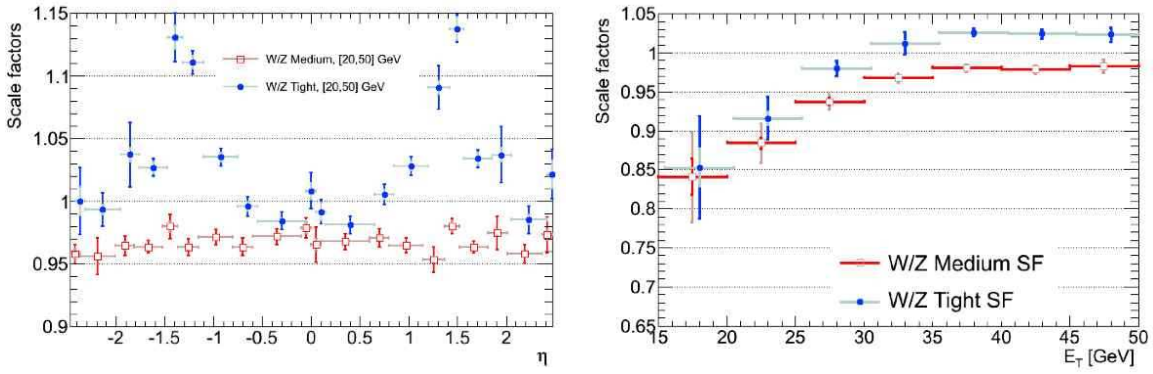

(a) (b)

Figure 6.1: Electron identification SF's versus η (with E_T between 20 and 50 GeV) and versus E_T (for all η) [72] (not public plots).

[2]The cut is η and E_{T} dependent and ranges from $0.7 - 0.8 < E/p < 2.5 - 5.0$.

Isolation requirements

Electrons emitted due to W-boson leptonic decay are isolated from jet activity, except for cases of accidental overlap with one of the jets in the event. There are three major sources of contamination for high p_{T} isolated electrons: hadrons faking an electron signature, electrons from heavy-flavor decays and photon conversions. In order to suppress these background events, an angular cone of $\Delta R = \sqrt{\Delta\eta^2 + \Delta\phi^2} = 0.2$ centered around the electron was required to be free of jet activity. In order to achieve this, we required that `EtCone20` < 3.5 GeV, where the electron EM cluster energy is subtracted from the `EtCone20` parameter. Additionally, two corrections to `EtCone20` were made:

- *A leakage-correction*, which accounted for the E_T-dependent and η-dependent slope of the average cone energy versus the electron E_T.
- *A pileup-correction*, which accounted for the effect of underlying events on the electron isolation variable.

6.1.3 Electron energy scale and resolution

In the kinematic range comparable to that of electrons in top events, the electron energy scale and electron energy resolution was derived from the measurement of the $Z \rightarrow ee$ invariant mass distribution [73]. A correction factor was applied to correct the electron energy scale in data as a function of the electron η_{cluster} (using 26 central and 6 forward η bins). Systematic uncertainties were within $\pm$1–1.5% for the $|\eta_{\mathrm{cluster}}| < 2.5$ range. The dominant uncertainty sources were the knowledge of detector material thickness and the presampler energy scale, pile-up effects and hardware modeling.

6.2 Muons

6.2.1 Trigger Chain

The muon trigger was required to obtain a suitable compromise between high trigger efficiency and stability throughout the dataset (no muon trigger Pre-Scaling). Events in the muon channel were selected at the trigger level requiring the `EF_mu18` trigger chain to have fired, with the Level 1 trigger requirement `L1_MU10`. The level 1 trigger required a muon spectrometer track with at least 10 GeV of estimated transverse momentum at two layers of the trigger system.

6.2.2 Muon Reconstruction, Identification and Kinematic Selections

Muon candidates were reconstructed by the MuID algorithm which started with a search for track segments in different layers of the muon chambers using Hough transforms [74]. These segments were then combined starting from the outermost layer, fitted to account for material effects, and matched with tracks found in the inner detector to form a combined muon. The final candidates were refitted using the complete track information from both detector systems. The reconstruction efficiency for combined muons was studied by the Muon Combined Performance group (MCP). The MCP group provided the scale factors to correct MC efficiencies in order to reproduce those obtained in data as a function of the muon η [75]. The reconstruction scale factors were roughly consistent with unity throughout the η range, with uncertainties at the level of a few per-mille. The muon reconstruction efficiency and muon momentum distribution width were corrected using official MCP software packages approved by ATLAS. The nominal acceptance was measured from MC simulated data after applying all of the muon corrections. The associated uncertainties of these corrections were then used to derive systematic uncertainties on the muon acceptance estimate.

Muons were further required to satisfy the 'tight' muon quality definition made available by the MCP group[3]. We required muons that were reconstructed by combining Inner Detector and Muon Spectrometer information. This requirement enhanced the muon sample purity; this definition of a muon was also consistent with the definition of a muon used in the muon term for calculating the missing E_{T} as used in this analysis. The following MCP recommendations for muon track quality were also implemented:

- Number of B-Layer hits > 0, if the `expectBLayerHit` returns `true`
- Number of pixel hits + number of crossed dead pixel sensors > 1
- Number of SCT hits + number of crossed dead SCT sensors ≥ 6
- Number of pixel holes + number of SCT holes < 3
- for $|\eta| < 1.9$: Number of TRT hits + Number of TRT outliers > 5 *and* (Number of TRT outliers)/(Number of TRT hits+outliers) < 0.9
- for $|\eta| > 1.9$: *if* Number of TRT hits + Number of TRT outliers > 5: (Number of TRT outliers)/(Number of TRT hits+outliers) < 0.9

Specific additional cuts were applied for the top analyses in order to reject muons coming from heavy and light flavor decays (such as b and c baryon and meson decays and π and K decays in flight) as opposed to prompt W decay. The following cuts were optimized based on simulation:

[3] https://twiki.cern.ch/twiki/bin/view/AtlasProtected/QualityDefinitionMuid

- $p_{\mathrm{T}}(\mu) > 20$ GeV
- $|\eta(\mu)| < 2.5$ (corresponding to the geometrical acceptance of the Inner Detector in muon combined tracking)
- $\Delta R(\mu, closest\ reconstructed\ jet) > 0.4$, where the closest jet was taken among the jets reconstructed by the anti-k_t algorithm, with a cone of 0.4 and calibrated using the EMJES scheme. We considered only jets with $p_{\mathrm{T}}(jet) > 20$ GeV
- $etcone30(\mu) < 4$ GeV
- $ptcone30(\mu) < 4$ GeV

Each pair of muons passing these cuts was checked against simple cosmic-muon rejection criteria. Cosmic ray muon candidates were removed if they had two muons with opposite signed transverse impact parameters, d_0 and both muon tracks had $|d_0| > 0.5$ mm and $\Delta\varphi > 3.10$ between their respective muon directions. While the calorimeter isolation requirement was sufficient to reject electrons from heavy flavor decays, muons were required to have angular separation distance ΔR greater than 0.4 from any jet with $p_{\mathrm{T}} > 20$ GeV in order to reject muons from heavy flavor decays.

6.2.3 Efficiencies and scale factors

The trigger efficiency of the muon trigger chain `EF_mu18` (that used `MU10` at level 1) was measured for the entire data taking period used in this analysis. The efficiency was measured using offline reconstructed muons that also passed all of the top-specific selections of Section 6.2.2. The selection requirements for so-called tag and probe muons are summarized in Table 6.1 and described in [76]. The top WG official Good Run List was used when selecting events from data. Alpgen $Z(\rightarrow \mu\mu)$ + N jets MC10b Monte Carlo sets were used as simulation samples. The muon trigger efficiency in MC and data was studied as a function of the muon η, ϕ and p_{T}. Fig.6.2 shows MC and data muon trigger efficiencies as a function of several variables.

Table 6.1: Definition of tag and probe muons for muon trigger efficiency measurement.

Tag Muons	**Probe Muons**
Tight muon passing all offline selections	
Combined muon requirement	
Matched to a trigger ROI object within $\Delta R = 0.2$	$\lvert M_{tag+probe} - M_Z \rvert \leq 12$ GeV
	opposite charge wrt the tag

Due to an extrapolation bug in MC simulation affecting combined muon triggers at L2 (`MuComb` algorithm) in the barrel region [77], a dependence of the SF on muon p_{T} was observed in this region (but not in the EC).

The misconfiguration problem was only present in the MC10b production, but not in the on-line menu used for collision data; it primarily affected very high-p_{T} muons. The p_{T} range of muons from Z decays was limited and therefore the tag-and-probe technique could not be used to measure the behavior of the simulated efficiency after $p_{\mathrm{T}} \approx 150$ GeV. Given this limitation, we did not impose a trigger decision requirement for Monte Carlo events that contained muons with p_{T}>150 GeV. MC events containing at least one muon, that passed all selection requirements and participated in the muon trigger were weighted by the SF to match the efficiency to values obtained from data. No data/MC disagreements were found vs. $\Delta R(\mu, closest\ jet)$.

These studies delivered muon trigger efficiencies as a function of η and ϕ and trigger scale factors separated into three p_{T} bins, [20-60 GeV], [60-120 GeV] and > 120 GeV. Figure 6.3(a) shows the scale factor maps for the low p_T bin and Figure 6.3(b) shows the efficiency maps.

The systematic uncertainty on the muon trigger SF evaluation was traced to the following sources: the di-muon invariant mass cut around the world average Z mass [78]; the trigger matching cut and the effect of isolation on the tag muon.

The reconstruction efficiency for `Muid` combined muons was factorized from the offline muon identification by normalizing the muon identification efficiency to the number of `Muid` combined muon probes. As for the muon trigger efficiency measurement, the tag-and-probe technique and the same MC simulation samples were used to evaluate the muon reconstruction and identification efficiency. Table 6.2 presents the requirements for tag and probe muon selection for reconstruction and identification efficiency estimation. The background contribution in data was estimated from a fit to the invariant mass shape of same-sign dimuon combinations close to the Z pole, as described in [76]. Figure 6.4 shows the top-specific identification efficiencies as a function of the most relevant kinematic and pile-up variables after background subtraction in data. No dependence was observed on the `etcone30` and `ptcone30` variables either. The following were considered as sources of systematic uncertainties: the background subtraction procedure; the effect of the Z mass constraint on the di-muon invariant mass by varying the constraint in both data and MC [76]; the effect of a mismeasurement of the muon momentum (in the tag/probe selection); the effect of quality cuts such as the number of Inner Detector hits; and finally, the effect of interaction pile-up at higher luminosities. The overall scale factor obtained from these muon studies for data-taking periods B to I was: $SF_{Id} = 1.0008 \pm 0.0003$ (stat) ± 0.0003 (syst).

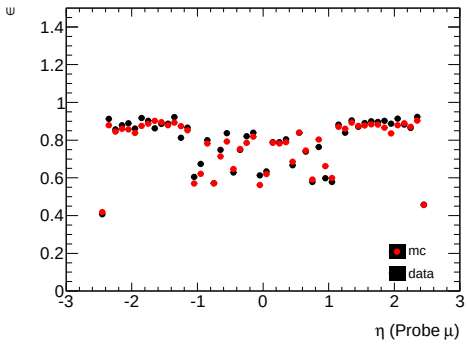

(a) Muon trigger efficiency vs η

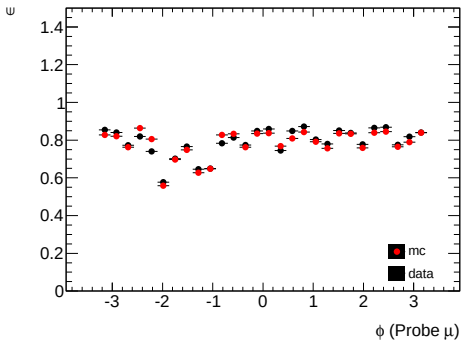

(b) Muon trigger efficiency vs ϕ

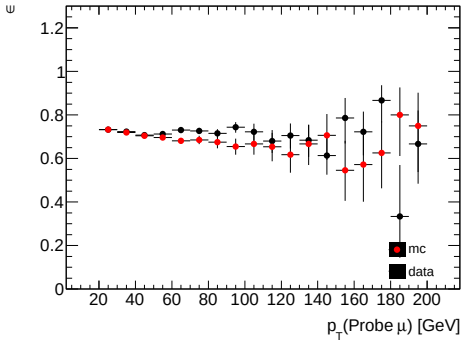

(c) Muon trigger efficiency vs p_T in Barrel

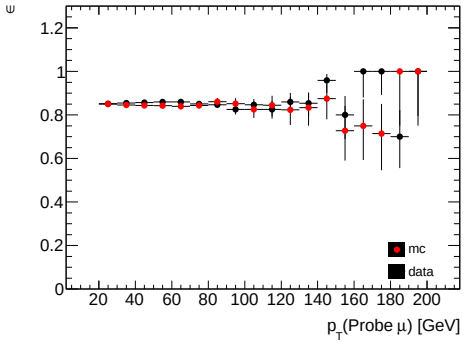

(d) Muon trigger efficiency vs p_T in EC

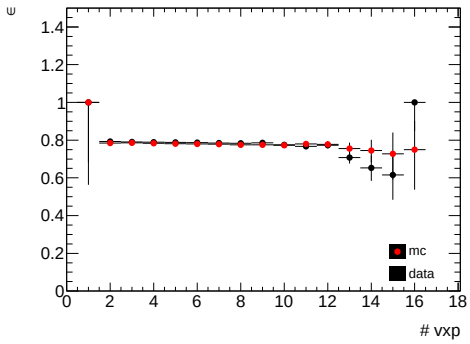

(e) Muon trigger efficiency vs N_{PV}

Figure 6.2: Comparison of muon EF trigger efficiency for data (black) and MC (red) as a function of the probe muon η, ϕ, p_{T} and number of reconstructed primary vertices (on-time pile-up). The dependence on muon p_{T} in the Barrel and EC was different, as shown. The plots use 490 pb^{-1} of 2011 collision data (periods B2 to F3) [72] (not public plots).

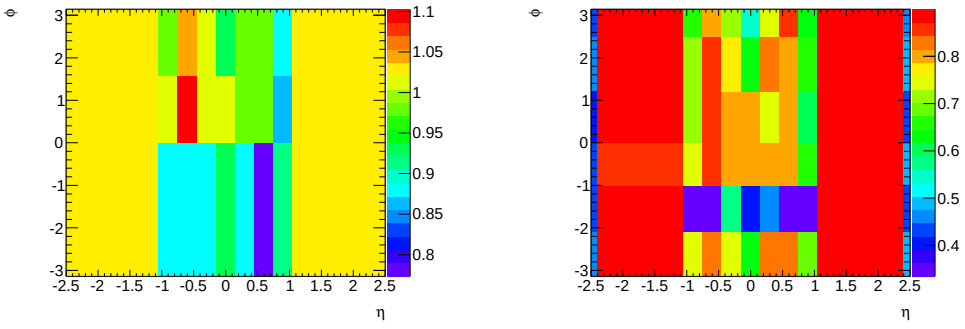

(a) (b)

Figure 6.3: (a) Muon trigger scale factor maps as a function of η and ϕ for periods B-I. The maps use offline muons with $20 < p_T < 60$ GeV. (b) Muon trigger efficiency maps as a function of η and ϕ for periods B-I [72] (not public plots).

Table 6.2: Definition of tag and probe muons for muon reconstruction and identification efficiency measurement.

Reco Tag
Tight muon passing all offline selections Combined muon requirement $\|d_0(\mu, PV)\| \leq 0.05$ mm matched to EF muon trig ROI within $\Delta R = 0.2$
Reco Probe ID Tag
Track passing InDet requirements $P_T \geq 22$ GeV, to allow for MS-InDet mismatch due to tracking resolution effects and avoid boundary effects around $P_T = 20$ GeV $\|d_0(\mu, PV)\| \leq 0.05$ mm $\|M_{tag+probe} - M_Z\| \leq 10$ GeV $\Delta\phi(tag - probe) \geq 1.5$ rad opposite charge wrt tag
ID Probe
Tight muon passing all offline selections Combined muon requirement $P_T = 20$ GeV $\|M_{tag+probe} - M_Z\| \leq 10$ GeV $\Delta\phi(tag - probe) \geq 1.5$ rad opposite charge wrt tag

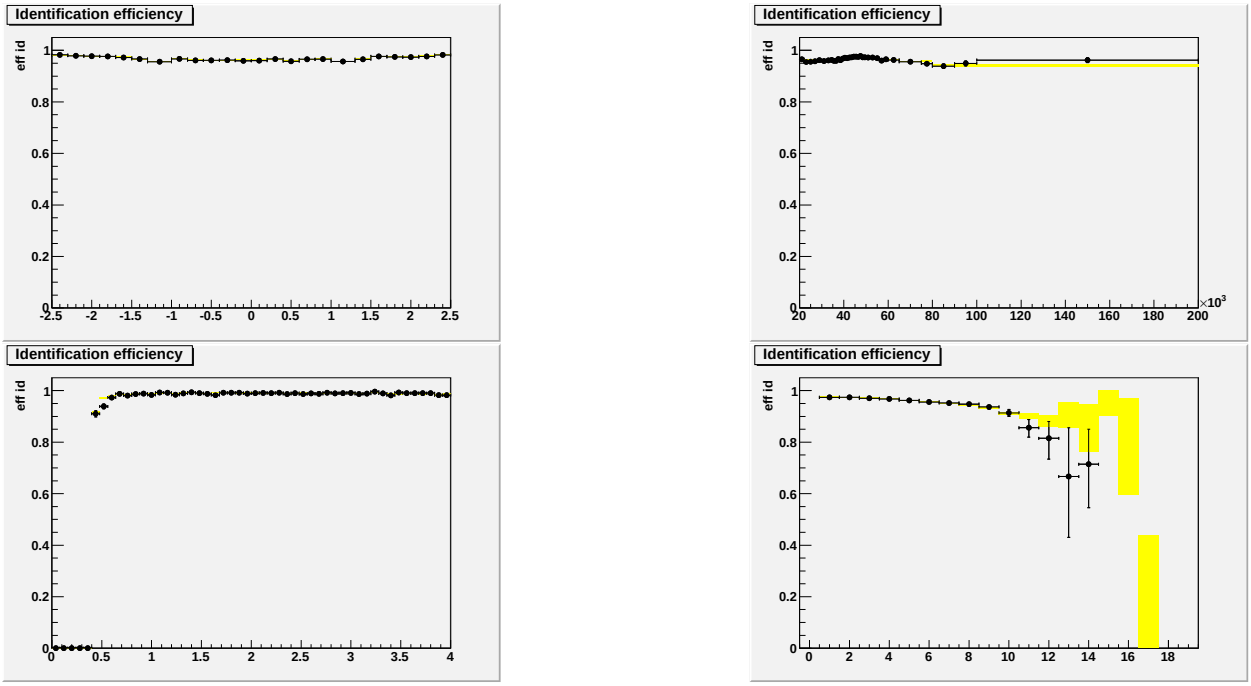

Figure 6.4: Muon identification efficiency measured with the tag-and-probe method for data (black dots) and MC (yellow rectangles) as a function of $\eta(\mu)$, $p_T(\mu)$, $\Delta R(\mu, closest\ jet)$ and N(PV) in the event. The data uses 690 pb^{-1} of 2011 collision data. The MC includes all background contributions [72] (not public plots).

6.3 Track Leptons

As described in Section 1.6.2, we relaxed the requirements on one of the lepton legs to require only a high-p_T, high quality Inner Detector track in order to enhance the analysis sensitivity to τ-leptonic decays of the $W^{\pm}$ boson and restore the signal events lost due to lepton identification inefficiencies. Below, I describe in detail the approach we used to define the minimal set of parameters required for Track Lepton (TL) selection and to determine the optimal cut thresholds per parameter.

6.3.1 Track Lepton Selection

We categorize the three main requirements on tracking parameters that we used to define the TL object:

1. Requirements on the number of track hits per Inner Detector subsystem. This group of cuts was mainly used to ensure high efficiency for Inner Detector track reconstruction.

2. Isolation requirements. The main purpose for track isolation requirements was to suppress tracks originating from parton fragmentation (so-called fakes).

3. Impact parameter requirements. The purpose of this group of cuts was to suppress tracks that were

not associated with the highest p_T hard scattering vertex or belonged to non-collision backgrounds.

In order to obtain the defining TL parameters along with their optimal cut values, we established the following prescription: we started off by relaxing all of the TL requirements with the exception of the $p_T > 20$ GeV cut. Further, for each tracking parameter group, we identified the parameter(s) with highest signal acceptance and maximal background suppression and associated cut threshold value(s) yielding the maximal significance in a dedicated optimization procedure. In view of the high TL fake rate, we enhanced the sensitivity of the TL optimization procedure to fake-TL backgrounds (mainly W+jets) by introducing into the figure of merit for the optimization an additional fake background term:

$$\alpha = \frac{S}{\sqrt{(\delta N^{Stat})^2 + \underbrace{(F \cdot B^{Fake})^2}_{\text{fake background systematic term}} + \sum(\delta B_i^{Stat})^2}} \tag{6.1}$$

where the statistical term $\delta N^{Stat} = \sqrt{S + \sum B_i}$, S, B_i are defined as the signal and background events respectively, δB_i^{Stat} was the statistical uncertainty per background, F was the factor describing the anticipated systematic uncertainty for fake Track-Lepton backgrounds. For this study, we assumed $F = 0.25$, which was the target level for the systematic uncertainty associated with fake TL background.

The above definition for the optimization figure of merit enabled identification of threshold values that allowed minimization of not only the statistical uncertainty on the $t\bar{t}$ cross section measurement, but also the systematic uncertainty on fake TL backgrounds.

Let us now return to the above mentioned categories of tracking parameter requirements for TL definition and focus on the optimization of the parameters that belong to the first category comprising:

- Pixel hits
- SCT hits
- Combined Pixel and SCT hits (often referred to as Silicon Hits (N_{Si}))
- B-layer hits

A cut on the Number of Pixel+SCT hits > 6 was identified as the optimal parameter emerging from the first category.

For the isolation requirement optimization we considered a 3×3 matrix of isolation parameters i.e. 3 types of isolation variables defined in 3 fixed cone sizes ($\Delta R = 0.2, 0.3, 0.4$).

1. Combined p_T of the tracks with $p_T > 0.5$ GeV around given track in a fixed cone size $\Delta R = 0.2, 0.3, 0.4$.

2. Combined p_T of the tracks with $p_T > 0.5$ GeV and $N_{Si} > 0$ hits around given track in a fixed cone size $\Delta R = 0.2, 0.3, 0.4$.

3. The number of tracks with $p_T > 0.5$ GeV and $N_{Si} > 0$ hits around given track in a fixed cone size $\Delta R = 0.2, 0.3, 0.4$.

The optimal isolation type was identified as the combined p_T of tracks with $p_T^{min} > 0.5$ GeV and $N_{Si} > 6$ hits around given track in a fixed cone size $\Delta R = 0.3$. As one can see from Figure 6.5, threshold values for the inclusive Lepton+Track analysis channels were $p_T \leq 2$ GeV, whereas optimal cut values for the exclusive analysis[4] were tighter $p_T \leq 1$ GeV, which was due to the enhanced fake rate for the case of the exclusive analysis. However, for the sake of simplicity, and in order to make the exclusive Lepton+Track analysis a subset of the inclusive analysis, a unique track isolation p_T cut value was chosen.

Lastly, we considered the transverse d_0 and longitudinal $z_0 \sin\theta$ impact parameters in the third group of parameters where optimal cuts were found to be $|d_0| < 0.2$ mm and no cut on the longitudinal impact parameter.

The results of the Track-Lepton optimization study are summarized in the Table 6.3.

Table 6.3: Track-Lepton Selection Requirements.

Parameter	Cut Value
p_T	> 25 GeV
Number of Pixel+SCT hits	> 6
Isolation($\Delta R = 0.3$)	< 2 GeV
$\lvert d_0 \rvert$	< 0.2 mm
Number of B-layer hits	> 0
$\lvert \eta \rvert$	< 2.4
$\sigma(q/p)/(q/p)$	< 0.2

Our detailed study of fake Track-Lepton backgrounds indicated the need for 3 additional cuts on Number of B-layer hits, the track pseudorapidity and relative uncertainty on the ratio of charge per momentum (q/p) parameter. This optimization study was carried out in the context of the 2010 analysis. Figures 6.6 and 6.7 present the data distribution and Monte Carlo simulation of the tracking parameters used for TL definition for the case of the inclusive l+track analysis. The corresponding plots for the exclusive analysis can be found in Figures 6.8 and 6.9.

[4]The definition of the inclusive and exclusive Lepton+track analysis was provided in Section 7.1.

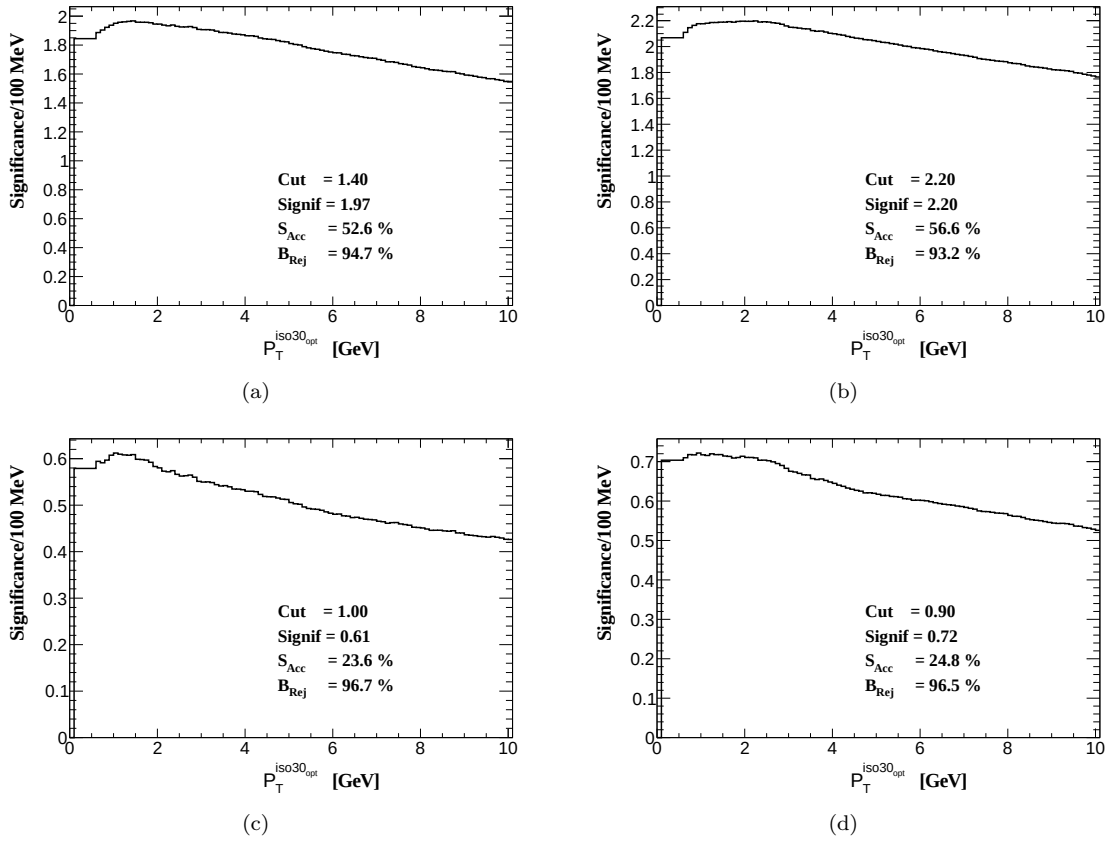

Figure 6.5: The significance for the Track Lepton optimization as a function of the threshold value on the isolation parameter p_T^{iso30} determined by combining the p_T of the tracks that were within a cone of $\Delta R = 0.3$ around the TL and have $p_T^{Min} > 500$ MeV, and $\mathrm{N_{Silicon}} > 0$. The upper plots depicts the significance for the Inclusive flavor of the Lepton+Track Analysis, while the lower ones are for the Exclusive flavor. The left-hand side ones are for the case of e+track final state, and the right-hand side plots are for μ+track final state.

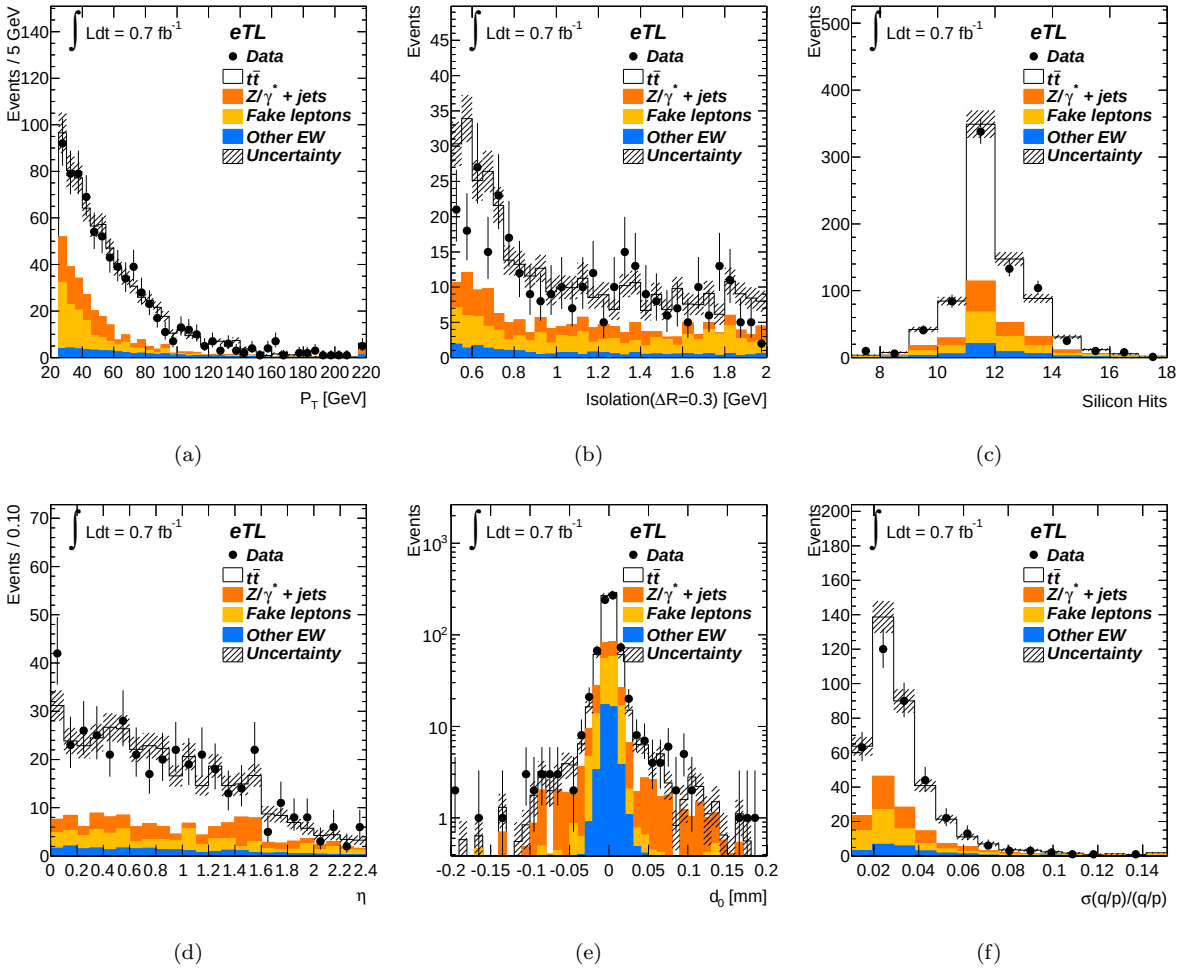

Figure 6.6: The comparison of e+track data and Monte Carlo simulation for the track parameters used for the TL definition. The distributions were obtained imposing all of the requirements described in Table 6.3. and the inclusive e+track event selection.

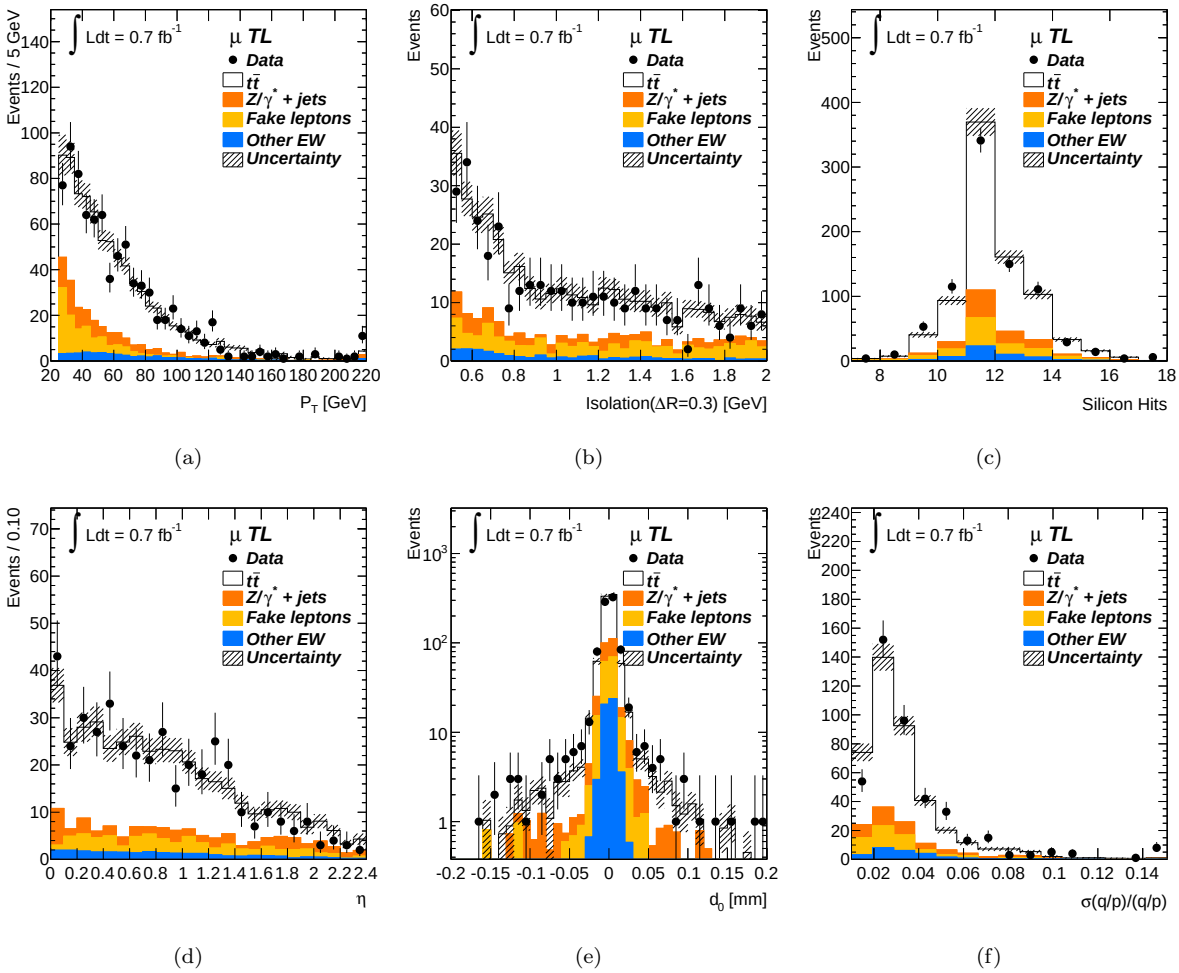

Figure 6.7: The comparison of μ+track data and Monte Carlo simulation for the track parameters used for the TL definition. The distributions were obtained imposing all of the requirements described in Table 6.3. and the inclusive μ+track event selection.

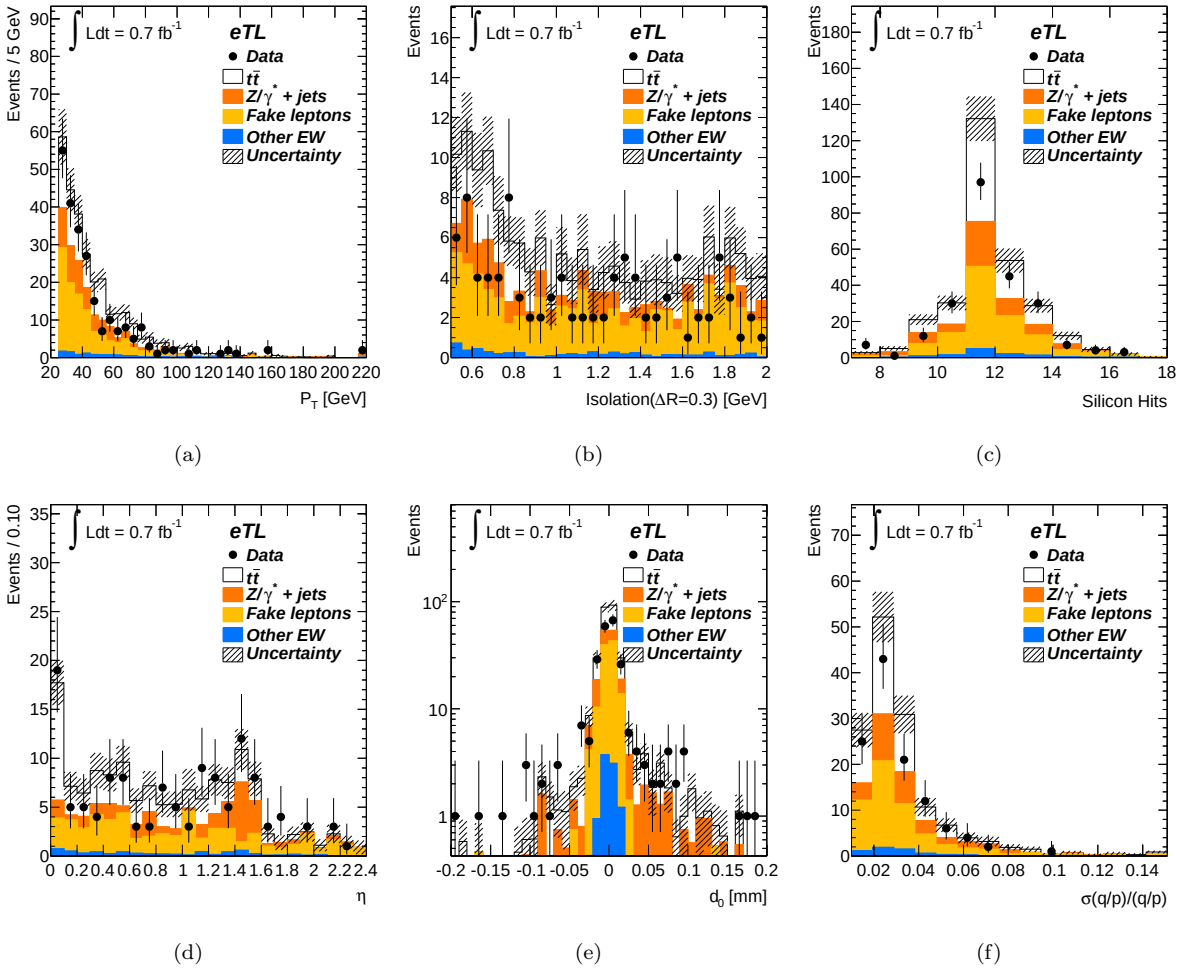

Figure 6.8: The comparison e+track of data and Monte Carlo simulation for the track parameters used for the TL definition. The distributions were obtained imposing all of the requirements described in Table 6.3. and the exclusive e+track event selection.

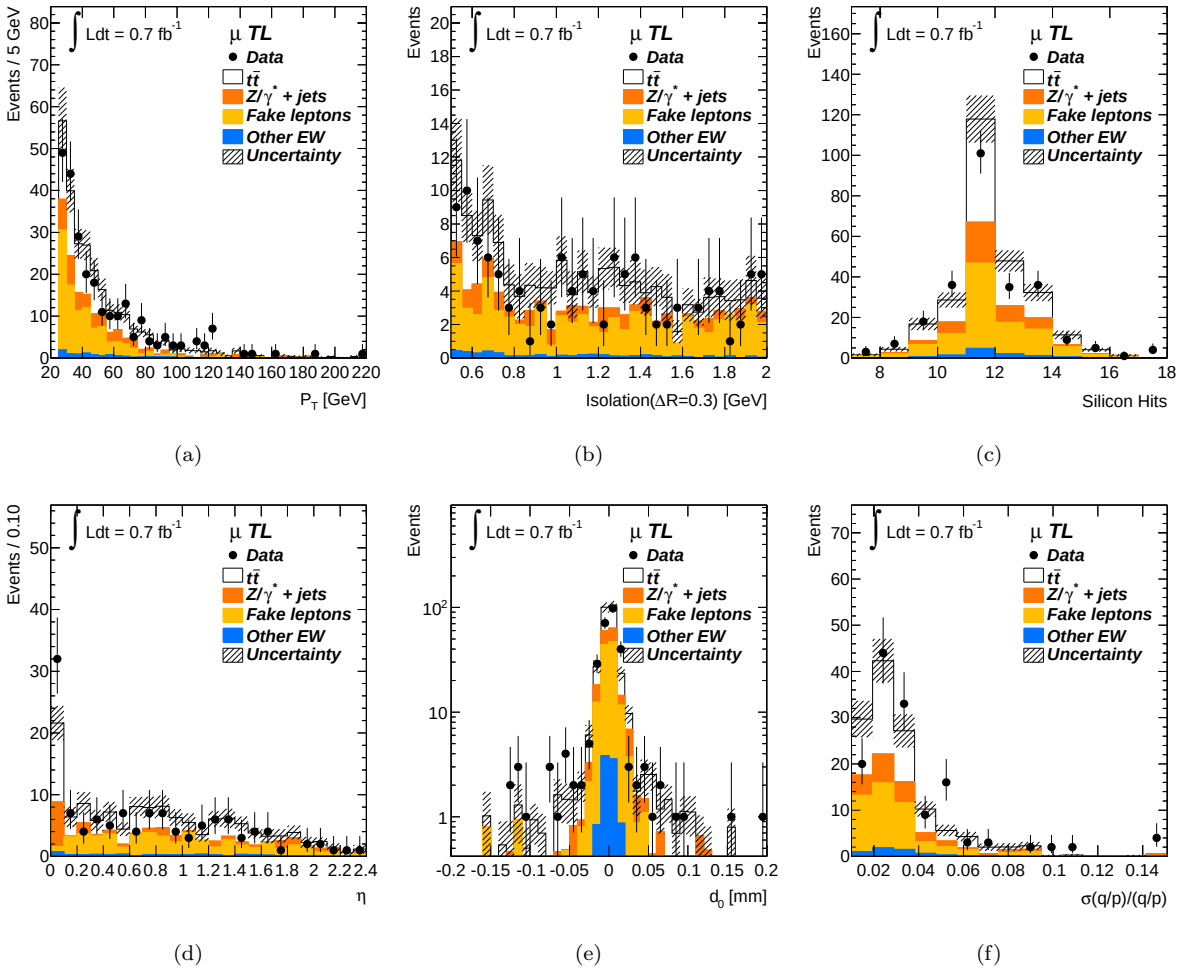

Figure 6.9: The comparison of μ+track data and Monte Carlo simulation for the track parameters used for the TL definition. The distributions were obtained imposing all of the requirements described in Table 6.3. and the exclusive μ+track event selection.

6.3.2 Track Lepton Efficiencies and Scale Factors

The tag-and-probe technique was used to measure the data/MC scale factor for TL in $Z \to \mu\mu$ and $Z \to ee$ events. The tag leg was defined using an identified electron or muon, while the probe leg was defined using either only calorimeter information, in the case of $Z \to ee$, or only muon spectrometer information in the case of $Z \to \mu\mu$. In the case of $Z \to ee$, we used electrons reconstructed by the cluster based algorithms and satisfying the above described OTX quality check. For $Z \to \mu\mu$ we used muons reconstructed by only the Muon Spectrometer information. For both cases we further required that probe-leg leptons had $P_T > 25$ GeV and $|\eta| \leq 2.4$. The charge for the tag legs was randomly chosen to be positive or negative, so that the probes had an equal mixture of both. The TL efficiency denominator consisted of all probe legs with p_{T} >25 GeV and $|\eta|$ <2.4 . The numerator consisted of denominator probe legs that passed the TL selection in Table 6.3. The efficiency was measured integrated over the entire 0.7 fb^{-1} dataset, and MC events were pile-up reweighted. Figure 6.10 shows the TL efficiency measurement in data (black) and Monte Carlo (red) for $Z \to \mu\mu$ events as a function of p_{T}, the number of vertices, η, and ϕ. The integrated scale factor (data/MC) was found to be 0.997±0.002. Similar results for $Z \to ee$ events are shown in Figure 6.11. The integrated scale factor for TLs from electrons was 1.047±0.005. The TL efficiency decreases with the number of primary vertices, due to the failure of the isolation requirement in events with large numbers of tracks from pile-up interactions. The Monte Carlo simulations modeled this effect reasonably well and the scale factor had little or no dependence on the number of primary vertices. Track leptons can be electrons, muons, or hadrons. In the case of hadrons in the MC, we applied the efficiency scale factor derived from $Z \to \mu\mu$ because hadronic interactions in the material of the Inner Detector are relatively rare, and therefore most hadrons faking isolated tracks behave like muons in the Inner Detector.

6.3.3 Track-Lepton-Specific Systematic Uncertainties

The above mentioned scale factors are values averaged over the kinematic distributions of muons and electrons from Z decays, and the uncertainties shown are statistical only. Due to the p_{T} and η dependence of the scale factor, a systematic uncertainty was associated to it by averaging over the p_{T} and η distributions of electrons or muons from $t\bar{t}$ decays. The difference between the $Z-$averaged and $t\bar{t}$-averaged scale factors was taken as a systematic uncertainty. The statistical uncertainty on the scale factor measurement was added to it in quadrature to obtain the total systematic uncertainty on the scale factor.

A systematic uncertainty associated with the TL momentum scale and resolution was also included. This was accomplished by selecting $Z \to \mu\mu$ and $Z \to ee$ using the muon and e-gamma streams and plotting the invariant mass of OS TLs. We fitted the invariant mass distributions in the data and MC to a Breit-Wigner

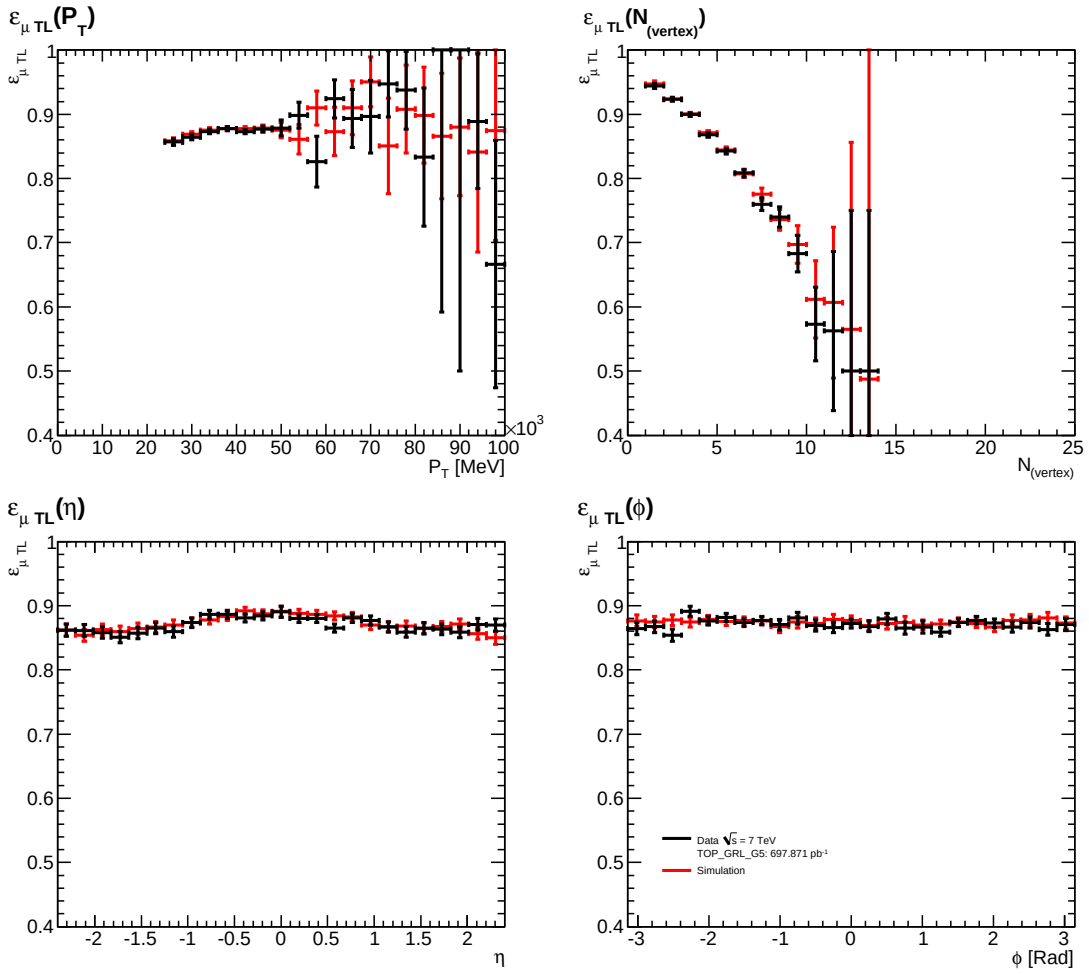

Figure 6.10: The TL efficiency measured from $Z \to \mu\mu$ events in data (black) and Monte Carlo (red).

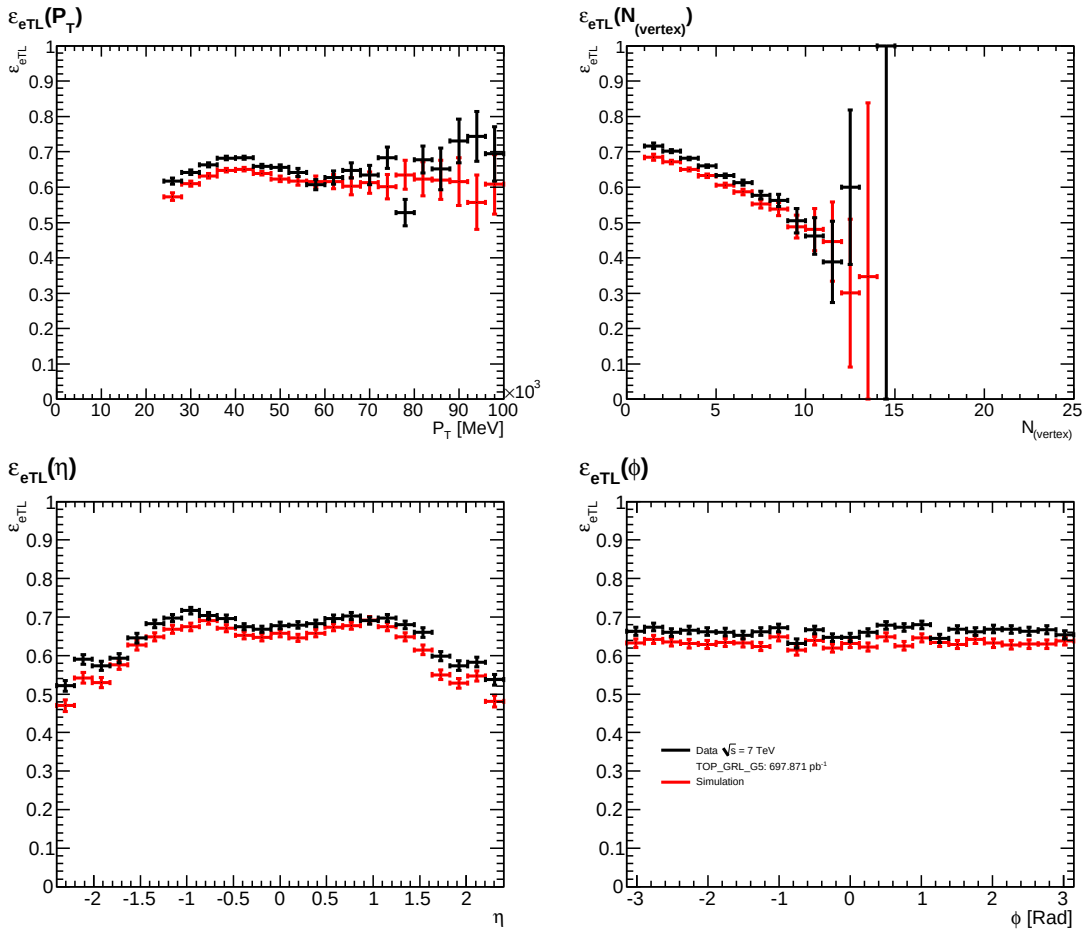

Figure 6.11: The TL efficiency measured from $Z \rightarrow ee$ events in data (black) and Monte Carlo (red).

convoluted with a Gaussian for the case of the muons, and to a pair of Crystal Ball functions [79] in the case of the electrons. Figure 6.12 shows the data and MC fits. We take half the difference in the peak of these fits between data and MC as a systematic uncertainty on the p_{T} scale, and the quadrature difference in the widths divided by $\sqrt{2}$ as a systematic uncertainty on the resolution. The MC modeling was quite good and the differences in the scale and resolution are small. In the muon channel the MC Z peak was at 90.9 GeV and in data was at 90.8, giving a systematic uncertainty on the p_{T} scale of 0.06% . The resolution uncertainty in the muon channel was extracted from the quadrature difference in the fit Gaussian width of 4.54 GeV in the data vs. 3.93 GeV in the MC. Using a mean p_{T} of 40 GeV, measured from the MC, the systematic uncertainty on the TL resolution in the MC was $\sqrt{4.54^2 - 3.93^2}/(\sqrt{2}\cdot 40)$=4.0%. Fits in the electron channel were more difficult to interpret because of the double Crystal Ball function fit and the lack of detailed quantitative knowledge of the radiator material in Inner Detector as a function of η. We used the Crystal Ball function that determines the approximately Gaussian falling edge in the ee figures on the left of Figure 6.12 to give a p_{T} scale systematic uncertainty of 0.04% (the data-MC difference in the peak position was 0.075 GeV) and a resolution uncertainty of 5.4%.

6.4 Jet Selection and Systematics

Jet were reconstructed using the anti-k_t algorithm [80, 81] (R=0.4). The anti-k_t algorithm takes as input reconstructed topological clusters in the calorimeter calibrated at the electromagnetic scale, as compatible with electron and photon energy depositions. In order to restore jet energies to the hadronic energy scale, one further needs to rescale cluster energies with Monte Carlo based p_T and η dependent correction factors. In order to derive the correction factors for the hadronic scale, we used inclusive QCD jet events simulated with 75 ns bunch spacing within the bunch train and with a pile-up level averaging 8 interactions per bunch crossing.

Jet quality criteria were applied in order to reject events that contained jets not associated with in-time real energy deposits in the calorimeters, caused by various sources ranging from hardware problems in the calorimeter, the LHC beam conditions and atmospheric muon cosmic ray induced showers.

The calorimeter jet reconstruction efficiency [82,83] was derived relative to jets built from charged tracks reconstructed in the inner detector system, again using a tag and probe technique. The reconstruction efficiency was defined as the fraction of probe track-jets matched to a calorimeter jet. The observed difference between data and MC was applied to MC by computing for each selected jet its probability to be badly reconstructed and vetoing that jet if its probability was greater than some threshold value.

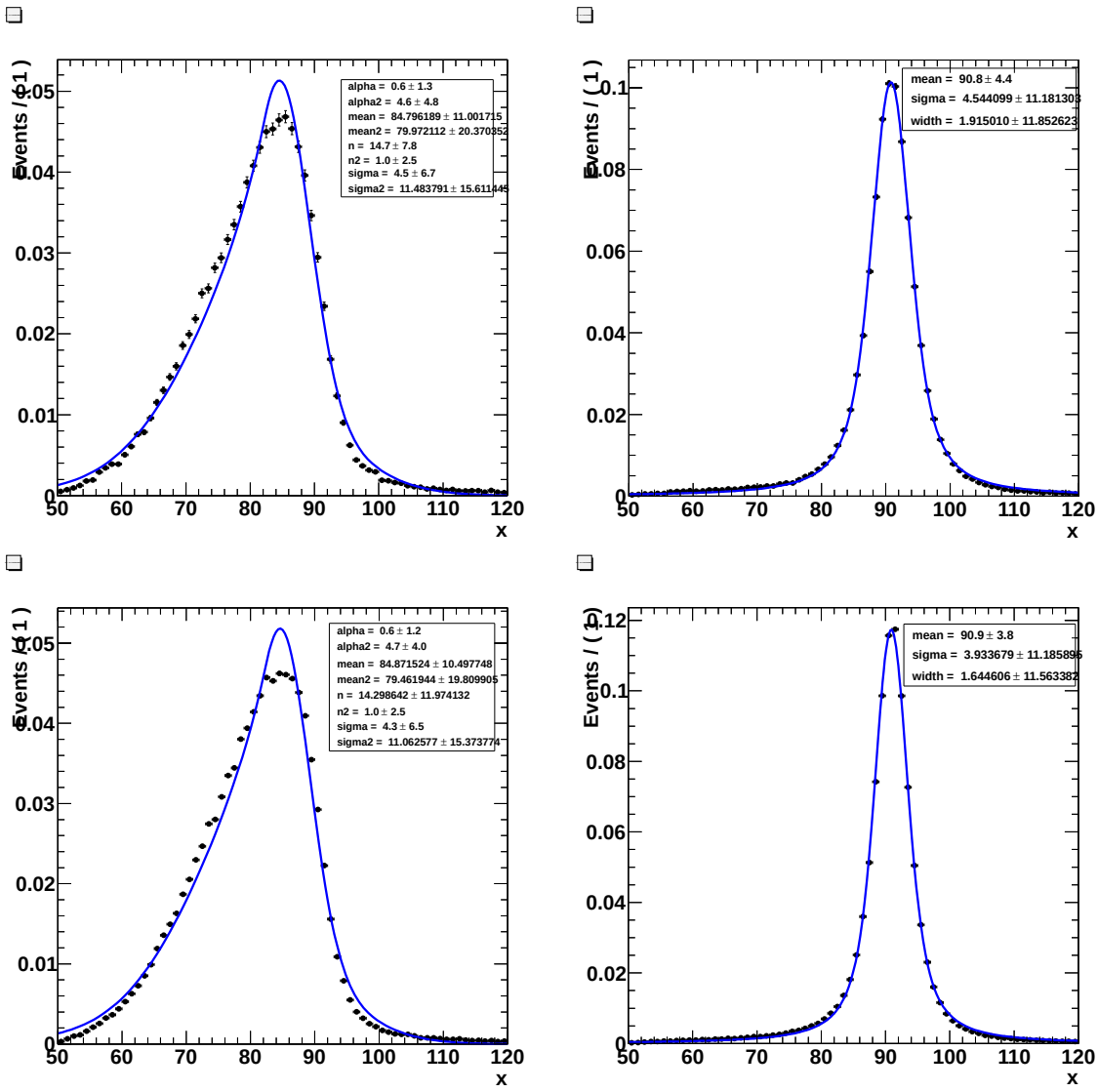

Figure 6.12: Opposite-sign TLs invariant mass for collision data (top) and MC (bottom), left-hand-side: electrons, right-hand-side: muons.

The jet energy resolution, as measured using the di-jet balance and the bi-sector techniques [84] achieved good agreement between data and MC simulation to within 2%. The uncertainty was propagated to the MC by Gaussian smearing the jet transverse momentum.

The jet energy scale uncertainty (JES) was based on the evaluation derived from 2010 data and MC. However, in-situ measurements showed that the overall estimate of the JES uncertainty from 2010 data was still valid for jets used in this analysis. Some of the dominant contributors to the JES uncertainty were the JES calibration method, the calorimeter response and the ATLAS detector simulation. [85]. The uncertainty associated with the pile-up contribution has been re-evaluated with 2011 data and was binned in three p_{T} bins for central and forward jets (see Table 6.4). Additional contributions were included in order to account for the top multi-jet environment: the flavour composition and close-by jet uncertainties.

In order to avoid double counting between electromagnetic and hadronic objects, a jet close to an electron candidate was removed if the corresponding distance between the jet and the electron track was $\Delta R < 0.2$. Finally, only jets with $p_{\mathrm{T}} > 20$ GeV and $|\eta_{\mathrm{detector}}| < 2.5$ were considered.

Table 6.4: The jet energy scale uncertainty associated with pile-up derived for central and forward jets in 3 p_{T} bins.

	$0 < \|\eta\| < 2.1$	$2.1 < \|\eta\| < 4.5$
$20 < p_{\mathrm{T}} < 50$ GeV	5 %	7 %
$50 < p_{\mathrm{T}} < 100$ GeV	2 %	3 %
$p_{\mathrm{T}} > 100$ GeV	0 %	0 %

6.5 The Missing Transverse Energy

We used the missing transverse energy algorithm `MET_RefFinal_em_loose` provided by the Top Working Group [86]. This algorithm takes as input topological clusters with calibration based on the physics object they are associated with. Muons, which are not primarily measured by the calorimeter, are included using their momentum as measured by the Inner Detector and Muon Spectrometer systems. Topological clusters are associated with electrons, high P_T jets and low P_T jets (`SoftJets`). The above mentioned order of the objects is important since it demonstrates the cluster to object association preference. The remaining clusters that are not associated with high P_T objects are included at the `EM` scale in a `CellOut` term. The E_T^{Miss} is calculated using Equations 6.2 and 6.3.

$$E_{x,y}^{Miss} = E_{x,y}^{Electrons} + E_{x,y}^{Jets} + E_{x,y}^{SoftJets} + E_{x,y}^{Muon} + E_{x,y}^{CellOut} \tag{6.2}$$

$$E_T^{Miss} = \sqrt{\left(E_x^{Miss}\right)^2 + \left(E_y^{Miss}\right)^2} \tag{6.3}$$

The electron term in the E_T^{Miss} uses clusters associated with electrons satisfying the `isEM::Loose` definition with $P_T > 10$ GeV [69]. The E_T^{Miss} electron term takes electrons at the energy scale that accounts for all electron correction factors except the out-of-cluster correction. Both $P_T > 20$ GeV jet and `SoftJet` jet terms do not include pile-up corrections to the jet energy scale. The latter term for jets in the 7 GeV$< P_T < 20$ GeV range enters into the E_T^{Miss} balance calibrated to the `EM` scale, while the former for jets with $P_T > 20$ GeV is corrected to the full hadronic energy scale `EM+JES`. The muon term in the E_T^{Miss} is determined from the `MuidMuonCollection` muon momentum for the full acceptance range of the muon spectrometers, $|\eta| < 2.7$. All combined muons within $|\eta| < 2.5$ are included in the E_T^{Miss} calculation. The muon term in the E_T^{Miss} also contains isolated muons (`MET_MU_TRACK`) and non-isolated muons (`MET_MU_SPECTRO`) [86].

Missing $\mathbf{E}_T$ in Lepton+Track events

By definition, the TL in exclusive events is not an identified lepton and therefore is typically not handled correctly in the $E_{\mathrm{T}}^{\mathrm{miss}}$ balance, giving rise to large $E_{\mathrm{T}}^{\mathrm{miss}}$ tails in the exclusive Lepton+Track events. While unidentified electrons enter the $E_{\mathrm{T}}^{\mathrm{miss}}$ calculation as a jet, unidentified muons are completely neglected from the $E_{\mathrm{T}}^{\mathrm{miss}}$ calculation.

MET_RefFinal_em_loose was found to have significantly better performance in Drell-Yan plus Z (DY/Z) events in the eTL channel, compared to other prescriptions for $E_{\mathrm{T}}^{\mathrm{miss}}$ calculations, and was therefore used for the $E_{\mathrm{T}}^{\mathrm{miss}}$ selection in the lepton+track analysis. In order to suppress backgrounds from DY/Z events in the μTL channel, the $E_{\mathrm{T}}^{\mathrm{miss}}$ was corrected by the p_{T} of the TL in μTL events if the $\Delta\phi$ between the $E_{\mathrm{T}}^{\mathrm{miss}}$ and the TL direction was less than 0.2 and there was no identified lepton within ΔR=0.05 of the TL. Figure 6.13 explicitly demonstrates the effect of this correction by comparing the 'No Correction' scenario to the 'With Correction' scenario for the full data sample. One can observe that the $E_{\mathrm{T}}^{\mathrm{miss}}$ correction helps to move a significant number of events from the bump around $E_{\mathrm{T}}^{\mathrm{miss}} \sim 40$ GeV to the bulk of events near the origin. This agrees well with what one expects from the $E_{\mathrm{T}}^{\mathrm{miss}}$ correction for DY/Z dilepton events, where mis-treated muons from Z decays are responsible for the bump around $E_{\mathrm{T}}^{\mathrm{miss}} = 40$ GeV.

6.5.1 E_T^{Miss} Uncertainties

Some of the most significant sources of uncertainty on the $E_{\mathrm{T}}^{\mathrm{miss}}$ calculation come from the scale and resolution of the objects energy and P_T, the description of the pile-up events and the impact of hardware failures [86].

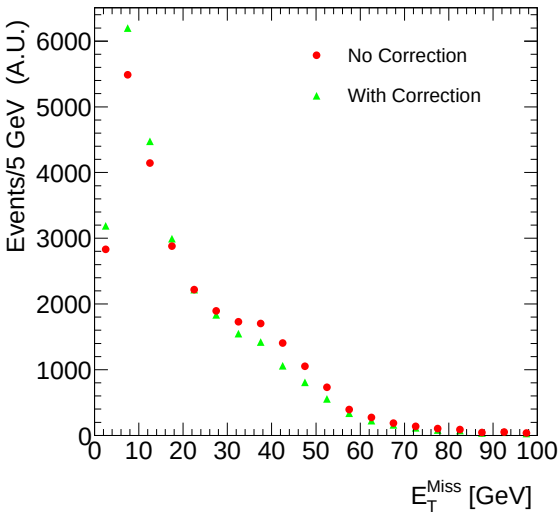

Figure 6.13: Measured $E_{\mathrm{T}}^{\mathrm{miss}}$ for exclusive μ+track events selected from the collision data set. Two scenarios are shown: 'No Correction' (red circles) and 'With Correction' (green triangles). No requirements on the event kinematics such as H_T, N_{jets}, M_{ll} and $E_{\mathrm{T}}^{\mathrm{miss}}$ were imposed.

Each of the objects in the E_T^{Miss} calculation has an uncertainty related to the scale of resolution of the energy or P_T of the object. For the electrons, high-P_T jets and muons, the uncertainties on the scale and resolution of the objects energy and P_T were propagated into the E_T^{Miss} calculation using the `METComposition` code [87], assuming a 100% correlation between the uncertainty on the objects and the E_T^{Miss}.

We note that special care was taken to ensure appropriate jet calibration when, due to an energy scale or resolution shift, jets transitioning through the $P_T > 20$ GeV boundary and thus being changed from the `SoftJet` category calibrated at the `EM` scale to the high P_T jets category calibrated at the `EM+JES` scale.

For high P_T jets, the E_T^{Miss} uncertainty also takes into account the jet efficiency uncertainty by reducing the jet contribution to E_T^{Miss} to the `EM` scale, and properly includes the transition between `EM` and `EM+JES` scale at the $P_T = 20$ GeV boundary.

For the `SoftJet` and `CellOut` terms, the main uncertainty comes from the topological cluster energy scale, estimated to be $\pm 10.5\%$ and $\pm 13.2\%$ respectively [88][5]. These values were used to scale up and down the `SoftJet` and `CellOut` terms assuming a 100% correlation.

Preliminary studies revealed a discrepancy between some data versus MC simulation in the low energy E_T^{Miss} attributed to pile-up. These effects were observed in the jet, `SoftJet` and `CellOut` terms, while for the high P_T jets, the effect of pile-up was already included in the JES uncertainty. Therefore, for the `SoftJet` and `CellOut` terms, both the x and y components of the E_T^{Miss} were shifted by $\pm 10\%$ to account

[5]The E_T^{Miss} definition studied in [88] is `MET_RefFinal`

for this discrepancy.

In April 2011, six front end boards (FEBs) were lost due to a Controller Board problem. This mainly caused jet and electron energy mis-measurement due to the dead FEBs. This failure occurred after the production of the MC10b Monte Carlo was complete, thus the MC simulation was FEB-problem blind. In order to account for it properly in Monte Carlo simulations, the following prescription was suggested by the Top Group: events with at least one low quality jet were identified. The jet was considered to be low quality if it was within $\Delta R < 0.1$ from the FEB hole and $P_T > P_{\text{Thres}}$. For the case of MC simulation $P_{\text{Thres}} = 20$ GeV, while for data $P_{\text{Thres}} = 20$ GeV was adjusted in order to account for the missing energy in the jet, $P_T > 20$ GeV $\times \frac{1-BCH\_CORR\_JET}{1-BCH\_CORR\_CELL}$. BCH_CORR_CELL is the corrected fraction of jet by `Cell Average Energy Density Correction` and BCH_CORR_JET is the estimated missing energy in the jets from "bad cells" based on the average jet shape in MC [89]. A $\pm 20\%$ systematic uncertainty was applied on the modified threshold in data in order to account for possible data/MC discrepancies in the event shape and differences between b-jets, quark jets, and gluon jets. We used the special software CheckOQ tool to identify electrons affected by the problematic FEBs and removed them from the $E_{\text{T}}^{\text{miss}}$ balance calculation both in the data and the MC simulation.

Chapter 7

$t\bar{t}$ Cross Section Measurements using Lepton+Track Selection

7.1 Introduction

We stated in Section 1.6.2 that we focussed on the inclusive and the exclusive l+track selection of dilepton events for the $t\bar{t}$ cross section measurement. Most of the events selected by the inclusive l+track analysis are also selected by the conventional 2ID analysis with two identified leptons. The sub-set of the inclusive l+track events that do not pass the 2ID analysis selection requirements compose the exclusive l+track events. In order to obtain the sample of exclusive l+track events we fully implemented the 2ID analysis event selections (parallel to l+track event selection requirements) and rejected those events that passed all 2ID requirements. As one expected, the exclusive l+track events most often failed 2ID analysis event selection requirements due to more stringent requirements on the second lepton leg or the higher cut threshold on missing transverse energy[1]. It is also important to note that a fraction of the 2ID events were never selected by the inclusive l+track analysis. This is primarily due to tighter requirements on isolation and transverse impact parameter of the TL (see Table 6.3), a shift in the measured M_{ll} of the l+track pair due to non-compensated radiation losses that a charged particle may undergo in the tracker, and the absence of the $E_{\mathrm{T}}^{\mathrm{miss}}$ cut for $e\mu$ events.

We adhered to the robust cut-and-count method in order to perform the $t\bar{t}$ cross section measurement. The robustness of the method is in its relative independence of shapes of distributions and its explicit clarity for the central value measurement. One only needs to define the signal selection requirements and perform the counting of signal and background events. Being simple, the method makes it relatively easy to comprehend and explain the causal relations and tendencies between the main processes that significantly affect the cross section measurement. Nevertheless, note that the estimation of systematic uncertainties still requires in-depth complex studies. One of the major components in the analyzer's arsenal to refine the measurement is establishing the optimal signal event selection requirements. Thus, we devoted special care to devise an event selection optimization algorithm that yielded the definition of a set of the most effective requirements for $t\bar{t}$ candidate event selection.

[1] The 2ID analysis used $E_{\mathrm{T}}^{\mathrm{miss}}$ >60 GeV in ee and $\mu\mu$ channels vs. $E_{\mathrm{T}}^{\mathrm{miss}}$ >45 GeV in l+track analysis.

7.2 Optimization Algorithm for Event Selection Requirements

The ultimate goal for optimization of $t\bar{t}$ event selection is to determine a set of requirements that enables a measurement of the $t\bar{t}$ pair production cross section with the smallest possible statistical and systematic uncertainties. In order to ensure minimal statistical uncertainty, the event selection should provide as pure as possible candidate event sampling while simultaneously suppressing background events. The optimal balance between background rejection and signal acceptance that yields the minimal statistical uncertainty is estimated by maximizing $S/\sqrt{(S+\sum B_i)}$, where S is the number of signal events and B_i is the number of background events of species i. The systematic uncertainty on the $t\bar{t}$ cross section measurement is directly traced to the systematic uncertainties on the signal acceptance ΔA and to each of the background contributions ΔB_i. This implies that the optimization should be made sensitive to the systematic uncertainties on the signal acceptance and the background contributions in order to ensure that the determination of the event selection requirements minimizes the effect of the uncertainty ΔA and ΔB_i on the $t\bar{t}$ cross section measurement.

In order to make the overall approach to optimization as robust as possible, we defined a single figure of merit which by construction was made sensitive not only to statistical but also to systematic uncertainties, the maximum of which yielded the optimal event selection for the analysis:

$$\alpha = \frac{S}{\sqrt{(\delta N^{Stat})^2 + \sum(\delta N_i^{Syst})^2 + \sum(\delta B_i^{Stat})^2}} \tag{7.1}$$

where the statistical term $\delta N^{Stat} = \sqrt{S+\sum B_i}$, S and B_i are defined as the number of signal and ith background type events respectively, and δB_i^{Stat} is the statistical uncertainty per ith background component. The ith systematic term is defined as:

$$\delta N_i^{Syst} = \frac{1}{2} \cdot (N_i^{+1\sigma} - N_i^{-1\sigma}). \tag{7.2}$$

The systematic uncertainties that were accounted for included the electron and muon energy scale and resolution uncertainties as well as the uncertainty on the jet energy scale. These uncertainties were determined by shifting their energy scales and resolution by $\pm 1\sigma$ within their uncertainty bands, recalculating E_T accordingly and measuring the change in the accepted number of signal and background events.

We further decided to take advantage of the fact that the data-driven estimation of the DY/Z opposite sign dilepton background has a smaller systematic uncertainty than MC simulation of this background, hence in the course of optimization, this also helped to retain signal acceptance. As described in Section 7.4.1, the

data-driven DY/Z evaluation uses a data to MC ratio $K(E_{\mathrm{T}}^{\mathrm{miss}})$ in a control region around the Z-boson mass, called the 'Z-window' to scale the MC prediction for DY/Z dilepton events in the signal region, outside of this Z-window. The $E_{\mathrm{T}}^{\mathrm{miss}}$ requirement in the CR can be different from that in the SR, and its value was included as a parameter to be optimized. The ratio $K(E_{\mathrm{T}}^{\mathrm{miss}})$ depends on the $E_{\mathrm{T}}^{\mathrm{miss}}$ threshold, thus one needs to include in the figure of merit a term to describe the systematic uncertainty due to data-driven approach itself:

$$\delta N_{DY}^{Syst} = \frac{1}{2} N_{MC}^{DY} \cdot [K(E_{\mathrm{T\ CR}}^{\mathrm{miss}}) - K(E_{\mathrm{T\ SR}}^{\mathrm{miss}})] \tag{7.3}$$

with $K(E_{\mathrm{T}}^{\mathrm{miss}})$ denoting the $E_{\mathrm{T}}^{\mathrm{miss}}$ dependent correction factor for data-driven DY/Z dilepton estimation (more details on $K(E_{\mathrm{T}}^{\mathrm{miss}})$ are available in section 7.4.1).

7.3 $t\bar{t}$ Candidate Event Selection for the l+Track Analysis

The $t\bar{t}$ candidate event selection requirements that were found to be effective for the l+track analysis were the cuts on the invariant mass of the opposite sign lepton-TL pair M_{ll}, the SR missing transverse energy $E_{\mathrm{T\ SR}}^{\mathrm{miss}}$ as well as the scalar transverse energy sum H_{T} of the selected leptons and jets. The prime reason for the Z-mass window cut is the suppression of DY/Z dilepton pair background. The $E_{\mathrm{T\ SR}}^{\mathrm{miss}}$ cut was applied to suppress residual DY/Z events outside the Z-mass window. Finally, we made use of the cut on H_{T} to suppress backgrounds that involve misidentified leptons (fakes), i.e. leptons that did not belong to $t \to Wb \to l\nu b$ decay chain or were faked by isolated jets that passed the lepton identification requirements.

We found that there were non-negligible correlations between the quantities effective for the l+track event selection, thus motivating a simultaneous grid optimization in the phase space spanned by the parameters effective for l+track event selection. Since 4D simultaneous optimization was excessively CPU intensive, the H_{T} cut was fixed at 150 GeV, and a three dimensional optimization of the M_{ll}, $E_{\mathrm{T\ SR}}^{\mathrm{miss}}$ and $E_{\mathrm{T\ CR}}^{\mathrm{miss}}$ was performed. Skimming through the 3D parameter phase space was performed after imposing several dilepton event selection requirements such as: the identified leptons were required to be oppositely-charged and the event had to have at least two identified jets. Events with more than two identified leptons were rejected. The phase-space cuts on the low invariant mass $m(l^+l^-)$ for the MC DY/Z dilepton samples also require a phase space cut on the selected events in data. Due to resolution effects, a cut on the reconstructed invariant dilepton mass of $m(l^+l^-) > 15$ GeV was used for both MC and data events. This cut removed dilepton contamination from all low mass resonances (e.g. Υ or J/ψ). In order to avoid double counting of background events with misidentified leptons present both in the MC and the data-driven backgrounds, for

the Monte Carlo $t\bar{t}$ samples we required that the reconstructed leptons originated from a leptonic W decay (or subsequent tau decay). This was achieved using a dedicated software tool developed by the ATLAS collaboration: `MCTruthClassifier`. The residual DY/Z dilepton background outside the Z-mass window was derived using the data-driven method described in Section 7.4.1. The M_{ll}, $E_{\mathrm{T\ SR}}^{\mathrm{miss}}$, $E_{\mathrm{T\ CR}}^{\mathrm{miss}}$ and H_{T} cuts were simultaneously optimized for e+track and μ+track channels. The optimization was run independently for the inclusive and exclusive modes of the l+track analysis.

In Figure 7.1, we present the dependence of the significance on the Z-mass window cut only. For this pair of plots we used the data-driven technique to estimate the expected number of DY/Z dilepton events. The optimization was performed in 2010 data analysis. One can observe in Figure 7.1 that the significance curves do not fall steeply from the maxima, allowing for small adjustments in the values of chosen cut threshold values at the price of losing only a few percent in significance. Therefore, for the sake of simplicity and consistency across the two analysis channels, we opted for a single set of event selection requirements for the inclusive l+track analysis: $E_{\mathrm{T\ SR}}^{\mathrm{miss}}$ >45 GeV, H_{T} > 150 GeV, a Z-mass window half width of 10 GeV (81-101 GeV), although the optimum values found for e+track channel were a Z-window width of zero and $E_{\mathrm{T\ SR}}^{\mathrm{miss}}$ >45 GeV. For the case of the μ+track channel, the optimization prefers $E_{\mathrm{T\ SR}}^{\mathrm{miss}}$ >35 GeV, $E_{\mathrm{T\ CR}}^{\mathrm{miss}}$ >15 GeV in the normalization region and a Z-mass window half width of 11 GeV. We opted for a Z-mass window cut of 10 GeV as found to be optimal in the μ+track channel, so that the DY/Z dilepton background suppression is not solely dependent on the $E_{\mathrm{T\ SR}}^{\mathrm{miss}}$ requirement. Inside the Z-mass window, i.e. in the control region the $E_{\mathrm{T\ CR}}^{\mathrm{miss}}$ >45 GeV cut was chosen to minimize the data-driven DY/Z dilepton background systematic uncertainty associated with the $E_{\mathrm{T}}^{\mathrm{miss}}$ dependence of the M_{ll} distribution in the CR.

For the exclusive l+track analysis mode, the optimum cut values were found to be not very different, although there were significant statistical fluctuations in the significance curves. Therefore, the inclusive results are used for both analysis modes, hence making the exclusive analysis a subset of the inclusive one. These event selection requirements for exclusive l+track analysis result in a 20% $t\bar{t}$ signal acceptance gain over the conventional 2ID lepton $t\bar{t}$ analysis. The left histogram Figure 7.2(a) shows the TL η for exclusive events. In addition to the gain over all η due to efficiency losses from the identified lepton selection, one notices various detector features such as the $\eta = 0$ gap between A and C sides of the Muon Spectrometer and the transition region in the calorimeter near $|\eta| = 1.4$. The right histogram in Figure 7.2(b) shows the exclusive acceptance by generator channel, demonstrating the increased acceptance for τ lepton channels.

The selection requirements on event kinematics are listed in Table 7.1.

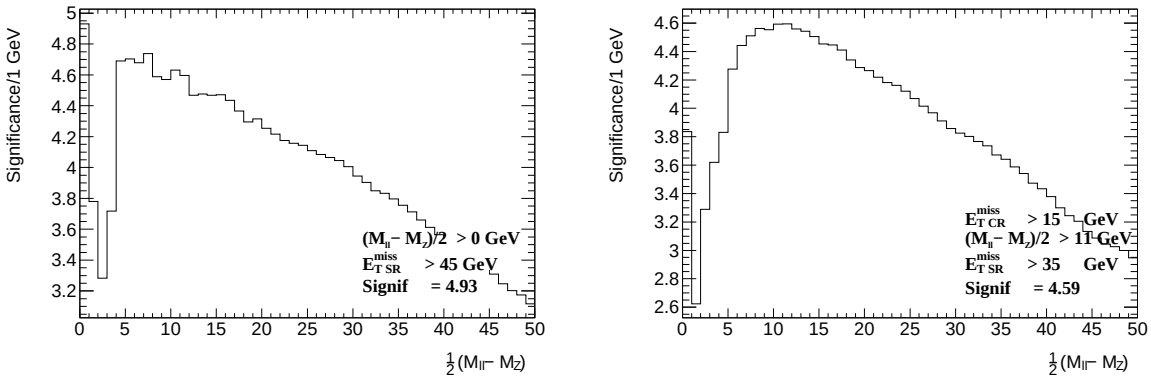

(a) e+track (b) μ+track

Figure 7.1: Significance vs. Z-mass window cut for the e+track and μ+track channels with $E_{\mathrm{T}}^{\mathrm{miss}}$ held at its optimized value, with $H_T > 150$ GeV and DY/Z dilepton background prediction extracted with data-driven approach.

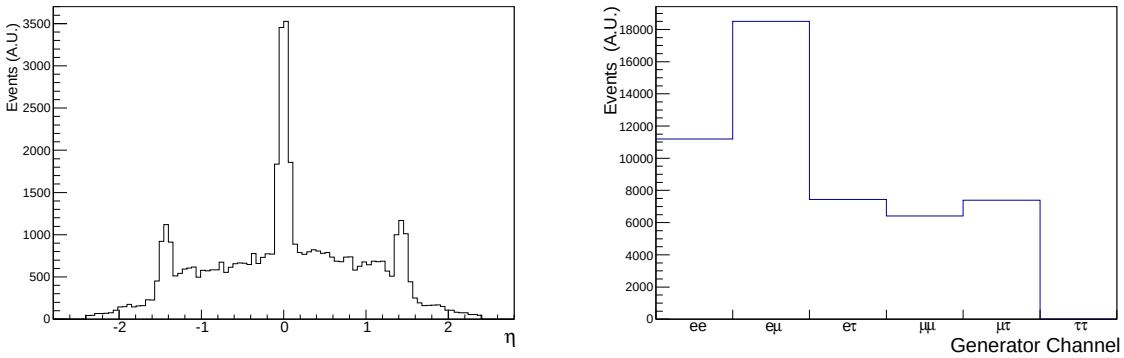

(a) (b)

Figure 7.2: Exclusive event track-lepton η distribution (left) and generator channel (right).

Cut	eTL	μTL
Pairs	Opp. Sign ID-Lepton+ TL, $\mathrm{P_T} > 25(20)$ GeVfor e (μ)	
Jets	≥ 2 jets, $E_{\mathrm{T}} > 20$ GeV, $\lvert\eta\rvert < 2.5$	
M_{ll} (l+TL pair)	15 GeV $< M_{\ell\ell} <$ 81 GeV or $M_{\ell\ell} >$ 101 GeV	
$E_{\mathrm{T\ SR}}^{\mathrm{miss}}$	$E_{\mathrm{T}}^{miss} > 45$ GeV	
H_{T}	$H_{\mathrm{T}} > 150$ GeV	

Table 7.1: Requirements on Event Kinematics.

7.4 $t\bar{t}$ Background Determination

We attempted to minimize the reliance on Monte-Carlo simulations by making maximal use of data-driven techniques for the evaluation of $t\bar{t}$ background contributions.

As discussed earlier there are three categories of background sources:

1. The background from DY/Z dilepton processes ($Z/\gamma^* \to \ell^+\ell^-$) produced with associated jets and with large $E_{\mathrm{T}}^{\mathrm{miss}}$ due to resolution effects and/or measurement errors.

2. Processes that contain jets misidentified as electrons, muons or TLs as well as processes where non-prompt leptons (i.e. leptons that do not originate from the decay of a W or Z boson) are misidentified as prompt. We refer to both the misidentified jets and the non-prompt leptons as "fakes". Fakes enter the sample in events with W bosons produced in association with jets, and QCD multi-jet events. In the case of W+jets events, one lepton is a real, prompt lepton from the W decay, the second is a fake lepton produced by one of the jets. In the case of QCD multi-jet events, both identified leptons (i.e. the electron or muon) and the TL are fakes. The latter contamination is negligible compared to fakes from W+jets events. Events with a fake TL are one of the most significant backgrounds in the l+track analysis channels.

3. Other background sources to the $t\bar{t}$ l+track analysis comprise electroweak processes with two opposite-sign leptons in the decay such as single top and diboson (WW, ZZ and WZ) production processes.

We make use of the data-driven approach for the DY/Z ($Z/\gamma^* \to \ell^+\ell^-$) and fake background evaluation. These methods and corresponding results are described in following sections. The $Z/\gamma^* \to \tau^+\tau^-$ background and the smaller backgrounds listed in 3) above are evaluated from Monte Carlo simulations.

7.4.1 DY/Z Background

As discussed above, we veto events close to the Z pole by imposing the Z-mass window requirement: 81 GeV $< M_{ll} <$ 101 GeV. We further suppress the surviving DY/Z dilepton events in the Z mass sidebands by imposing the $E_{\mathrm{T\ SR}}^{\mathrm{miss}} > 45$ GeV cut. However, there are residual DY/Z dilepton events that pass the event selection requirements. These events are difficult to model properly in the MC simulation due to uncertainties in the non-Gaussian nature of the missing transverse energy tails, the lepton energy and momentum resolution and the Z cross section in higher jet multiplicity bins.

In order to evaluate the DY/Z dilepton background in the l+track channels, we used the following expression:

$$\text{DY/Z dilepton background estimates} = \frac{(\text{Data(CR)} - \text{MC}_{\text{other}}\text{(CR)})}{\text{MC}_{\text{DY/Z}}\text{(CR)}} \times \text{MC}_{\text{DY/Z}}\text{(SR)}\,, \tag{7.4}$$

$$\text{DD}_{\text{DY/Z}}\text{(SR)} = \frac{(\text{Data(CR)} - \text{MC}_{\text{other}}\text{(CR)})}{\text{MC}_{\text{DY/Z}}\text{(CR)}} \times \text{MC}_{\text{DY/Z}}\text{(SR)}\,, \tag{7.5}$$

where Data(CR) represents the observed number of events in the control region in $\mathcal{L}$=698 pb^{-1} of collision data, $\text{MC}_{\text{DY/Z}}$(CR) is the number of MC DY/Z dilepton events measured in the control region. The control region is formed by events with an invariant dilepton mass inside the 'Z-mass window', with at least two jets and with $E_{\text{T}}^{\text{miss}} > 45$ GeV. Figure 7.3 shows a cartoon picture of the control region, which by construction is orthogonal to the signal region. MC_{other}(CR) is the contamination from some non-Z physics processes in the control region as predicted using Monte Carlo. DY/Z(SR) is the number of DY/Z dilepton events measured in the signal region using MC simulation. Taking the ratio of the measured number of events in data and MC simulation inside the Control Region, one can define a correction factor $K(E_{\text{T}}^{\text{miss}})$ that was further used to normalize the MC prediction for DY/Z dilepton events to data. Figure 7.4 shows the dependence of the correction factor $K(E_{\text{T}}^{\text{miss}})$ on the $E_{\text{T CR}}^{\text{miss}}$ requirement for the case of inclusive l+track analysis. For both inclusive channels, the MC simulation reasonably reproduces the data in the low $E_{\text{T CR}}^{\text{miss}}$ region yielding $K(E_{\text{T}}^{\text{miss}}) \sim 1$. However, in the region of $E_{\text{T CR}}^{\text{miss}} > 45$ GeV for the e+track channel, the MC over-predicts the number of DY/Z dilepton events (by ~ 30 %), while for the μ+track channel there is slight under-prediction. Similarly, Figure 7.5 shows the dependence of the correction factor $K(E_{\text{T}}^{\text{miss}})$ on the $E_{\text{T CR}}^{\text{miss}}$ requirement for the case of the exclusive l+track analysis. The dependence of the correction factor $K(E_{\text{T}}^{\text{miss}})$ on the $E_{\text{T CR}}^{\text{miss}}$ threshold is essentially the same as that for the inclusive mode. The main difference is that in the large $E_{\text{T CR}}^{\text{miss}}$ region for the μ+track channel, the mild over-prediction of the DY/Z events by

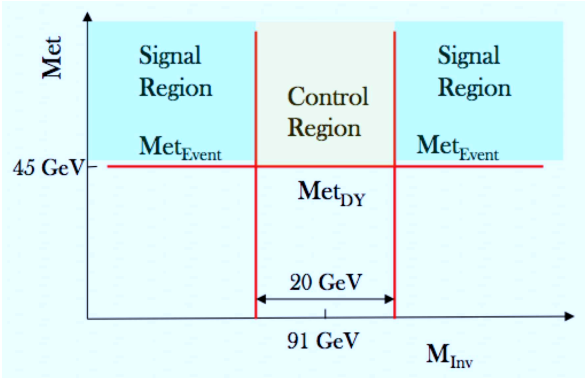

(a)

Figure 7.3: Cartoon picture of the control region that by construction is orthogonal to the signal region.

the MC is changed to a slight under-prediction.

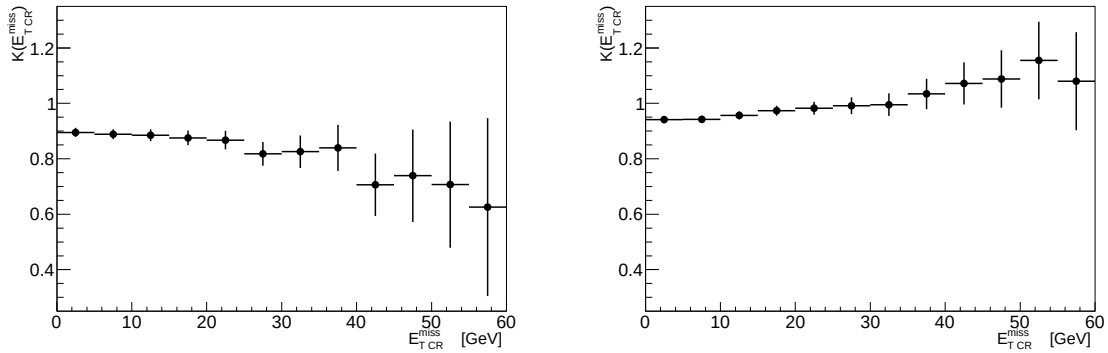

(a) e+track channel (b) μ+track channel

Figure 7.4: The dependence of the correction factor $K(E_{\mathrm{T}}^{\mathrm{miss}})$ on the $E_{\mathrm{T\ CR}}^{\mathrm{miss}}$ threshold requirement for the inclusive l+track analysis.

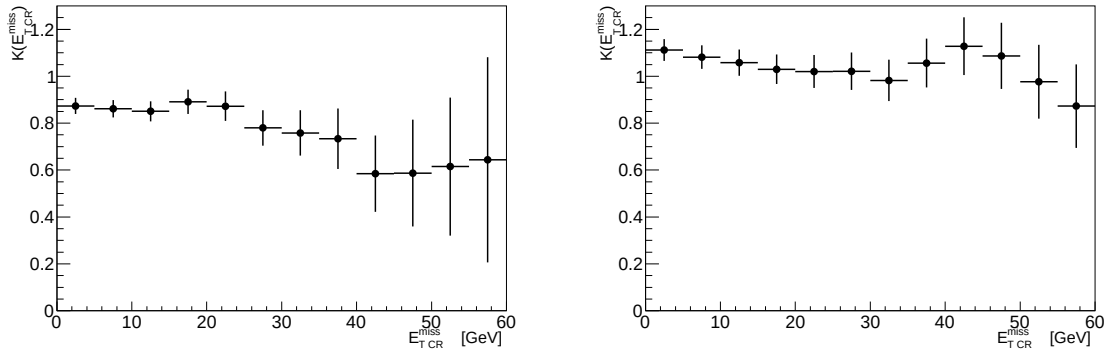

(a) e+track channel (b) μ+track channel

Figure 7.5: The dependence of the correction factor $K(E_{\mathrm{T}}^{\mathrm{miss}})$ on the $E_{\mathrm{T\ CR}}^{\mathrm{miss}}$ threshold requirement for the exclusive l+track analysis.

The observed and expected numbers in the control and signal regions are summarized in Table 7.2 for the eTL, and μTL channels for both inclusive and exclusive modes of the analysis. The predictions for DY/Z dilepton background events using the data-driven method are summarized in Table 7.3. The uncertainties include both statistical and systematic components, discussed in detail in Section 8.1.

7.4.2 Fake Track-Lepton Backgrounds

The fake TL contamination is evaluated using a fake TL matrix which gives the probability that a jet will be mis-reconstructed as a TL. The fake TL matrix is parameterized in jet E_{T} and N_{PV}, the number of primary vertices with four or more tracks. The γ+jet events are used to build the elements of the fake TL matrix.

Channel	Data(CR)	DY sources		Physics background sources (CR)					
		MC(CR)	MC(SR)	$t\bar{t}$	$Z\tau\tau$	W/Z fake	Diboson	Single top	Total
eTL Inclusive	218	134.7	82.1	88.3	0.1	17.8	9.7	4.0	119.9
μTL Inclusive	468	295.8	52.2	107.0	0.8	19.3	14.6	5.7	147.3
eTL Exclusive	74	54.3	40.7	21.2	0.1	16.8	2.6	0.8	41.5
μTL Exclusive	170	110.1	19.4	23.0	0.6	18.2	2.6	0.6	45.1

Table 7.2: The number of observed data events in the control region (Data(CR)), the number of Monte Carlo events in the signal (MC(SR)) and control (MC(CR)) regions and the number of events from other physics background sources contaminating the control region for DY background estimation in the inclusive and exclusive l+track channels.

	Inclusive		Exclusive	
	eTL	μTL	eTL	μTL
DD	$59.9^{+15.0}_{-15.0}$	$56.6^{+8.4}_{-8.6}$	$24.3^{+10.7}_{-9.4}$	$22.0^{+5.3}_{-5.8}$
MC	$82.1^{+71.0}_{-48.4}$	$52.2^{+36.4}_{-26.5}$	$40.7^{+23.9}_{-20.0}$	$19.4^{+8.8}_{-8.5}$

Table 7.3: Estimates of the contamination from DY/Z dilepton processes in the signal region of the $t\bar{t}$ analysis from both the data-driven method and from Monte-Carlo methods.

Relative to QCD dijet events, photons are easily identifiable, robust trigger objects that make it easier to avoid potential trigger biases that may occur in the fake probability measurement due to trigger object use. The EM clusters associated with photons were not used in the calculation of the fake matrix elements. The elements of the fake TL matrix were defined as:

$$\text{FakeRate}(E_{\text{T}}, N_{PV}) \quad = \quad \frac{\text{Number of all selected track leptons } (E_{\text{T}}, N_{PV})}{\text{Number of all ID jets \& jet} - \text{elements } (E_{\text{T}}, N_{PV})}$$

where the TLs in the numerator pass all required ID cuts for the analysis. The denominator includes both jets with E_{T} >25 GeV and 'jet-elements', which are track leptons that are not within ΔR <0.4 of a jet. In case it is not, in the denominator of the equation above, the track lepton is treated as if it were a jet (the 'jet-element') that fragmented to a single high P_{T} track, leaving no remnants that are reconstructed as a jet. The fake rates for track-leptons vs. jet E_{T} and N_{PV} are shown in Figure 7.6. The γ+jet events are selected using the following requirements:

Photon trigger: EF_g20_loose or EF_g40_loose

Reconstructed photon, $p_{\text{T}} > 25$ GeV, $|\eta| < 2.37$, excluding the crack region $1.37 < |\eta| < 1.52$.

The photon must pass the egamma tight photon identification requirements and have calorimeter

isolation in a $dR = 0.4$ cone of less than 2.5 GeV.

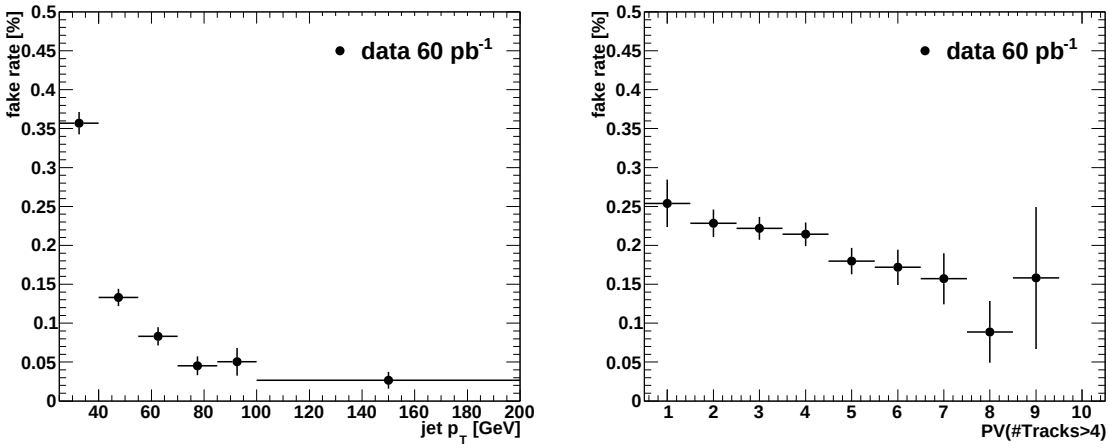

Figure 7.6: Track lepton fake rate measured from γ+jets events vs. jet E_{T} and number of primary vertices.

7.4.3 Determination of the Fake Track-Lepton Background

The prescription that we adopted for evaluation of the fake TL background contribution is as follows:

- From data, select events with exactly one ID lepton (e or μ), exactly zero TLs, at least one jet, and $E_{\mathrm{T}}^{\mathrm{miss}}$ >45 GeV. In the signal region of $\geq$2 jets, H_{T} >150 GeV is required.
- Sub-divide this data sample as a function of the number of identified jets.
- Sum the fake probabilities for events with N jets to obtain the predicted number of fake leptons in events with $N-1$ jets (because the model is that one jet is reconstructed as a lepton, as illustrated in Figure 7.7).

A few comments are in order: this prediction includes the contribution of W+jets, s and t channel single top, and single-leptonic $t\bar{t}$ events that enter the signal region, because these are all in the parent sample defined in the first bullet above. The sum over all jets in all events predicts the total number of *fake leptons*, not the number of *events with at least one fake lepton* in the data sample. We ignore this distinction because the probability of multiple fakes in a single event is very small.

Finally, the fake prediction must be corrected for fraction of the fake leptons that:

- Have opposite sign (OS) charge to the ID lepton.

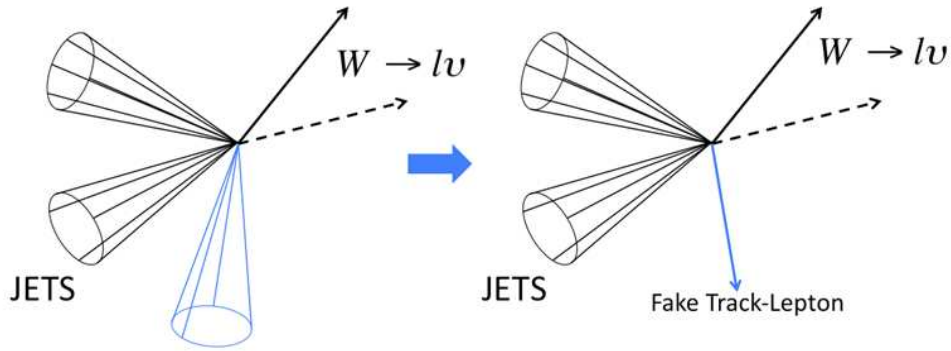

Figure 7.7: Illustration showing a W+3 jet event being reconstructed as a W+2 jet event with a fake lepton.

- Form a l+track pair with invariant mass outside the Z-mass window.

The OS fraction is measured using Monte Carlo simulation and is parametrized as a function of jet multiplicity. Table 7.4 shows, in each jet multiplicity bin, the total fake prediction, the expected fraction of opposite-sign fakes and the opposite-sign fake prediction. Similarly, the fraction of events with l+track pair invariant mass outside the Z-mass window was evaluated using W+jets, single top and semi-leptonic $t\bar{t}$ MC simulation. Due to the less stringent requirements on TL selection for the prompt lepton, the fake rate for the TL is significantly higher than that for identified leptons. Due to the much lower fake rate, we neglect fakes associated with misidentified electrons and muons and assume that the fakes are entirely from events with one real electron or muon and a fake TL.

	e**TL** inclusive		μ**TL** inclusive	
# jets	OS fraction	OS fake prediction	OS fraction	OS fake prediction
0	0.97 ± 0.03	5.5 ± 1.3	0.94 ± 0.14	5.2 ± 1.4
1	0.79 ± 0.02	31.4± 6.4	0.80 ± 0.02	35.0± 7.2
2	0.82 ± 0.01	42.8± 8.7	0.79 ± 0.01	48.1± 9.8
3	0.81 ± 0.02	26.2± 5.3	0.78 ± 0.02	30.2 ± 6.2
4	0.71 ± 0.03	10.7± 2.2	0.79 ± 0.03	13.4± 2.8
≥5	0.71 ± 0.03	4.5 ± 0.9	0.73 ± 0.04	4.9± 1.0
	e**TL** exclusive		μ**TL** exclusive	
# jets	OS fraction	OS fake prediction	OS fraction	OS fake prediction
0	0.97 ± 0.03	3.0± 0.7	0.94 ± 0.14	2.9 ± 0.8
1	0.80 ± 0.02	26.2± 5.4	0.80 ± 0.02	28.6± 5.9
2	0.83 ± 0.01	37.9± 7.7	0.79 ± 0.01	42.0± 8.6
3	0.81 ± 0.02	22.9± 4.7	0.79 ± 0.02	26.7± 5.5
4	0.71 ± 0.03	9.4± 2.0	0.78 ± 0.03	11.6± 2.4
≥5	0.68 ± 0.02	3.8± 0.8	0.73 ± 0.03	4.3 ± 0.9

Table 7.4: Opposite-sign fraction and opposite-sign fake prediction for each jet multiplicity. The uncertainty on the fake predictions is the statistical plus the 20% systematic uncertainty discussed in this Section.

7.4.4 MC-based backgrounds

The contamination in the signal region due to other small cross section electroweak background processes, such as single top, DY/Z→ $\tau\tau$ and dibosons was estimated directly from Monte Carlo simulations. By inverting expression 2.4 one obtains the number of events:

$$N_{\text{obs}} = (A \cdot \epsilon) \cdot \sigma_{\text{Theory}} \cdot \int Ldt \tag{7.6}$$

We considered the effect of all sources of systematic uncertainties on the MC-based background prediction(s), including analysis object related uncertainties (JES, ElES, MuES, etc) as well as the uncertainty due to the uncertainty on the theoretical cross section productions. Event yields for these background sources are summarized in Table 8.5 and Table 8.7 for the inclusive analysis. The corresponding information for the exclusive mode is summarized in Table 8.9 and Table 8.11.

7.5 Observed Event Yields

Control Regions Following the signal selection optimization step that defined the signal region and control region orthogonal to it, we validated the acceptance and efficiency modeling by comparing Monte Carlo simulation with data in the background dominated Z-mass window control region where there are relatively few $t\bar{t}$ dilepton events. In particular, the Z mass window, defined as $|M_{ll} - M_Z| \leq 10$ GeV, $E_{\text{T CR}}^{\text{miss}} > 45$ GeV and $H_{\text{T}} > 150$ GeV cuts were used. For the case of the inclusive l+track analysis, Figures 7.8 (a) and (d) show $E_{\text{T}}^{\text{miss}}$ for events in the Z mass region with at least 2 jets, Figures 7.8 (b) and (e) show the jet multiplicity for events where the dilepton mass lies inside the Z peak, $E_{\text{T CR}}^{\text{miss}} > 45$ GeV and $H_{\text{T}} > 150$ GeV. Figure 7.8 (c) and (f) probe the Monte Carlo modeling of the scalar P_T sum of leptons and jets. Figure 7.9 presents the distributions of the corresponding quantities for the case of exclusive l+track analysis. In general, good agreement between the background model and the data is observed.

Along with the Z mass window region, we use the zero and the one jet bins as additional, background dominated control regions, due to the at least 2 jet requirement for the signal region. Table 7.5 summarizes the number of observed data events, predicted background contributions and the $t\bar{t}$ signal expectation for cases with zero or 1 jet per analysis channel for the the inclusive l+track analyses. Table 7.6 presents the same information for the exclusive l+track case. The $E_{\text{T}}^{\text{miss}}$ distributions in the low jet multiplicity control region are shown in Figures 7.10 (a) and (d). The invariant mass distribution of the lepton-TL pair are shown

	e+track		μ+track	
Process	0 jets	1 jet	0 jets	1 jet
DY/Z+jets (DD)	$310.1^{+131.9}_{-128.9}$	$107.9^{+51.3}_{-56.4}$	$109.9^{+41.7}_{-41.9}$	$82.7^{+35.2}_{-33.6}$
DY/Z($\rightarrow \tau\tau$)+jets (MC)	$15.1^{+4.0}_{-6.9}$	$28.5^{+9.4}_{-7.5}$	$20.9^{+14.4}_{-9.4}$	$55.2^{+15.3}_{-14.8}$
Fake leptons (DD)	221.5 ± 45.4	109.6 ± 22.4	355.2 ± 88.8	159.7 ± 32.9
Single top (MC)	$5.8^{+1.1}_{-1.0}$	$28.5^{+3.5}_{-3.4}$	$7.0^{+1.3}_{-1.2}$	$36.2^{+4.3}_{-4.1}$
Dibosons (MC)	$47.6^{+4.4}_{-4.2}$	$30.7^{+3.1}_{-3.0}$	$60.9^{+5.3}_{-5.0}$	$35.4^{+2.6}_{-2.7}$
Total background	$600.0^{+140.0}_{-137.0}$	$305.2^{+56.9}_{-61.3}$	$552.8^{+99.3}_{-98.8}$	$369.2^{+50.6}_{-49.4}$
$t\bar{t}$ ($\sigma_{\text{Theory}} = 164.6$ pb^{-1})	$9.72^{+4.9}_{-4.5}$	$100.9^{+34.2}_{-36.0}$	$100.9^{+34.2}_{-36.0}$	$119.8^{+25.4}_{-26.2}$
Total expected events	$609.7^{+139.7}_{-137.0}$	$406.1^{+66.4}_{-70.7}$	$444.2^{+85.3}_{-84.7}$	$488.9^{+56.6}_{-55.9}$
Observed events	590	391	584	467

Table 7.5: Summary of background contributions to the inclusive l+track analysis in the 0 and 1 jet control regions. No H_T cut is applied.

in Figures 7.10 (b) and (e). Figures 7.10 (c) and (f) present the H_T distributions for the inclusive l+track channels. A similar set of plots for the exclusive mode of the l+track analysis are shown in Figures 7.11 (a-f). We again have good agreement between MC and the data.

Signal Region In Table 7.7 we summarize the number of observed data events, predicted background contributions and the $t\bar{t}$ signal expectation per analysis channel for the the inclusive and the exclusive l+track analyses. In a data set of $\mathcal{L}$=698 pb^{-1} a total of 1597 $t\bar{t}$ candidate events are observed in the inclusive l+track analysis, with 760 candidates in the eTL channel and 837 in μTL. In the exclusive mode of the analysis a total of 491 candidate events are observed, with 236 events in eTL and 255 in μTL analysis channels. Atlantis event display [90] pictures for the first e+track candidate event (run number 150530, event number 42761229) and μ+track candidate (run number 161379, event number 49866533) observed by ATLAS are shown in Appendix A.

In Figure 7.12 we present the main kinematic distributions describing the inclusive l+track events. Corresponding plots for the exclusive l+track channels are shown in Figure 7.13.

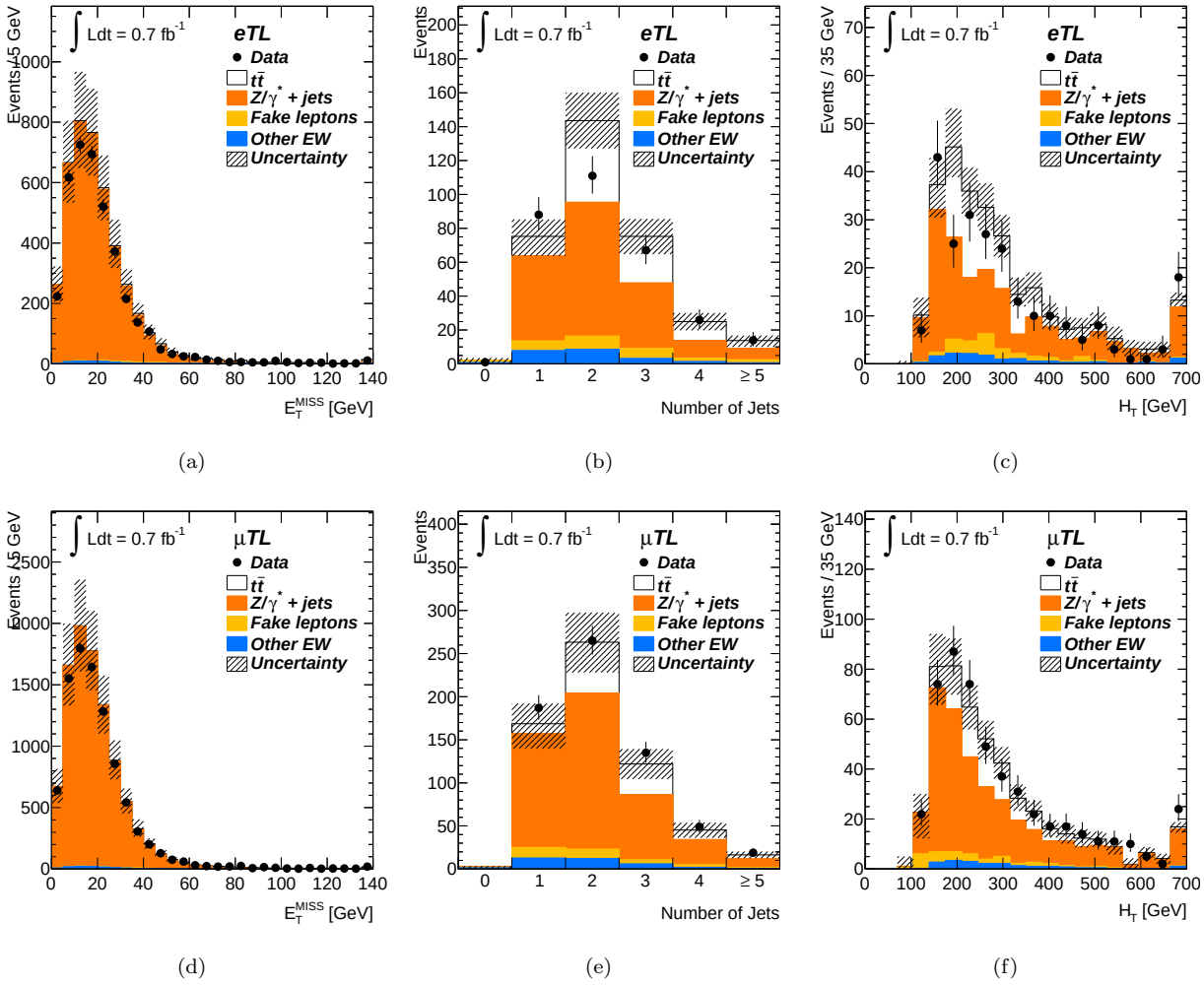

Figure 7.8: Control region plots for inclusive eTL (top row) and inclusive μTL (bottom row): (a),(c) $E_{\mathrm{T}}^{\mathrm{miss}}$ in events with a lepton-TL mass inside the Z mass window with $\geq$ 2 jets and H_T >150 GeV, (b),(d) the number of jets in events with a lepton-TL mass inside the Z mass window and $E_{\mathrm{T}}^{\mathrm{miss}} > 45$ GeV and H_T >150 GeV, (c),(f), H_{T} in events with a lepton-TL mass inside the Z mass window, $\geq$2 jets and $E_{\mathrm{T}}^{\mathrm{miss}}$ 45 GeV. The error bands reflect the statistical and systematic uncertainties of the MC prediction.

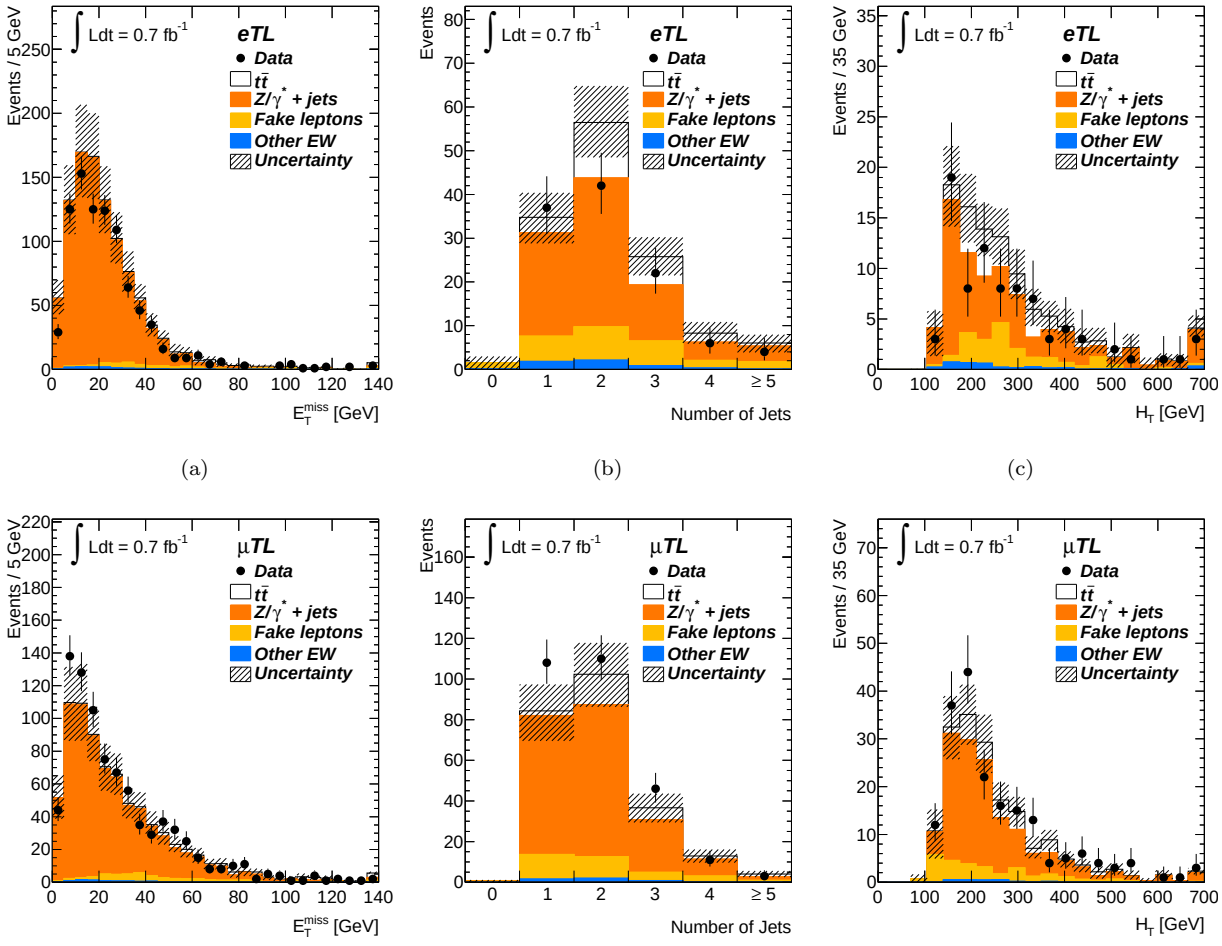

Figure 7.9: Control region plots for exclusive eTL (top row) and exclusive μTL (bottom row): (a),(c) $E_{\mathrm{T}}^{\mathrm{miss}}$ in events with a lepton-TL mass inside the Z mass window with $\geq$ 2 jets and H_T >150 GeV, (b),(d) the number of jets in events with a lepton-TL mass inside the Z mass window and $E_{\mathrm{T}}^{\mathrm{miss}} > 45$ GeV and H_T >150 GeV, (c),(f), H_{T} in events with a lepton-TL mass inside the Z mass window, $\geq$2 jets and $E_{\mathrm{T}}^{\mathrm{miss}}$ 45 GeV. The error bands reflect the statistical and systematic uncertainties of the MC prediction.

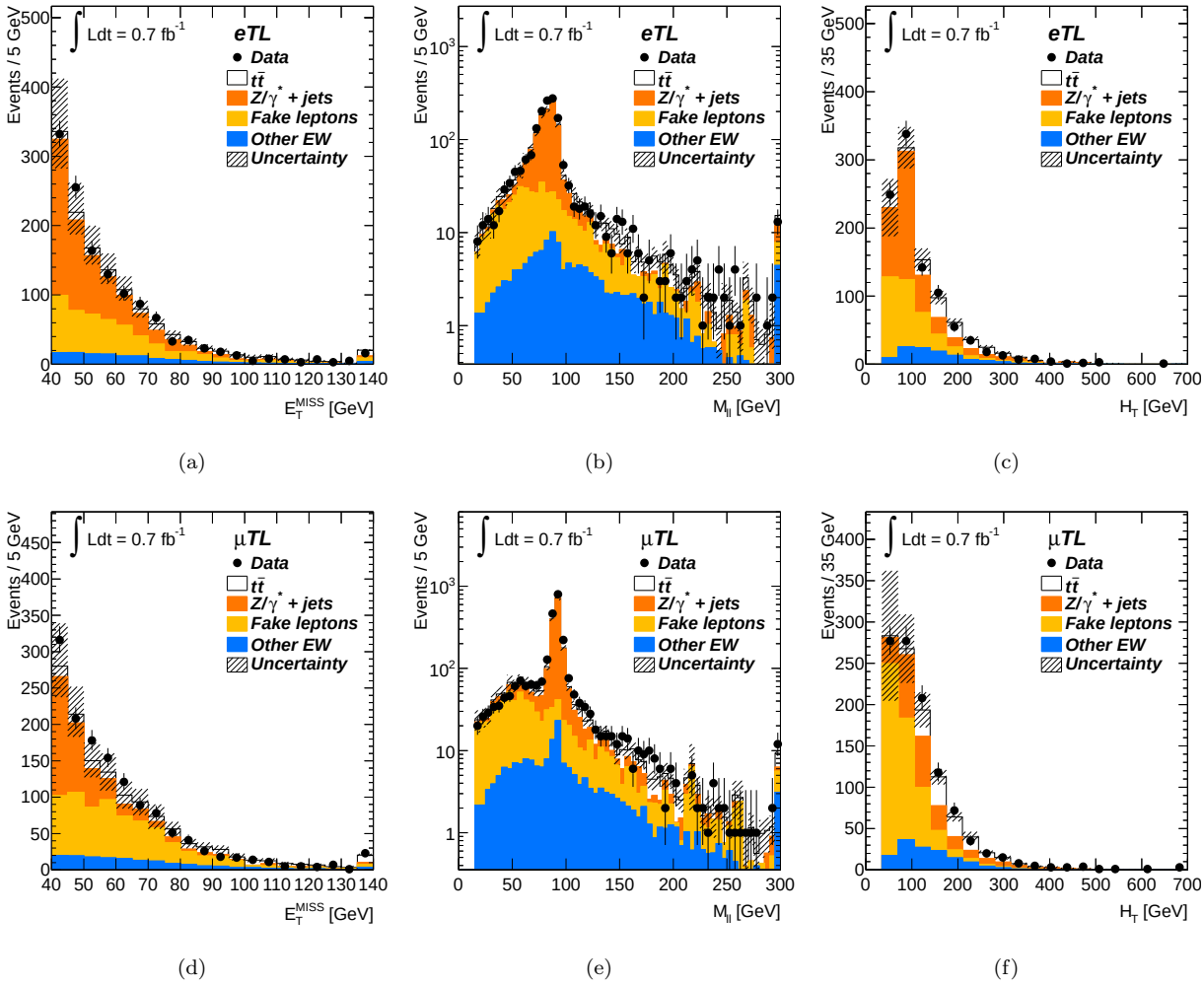

Figure 7.10: Control region plots for inclusive eTL (top row) and inclusive μTL (bottom row): (a),(c) $E_{\mathrm{T}}^{\mathrm{miss}}$ in events with a lepton-TL mass outside the Z mass window with < 2 jets, (b),(d) the lepton-TL in events with < 2 jets and $E_{\mathrm{T}}^{\mathrm{miss}} > 45$ GeV (c),(f), H_{T} in events with a lepton-TL mass outside the Z mass window, <2 jets and $E_{\mathrm{T}}^{\mathrm{miss}}$ 45 GeV. The error bands reflect the statistical and systematic uncertainties of the MC prediction.

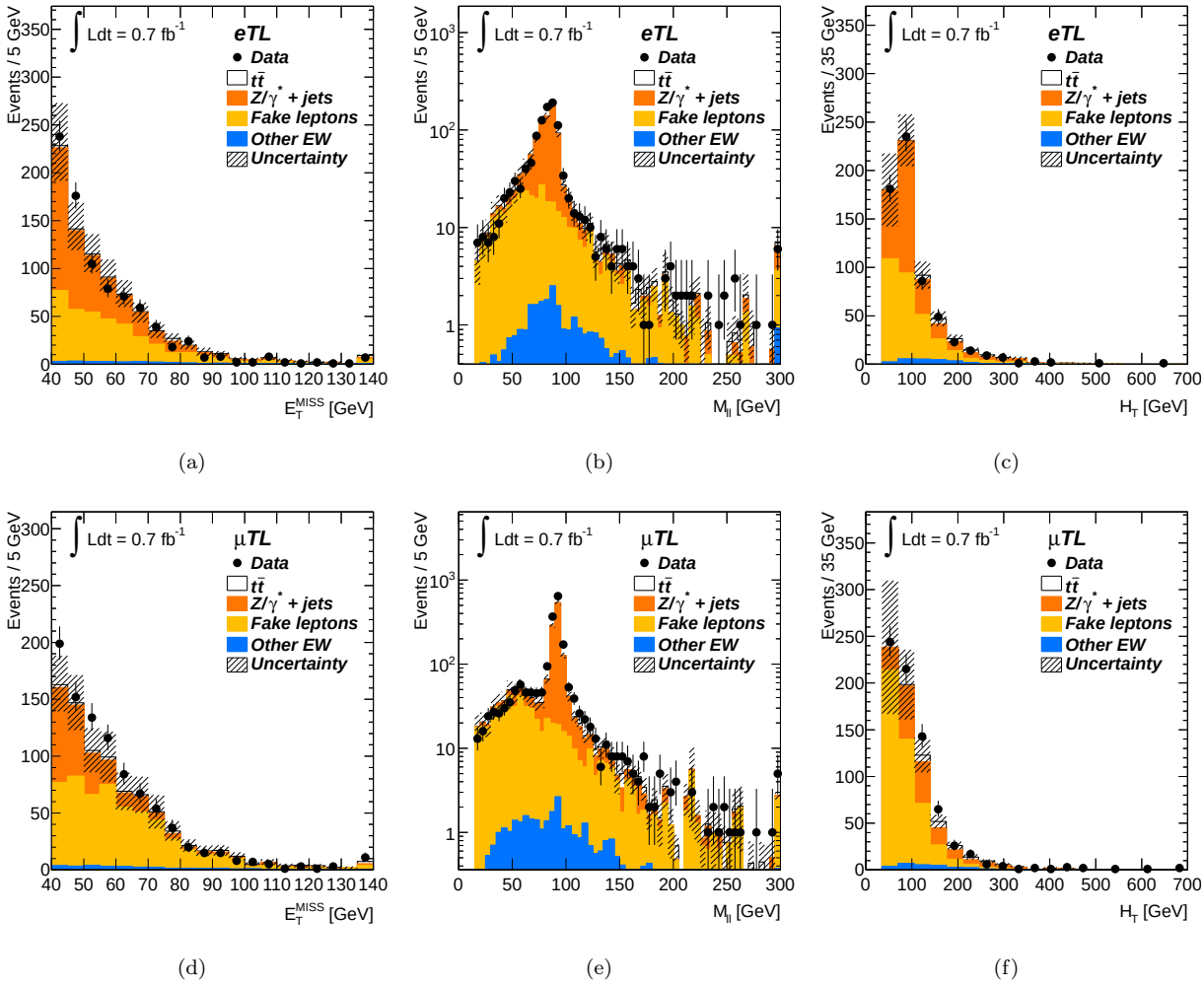

Figure 7.11: Control region plots for exclusive eTL (top row) and exclusive μTL (bottom row): (a),(c) $E_{\mathrm{T}}^{\mathrm{miss}}$ in events with a lepton-TL mass outside the Z mass window with < 2 jets, (b),(d) the lepton-TL in events with < 2 jets and $E_{\mathrm{T}}^{\mathrm{miss}} > 45$ GeV (c),(f), H_{T} in events with a lepton-TL mass outside the Z mass window, <2 jets and $E_{\mathrm{T}}^{\mathrm{miss}}$ 45 GeV. The error bands reflect the statistical and systematic uncertainties of the MC prediction.

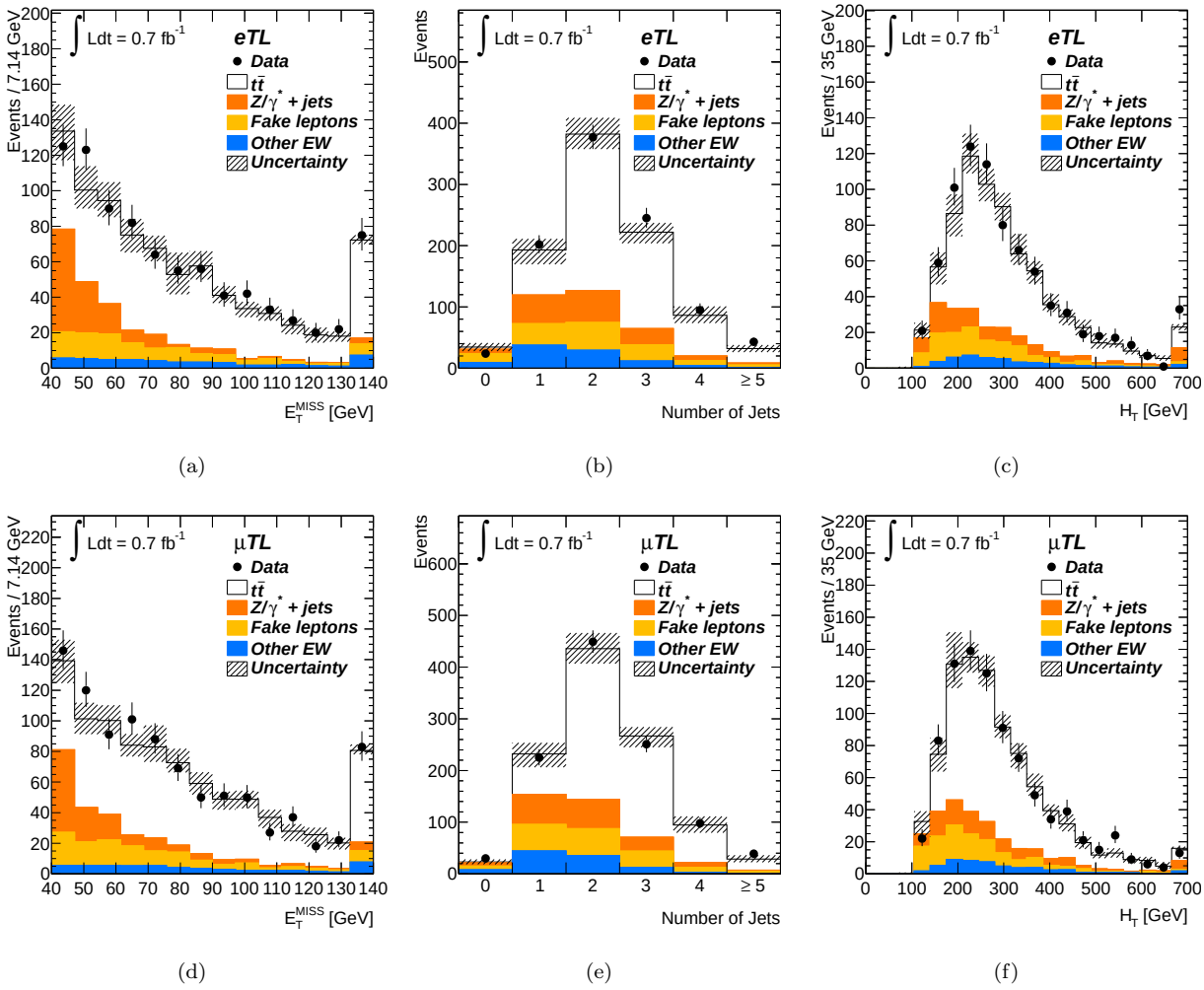

Figure 7.12: Signal region plots for inclusive eTL (top row) and inclusive μTL (bottom row): (a),(c) $E_{\mathrm{T}}^{\mathrm{miss}}$ in events with a lepton-TL mass outside the Z mass window with $\geq$ 2 jets and H_T >150 GeV, (b),(d) the number of jets in events with a lepton-TL mass outside the Z mass window and $E_{\mathrm{T}}^{\mathrm{miss}} > 45$ GeV and H_T >150 GeV, (c),(f), H_{T} in events with a lepton-TL mass outside the Z mass window, $\geq$2 jets and $E_{\mathrm{T}}^{\mathrm{miss}}$ 45 GeV. The error bands reflect the statistical and systematic uncertainties of the MC prediction.

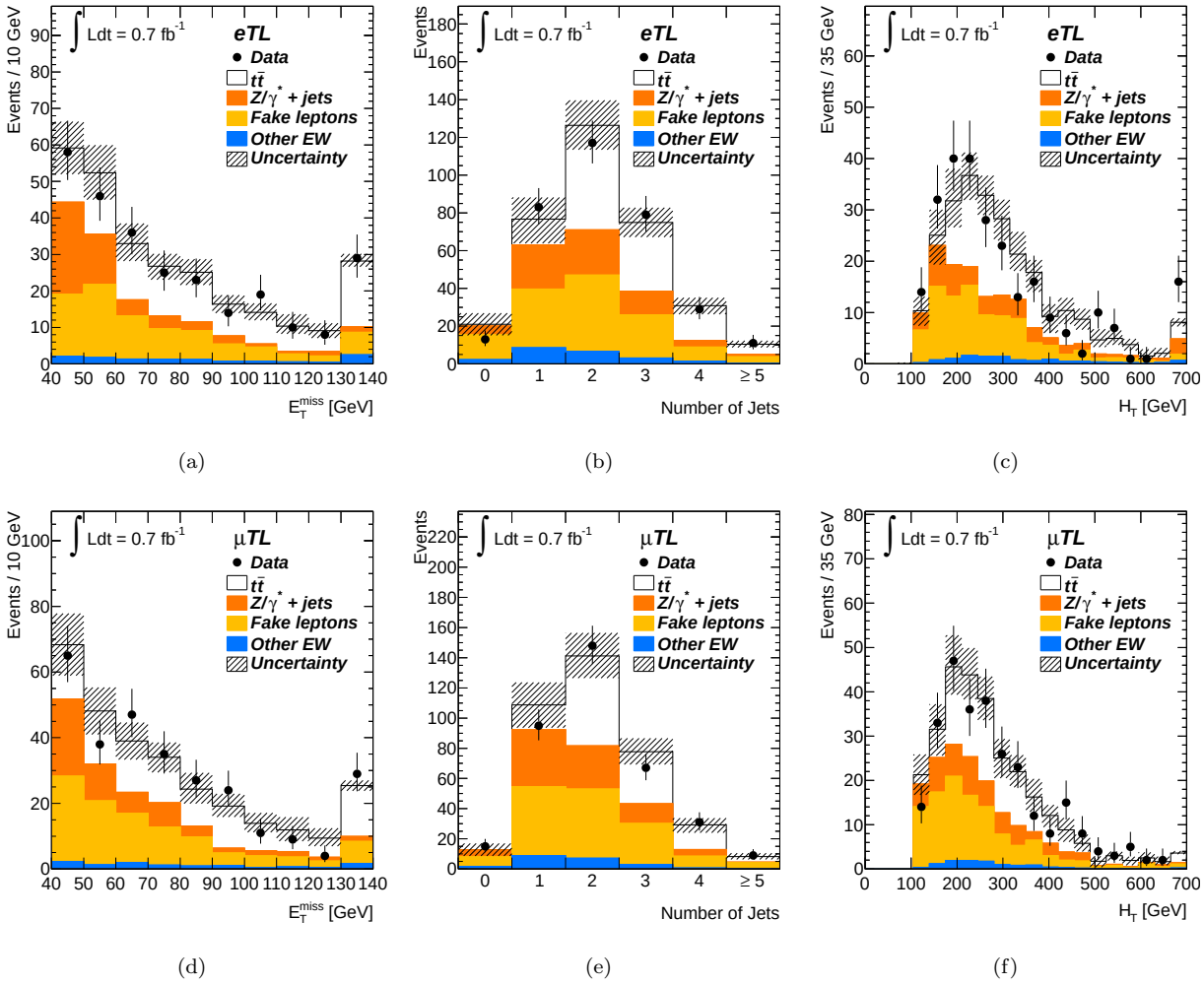

Figure 7.13: Signal region plots for exclusive eTL (top row) and exclusive μTL (bottom row): (a),(c) $E_{\mathrm{T}}^{\mathrm{miss}}$ in events with a lepton-TL mass outside the Z mass window with $\geq$ 2 jets and H_T >150 GeV, (b),(d) the number of jets in events with a lepton-TL mass outside the Z mass window and $E_{\mathrm{T}}^{\mathrm{miss}} > 45$ GeV and H_T >150 GeV, (c),(f), H_{T} in events with a lepton-TL mass outside the Z mass window, $\geq$2 jets and $E_{\mathrm{T}}^{\mathrm{miss}}$ 45 GeV. The error bands reflect the statistical and systematic uncertainties of the MC prediction.

	e+track		μ+track	
Process	0 jets	1 jet	0 jets	1 jet
DY/Z+jets (DD)	$208.9^{+81.6}_{-80.8}$	$55.6^{+22.8}_{-29.8}$	$90.1^{+24.6}_{-24.9}$	$53.9^{+14.2}_{-12.8}$
DY/Z($\rightarrow \tau\tau$)+jets (MC)	$14.1^{+3.8}_{-6.9}$	$18.9^{+6.9}_{-5.1}$	$17.3^{+12.9}_{-8.0}$	$35.5^{+11.1}_{-10.6}$
Fake leptons (DD)	$199.1^{+40.9}_{-40.9}$	$99.0^{+20.2}_{-20.2}$	$322.0^{+80.6}_{-80.6}$	$142.7^{+29.2}_{-29.2}$
Single top (MC)	1.5 ± 0.4	7.0 ± 1.0	$1.3^{+0.3}_{-0.3}$	$6.9^{+0.9}_{-0.9}$
Dibosons (MC)	$10.3^{+0.9}_{-0.9}$	$6.6^{+0.7}_{-0.8}$	$11.7^{+1.0}_{-1.0}$	$6.9^{+0.7}_{-0.7}$
Total background	$433.7^{+91.4}_{-90.8}$	$187.1^{+31.3}_{-36.4}$	$442.3^{+85.3}_{-84.7}$	$245.9^{+34.3}_{-33.6}$
$t\bar{t}$ ($\sigma_{\text{Theory}} = 164.6$ pb^{-1})	$2.2^{+1.6}_{-1.7}$	$19.6^{+6.9}_{-7.9}$	$1.9^{+1.7}_{-1.8}$	$25.3^{+5.0}_{-5.6}$
Total expected events	$436.0^{+91.4}_{-90.9}$	$206.6^{+32.0}_{-37.3}$	$444.2^{+85.3}_{-84.7}$	$271.1^{+34.7}_{-34.1}$
Observed events	411	201	471	262

Table 7.6: Summary of background contributions to the exclusive l+track analysis in the 0 and 1 jet control regions. No H_T cut is applied.

	Inclusive		Exclusive	
	eTL	μTL	eTL	μTL
DY/Z+jets (DD)	$59.9^{+15.0}_{-15.0}$	$56.6^{+8.4}_{-8.6}$	$24.3^{+10.7}_{-9.4}$	$22.0^{+5.3}_{-5.8}$
DY/Z($\rightarrow \tau\tau$)+jets (MC)	$29.8^{+13.4}_{-13.6}$	$47.5^{+20.24}_{-21.0}$	$17.0^{+8.4}_{-7.6}$	$24.7^{+11.4}_{-11.5}$
Fake leptons (DD)	84.2 ± 17.0	96.6 ± 19.5	74.0 ± 14.9	84.6 ± 17.1
Single top (MC)	$24.5^{+3.9}_{-3.9}$	$30.3\ ^{+3.9}_{-4.9}$	$5.7^{+1.0}_{-0.9}$	$6.3\ ^{+0.8}_{-1.1}$
Dibosons (MC)	$22.1^{+3.1}_{-3.2}$	$22.0\ ^{+3.2}_{-2.9}$	$5.9^{+0.9}_{-0.8}$	$4.8\ ^{+0.6}_{-0.7}$
Total background	$220.4^{+26.7}_{-26.9}$	$253.0^{+29.8}_{-30.4}$	$126.4^{+20.2}_{-19.2}$	$142.3^{+21.2}_{-21.4}$
$t\bar{t}$ ($\sigma_{\text{Theory}} = 164.6$ pb^{-1})	$485.5^{+51.7}_{-55.2}$	$562.0^{+61.5}_{-61.0}$	$111.7^{+16.1}_{-18.0}$	$110.2^{+16.7}_{-15.8}$
Total expected events	$705.9^{+58.2}_{-61.4}$	$815.0^{+68.4}_{-68.2}$	$238.6^{+25.8}_{-26.3}$	$252.5^{+27.0}_{-26.6}$
Observed events	760	837	236	255

Table 7.7: The full breakdown of the expected $t\bar{t}$-signal and background in the signal region compared to the observed event yields, for each of the dilepton channels (MC is simulation based, DD is data-driven). All systematic uncertainties are included and the correlations between the different background sources are taken into account.

Chapter 8

Estimation of Systematic Uncertainties

8.1 Introduction

The most significant sources of systematic uncertainty related to analysis object selection were discussed in detail in Sections 6.3.3, 6.4, 6.5.1. Below, I present a description of the systematic uncertainties associated with Monte-Carlo modeling, Z/γ^* background, and the fake TL predictions.

It was reported in [91] that Monte Carlo simulation-based predictions for W/Z+jet events with high jet multiplicities have uncertainties of $O(50\%)$. The use of data-driven methods for the W/Z+jet background predictions enabled a significant reduction of associated uncertainties. The $Z \to \tau\tau$ background expectation is fully MC-based. For the case of $Z \to ll$ ($l = e$ or μ), we take the shapes from MC simulation, and use the data/MC correction factor estimated in the control region to normalize the MC prediction to the data. Then, the product of the correction factor and the MC-based residual DY/Z prediction is much less prone to MC normalization uncertainty. The uncertainty due to the normalization in the Monte Carlo simulation is taken from the Berends-scaling uncertainty [92] and is a function of parton multiplicity. For Z+0 jet the MC normalization has an uncertainty of 4%, for Z+1 jet 20%, Z+2 jets 30%, Z+3 jets 40% and 60% for Z+4,5 jets. For the fake TL background, both the prediction and associated uncertainty are fully data-driven.

For the case of the single top and diboson background contributions, no dependence of the Monte Carlo simulation on jet multiplicity was considered. The overall normalization uncertainty was taken to be 10% [93, 94] and 5% [95] for single top and dibosons, respectively.

In order to evaluate the effect of the $t\bar{t}$ matrix element generation uncertainty on the signal acceptance, we compare the baseline $t\bar{t}$ sample (MC@NLO interfaced with HERWIG) with $t\bar{t}$ simulation using POWHEG [96] interfaced with HERWIG. Similarly, in order to account for the uncertainty due to parton shower simulation we used the $t\bar{t}$ MC generated with POWHEG and interfaced to HERWIG and PYTHIA. The effects of variations in the amount of initial- and final-state radiation (ISR/FSR) were studied using the AcerMC generator [97] interfaced to PYTHIA, varying the parameters controlling ISR and FSR in a range consistent with experimental data [98]. Due to the insufficient ISR/FSR sample sizes, it was not feasible

to determine whether the associated uncertainties on the signal acceptance were asymmetric. Therefore, these systematic uncertainties were assumed to be symmetric and were calculated as $\frac{(u-d)}{2n}$, where $u(d)$ is the number of events accepted from the samples with increased (reduced) ISR or FSR and n is the number of events accepted from the nominal AcerMC sample. The effect of modeling uncertainties associated with the parton density functions (PDF) used for signal $t\bar{t}$ event generation was evaluated using the envelope of error bands from CTEQ66, MSTW08 [99] and NNPDF 2.0 [100] MC sets, determined using the procedure described in previous ATLAS studies [98].

8.1.1 Pile-up correction

The mean number of interactions per proton bunch crossing for the 2011 ATLAS $\int Ldt = 698$ pb^{-1} data sample is $\langle\mu\rangle \sim 6$ (see Section 4.2 for details on $\langle\mu\rangle$). In order to properly model the observed multiple interactions in the Monte Carlo samples, additional minimum bias events were simulated along with the hard-scattering process. The number of additional minimum bias interactions per $t\bar{t}$ simulated event obeys a Poisson distribution, where the mean number of interactions $\langle\mu\rangle$ in the Monte Carlo varies from 0 to 18, in order to describe the various conditions of LHC instantaneous luminosity. The mean number of interactions per bunch crossing can be obtained by inverting expression 4.3 to get $\langle\mu\rangle = \frac{L \cdot \sigma_{vis}}{n_b \cdot f_r}$. The $\langle\mu\rangle$ distribution for data and MC is shown in Figure 8.1. The Monte Carlo samples are weighted such that the $\langle\mu\rangle$ distribution for the MC matches the distribution observed in the data.

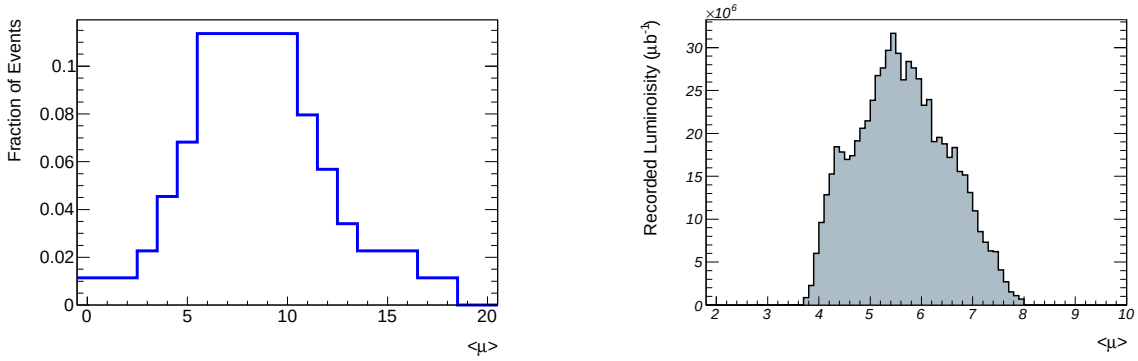

Figure 8.1: $< \mu >$ distributions in the MC (MC10b, left figures) and in the data (from run 178044 to 183347, right figure). The MC is weighted to match this $\langle\mu\rangle$ distribution between data and MC. The mean number of interactions assumed when the MC was generated is larger than the number seen in the collision data.

8.1.2 Z p_{T} uncertainties

In the dilepton final state of $t\bar{t}$ decays, the DY/Z dilepton process represents a major background where the Z boson can be boosted in the transverse plane if high p_{T} jets are produced in association with the Z. In order to account for possible differences of the Z p_{T} modeling in the MC versus real data and estimate the effect of that mis-modeling on the $t\bar{t}$ cross section measurement, we reweight the $Z \to ee$, $Z \to \mu\mu$, and $Z \to \tau\tau$ MC events with a predefined Z p_{T} dependent set of weights in order to match the dilepton system p_{T} distribution observed in the data control region, defined with $|m_{ll} - m_Z| < 10$ GeV and $E_{\mathrm{T}}^{\mathrm{miss}} > 45$ GeV. The predicted MC Z background is then recalculated and the difference is assigned as an uncertainty on the $Z \to ee$, $Z \to \mu\mu$, and $Z \to \tau\tau$ backgrounds. This reweighting factor is evaluated using normalized distributions so that the reweighting does not change the normalization, only the shape of the Z p_{T} distribution.

8.2 Systematic Uncertainties Associated with the DY/Z Backgrounds

The uncertainties on the DY/Z dilepton background evaluation are presented in Tables 8.1 and 8.2 for the inclusive and exclusive lepton+track analyses, respectively. The systematic uncertainty associated with the data-driven technique for the DY/Z dilepton background prediction of the method is evaluated by varying the $E_{\mathrm{T}}^{\mathrm{miss}}$ cut in the control region by ± 5 GeV. This corresponds to the quadratic sum of the uncertainty $\Delta(E_{\mathrm{T}}^{\mathrm{miss}}) \sim 3.5$ GeV at an average $\sum E_{\mathrm{T}} \sim 15$ GeV found for the events in the control region, and the uncertainty on the lepton energy scale [101].

The other uncertainties include:

- Statistical uncertainty of data and MC (Data stat., MC stat.)
- The jet energy scale, resolution and efficiency (JES, JER, JEF),
- The $E_{\mathrm{T}}^{\mathrm{miss}}$ soft-jet term measurement (MET(SoftJet)),
- The $E_{\mathrm{T}}^{\mathrm{miss}}$ from pileup uncertainties (MET(PileUp)),
- The lepton identification and trigger scale factors (ID SF, Trig. SF),
- The lepton energy scale and resolution (ES, ER),
- The theoretical cross section for MC backgrounds (MC x-sec).

As one would expect, use of the data-driven method decreases the reliance on the MC simulation, subsequently yielding a reduction in the total uncertainty on the DY/Z dilepton background prediction. The uncertainties other than the statistical uncertainties for the data-driven method largely cancel in the ratio between the MC signal and control region in Equation 7.5.

Uncertainty(%)	eTL (DD)	eTL (MC)	μTL (DD)	μTL (MC)
Yield(events)	59.6	82.1	56.6	52.2
Lumi	±4.5	±3.7	±1.7	±3.7
Stat(Data)				
JES	-10.6/+8.7	+71.9/-33.3	-0.6/+3.2	+51.7/-19.4
JER	±1.7	±31.1	±4.3	±30.0
JEF	±0.1	±0.0	±0.1	±0.0
MET(Softjet)	-1.5/+6.8	+1.8/+6.5	-1.1/-1.6	-0.3/+1.5
MET(PileUp)	-0.3/+4.9	+1.5/+5.9	+1.6/-3.3	-0.2/0.0
LAr(JetCleaning)	+1.2/+1.1	+2.6/-1.5	-0.5/-0.3	+0.5/-1.6
SF(El.ID)	±1.8	±4.3	-	-
SF(El.Trig)	±0.2	±0.7	-	-
SF(Mu.ID)	-	-	±0.2	±0.5
SF(Mu.Trig)	-	-	-0.1/+0.2	±0.3
SF(Trk ID)	±0.8	±0.7	±0.3	±0.7
x-sec(Theory)	-9.9/+9.2	±35.1	-3.4/+2.5	±34.5
Stat(MC)	±11.0	±4.5	±8.0	±5.4
Z pT	±5.5	±4.3	±2.3	±5.4
El.ES	-3.3/+1.9	-1.8/+1.0	-	-
El.ER	+2.9/+1.5	+1.9/-0.7	-	-
Trk ES	±1.5	±0.9	±0.8	± 0.8
Trk ER	±0.1	±3.1	±5.4	±5.7
Mu.ES	-	-	-0.9/-0.3	-0.7/-0.5
Mu.ER	-	-	±1.0	±1.4
Method	±14.6	-	±8.9	-
total($syst$+$lumi$+$stat$)	+25.0/-25.1	+71.0/-48.4	+14.8/-15.3	+69.8/-50.8

Table 8.1: Uncertainties (in %) on the predicted number of DY/Z events in the signal region for inclusive lepton+track events. The uncertainties are compared between the data driven (DD) determination and the determination from Monte Carlo simulations (MC). The uncertainty due to the method was evaluated from the variation of the prediction when the $E_{\mathrm{T}}^{\mathrm{miss}}$ cut in the control region was varied by ±5 GeV. The larger difference was applied as a symmetric uncertainty on the background yield. The uncertainties on the prediction are presented as $+1\sigma/-1\sigma$ variation of the systematic source.

8.3 Systematic uncertainty associated with Fake Track-Lepton backgrounds

In order to evaluate the systematic uncertainty associated with the fake TL background prediction, we compared the predicted and observed fakes in W+jets events selected from data samples in a control region, orthogonal to the signal region by construction. The control region comprised events that included W+0,1

Uncertainty(%)	eTL (DD)	eTL (MC)	μTL (DD)	μTL (MC)
Yield(events)	24.3	40.7	22.0	19.4
Lumi	±4.7	±3.7	±1.3	±3.7
Stat(Data)				
JES	-19.3/+0.1	+42.0/-26.7	+2.4/-1.3	+25.7/-19.7
JER	±3.4	±18.5	±12.1	±15.4
JEF	±0.0	±0.0	±0.0	±0.0
MET(Softjet)	-2.8/+2.7	+1.3/+4.0	+1.2/-7.1	+2.1/-7.8
MET(PileUp)	-2.6/+2.3	-0.7/+3.2	+4.0/-9.5	+2.7/-7.8
LAr(JetCleaning)	-1.7/+0.7	+2.2/-1.8	-0.6/-0.1	+0.0/-1.3
SF(El.ID)	±1.3	±3.9	-	-
SF(El.Trig)	±0.1	±1.5	-	-
SF(Mu.ID)	-	-	±0.1	±0.5
SF(Mu.Trig)	-	-	-0.4/+0.5	±0.8
SF(Trk ID)	±0.6	±0.7	±0.2	±0.7
x-sec(Theory)	-15.4/+14.1	±35.2	-6.4/+7.0	±31.7
Stat(MC)	±18.6	±6.9	±13.7	±9.6
Z pT	±6.8	±3.3	±1.1	±6.1
El.ES	-2.8/+3.6	-1.4/+0.6	-	-
El.ER	+5.2/-1.0	+2.7/-0.9	-	-
Trk ES	±2.0	±1.0	±1.7	± 1.4
Trk ER	±6.9	±2.5	±0.2	±0.8
Mu.ES	-	-	-1.6/+0.1	-1.4/+0.0
Mu.ER	-	-	±0.9	±1.1
Method	±27.9	-	±13.1	-
total($syst$+$lumi$+$stat$)	+43.8/-38.5	+58.8/-49.2	+24.0/-26.9	+45.4/-43.7

Table 8.2: Uncertainties (in %) on the predicted number of DY/Z events in the signal region for exclusive lepton+track events. The uncertainties are compared between the data driven (DD) determination and the determination from Monte Carlo simulations (MC). The uncertainty due to the method was evaluated from the variation of the prediction when the $E_{\mathrm{T}}^{\mathrm{miss}}$ cut in the control region was varied by ±5 GeV. The larger difference was applied as a symmetric uncertainty on the background yield. The uncertainties of the prediction are presented as $+1\sigma/-1\sigma$ variation of the systematic source.

jet OS fakes and W+≥2 jets SS fakes with $H_T > 150$ GeV. The number of predicted fakes (P) was estimated using the same procedure as for the fake prediction in signal region. The observed fakes in W+jets sample (O) was evaluated by counting the number of selected l+track pairs in control region. Note that the observed fakes in W+jets events, in particular the OS events, contain l+track pairs associated with DY/Z and diboson backgrounds. Therefore, these backgrounds must be included when comparing observed (O) and predicted (P) fakes. This was achieved by adding the number of DY/Z and diboson background events to the prediction (P) to get the total number of background events (B) in the control region. MC simulation was used to estimate the DY/Z and diboson background contribution in W+≥2 jet bins, while the data-driven technique described in Section 7.4.1 was used to estimate the number of DY/Z events in W+0,1 jet bins. The systematic uncertainty was determined by comparing observed and predicted events.

A few remarks are in order. As a result of including DY/Z and diboson backgrounds in (B), the fractional

difference between predicted and observed TLs absorbs fluctuations and systematic uncertainties due to these MC predictions. As discussed in Section 7.4.2, the final fake TL background prediction in the signal region was obtained after correction by the fraction of fake leptons that had opposite charge to the ID lepton. This fraction was measured using Monte Carlo simulation and the accuracy of this fraction was included in the overall systematic uncertainty. This was achieved via the above mentioned explicit OS or SS charge charge requirement for l+track pairs in control region. The uncertainty on the estimation of the l+track pairs that were outside the Z-mass window was propagated into the statistical uncertainty of the fake background prediction. Table 8.3 shows the comparison. The overall agreement is impressive. We conservatively use a 20% systematic uncertainty on the prediction of fake TLs in the signal region, which is roughly one standard deviation above the measured deviation between the predicted and observed fakes. Finally, the statistical uncertainty was added in quadrature to the estimated 20% systematic uncertainty in order to obtain the total uncertainty on the fake background prediction.

	e**TL**				μ**TL**			
#jets	O	B	P	(B-O)/P [%]	O	B	P	(B-O)/P [%]
0 (OS)	411	$436.3^{+38.4}_{-36.8}$	199.1 ± 9.3		460	$441.1^{+52.9}_{-52.0}$	321.9 ± 48.4	
1 (OS)	201	$207.1^{+16.9}_{-27.3}$	99.0 ± 4.2		247	$270.5^{+17.2}_{-16.5}$	142.5 ± 6.0	
2 (SS)	10	10.7 ± 0.8	7.6 ± 0.7		14	13.9 ± 1.0	11.1 ± 0.9	
3 (SS)	7	6.2 ± 0.5	5.4 ± 0.5		9	8.3 ± 0.7	7.0 ± 0.6	
4 (SS)	4	4.1 ± 0.4	3.8 ± 0.4		1	3.2 ± 0.4	3.1 ± 0.4	
≥ 5 (SS)	2	1.9 ± 0.1	1.8 ± 0.1		0	1.5 ± 0.2	1.4 ± 0.2	
Total	635	$666.4^{+41.9}_{-45.8}$	316.6 ± 10.3	$9.9^{+15.6}_{-16.5}$	731	$738.5^{+55.6}_{-54.6}$	487.0 ± 48.8	$1.5^{+12.7}_{-12.5}$

Table 8.3: Comparison of predicted and observed fake exclusive TLs in W+jets events. The columns labeled 'O' are the observed TLs, 'B' is the total background including the non-fake backgrounds, such as DY/Z, and 'P' is the predicted fake contribution to 'B'.

Samples of Z+jets events, reconstructed as identified ee or $\mu\mu$ (no TLs) were also used as a cross check of the predictive power of the TL fake matrix. For this validation test, we adhered to the same procedure as that for the fake prediction in the signal region. The fake matrix is applied to Z+N jet events to predict the number of Z+(N-1) jets events with a TL in addition to the ee or $\mu\mu$ from the Z decay. Table 8.4 shows the predicted and observed TLs in $Z \to ee$ and $Z \to \mu\mu$ events as function of number of jets. The agreement between the two is impressive, considerably better than our quoted 20% systematic uncertainty.

	$Z \to ee$+fake		
# jets	Obs.	Pred.	(P-O)/P [%]
0	46	42.8±1.6	
1	20	17.2±0.6	
2	3	5.5 ±0.2	
3	2	1.61 ±0.06	
4	1	0.53 ±0.02	
≥ 5	1	0.17 ±0.00	
All	73	67.8 ±1.7	-7.8 ± 0.9
	$Z \to \mu\mu$+fake		
# jets	Obs.	Pred.	(P-O)/P [%]
0	86	87.0±3.2	
1	41	35.2±1.3	
2	10	11.6±0.4	
3	5	3.0±0.1	
4	2	0.79±0.03	
≥ 5	1	0.26±0.01	
All	151	137.8±3.4	-9.6 ± 0.8

Table 8.4: Observed and predicted fakes in $Z \to ee$ and $Z \to \mu\mu$ events.

8.4 Evaluation of the Systematic and Statistical Uncertainties for the $t\bar{t}$ Cross-Section Measurement

Below, I summarize the main sources of the systematic uncertainties on the $t\bar{t}$ cross section measurement and present detailed results for the systematic and statistical uncertainty estimates for acceptance, background predictions and subsequently on the $t\bar{t}$ cross section measurement per analysis channel.

- Statistical uncertainty in data from data-driven estimations (Stat(Data))
- Statistical uncertainty in MC (Stat(MC)) for MC based backgrounds
- Uncertainty from the fake estimations (Fake)
- Uncertainty from the data-driven DY/Z dilepton background estimation (DY Method)
- Uncertainty from the theoretical MC cross sections (MC xsect.)
- Jet energy scale (JES), resolution (JER) and efficiency (JEF) uncertainties which are also propagated into $E_{\mathrm{T}}^{\mathrm{miss}}$ by rescaling the fractional contribution of the jet to the total $E_{\mathrm{T}}^{\mathrm{miss}}$
- Lepton identification (SF(Mu./El.ID)) and trigger scale factor uncertainties SF(Mu./El.Trig)
- Track-lepton identification scale factor uncertainties (TrID SF)
- Lepton energy scale and resolution (ES, ER, in the muon case the maximum deviation of the resolution uncertainties from in the muon spectrometer (MS) and the inner detector (ID) track are considered) also propagated into $E_{\mathrm{T}}^{\mathrm{miss}}$
- Track-lepton p_{T} scale and resolution (TrES, TrER)
- Uncertainty due to pile-up (Pile-up)
- Uncertainty using different parton shower programs (P.Shower: HERWIG and PYTHIA) for the signal MC
- Uncertainty using different generators for the signal MC (Generator: MC@NLO and POWHEG)
- Uncertainties due to ISR/FSR (varied individually)

The uncertainty on the $t\bar{t}$ cross section measurement due to a given parameter is evaluated by shifting the parameter up and down by one standard deviation and redoing the full analysis chain. Some of the

uncertainty sources were expected and observed to have different effects on different analysis channels. For example, the jet-related uncertainties were propagated to the jet term of $E_{\mathrm{T}}^{\mathrm{miss}}$ and because of longer tails in the $E_{\mathrm{T}}^{\mathrm{miss}}$ distribution (due to misidentified or missing muons not accounted in $E_{\mathrm{T}}^{\mathrm{miss}}$balance properly) they manifest differently in the muon+track channel. Also, electrons and muons are not on equal footing within the analysis due to different order of overlap removal against jets. Hence, the different channels are affected differently by scaling the leptons and jets. Limited statistics for some of the background processes may also cause large fluctuations, especially between 'up' and 'down' variations of certain systematics.

The results are summarized for the total $t\bar{t}$ acceptance in Table 8.5, Table 8.7 for the inclusive l+track analysis and Table 8.9, Table 8.11 for the exclusive case. The systematic uncertainties for the backgrounds evaluated with Monte Carlo simulations are shown in Table 8.6 and Table 8.8 for inclusive mode, and Table 8.9 and Table 8.12 for the exclusive l+track analysis. The largest uncertainty is the jet energy scale uncertainty in almost all channels. Channels with electrons have a large contribution from electron identification efficiency scale factors. A significant contribution in the overall uncertainty comes from the fake background estimate. The Monte Carlo modeling of the parton shower, the ISR/FSR and the limited statistics of the background MC also contribute to the total uncertainty.

	Δ Acceptance (%)	Δ Cross Section %
Luminosity		±3.7
Data Stat		±5.1
MC Stat	± 1.5	$^{+2.9}_{-2.8}$
Pile-up	$^{-0.1}_{-0.3}$	$^{+0.9}_{-0.2}$
LAr Hole	$^{+0.5}_{-0.9}$	$^{+1.0}_{-0.6}$
Fake	-	± 3.1
DY Method	-	±1.6
Z pT	-	±0.9
MC xsect.	-	$^{+2.3}_{-2.4}$
JES	$^{+5.6}_{-6.8}$	$^{+9.1}_{-7.0}$
JER	± 0.1	±0.4
JEF	± 0.0	±0.04
Mu ID SF	-	-
Mu Trig SF	-	-
Ele ID SF	±3.3	$^{+3.7}_{-3.5}$
Ele Trig SF	±2.2	±0.2
TrID SF	±0.7	±0.9
Mu ES	-	-
Mu ER (MS)	-	-
Mu ER (ID)	-	-
El ES	$^{+0.4}_{-0.4}$	$^{+0.7}_{-0.7}$
El ER	$^{-0.2}_{+0.8}$	$^{+1.0}_{-0.5}$
TrES	± 0.0	±0.2
TrER	± 0.3	±0.5
P.Shower	± 0.7	±0.7
Generator	± 0.3	±0.3
ISR	±3.2	±1.1
FSR	±1.1	±0.1
PDF	± 2.5	$^{+2.6}_{-2.4}$
Syst total	$^{+8.0}_{-8.9}$	$^{+12.2}_{-10.3}$

Table 8.5: Uncertainties on the acceptance and $t\bar{t}$ cross section in the inclusive eTL channel. The uncertainties are presented as $+1\sigma/-1\sigma$ variation of the systematic source.

	Single top	Diboson	$DY/Z \to \tau\tau$
Yield (events)	24.5	22.1	29.8
Uncertainty(%)			
Lumi	$\pm$ 3.7	$\pm$ 3.7	$\pm$ 3.7
JES	$^{+10.1}_{-10.6}$	$^{+12.0}_{-12.5}$	$^{+19.9}_{-20.6}$
JER	$\pm$ 1.4	$\pm$ 0.4	$\pm$ 4.1
JEF	$\pm$ 0.1	$\pm$ 0.1	$\pm$ 0.0
El. ID SF	$\pm$2.9	$\pm$3.2	$\pm$3.8
El. Trig SF	$\pm$0.1	$\pm$0.1	$\pm$0.3
Mu. ID SF	-	-	-
Mu. Trig SF	-	-	-
TrID SF	$\pm$0.7	$\pm$0.7	$\pm$0.7
Z pT	-	-	$\pm$ 12.5
MC xsect.	$\pm$10.0	$\pm$5.0	$\pm$36.6
MC Stat.	$\pm$ 3.3	$\pm$ 2.4	$\pm$ 7.4
Pile-up	$^{-1.4}_{+0.9}$	$^{+0.1}_{-0.3}$	$^{+0.9}_{-4.1}$
LAr Hole	$^{+0.2}_{-1.4}$	$^{+0.9}_{-0.7}$	$^{+0.0}_{-0.0}$
El ES	$^{+0.4}_{-0.3}$	$^{+0.6}_{+0.1}$	$^{+1.4}_{-0.0}$
El ER	$^{-0.4}_{+0.2}$	$^{+0.3}_{+0.8}$	$^{-0.9}_{+1.8}$
TrES	$\pm$ 0.0	$\pm$ 0.1	$\pm$ 0.0
TrER	$\pm$ 2.4	$\pm$ 0.3	$\pm$ 3.8
Mu ES	-	-	-
Mu ER (MS)	-	-	-
Mu ER (ID)	-	-	-
total (syst+ lumi)	$^{+15.7}_{+16.1}$	$^{+15.4}_{-14.0}$	$^{+44.9}_{+45.7}$

Table 8.6: Uncertainties on the MC background contributions in the inclusive eTL channel. The uncertainties are presented as $+1\sigma/-1\sigma$ variation of the systematic source.

	Δ Acceptance (%)	Δ Cross Section %
Luminosity		±3.7
Data Stat		5.0
MC Stat	± 1.5	$^{+2.37}_{-2.30}$
Pile-up	$^{-0.1}_{+0.3}$	$^{+0.50}_{-0.85}$
LAr Hole	$^{-0.14}_{-0.27}$	$^{+1.15}_{-0.65}$
Fake	-	± 3.33
DY Method	-	±0.86
Z pT	-	±0.79
MC xsect.	-	$^{+3.12}_{-3.12}$
JES	$^{+5.63}_{-6.79}$	$^{+7.08}_{-6.23}$
JER	± 0.05	$^{+2.25}_{-2.18}$
JEF	± 0.03	±0.02
Mu ID SF	$^{+0.52}_{-0.52}$	$^{+0.58}_{-0.57}$
Mu Trig SF	$^{+0.24}_{-0.25}$	$^{+0.28}_{-0.28}$
Ele ID SF	±3.25	-
Ele Trig SF	±0.22	-
TrID SF	±0.73	±0.8
Mu ES	$^{+0.03}_{-0.11}$	$^{+0.1}_{-0.1}$
Mu ER	± 0.05	$^{+0.16}_{-0.16}$
El ES	$^{+0.37}_{-0.44}$	$^{+0.00}_{-0.11}$
El ER	$^{-0.15}_{+0.77}$	$^{+0.08}_{-0.13}$
TrES	± 0.03	±0.2
TrER	± 0.26	$^{+1.06}_{-1.05}$
P.Shower	± 0.69	$^{+2.52}_{-2.40}$
Generator	± 0.31	$^{+0.06}_{-0.06}$
ISR	±3.16	$^{+2.46}_{-2.35}$
FSR	±1.1	$^{+4.60}_{-4.21}$
PDF	± 2.5	$^{+2.35}_{-2.25}$
Syst total	$^{+7.98}_{+8.91}$	$^{+11.23}_{-10.46}$

Table 8.7: Uncertainties on the acceptance and $t\bar{t}$ cross section in the inclusive μTL channel. The uncertainties are presented as $+1\sigma/-1\sigma$ variation of the systematic source.

	Single top	Diboson	$DY/Z \to \tau\tau$
Yield (events)	30.3	22.0	47.5
Uncertainty(%)			
Lumi	±3.7	±3.7	±3.7
JES	$^{+6.62}_{-9.92}$	$^{+12.80}_{-10.96}$	$^{+15.37}_{-19.56}$
JER	± 1.13	± 0.3	± 4.1
JEF	± 0.00	± 0.1	± 0.0
El. ID SF	-	-	-
El. Trig SF	-	-	-
TrID SF	±0.8	±0.8	±0.7
Z pT	-	-	± 9.2
Mu. ID SF	±0.5	±0.5	±0.5
Mu. Trig SF	±0.2	±0.1	±0.4
MC x-sec	±10.0	±5.0	±37.6
MC Stat.	± 3.0	± 2.4	± 6.2
Pile-up	$^{-0.10}_{-0.82}$	$^{+0.40}_{-0.74}$	$^{-1.92}_{-1.03}$
LAr Hole	$^{+0.19}_{-1.69}$	$^{+0.42}_{-0.79}$	$^{+1.00}_{-0.85}$
El ES	-	-	$^{-0.91}_{+0.00}$
El ER	-	-	$^{+0.00}_{-0.91}$
TrES	-	-	± 0.0
TrER	± 0.7	± 1.3	± 1.1
Mu ES	$^{-0.08}_{-0.20}$	$^{-0.00}_{-0.05}$	0.0
Mu ER	± 0.1	± 0.3	±0.5
total (syst + lumi)	$^{+13.00}_{+15.12}$	$^{+14.53}_{+12.99}$	$^{+42.66}_{+44.24}$

Table 8.8: Uncertainties on the MC background contributions in the inclusive μTL channel. The uncertainties are presented as $+1\sigma/-1\sigma$ variation of the systematic source.

	Δ Acceptance (%)	Δ Cross Section %
Luminosity		±3.7
Data Stat		14.0
MC Stat	± 3.2	$^{+7.9}_{-7.4}$
Pile-up	$^{-0.1}$	$^{+1.2}$
LAr Hole	$^{+0.3}$	$^{-0.7}$
Fake	$^{+0.7}_{-0.8}$	$^{+1.0}_{-1.1}$
DY Method	-	± 13.7
Z pT	-	±6.2
MC xsect.	-	±2.0
JES	$^{+4.9}_{-8.9}$	$^{+6.5}_{-6.6}$
JER	± 0.8	$^{+13.1}_{-10.8}$
JEF	± 0.1	$^{+1.8}_{-1.8}$
Mu ID SF	-	±0.2
Mu Trig SF	-	-
Ele ID SF	±3.2	$^{+3.9}_{-3.6}$
Ele Trig SF	±0.9	±1.0
TrID SF	±0.7	±0.9
Mu ES	-	-
Mu ER (MS)	-	-
Mu ER (ID)	-	-
El ES	$^{+0.4}_{-0.1}$	$^{+0.9}_{-1.0}$
El ER	$^{+0.9}_{+0.4}$	$^{+0.6}_{-2.1}$
TrES	± 0.1	±0.5
TrER	± 2.1	$^{+3.8}_{-3.6}$
P.Shower	± 9.2	$^{+10.1}_{-8.4}$
Generator	± 1.5	±1.5
ISR	±3.3	$^{+3.5}_{-3.2}$
FSR	±0.1	±0.1
PDF	± 2.5	$^{+2.6}_{-2.4}$
Syst total	$^{+12.5}_{-14.5}$	$^{+25.9}_{-24.0}$

Table 8.9: Uncertainties on the acceptance and $t\bar{t}$ cross section in the exclusive eTL channel. The uncertainties are presented as $+1\sigma/-1\sigma$ variation of the systematic source.

	Single top	Diboson	$DY/Z \to \tau\tau$
Yield (events)	5.7	5.7	17. 0
Uncertainty(%)			
Lumi	± 3.7	± 3.7	± 3.7
JES	$^{+9.4}_{-7.0}$	$^{+12.5}_{-10.9}$	$^{+29.8}_{-19.5}$
JER	± 4.1	± 2.6	± 4.1
JEF	± 0.0	± 0.2	± 0.0
El. ID SF	±2.5	±2.6	±2.6
El. Trig SF	±0.5	±0.5	±0.5
Mu. ID SF	-	-	-
Mu. Trig SF	-	-	-
TrID SF	±0.7	±0.7	±0.7
Z pT	-	-	± 8.8
MC xsect.	±10.0	±5.0	±36.2
MC Stat.	± 7.0	± 4.8	± 9.4
Pile-up	$^{+1.5}_{-1.3}$	$^{+0.3}_{-0.1}$	$^{+1.5}_{-4.7}$
LAr Hole	$^{+0.0}_{-1.6}$	$^{+1.9}_{-0.8}$	$^{+0.0}_{-0.0}$
El ES	$^{-0.0}_{+0.0}$	$^{+0.3}_{-0.0}$	$^{-0.00}_{-0.01}$
El ER	$^{+0.8}_{-0.3}$	$^{+0.5}_{+0.4}$	$^{-0.01}_{+0.05}$
TrES	± 0.0	± 0.0	± 0.0
TrER	± 5.3	± 0.9	± 2.2
Mu ES	-	-	-
Mu ER (MS)	-	-	-
Mu ER (ID)	-	-	-
total (syst+ lumi)	$^{+17.5}_{-16.4}$	$^{+15.4}_{-14.0}$	$^{+49.1}_{-44.4}$

Table 8.10: Uncertainties on the MC background contributions in the exclusive eTL channel. The uncertainties are presented as $+1\sigma/-1\sigma$ variation of the systematic source.

	Δ Acceptance (%)	Δ Cross Section (%)
Luminosity	-	±3.7
Data Stat	-	±14.2
MC Stat	± 3.1	$^{+6.7}_{-6.3}$
Pile-up	±0.3	$^{+2.2}_{+1.3}$
LAr Hole	$^{+0.8}_{-0.5}$	$^{+0.6}_{-1.2}$
Fake	-	± 15.1
DY Method	-	±2.6
Z pT	-	±1.8
MC xsect.	-	±8.7
JES	$^{+7.1}_{-4.8}$	$^{+10.1}_{-10.6}$
JER	± 2.8	$^{+5.6}_{-5.3}$
JEF	± 0.0	±0.0
Mu ID SF	±0.5	$^{+0.6}_{-0.6}$
Mu Trig SF	$^{+1.2}_{-1.3}$	$^{+1.5}_{-1.4}$
Ele ID SF	-	-
Ele Trig SF	-	-
TrID SF	±0.8	±0.9
Mu ES	±0.2	$^{+0.3}_{-0.5}$
Mu ER	± 0.1	±0.4
El ES	-	-
El ER	-	-
TrES	± 0.3	±0.6
TrER	± 0.8	±1.3
P.Shower	± 6.9	$^{+7.4}_{-6.5}$
Generator	± 1.4	±1.4
ISR	±6.1	$^{+6.5}_{-5.8}$
FSR	±4.1	$^{+4.3}_{-4.0}$
PDF	± 2.3	$^{+2.4}_{-2.3}$
Syst total	$^{+13.5}_{-12.5}$	$^{+25.1}_{-24.5}$

Table 8.11: Uncertainties on the acceptance and $t\bar{t}$ cross section in the exclusive μTL channel. The uncertainties are presented as $+1\sigma/-1\sigma$ variation of the systematic source.

	Single top	Diboson	$DY/Z \to \tau\tau$
Yield (events)	6.3	4.8	24.7
Uncertainty(%)			
Lumi	± 3.7	± 3.7	± 3.7
JES	$^{+2.9}_{-11.9}$	$^{+9.5}_{-11.1}$	$^{+19.2}_{-21.2}$
JER	$\pm$ 1.9	$\pm$ 1.0	$\pm$ 4.8
JEF	$\pm$ 0.0	$\pm$ 0.0	$\pm$ 0.0
El. ID SF	-	-	-
El. Trig SF	-	-	-
TrID SF	± 0.8	± 0.8	± 0.7
Z pT	-	-	$\pm$ 8.3
Mu. ID SF	± 0.5	± 0.5	± 0.5
Mu. Trig SF	± 1.0	$^{+0.6}_{-0.7}$	$^{+0.8}_{-0.7}$
MC x-sec	± 10.0	± 5.0	± 38.9
MC Stat.	$\pm$ 6.6	$\pm$ 5.1	$\pm$ 8.8
Pile-up	$^{+0.1}_{-0.8}$	$^{+0.9}_{-1.1}$	$^{+3.1}_{-1.9}$
LAr Hole	$^{+0.6}_{-1.3}$	$^{+0.5}_{-0.1}$	$^{+1.8}_{-0.5}$
El ES	-	-	$^{+0.0}_{-1.7}$
El ER	-	-	$^{+0.0}_{-1.7}$
TrES	$\pm$ 0.0	$\pm$ 0.0	$\pm$ 0.0
TrER	$\pm$ 1.8	$\pm$ 2.0	$\pm$ 2.2
Mu ES	± 0.0	$^{-0.02}_{+0.00}$	0.0
Mu ER	$\pm$ 0.7	$\pm$ 0.12	± 0.9
total (syst + lumi)	$^{+13.2}_{-17.9}$	$^{+12.8}_{-14.1}$	$^{+46.0}_{-46.6}$

Table 8.12: Uncertainties on the MC background contributions in the exclusive μTL channel. The uncertainties are presented as $+1\sigma/-1\sigma$ variation of the systematic source.

Chapter 9

Lepton+Track $t\bar{t}$ Cross Section Extraction and Combination of Channels

9.1 Profile Likelihood Technique

The eTL, μTL and combined value of the $t\bar{t}$ production cross sections were computed using a profile likelihood technique. The observed event count for each channel N^{obs} was modeled according to a Poisson distribution with mean given by the value $N_{\text{tot}}^{\text{exp}}$, which is the sum of the signal and background contributions. The variation in the expected number of events attributed to signal and background processes associated with systematic uncertainties was parameterized with a Gaussian distribution and additional terms were included in a likelihood function that summarized the uncertainty in the corresponding nuisance parameters. Scaling the number of expected signal events with the integrated luminosity, the parameter of interest (i.e. σ_{sig}) was kept as a free parameter of the fit.

Systematic uncertainty sources were aggregated into groups of uncorrelated and 100% correlated parameters. Each of the uncertainty sources (index by j) has a nuisance parameter α_j associated to it such that $\alpha_j = 0$ represents the nominal estimate and $\alpha_j = \pm 1$ represents a $\pm 1\sigma$ variation of that source. Next, the sources of the systematics were varied (e.g. jet energy scale, trigger efficiencies, etc.) and a piecewise-linear interpolation was used to parameterize the expected number of events $N_i^{\text{exp}}(\vec{\alpha})$ for each signal and background using the RooFit/RooStats software package [102, 103].

Additional terms were added to the likelihood function, enabling incorporation of additional knowledge of the α_j derived from auxiliary measurements or assumptions about the uncertainty in the Monte Carlo modeling. This led to the following form of the likelihood function [104]:

$$\mathcal{L}(\sigma_{\text{sig}}, L, \alpha_j) = \prod_{i \in \text{ channel}} \text{Pois}\left(N_i^{\text{obs}} \,|\, N_{i,\text{tot}}^{\text{exp}}(\vec{\alpha})\right) \times G(L_0|L, \sigma_L) \times \prod_{j \in \text{syst}} G(0|\alpha_j, 1)\,. \tag{9.1}$$

The $t\bar{t}$ cross section was inferred from the profile likelihood ratio $\lambda(\sigma_{\text{sig}}) = \mathcal{L}(\sigma_{\text{sig}}, \hat{\hat{L}}, \hat{\hat{\alpha}}_j)/\mathcal{L}(\hat{\sigma}_{\text{sig}}, \hat{L}, \hat{\alpha}_j)$, where a single circumflex represents the maximum likelihood estimate (MLE) of the parameter and the double circumflex represents the conditional MLE with σ_{sig} fixed. Ensembles of pseudo-data were generated

for $N_i^{\rm obs}$ and the resulting estimate of $\hat{\sigma}_{\rm sig}$ was confirmed to be unbiased.

9.2 Results

Table 9.1 summarizes the $t\bar{t}$ cross sections extracted from the profile likelihood ratio for the individual channels and for the combination of the inclusive l+track analysis. Note that the measurements of the $t\bar{t}$ cross section per analysis channel are consistent with each other, in agreement with the lepton universality principle. For the exclusive l+track analysis, the $t\bar{t}$ cross sections measured per analysis channel and for the combined eTL and μTL $t\bar{t}$ cross section measurement are summarized in Table 9.2. Similar to the inclusive case, the $t\bar{t}$ cross section measurements per exclusive l+track channel are also consistent with each other, in accordance with the lepton universality principle. Tables 9.3, 9.4 provide the systematic uncertainties for each systematic contribution for the inclusive and exclusive analysis modes, respectively. The eTL and μTL combined results agree well with the weighted average of the individual $t\bar{t}$ cross sections. The combination results in improved uncertainties. This $t\bar{t}$ cross section measurement is systematic uncertainty dominated.

The results of the exclusive e, μ+track analysis channels were also combined with those of 3 channels of the 2ID $t\bar{t}$ analysis to obtain the so-called 5-channel combination result: 176$\pm$5 (stat.) $\pm$12(syst.) $\pm$8 (lum.) pb^{-1}. In addition, exclusive ee and $\mu\mu$ events with at least 1 b-tagged jet were combined with the above 5 channels to form the so-called 7-channel combination: 176 ± 5 (stat.) $^{+14}_{-10}$ (syst.) $^{+9}_{-8}$ (lum.) pb^{-1}. A paper summarizing the analyses and the result of the $t\bar{t}$ cross section measurements using dilepton final states was submitted to and accepted for publication by *The Journal of High Energy Physics* [105].

Channel	$\sigma_{t\bar{t}}$ (pb) (stat., syst., lumi.)
eTL	$182.9 \pm 9.3\ ^{+21.9}_{-16.7}\ ^{+8.2}_{-7.3}$
μTL	$171.0 \pm 8.5\ ^{+20.6}_{-17.5}\ ^{+7.8}_{-7.0}$
Combined	$177.4 \pm 6.3\ ^{+18.4}_{-15.2} \pm 7.6$

Table 9.1: The measured $t\bar{t}$ cross sections in each of the individual inclusive l+track channels, and the combined measurement. The central values and uncertainties are obtained from the likelihood maximization.

Channel	$\sigma_{t\bar{t}}$ (pb) (stat., syst., lumi.)
eTL	$160.8 \pm 22.6\ ^{+45.1}_{-33.1}\ ^{+8.3}_{-6.8}$
μTL	$168.3 \pm 23.9\ ^{+45.8}_{-39.0}\ ^{+9.0}_{-7.5}$
Combined	$164.5 \pm 16.4\ ^{+39.0}_{-30.5}\ ^{+8.6}_{-7.1}$

Table 9.2: The measured $t\bar{t}$ cross sections in each of the individual exclusive l+track channels, and the combined measurement. The central values and uncertainties are obtained from the likelihood maximization.

	eTL	μTL	Combined
Uncertainties (%)			
Data Stat	-5.0 / 5.2	-4.9 / 5.0	-3.5 / 3.6
Lumi	-4.0 / 4.5	-4.1 / 4.6	-4.1 / 4.5
MC Stat	-1.9 / 2.0	-1.6 / 1.8	-1.2 / 1.3
El/Mu ES	-0.0 / 0.3	-0.0 / 0.0	-0.0 / 0.0
El/Mu ER	-0.0 / 0.0	-0.3 / 0.0	-0.0 / 0.3
El/Mu Eff	-3.4 / 3.7	-0.6 / 0.7	-1.4 / 1.5
JES	-6.0 / 8.7	-6.8 / 7.6	-5.9 / 6.7
JER	-0.3 / 0.7	-2.4 / 2.6	-1.5 / 1.6
JEF	-0.0 / 0.0	-0.0 / 0.0	-0.0 / 0.0
DY	-1.6 / 1.6	-0.8 / 0.9	-0.9 / 0.8
ZpT	-0.7 / 1.1	-0.8 / 0.8	-0.6 / 0.5
Fakes	-3.1 / 3.1	-3.4 / 3.3	-2.3 / 2.3
Generator	-0.0 / 0.5	-0.0 / 0.0	-0.0 / 0.0
P.Shower	-0.3 / 0.9	-2.4 / 2.6	-1.6 / 1.7
ISR	-3.0 / 3.3	-2.3 / 2.5	-1.8 / 2.0
FSR	-1.0 / 1.1	-4.1 / 4.7	-2.1 / 2.3
PDF	-2.4 / 2.6	-2.2 / 2.4	-2.3 / 2.5
Met(CellOut & SoftJet)	-0.0 / 0.3	-0.3 / 0.0	-0.0 / 0.3
Met(PileUp)	-0.0 / 0.0	-0.0 / 0.0	-0.0 / 0.0
LAr	-0.5 / 0.9	-0.6 / 1.3	-0.9 / 1.1
Track Eff	-0.4 / 1.0	-0.8 / 0.9	-0.7 / 0.9
Track ES	-0.0 / 0.4	-0.3 / 0.0	-0.0 / 0.3
Track ER	-0.3 / 0.8	-1.2 / 1.2	-0.9 / 0.9
σ_{theory}	-2.3 / 2.4	-3.1 / 3.1	-2.7 / 2.7
Syst	-9.1 / 12.0	-10.2 / 12.1	-8.6 / 10.4
Syst + Lumi	-10.0 / 12.8	-11.0 / 12.9	-9.4 / 11.3
Syst + Lumi + Stat	-11.2 / 13.8	-12.0 / 13.9	-10.0 / 11.9

Table 9.3: Summary of the $t\bar{t}$ cross section uncertainties for each inclusive channel and combined inclusive eTL+μTL obtained from the likelihood maximization.

	eTL	μTL	Combined
Uncertainties (%)			
Data Stat	-13.8 / 14.4	-13.9 / 14.5	-9.8 / 10.1
Lumi	-4.2 / 5.1	-4.4 / 5.4	-4.3 / 5.2
MC Stat	-5.3 / 5.6	-4.4 / 4.8	-3.5 / 3.7
El/Mu ES	-0.9 / 0.5	-0.0 / 0.8	-0.0 / 0.0
El/Mu ER	-0.0 / 0.0	-0.5 / 0.8	-0.8 / 0.5
El/Mu Eff	-3.4 / 4.1	-1.6 / 1.6	-1.9 / 2.4
JES	-5.8 / 14.5	-11.1 / 11.7	-9.3 / 13.1
JER	-2.6 / 2.6	-6.0 / 6.7	-4.1 / 4.5
JEF	-0.0 / 0.5	-0.0 / 0.0	-0.0 / 0.0
DY	-6.3 / 6.1	-2.7 / 2.4	-3.3 / 3.3
ZpT	-2.3 / 1.8	-2.0 / 1.7	-1.3 / 1.4
Fakes	-13.8 / 13.6	-15.2 / 15.0	-10.2 / 10.1
Generator	-1.6 / 1.5	-1.5 / 1.4	-1.3 / 1.6
P.Shower	-7.8 / 10.8	-6.0 / 8.0	-7.1 / 9.2
ISR	-3.0 / 3.7	-5.3 / 7.0	-2.9 / 3.7
FSR	-0.0 / 0.5	-3.7 / 4.7	-1.8 / 2.0
PDF	-2.3 / 2.7	-2.1 / 2.6	-2.1 / 2.7
Met(CellOut & SoftJet)	-0.0 / 0.5	-0.0 / 0.5	-0.0 / 0.9
Met(PileUp)	-0.0 / 0.0	-0.0 / 0.0	-0.0 / 0.0
LAr	-1.1 / 0.9	-1.2 / 0.8	-1.3 / 0.5
Track Eff	-0.5 / 0.5	-1.0 / 0.0	-0.4 / 0.6
Track ES	-0.5 / 0.5	-1.0 / 0.0	-0.4 / 0.6
Track ER	-4.1 / 4.5	-1.6 / 1.4	-2.7 / 3.1
σ_{theory}	-6.6 / 6.5	-8.8 / 8.6	-7.4 / 7.5
Syst	-20.6 / 28.1	-23.2 / 27.2	-18.5 / 23.7
Syst + Lumi	-20.9 / 28.6	-23.5 / 27.8	-19.0 / 24.3
Syst + Lumi + Stat	-25.0 / 32.0	-27.3 / 31.3	-21.4 / 26.3

Table 9.4: Summary of the $t\bar{t}$ cross section uncertainties for each exclusive channel and combined exclusive eTL+μTL obtained from the likelihood maximization.

Chapter 10

Conclusions and Outlook

We have measured the $t\bar{t}$ pair production cross section in $\sqrt{S} = 7$ TeV pp collisions using the dilepton decay final state of the top pair. Within uncertainties, we observe good agreement between the SM prediction and the measured values of the $t\bar{t}$ pair production cross section. No statistically significant evidence for anomalous $t\bar{t}$ pair production or decay was seen, although we emphasize the limited sensitivity of this measurement to physics processes beyond Standard Model top pair production and decay. We performed the measurement by utilizing the l+track approach, where the requirements on one of the lepton legs was relaxed to require only a high quality Inner Detector track. This approach enables enhancement of the analysis sensitivity to τ-leptonic decays of $W^{\pm}$ and restores $t\bar{t}$ signal events lost due to lepton identification inefficiencies (a $\sim 20\%$ signal acceptance gain). In order to achieve this, we defined a new analysis object: the track-lepton, and built a systematic prescription for TL determination optimal for high-p_{T} lepton identification in the scope of the present analysis.

In general, the MC descriptions of the quantities central for this analyses are in good agreement between data and MC simulation. The reasonable compatibility between the shapes and scales for the distributions in the control and signal regions provides confidence in our estimates of background contamination. However, in order to minimize the dependence on MC simulations, wherever possible we used data-driven techniques for background evaluation. Specifically, data-driven techniques were developed to predict the number of DY/Z dilepton events and backgrounds associated with mis-identified TLs.

The dominant systematic uncertainty for both modes of the l+track analysis is the jet energy scale. The electron identification efficiency scale factor uncertainty affects the analysis in the electron+track channel. The contribution to the total uncertainty from the MC modeling of the PDFs, parton shower and ISR/FSR is also sizable in all analyses. For the case of the exclusive l+track analysis, fakes are a major source of background, and therefore a major source of systematic uncertainty. The statistical uncertainty can be reduced by combination of the individual eTL and μTL results obtained with individual l+track channels. The combined results are dominated by the systematic uncertainties.

The measured $t\bar{t}$ cross section values per individual analysis channel and the combined $t\bar{t}$ cross sections

are compatible with each other and with the approximate NNLO prediction of the Standard Model as shown in Figure 10.1. The results of 3-channel (i.e. the combined result of the three 2ID channels - ee, $e\mu$ and $\mu\mu$), 5-channel and 7-channel combinations are also presented in Figure 10.1. One may expect an improvement of the statistical and systematic uncertainties by virtue of using the full 2011 collision data sample with integrated luminosity of 4.9 fb^{-1}. The statistical uncertainty is expected to decrease as $1/\sqrt{N_{\rm obs}}$, where $N_{\rm obs}$ is the number of observed $t\bar{t}$ candidate events. The statistical component of systematic uncertainties (e.g. such as those associated with the energy scale and resolution of jets, electrons and muons) is also expected to decrease as $1/\sqrt{N_{\rm obs}}$, although the full 2011 data sample may have additional systematic uncertainties due to increased pile-up. Hence, a reasonable assumption is that the systematic uncertainty would be half way between the current value and the case where the uncertainty is reduced by $1/\sqrt{N_{\rm obs}}$. We do not expect that the integrated luminosity uncertainty would be significantly different from its current value of 3.7 %. Using the uncertainty measurements summarized in Table 9.3 and Table 9.4 we expect $\sim$ 8.5% for inclusive l+track analysis and $\sim$ 17% for the exclusive l+track analysis in the full 2011 data sample ($\sim$ 5 fb^{-1}). Figure 10.2 summarizes the $t\bar{t}$ cross section measurement results obtained by CDF and D0 collaborations using the $\sqrt{S} = 1.9$ TeV $p\bar{p}$ collision data at Tevatron and measurement results of ATLAS and CMS collaborations using $\sqrt{S} = 7$ TeV collision data provided by the LHC.

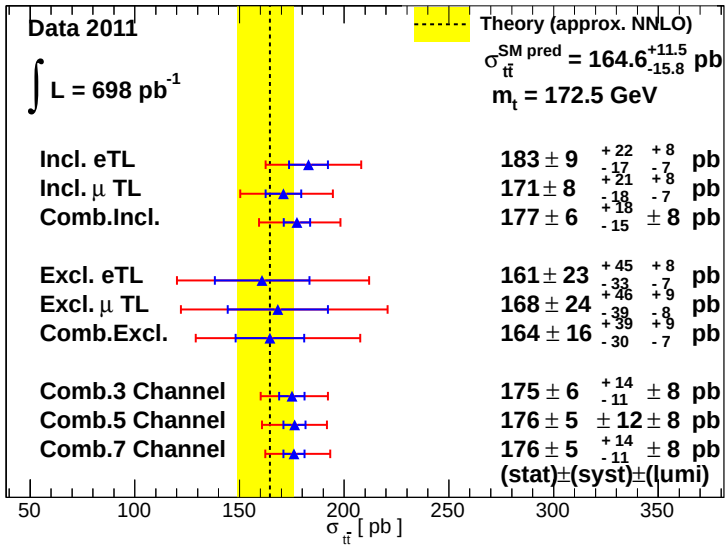

Figure 10.1: Summary of the $t\bar{t}$ cross section measurements per l+track channel and the combined measurement (error bars indicate the statistical and the total uncertainty) and comparison with the theoretical prediction (error band) at approx. NNLO [63]. Five channel combination of the exclusive l+track analysis with conventional dilepton channels, as well as 7-channel combination with with exclusive ee and $\mu\mu$ events with b-tag are also presented.

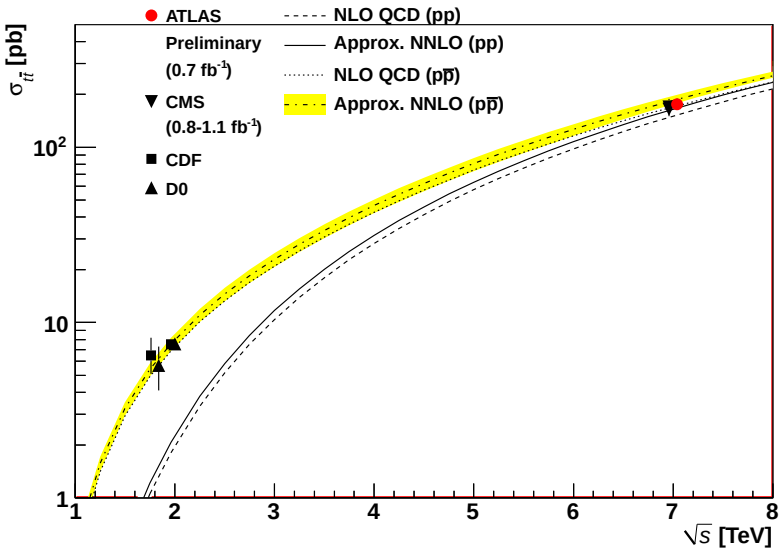

Figure 10.2: Summary of the $t\bar{t}$ cross section measurements in 1.9 TeV $p\bar{p}$ collision data with Tevatron and 7 TeV pp collision data with LHC. Figure adapted from [106] by Tony Liss.

There are several ways the results of this analysis may be improved. One may consider using more sophisticated tools for the TL and l+track event selection requirement optimization such as multivariate analysis tools. Since the DY/Z dilepton process is the major background in dilepton final states and the $E_{\mathrm{T}}^{\mathrm{miss}}$ cut is the main tool to suppress it, a special treatment is required for the high $E_{\mathrm{T}}^{\mathrm{miss}}$ tails. This for example could be achieved by ensuring that electromagnetic clusters, associated with electrons reconstructed as TLs, enter the $E_{\mathrm{T}}^{\mathrm{miss}}$ calculation as an electromagnetic object as opposed to a jet. The $E_{\mathrm{T}}^{\mathrm{miss}}$ correction deployed in the μ+track channel may also be improved by trading the cut on $\Delta\phi$ between TL and $E_{\mathrm{T}}^{\mathrm{miss}}$ with a criteria on the TL being a minimum ionizing particle. Another promising tool that could be used to further suppress the background and systematic uncertainties is b-tagging jets. Last but not least, the track-lepton object may be successfully used to gain signal acceptance in new physics searches involving leptonic final states. Examples of such searches that deploy the l+track approach are searches for flavor changing weak neutral currents (FCNC) and high mass dilepton resonances.

Appendix A

Atlantis Event Display of the First l+track Events

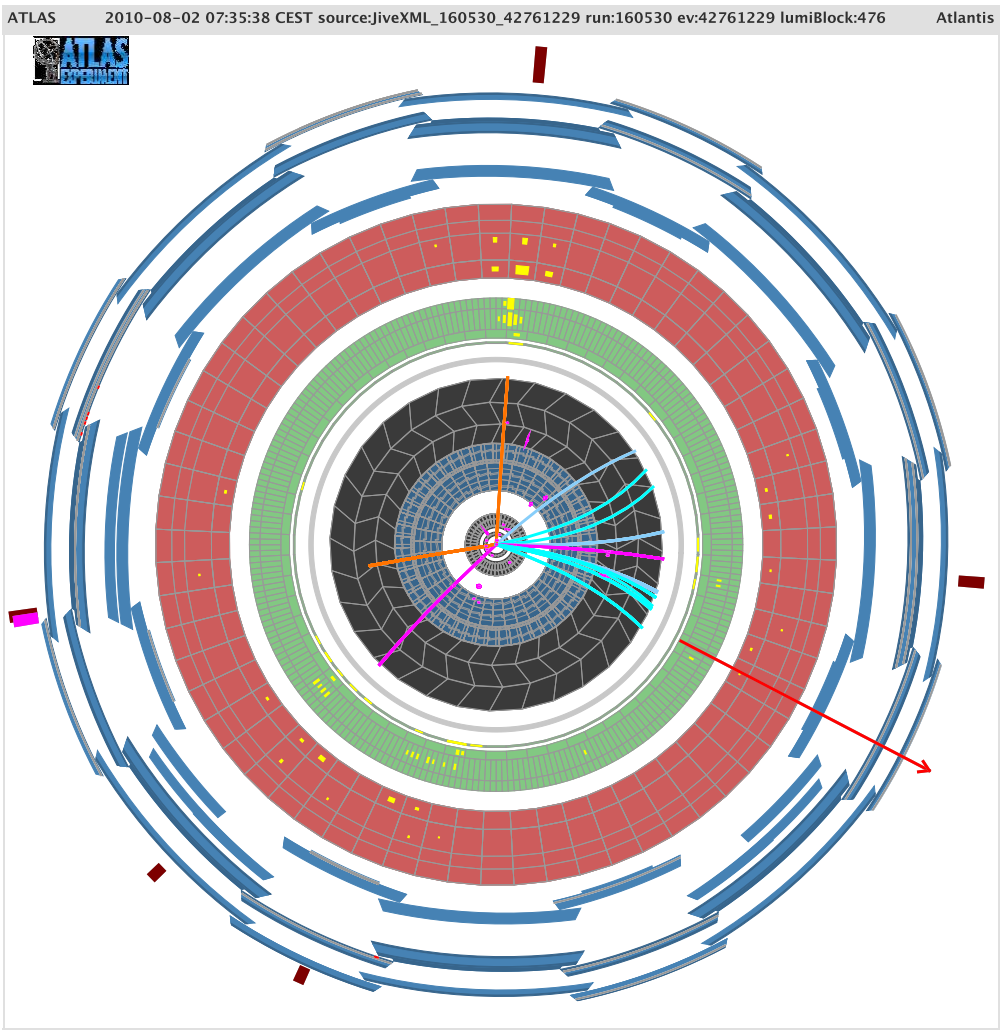

Figure A.1: Atlantis event display of the first e+track candidate event observed by ATLAS. Run number 160530, event number 42761229. Inner Detector is zoomed in with respect to other sub-systems. The color code on the display is as follows: jets are depicted in brown, b-tagged jets are in blue, electrons in purple, muons in green, τ-leptons are in grey, $E_{\mathrm{T}}^{\mathrm{miss}}$ is shown with red arrow and track are color coded as a function of their P_T.

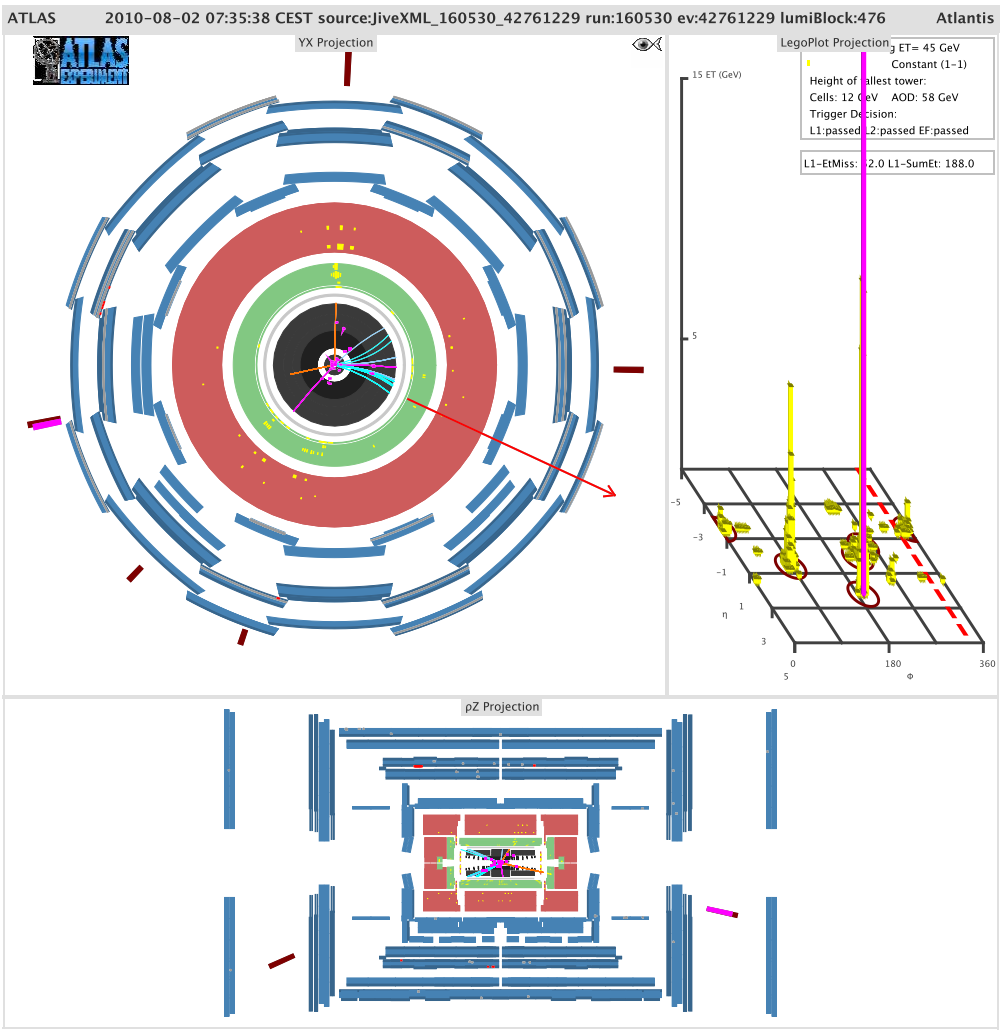

Figure A.2: Atlantis event display of the first e+track candidate event observed by ATLAS. Run number 160530, event number 42761229. The color code on the display is as follows: jets are depicted in brown, b-tagged jets are in blue, electrons in purple, muons in green, τ-leptons are in grey, $E_{\mathrm{T}}^{\mathrm{miss}}$ is shown with red arrow and track are color coded as a function of their P_T.

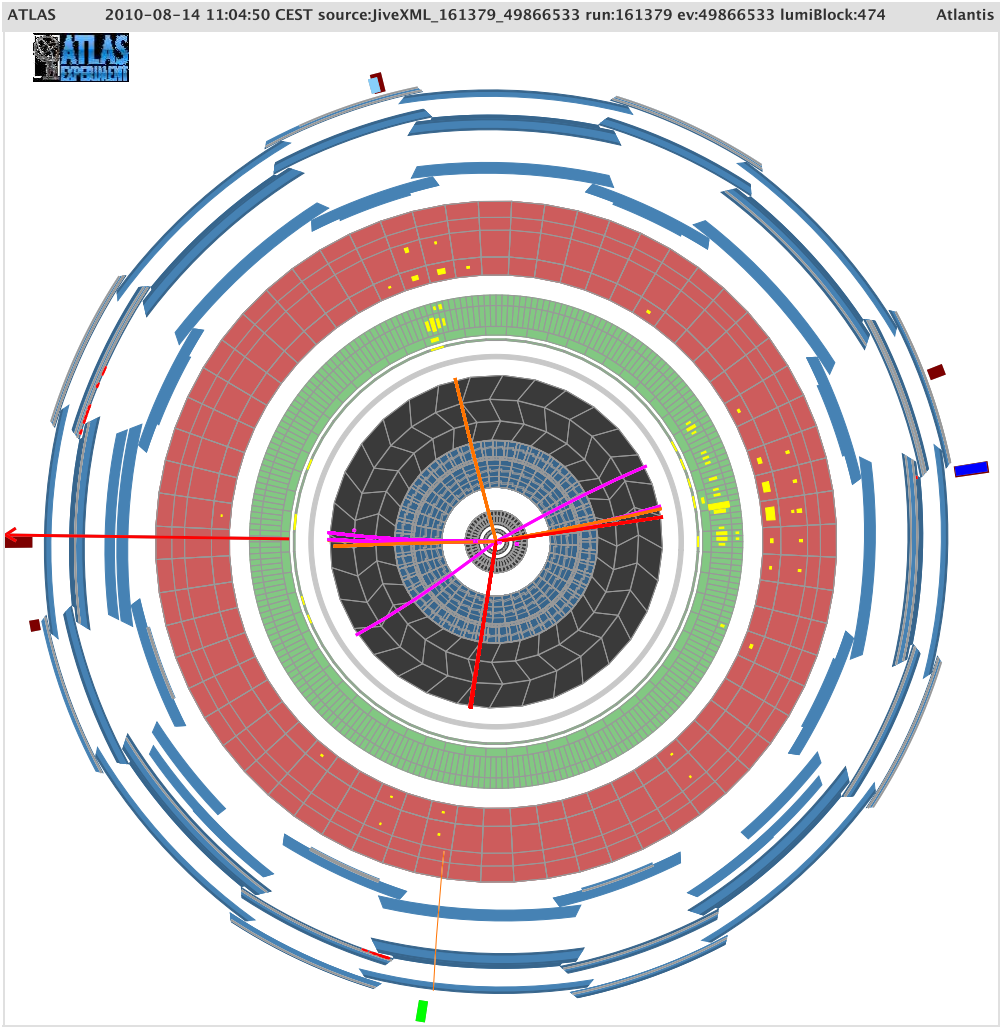

Figure A.3: Atlantis event display of the first μ+track candidate event observed by ATLAS. Run number 161379, event number 49866533. The color code on the display is as follows: jets are depicted in brown, b-tagged jets are in blue, electrons in purple, muons in green, τ-leptons are in grey, $E_{\mathrm{T}}^{\mathrm{miss}}$ is shown with red arrow and track are color coded as a function of their P_T.

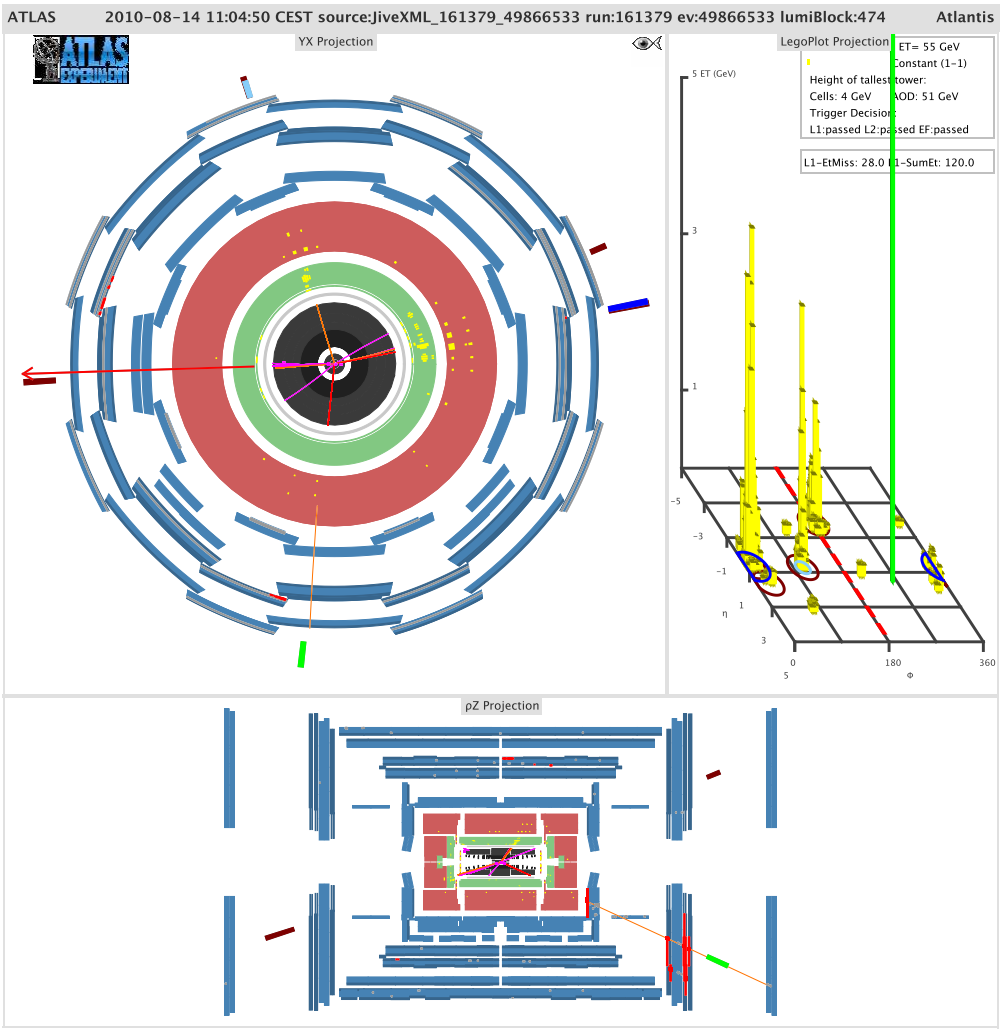

Figure A.4: Atlantis event display of the first μ+track candidate event observed by ATLAS. Run number 161379, event number 49866533. Inner Detector is zoomed in with respect to other sub-systems. The color code on the display is as follows: jets are depicted in brown, b-tagged jets are in blue, electrons in purple, muons in green, τ-leptons are in grey, $E_{\mathrm{T}}^{\mathrm{miss}}$ is shown with red arrow and track are color coded as a function of their P_T.

Appendix B

A Study of the Tile Calorimeter Response Uniformity as a Function of Radial Depth

B.1 Introduction

As discussed in Section 3.3.2 the ATLAS calorimetry in general and TileCal in particular must provide accurate energy and position measurement for electrons, photons, isolated hadrons, jets and transverse missing energy. In order to accomplish this, for each TileCal cell, the electromagnetic (EM) scale calibration constant must be determined, converting the calorimeter PMT signals (measured as electric charge in pC) to the kinetic energy deposited by electrons.

In order to obtain the EM scale calibration constant, 11% of the 4x64 TileCal modules were exposed to electron, muon, hadron (pion and proton) beams, at various energies with different geometrical set-ups in the scope of TileCal test-beam program that was situated in the H8 area of the CERN SPS facility, as shown in Fig. B.1. The main goal of the test-beam program was not only to obtain the TileCal EM scale, but also to explore the uniformity of the modules and to determine the calorimeter performance at projective pseudorapidity. The following experimental setup was put in place to address these goals. On a massive scanning table capable of x, y, θ and ϕ motion, the prototype TileCal Module 0 was the lowest in a stack of three modules. The middle layer was a production barrel module, and the top layer was either a pair of

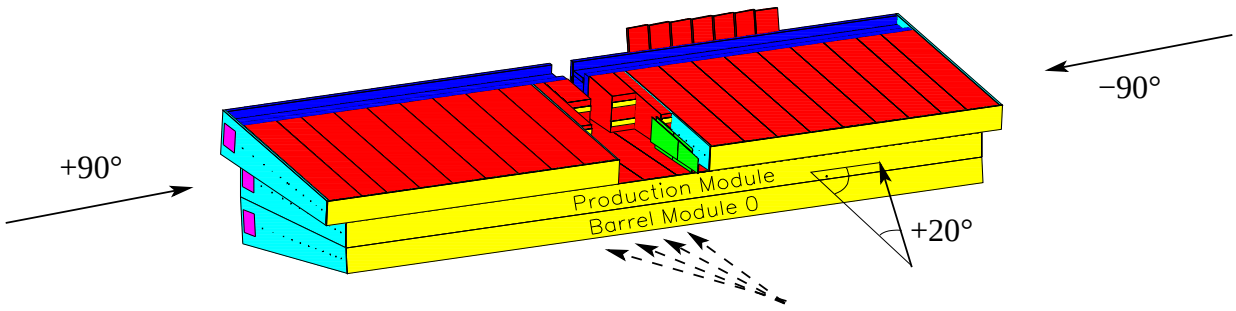

Figure B.1: Tile Calorimeter module layout during beam test operation in the H8 area of the CERN SPS. From bottom to top the Module 0, a production barrel module and two extended barrel modules are shown. Approximate beam directions for $\theta = +90°$, $\theta = -90°$, $\theta = +20°$ and η-projective setup (dashed arrows) are shown.

production extended barrel modules (as shown in the figure) or another production barrel. Since some data was taken with projective geometry, module orientation is denoted by positive or negative η, with positive η being the beam-right side of the scanning table.

Calibration of each module consisted of using the beam with the following geometries:

- Beam incident at the center of the front face of each A cell at $\pm 20^\circ$ from the normal (see Figure 3.6).
- Beam incident at the projective angles across the front face of the calorimeters.
- Beam incident at the sides of the calorimeters into the center of each tile row. This is referred to as the $\pm 90^\circ$ measurements.

Beam energies for TileCal measurements were between 20 GeV and 180 GeV. In general, the beam composition was a mixture of hadrons, muons and electrons. The particle type was identified mainly by using the calorimeter response and a pair of beam line Cerenkov counters assisting in further particle identification.

B.2 TileCal Electromagnetic Scale Calibration

The TileCal EM scale calibration constant was obtained from an analysis of the TileCal response to electron test beams of over 200 TileCal cells, where the charge collected in one TileCal cell was equal to the sum of charges collected by the two PMTs reading out the cell. The response of the calorimeter modules to electron beams was defined as:

$$R = \frac{Q_{\mathrm{PMT1}} + Q_{\mathrm{PMT2}}}{\langle E^e_{\mathrm{Beam}} \rangle} \tag{B.1}$$

where $Q_{\mathrm{PMT1(2)}}$ is the charge collected by the first (second) PMT reading out the cell respectively, and $\langle E^e_{\mathrm{Beam}} \rangle$ is the average electron beam energy.

In order to derive the TileCal EM scale calibration constant, the response of all A cells of the three long barrel modules and five extended barrel modules to electron beams was studied[1]. The beams entered the modules at $\theta = \pm 20^\circ$, having energies of 20, 50, 100 and 180 GeV. Only runs with all PMTs working were included in the analysis.

A distribution of all obtained responses of over 200 calorimeter cells is presented in Fig B.2. The mean value of this distribution is 1.050 ± 0.003 pC/GeV and is taken as the TileCal electromagnetic scale. The

[1]The following modules were analyzed in this case: extended barrel modules ANL-23, ANL-30, ANL-44, IFA-27 and IFA-42; long barrel modules JINR-12, JINR-27 and JINR-55.

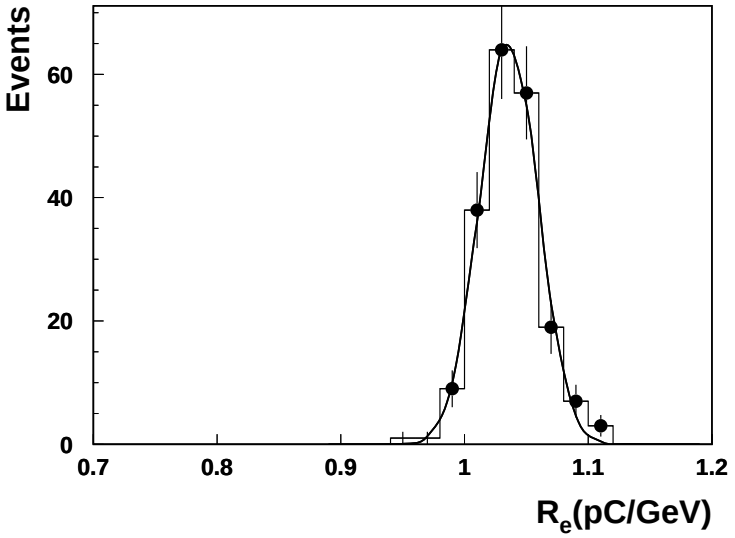

Figure B.2: The cell response of electrons at the angle $\theta = \pm 20°$ (Mean = 1.050 ± 0.003 pC/GeV, RMS = $2.4 \pm 0.1\%$), with one entry for each A-cell measured. The plot contains data taken at 20, 50, 100 and 180 GeV electron beam energies.

RMS spread of the measurement is 2.4 ± 0.1 % [107].

B.3 Tile Light Collection Uniformity Studies

In early testbeam studies of the light collection properties of scintillating tiles, we did not explicitely investigate the possibility of a non-uniform response of the tile surface along the radial depth direction of the ATLAS detector. While electron beams used for setting the calorimeter EM scale deposit most of their energy in the A compartment of the Tile calorimeter modules, the question of whether the cells in the BC and D compartments are properly calibrated at the EM scale after calibration with the cesium γ-source remains open. In order to address this question, the data from muon beams entering the calorimeter modules at $\theta = \pm 90°$ along the centers of the tiles was used. The total muon signal was measured in every tile-row. In-depth analysis of that data was performed and summarized in [107]. The response of TileCal modules to muon beams at $\theta = 90°$ is presented in Fig. B.3. As one can see after the gain of all cells in the calorimeter is equalized with Cs calibration, the muon response depends on the tile row number.

The main goal of this section is to investigate the cause for this response non-uniformity, more specifically to compare the light collection of the tile central region within a radius of 2.5 cm (where electrons and muons incident on the calorimeter at $\theta = 90°$ and $20°$ are used for the absolute electromagnetic calibration scale determination), with the light collection area around the tile outer radius hole (where the ^{137}Cs calibration source passes) and with light collection from the entire tile surface (illuminated by hadronic showers). For an

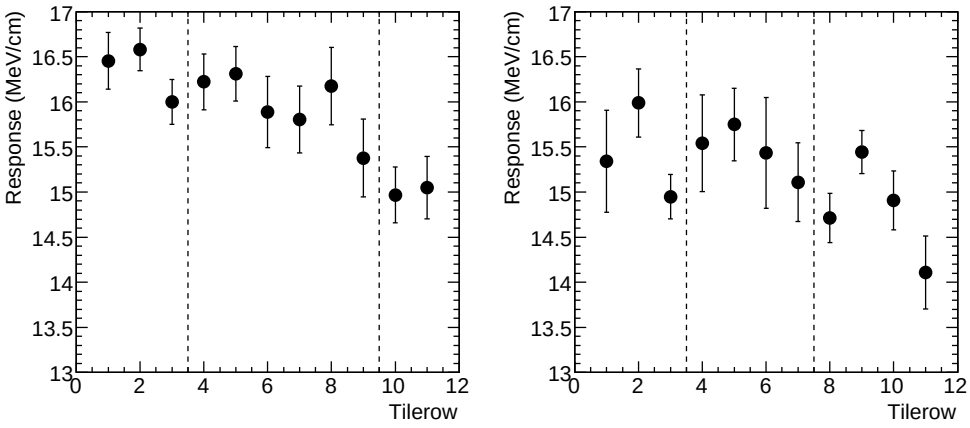

Figure B.3: The muon response summed over the full calorimeter module length in the 90° configuration, averaged over all analyzed modules and divided by the muon path length (560 cm in barrel and 255.5 cm in extended barrel module, end-plates excluded). Results for barrel modules (left) and extended barrel modules (right) are presented. The dashed lines show the edges of radial compartments (A, BC and D from left to right), for which the particle/Cs correction factors are computed. The fact that the path length normalized response to muons is on average lower in EB than in LB is understood and confirmed by Monte Carlo studies. Details are given in the text.

in-depth discussion see [108]. Section B.3.1 presents the results of the tile surface uniformity studies using a ^{90}Sr β-source. This section also discusses the effect of the read-out fiber configuration on tile light collection and introduces the *Tile Optical Model* which describes the light collection mechanism in the trapezoidal tiles. Section B.3.2 focuses on the studies with ^{137}Cs γ-source on individual tiles, and in Section B.3.3 we describe the results of ^{137}Cs calibration scans of TileCal modules at the Test Beam and in the ATLAS pit. Section B.4 presents our conclusions.

B.3.1 Individual Tile Measurements with ^{90}Sr β-source

Setup and Experimental Results

A collimated ^{90}Sr β-source with $\sim 30MBq$ intensity and electron beam size of less than 3mm (determined by the plastic collimator) was used for tile surface uniformity studies by scanning the source over the tile surface in a predefined grid as shown in Figure B.4. A dummy non-aluminized fiber was attached to the other side of the tile to provide realistic conditions of light reflection between the tile and the fiber. The measurements were done with masked tiles using a single readout fiber (of fixed length of 1 m) in the 'Standard' configuration, i.e. with the PMT close to the tile outer radius edge as in the Tile Calorimeter. The measurements with the ^{90}Sr β-source were performed with an ammeter connected to the PMT anode and application of the β^- source on the tile surface. The accuracy of the measured response at a point was

estimated from the $\sim 4\%$ dispersion of repeated measurements at all points of tile size 1 and tile size 11.

In the following, the y-axis is along the TileCal radius, i.e. parallel to the line joining the holes with y=0 located at the outer radius. The x-axis is parallel to the sides of the tile.

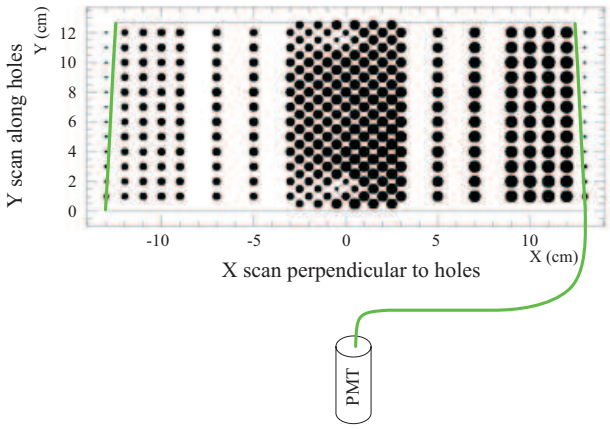

Figure B.4: Schematic view of the tile with predefined grid of points for ^{90}Sr measurements in the 'Standard' configuration with single fiber readout

In order to obtain a picture of the tile response to the ^{90}Sr source in the 'double fiber' readout configuration with additional equidistant points, we constructed a two-dimensional grid of equally weighted points using the following procedure:

- The measured points in one half of the tile (obtained with a step size of 0.5 cm or 1 cm in the central X-strip of ± 2 cm, and with 1 cm or 2 cm step size elsewhere) were mirror reflected with respect to the plane perpendicular to the tile surface and passing through tile holes (the $X = 0$ axis) and the results were summed over. These points were considered as the measured response values at respective (X, Y) coordinates

- A grid of a fixed step size (using 1cm steps) was placed over the measured points along lines parallel to X axis, by interpolating and extrapolating the measured points with a 3^{rd} degree polynomial fit. When all the X-lines were filled with these fitted points, the same procedure was applied to lines parallel to the Y axis with the same step size of 1 cm

- The grid step size was decreased to 0.25 cm and repeated once more along the X-direction and then along the Y-direction

- When the new fitted points appeared to overlap with the previously fitted points, the average number was stored.

- A 2-dimensional grid of measured and fitted points covering the entire tile surface with 0.25 cm step size was thereby obtained.

The resulting response to the ^{90}Sr β-source over the whole tile surface is shown in Fig. B.5 for individual masked tiles of sizes 1 and 11 in arbitrary units. The measured points (green crosses) and the meshed fitted points are shown in the 3D response map of Figure B.5(a). The blue colored mesh represents regions with response less than the average of the tile surface, whereas the red colored mesh represents the regions with higher than the average response.

From Figure B.5(a) and B.5(b) we observe a hump in the central region along the tile hole direction with response higher than the average, as well as a decrease in response in the direction from the outer to the inner radius. The slight increase of light in the central strip between the holes is due to the reflection of scintillation light from the surfaces of the holes. In the direction perpendicular to the holes a ∼5% increase of light near the tile sides coupled to the fibers is observed, even in tiles masked with black ink. The increase would have been much higher (>20%) if the tiles had not been masked [109], [110]. The RMS of the measurements in the mesh over the whole tile surface is ∼5% for all tile sizes, which is well within the uniformity specifications of TileCal.

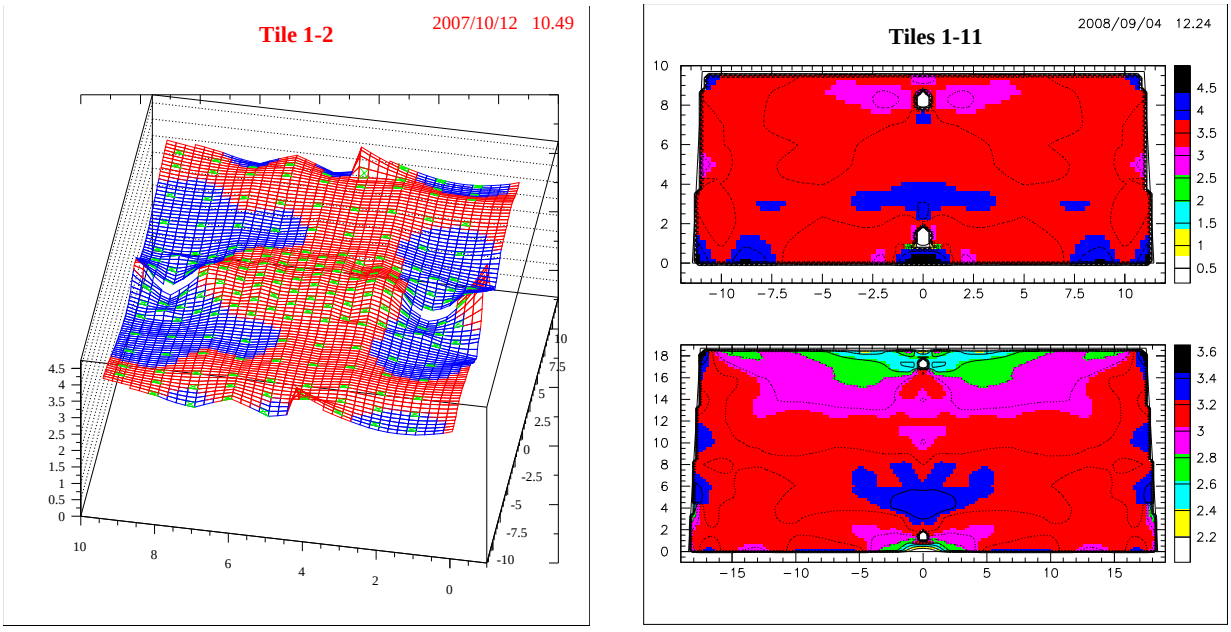

(a) 3D Scan Map

(b) 2D Scan Map

Figure B.5: (a) Reconstructed 3D response of a tile to the ^{90}Sr β-source (mesh) based on individual measurements (green dots). (b) The 2D response map to ^{90}Sr of a tile size 1 (top) and a tile size 11 (bottom). The Y-axis is parallel to the holes and Y=0 is the outer radius edge.

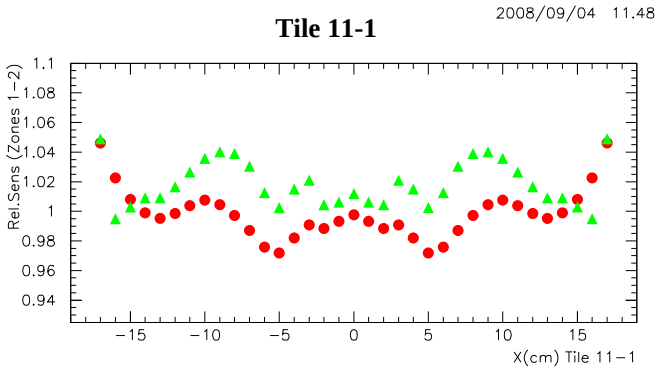

Figure B.6: Tile response to ^{90}Sr-source along the $X(\phi)$ direction (perpendicular to the line joining the holes) for all Y scans (circles); Averaging only the radial scans in the central region of 2.5 cm between the holes (triangles).

Figure B.6 shows the average response along the X (ϕ) coordinate for the case of taking the average of all the Y radial scans (red circles) and the case of taking the average of only central Y scan values within a strip of $\pm$ 2.5 cm around Y=0 (green triangles) for tile size 11. As expected, one observes the typical W-shape profile for the case of double-sided tile signal read out.

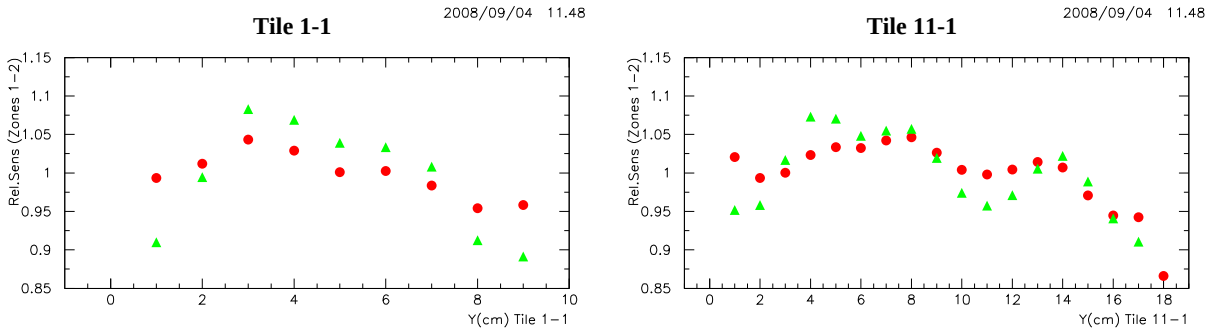

(a) Tile Size 1

(b) Tile Size 11

Figure B.7: Tile response to ^{90}Sr-source along the Y radial direction (parallel to the line joining the holes) for all the X values (circles); Averaging only central Y scans in a region of 2 cm (triangles).

Fig. B.7 shows the average tile response to the ^{90}Sr β-source along the Y radial coordinate after averaging all the X scans for tile size 1 and 11. $Y = 0$ corresponds to the outer radius extremity of the tiles. For tile size 1, $Y = 97$ mm is the inner radius extremity while for tile size 11, it is $Y = 187$ mm as shown in Table 3.2. The tile response to the ^{90}Sr source decreases when moving from the tile outer to inner radius holes (Y scan). This decrease is due to the trapezoidal shape of the tiles. The scintillation light is more efficiently collected at the outer radius. A detailed explanation of this effect is discussed later in this Appendix.

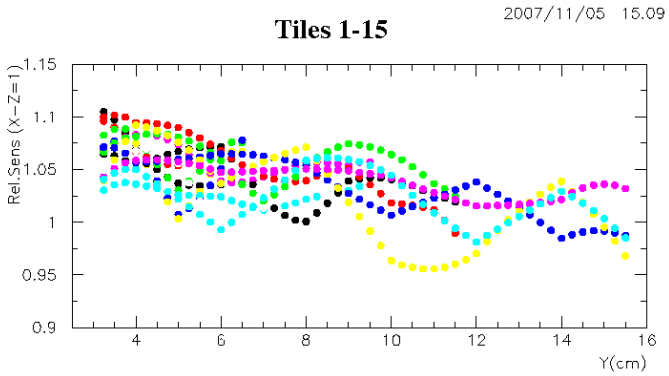

Figure B.8: Relative tile response to ^{90}Sr-source along the Y radial direction. Y=0 is always the outer radius edge for all tile 11 sizes.

The radial decrease in scintillation light response is confirmed for all tile sizes. Fig. B.8 shows the relative tile response to the ^{90}Sr β-source parallel to the tile hole direction upon averaging over the central X-region of ± 2 cm for all available measurements of tiles sizes 1 to 11. A clear negative slope is observed of the order of $\sim 1\%$ to 2% per cm for all tile sizes. Our estimate of the statistical uncertainty of this estimate is $\sim 2\%$. The systematic uncertainty is represented by the width of the band of all 11 measurements, which on average is $\sim 7\%$. Hence an upper limit for the uncertainty can be estimated as $3 \times 2\% + 7\% = 13\%$.

A more precise quantitative estimate of this effect was achieved using measurements carried out with the ^{137}Cs γ-source passing through the entire calorimeter module and sequentially exciting the areas around the inner and outer radius holes of hundreds of scintillating tiles of size 7 and several individual tiles of all 11 sizes. This is described later in Sections B.3.2 and B.3.3.

The effect of scintillation light collection reduction in the trapezoidal tiles when moving from the tile outer to inner radius holes gives an indication of the reason for the observed undercalibration of the middle and rear longitudinal depth cells after the calibration of TileCal with the Cesium γ-source (passing always in the outer radius holes) [107]. We set the absolute electromagnetic scale in TileCal with electrons and muons impinging the center of the tiles at $\theta = 90°$ and $20°$ and exciting the central region of the tiles (radius of 2.5 cm), whereas TileCal cells are intercalibrated with the ^{137}Cs γ-source using the response in the area around the outer radius hole. Thus, the discrepancy between the response to electrons or muons and ^{137}Cs γ-source grows larger for larger tiles. The radial distance between these 2 regions, hence the magnitude of undercalibration, increases with the tile size (H/2 dimension) as is shown in Table 3.2.

The remaining question is whether or not the light response from the center of the tile is an accurate representation of its surface and how this response depends on the tile size. Fig. B.9 shows the ratio of ^{90}Sr response in the central region of radius $\sim$ 2.5 cm to the response averaged over the total tile area as a

function of the tile row number. This ratio is tile size independent. Fig. B.9 shows this measurement for 2 sets of 15 tiles, 1 tile of each size except for tile size 1 and 11 where 3 tiles were measured. Merging the 2 tile samples (30 tiles) we obtain a mean of the ratio in the central region (radius = 2.5 cm) over the total tile surface of 1.03 with $RMS = 1.4\%$ as shown in Fig. B.10.

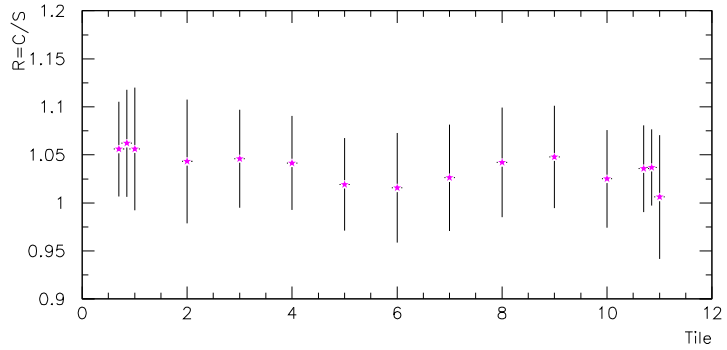

(a) March-2002 Sample.

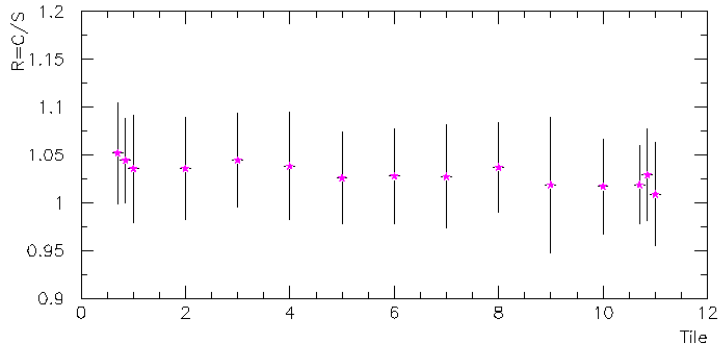

(b) April-2002 Sample

Figure B.9: The ratio of the response to the Sr β-source within a circle of 2.5 cm radius located at the center of the tile over the response of the whole surface as a function of the tile row number. Three different tiles of size 1 and 11 were measured.

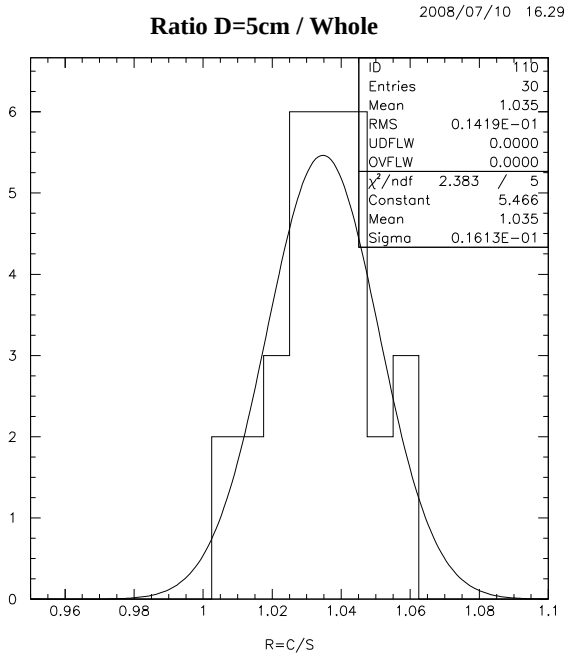

Figure B.10: The ratio of the response to the ^{90}Sr-source within a circle of 2.5 cm radius located at the center of the tile to the response of the whole tile surface. A sample of 30 tiles was used; 6 tiles of size 1 and 11 and 2 tiles of each size for tile sizes 2 to 10.

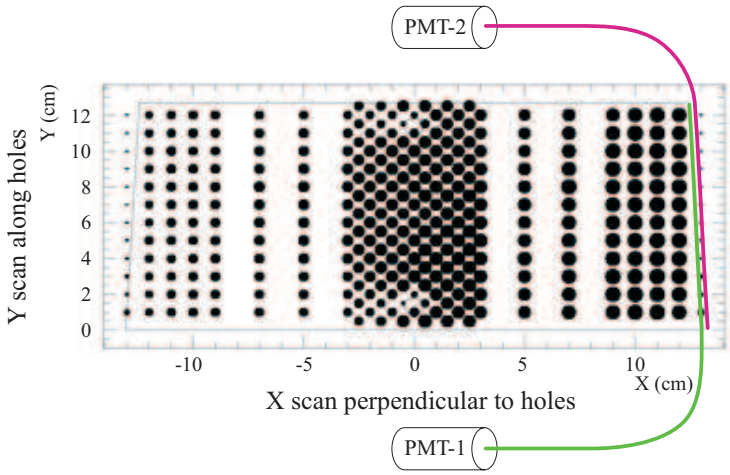

Figure B.11: Scheme of fiber readout by PMT-1 as in the calorimeter with PMT-1 closer to the tile outer radius. The fiber was inverted and PMT-2 placed closer to the tile inner radius edge for the special test with inverted fiber configuration.

Read-out Fiber Configuration Effects on Tile Light Collection

In order to address the possible impact of the read out fiber attenuation length on light collection reduction as a function of tile radius the response of tile size 11 to the ^{90}Sr-source was measured in the Standard configuration of TileCal modules, i.e. the PMT closer to the tile outer radius edge (green fiber and PMT-1 in Fig. B.11). The same measurements were also conducted in the 'Inverted' configuration, i.e. the PMT closer to the tile inner radius edge (PMT-2 and pink fiber in Figure B.11). The same fiber of 97 cm length was used for both fiber configurations. Scintillating light was collected from one tile side via the WLS fiber connected to the PMT, while the other tile side was coupled to a dummy fiber. Figure B.12 shows the ratio of tile mean response in the Standard and the Inverted configurations for 7 radial scans inside the X range from +3 to +9 cm from the tile center (Figure B.11). One can see from Figure B.12 that the S/I ratio distribution is consistent with a flat response. This is clear evidence that this effect is not correlated to the light attenuation in the WLS fibers and has to do with the tile geometry, i.e. the tile trapezoidal shape only.

The Tile Optical Model

In order to address the issue of tile light collection reduction from the outer to the inner radius holes described in the previous section, we developed the *Tile Optical Model*, based on simple statements of geometrical optics and Liouville's theorem. We assume here that scintillation light collection is due only to only the direct light incident on the read out WLS fiber side and single reflections from the tile sides to the WLS fiber. We further assume total internal reflection from the tile edges. More specifically, this means that the scintillation

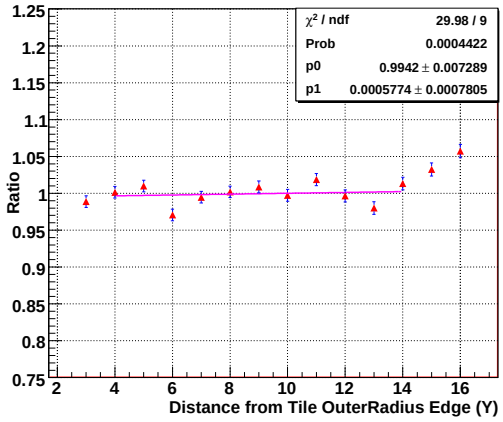

Figure B.12: The ratio of average responses of the 3 cm < X < 9 cm strip of the tile to the ^{90}Sr β-source along the radial direction between the standard and inverted fiber readout (see Figure B.11). A tile of size 11 was used.

light at source S_R will be collected by the WLS read out fiber (see Figure B.13):

- Due to direct incidence of scintillation light on the fiber, associated with solid angle Θ_0
- Due to light reflection from the outer radius edge, an extra acceptance in solid angle Θ_1, which corresponds to an imaginary source S_I^1 at the mirror image location of S_R with respect to the tile outer radius edge.
- Similarly, an additional acceptance due to reflection from the tile inner radius edge in solid angle Θ_2, corresponds to an imaginary source S_I^2 at the S_R mirror image position with respect to the tile inner radius edge.

Also note that the light collection intensity depends on the length (L) of the propagation of the light in the tile material due to light attenuation (L_{Att}) according to the $I = I_0 \exp^{-L/L_{Att}}$ rule. This means that the weights of contributions to the tile light collection are different in each of the solid angles described above. We further assume that the weight of the contribution from the tile inner (outer) radius edge reflection is negligible (i.e. its weight is zero) for the source in proximity to the outer (inner) radius tile edge, respectively.

As is well known, Liouville's theorem states that the light flux per unit area and solid angle is constant. This means that the larger the solid angle (in which the read out fiber is seen from the source position) the greater the light flux, hence greater light collection from the source. Consider two sources S^1 and S^2 the same distance away from the tile outer and inner radius edges respectively. Both are the same distance away from the axis passing through the tile holes (see Figure B.14). Figure B.14 clearly shows that due to

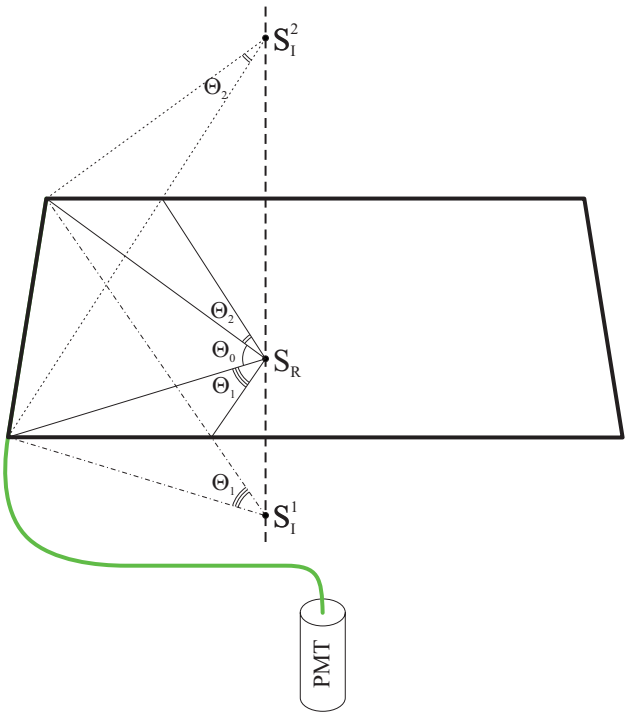

Figure B.13: Schematic view of tile light collection from the β-source at S_R.

the tile trapezoidal shape the solid angle at S^1 is greater than the one at S^2 resulting in the light collection reduction effect from outer to inner radius described earlier in this section.

Based on the Tile Optical Model, one can predict that black-painting the tile outer radius edge (i.e. suppressing the reflection from that edge) will result in a deterioration of tile light collection, and this degradation will be greater in proximity to the tile outer radius edge, hence resulting in a flatter reduction in the response curve (see comparison of solid and dashed lines of Figure B.15).

Similarly, black-painting the tile inner radius edge also causes deterioration of tile light collection, however this deterioration must be more notable for the region close to the inner radius edge. Hence, the decrease in the response curve should become steeper (compare solid and dash-dotted lines in Figure B.15).

In order to further investigate the issue of the light collection reduction and study the validity of the Tile Optical Model and predictions suggested by it, a set of measurements with the collimated ^{90}Sr β-source was carried out. A collection of three different tiles without Tyvek wrapping nor masking was used. The settings of the experimental equipment were described earlier in this section.

Figure B.16(b) shows a comparison of light collection of the tile in the standard configuration (circles) versus that for the outer radius 3 mm thick edge painted black (triangles) as in Fig. B.16(a). As can be seen, the characteristic negative slope is less steep. This is expected, since by suppressing the reflection from

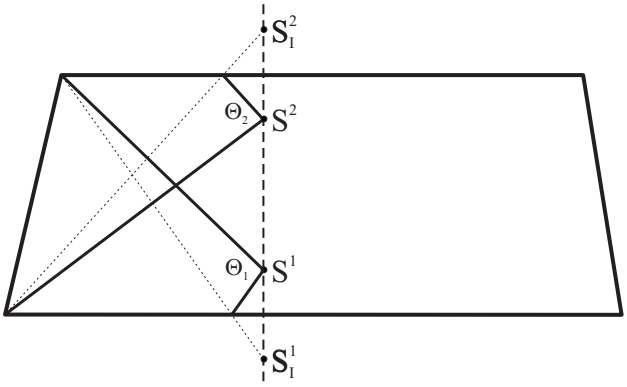

Figure B.14: The comparison of light collection in proximity to the tile inner radius (position at S^2) versus tile outer radius (position at S^1) edges.

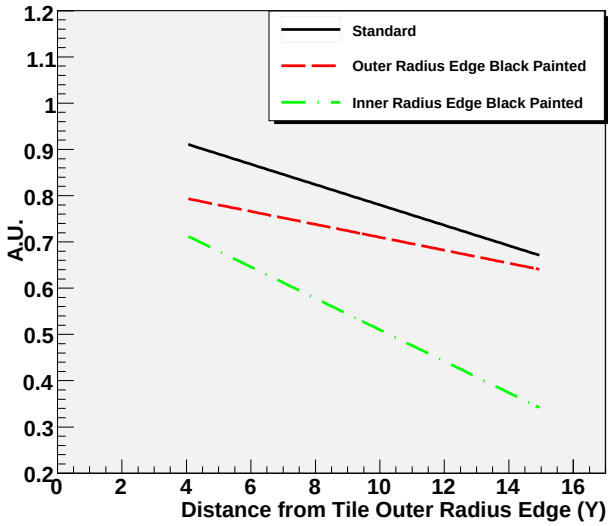

Figure B.15: Prediction for the behavior of the tile light collection reduction curve for masking with black ink on the tile outer radius edge (dashed red line) versus masking the inner radius edge (dash-dotted green line).

the tile outer radius edge, we essentially suppress the acceptance in the solid angle Θ_1 (see Fig. B.13), the contribution of which is apparently greater when the β-source is closer to the outer tile radius edge. We also obtain good agreement between the Tile Optical Model prediction (dashed red line of Fig. B.15) for the tile outer radius edge black-painted configuration with experimental data collected with the ^{90}Sr β-source. One can also note from Fig. B.16(b) that there is always a decreasing tail in proximity to the tile outer radius edge i.e. the region of $+3$ cm $< Y < +7$ cm. This is due to non-ideal reflection from the tile outer radius edge. Note also, that it is steeper for the black-painted case.

Figure B.17(b) shows the comparison of the tile light collection in the standard versus the tile inner radius edge black-painted configurations. One can now see that the negative slope is steeper. This can be explained by the suppression of the reflection from the tile inner radius edge, the contribution of which is more significant in proximity to the tile inner radius edge. Again, we obtain good agreement between the Tile Optical Model prediction (dash-dotted line of Fig. B.15) for the tile inner radius edge black-painted configuration and experimental data collected with the ^{90}Sr β-source.

Figure B.18(b) shows the comparison of tile light collection from standard versus the side opposite to single fiber readout black-painted configurations. One can see that the reduction in slope does not change significantly. This explicitly justifies our approximation in which we neglect light collection due to double, triple, etc. reflections.

Lastly, note that there is a discrepancy[2] in light collection from three different tiles probed in the Standard configuration, which is due to tile-to-tile, tile-to-fiber optical fluctuations (compare red data curve and the red boxes of Figure B.16(b), Figure B.17(b), Figure B.18(b)). We estimate the fractional uncertainty of the light collection reduction measurement as the ratio of the uncertainty of the 'p1' parameter (see red boxes of Figure B.16(b), Figure B.17(b), Figure B.18(b)) to its value. The numerical estimate is $30\% - 40\%$.

B.3.2 Measurements of Individual Tiles with ^{137}Cs γ-source

The same individual tiles that were measured with the ^{90}Sr β-source (Section B.3.1), were measured in a special test bench setup at CERN in the barrel module instrumentation workshop using the ^{137}Cs γ-source calibration system [111]. Fig. B.19 shows the picture of the setup.

Each of the tiles was positioned on the Cs γ-source tube in between two steel plates $10mm$ thick. The scintillation light was collected from both tile sides connected to a PMT in the drawer. The response of the individual tile was defined as the amplitude of the fit of the tile response curve. Fig. B.20 depicts a typical fit for an individual tile response curve. For the individual tile measurements the response to the

[2] 1.5 % to 2.2 % per cm decrease from outer to inner radius edges from 3 different tiles.

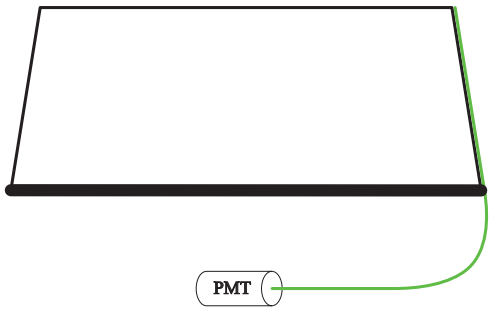

(a) Tile outer radius edge black painted configuration

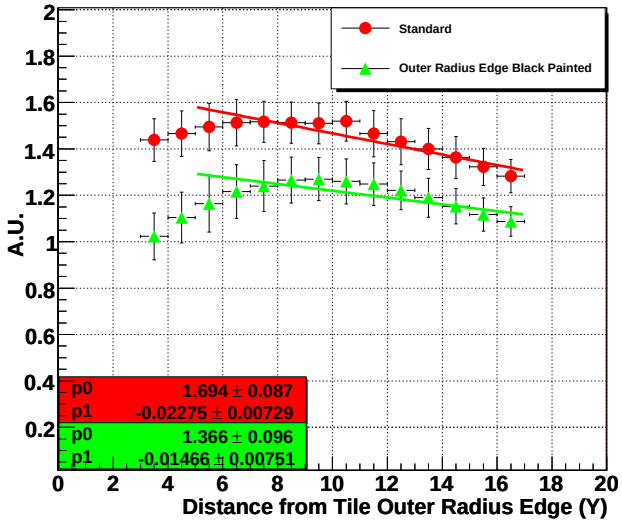

(b) Tile light collection reduction curves

Figure B.16: Schematic view of the tile outer radius black-painted configuration (a) and average response to ^{90}Sr β-source along Y radial scans in a region of $+3 < X < +9$ cm. (Circles) for tile size 11 without Tyvek in the 'Standard' configuration, (triangles) after painting the tile outer radius 3 mm thick edge to suppress light reflection from that edge.

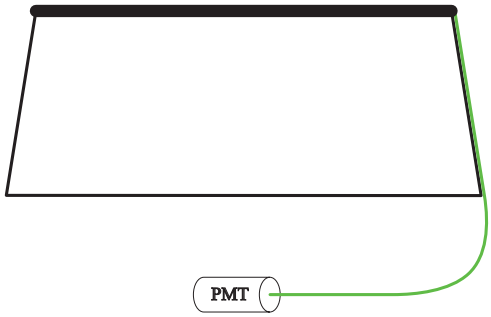

(a) Tile inner radius edge black painted configuration

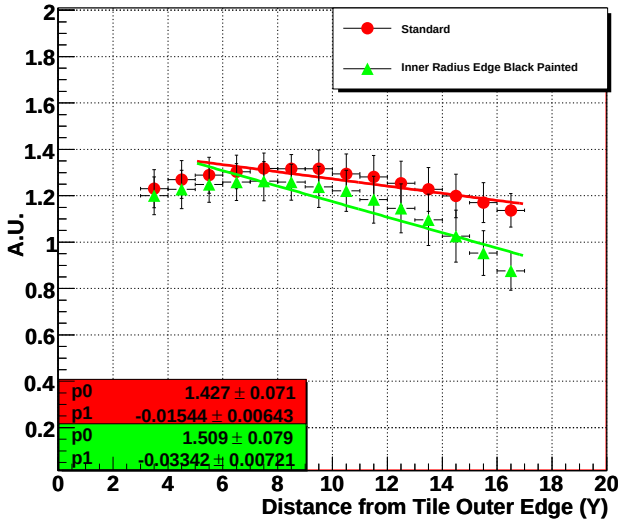

(b) Tile light collection reduction curves

Figure B.17: Schematic view of the tile inner radius black-painted configuration (a) and average response to ^{90}Sr β-source along Y radial scans in a region of $+3 < X < +9$ cm. (Circles) for tile size 11 without Tyvek in the 'Standard' configuration, (triangles) after painting the tile inner radius 3 mm thick edge to suppress light reflection from that edge (b).

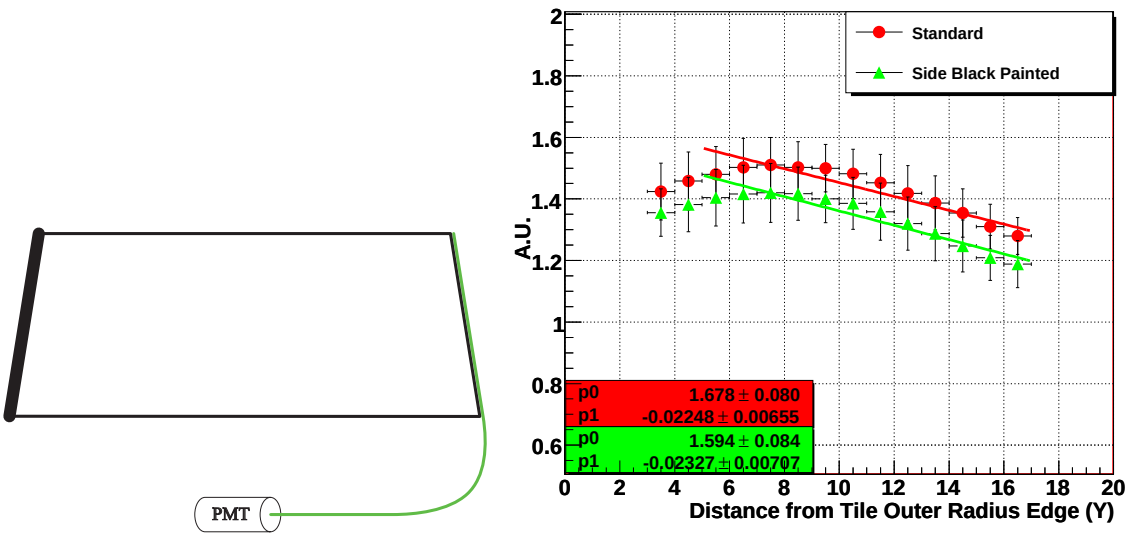

(a) Tile side (opposite to fiber read-out) black painted configuration

(b) Tile light collection reduction curves

Figure B.18: Schematic view of tile side (opposite to fiber read-out) black-painted configuration (a) and average response to ^{90}Sr β-source along Y radial scans in a region of $+3 < X < +9$ cm. (Circles) for tile size 11 without Tyvek in 'Standard' configuration, (triangles) after painting the tile side (opposite to fiber read-out) black (b).

Figure B.19: Setup for measuring individual tile responses with ^{137}Cs γ-source at the instrumentation lab

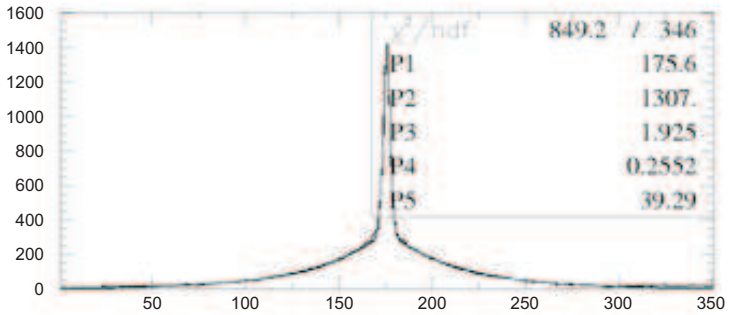

Figure B.20: Typical fitted response of one tile to ^{137}Cs γ-source in the setup of Fig. B.19

^{137}Cs γ-source was measured for the source passing through the outer and the inner tile radius holes.

Fig. B.21(a) shows that the tile response to ^{137}Cs γ-source (circles) passing through the outer radius hole for the case of larger tile sizes is overestimated compared to the tile response from the whole tile surface as obtained using the ^{90}Sr β-source (triangles). This figure should be treated as a qualitative illustration of this effect. The experimental uncertainties associated with the square points are dominated by the fact that the ^{137}Cs and ^{90}Sr measurements were done using two different setups. The tile outer radius hole was enlarged to enable passage of the Cs γ-source and the tile/fiber coupling was changed for these two measurements. It is an independent verification of the light collection reduction effect as observed in other ^{90}Sr β-source studies (Section B.3.1). One should also note that the ratio presented in Fig. B.21(a) (triangles) was also depicted in Fig. B.9(b) for the same sample of 15 tiles. Our estimate of the statistical uncertainty (using the measurement for the tile size 9) is $\sim 7\%$ and the systematic uncertainty is $\sim 17\%$. Hence an upper limit on the overall uncertainty can be estimated to be $3 \times 7\% + 17\% = 38\%$.

More precise evidence of this effect is depicted in Fig. B.21(b), showing the ratio of the response of the probed tile to the ^{137}Cs γ-source passing through the inner radius hole to the response at the outer radius hole. One clearly sees the dependence of the light collection reduction effect on tile size. From these measurements the estimate of light collection reduction from the tile outer radius hole to the inner radius hole is on average $\sim 0.8\%$ per cm. For example, for tile row 7 (where the distance between holes is 12 cm) the ratio $R(O/I) = 1/0.91 = 1.1$ or 0.83% per cm. The uncertainty on this measurement can be estimated as the repeatability of the measurement, which for tile size 9 is 15%. This value is compatible with the value obtained with the ^{90}Sr measurements described in Section B.3.1. In the next section, we will compare this value with that computed from Cesium source data at the Test Beam over a sample of $\sim 10\%$ of EB modules and data collected with Cesium source scans of the majority of the EBC modules during cesium

source calibration runs in the pit.

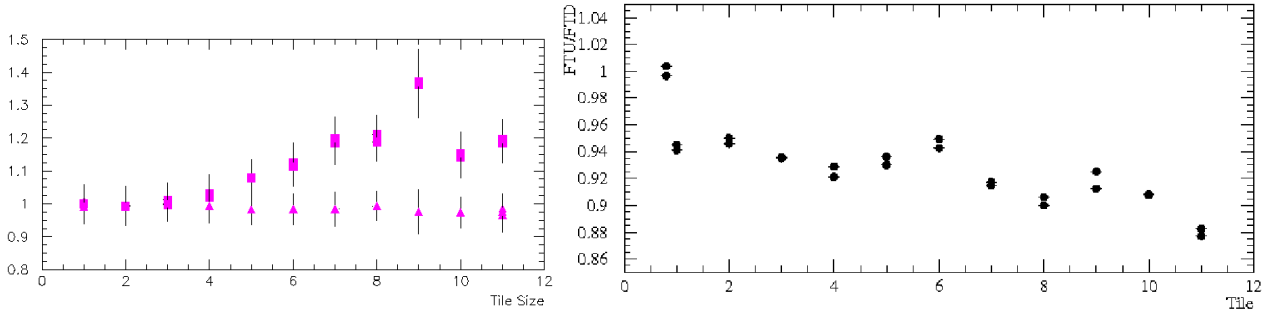

(a) (b)

Figure B.21: (a) The ratio of the response to ^{90}Sr of the tile central region with 5 cm diameter (outer hole region) to tile overall surface (triangles) and the ratio of response to ^{137}Cs to the response to ^{90}Sr of the tile overall surface (circles) vs tile size (1 to 11), both sets normalized to the corresponding ratio at tile size 1. (b) The ratio of response to ^{137}Cs γ-source at the source passage from the inner radius over the one at the passage through the outer radius hole, tile sizes 1 to 11.

B.3.3 ^{137}Cs γ-source in TileCal Modules

The Setup at TB and in the ATLAS Pit

As described in Section 3.3.2, each scintillating tile has two 9.0 mm diameter holes positioned always at the same distance (13.5 mm) from the inner and the outer radius edges where the ^{137}Cs calibration source passes through. A schematic view of the barrel module source tube installation is shown in Fig. B.22(a). The capsule containing the radioactive $\sim$ 10 mCi ^{137}Cs γ-source is carried along by a liquid flowing inside the calibration tubes passing through all cells of the calorimeter, hence measuring the response and monitoring the optical quality of more than 463000 tiles coupled to fibers in all 256 TileCal modules [112]. Typically the Cesium source passes through the tile outer radius hole. Figure B.22(b) shows the concept of the γ-source path in a calorimeter module. The cesium tube installation has a peculiarity in the EB modules, since in those, the ^{137}Cs γ-source passes through both holes in tile row 7. This enables an independent estimate of the light collection reduction between the outer radius and the inner radius regions, similar to what was previously presented for individual tiles with ^{90}Sr and ^{137}Cs systems. The advantage of exciting many tiles of the same size at the same time allows reducing the effect of optical fluctuations that are present in individual tile measurements compared to the thousands of tiles excited inside the Tilecal modules. As opposed to studies of individual tile response to ^{137}Cs γ-source, where the quantitative estimate of this effect is simply the ratio of the tile responses for tile outer to inner hole cases, the studies of the γ-source scans

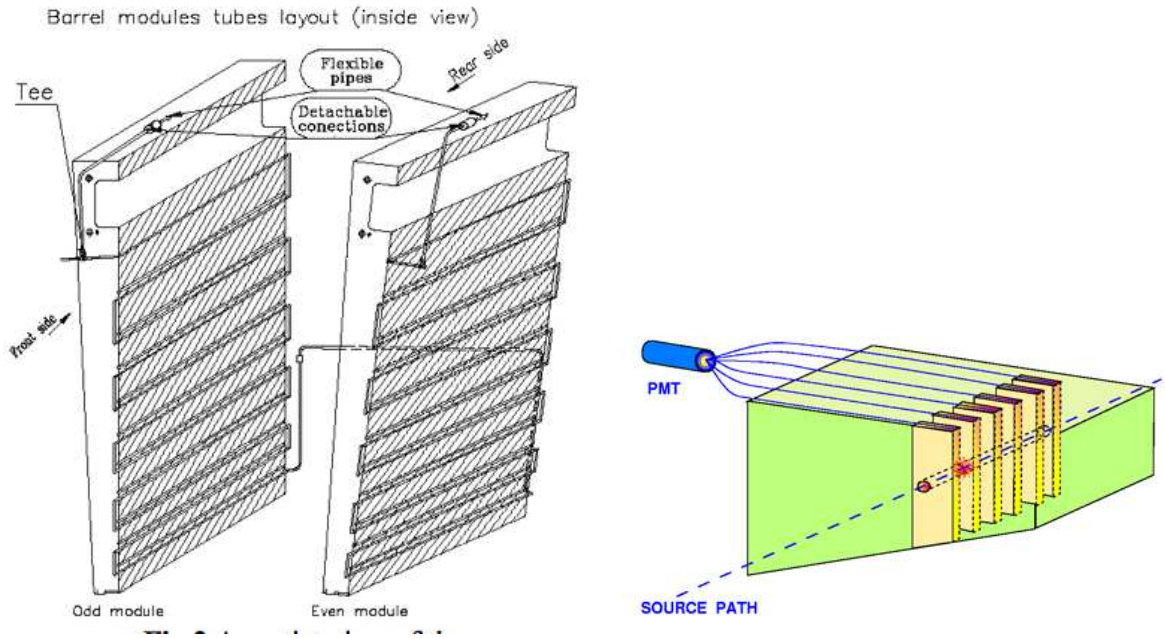

(a) (b)

Figure B.22: (a) Schematics of source path in TileCal. (b) Source passing through a tile row in a cell.

of the entire tile module need to address carefully the issue of energy leakage into the adjacent tile rows. In the EB modules tile row 7 and 6 belong to BC cells while tile row 8 belongs to D cells. Hence, when computing the response of tile 7 with the Cs source passing through the inner radius hole, the leakage from tile row 7 to 6 must be taken into account. The method used to unfold the effect of leakage between tile rows is addressed in Appendix C.

Results of ^{137}Cs Scans at Test Beam and in the ATLAS Pit

As was discussed in Section B.3.2, the quantitative measure of the light collection reduction effect is the ratio of tile response to ^{137}Cs γ-source passing through the tile outer radius hole to the response at the tile inner radius hole; R(O/I). The distribution of that ratio estimated from the data collected during the calibration runs in the Test Beam in periods 2001 to 2004 is presented in Fig. B.23(a). We use this data to measure the $Mean = 1.104$ and $RMS = 11\%$ for R(O/I). The leakage into adjacent tile rows is corrected for. The ^{137}Cs leakage corrections in Tile 7 outer and inner radius holes are discussed in detail in Appendix C. The length of the fibers reading out the tiles in those cells vary between 160 cm and 190 cm [109]. Fig. B.23(b) provides evidence of η-uniformity of the measured ratio R(O/I) reinforcing the conclusions described in Section B.3.1,

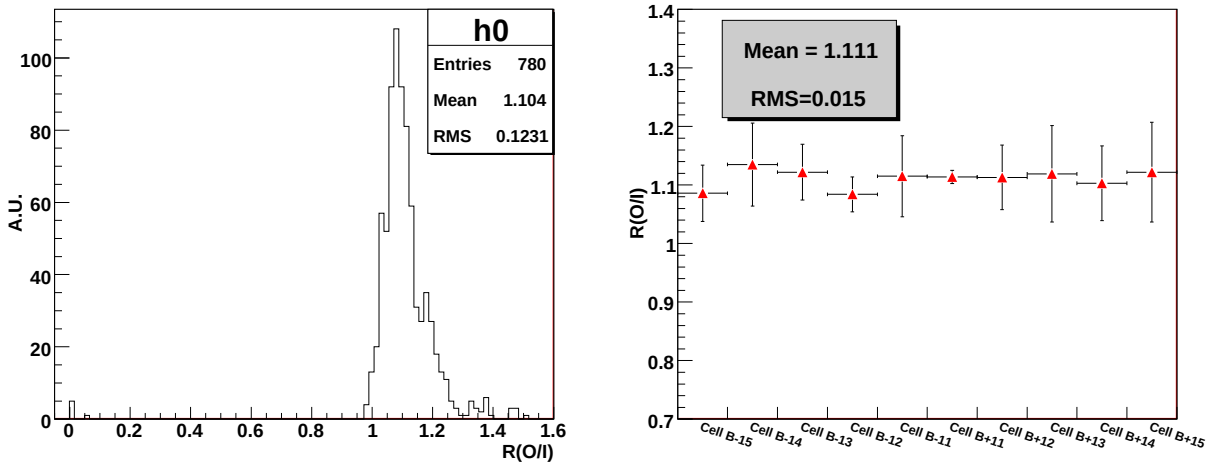

(a) (b)

Figure B.23: (a) The distribution of the ratio of the tile row 7 responses to Cs for its passage through the outer radius hole over the inner radius hole. (b) The same ratio for all the B cells' tile row 7 vs the cell position. The sample represents multiple runs of the testbeam EB calibrated modules.

e.g. the WLS fiber plays no role in the reduction of the light collection along the tile radius. We remind the reader that the typical effective attenuation length of these aluminized fibers is more than 3 m [113].

Similar results were acquired by the analysis of ^{137}Cs scans of the entire EBC partition of TileCal in the ATLAS pit. Those results are shown in Fig. B.24 and confirm with high statistics[3] that the tile response to the ^{137}Cs γ-source is $\sim$ 10% higher in the outer radius hole than in the inner radius hole for tile size 7, compatible with the values extracted from the ^{137}Cs and ^{90}Sr results done on individual tiles (Fig. B.5, Fig. B.7, Fig. B.21(b)). We remind the reader that the distance between the holes in tile 7 is 120 mm leading to an average reduction of the light collection between the holes of 0.87% per cm.

The Effect of Tile Polystyrene Type on Light Collection

Two types of polystyrene were used for the TileCal module instrumentation: BASF and PSM [110], [114]. Concerning the polystyrene types of BC and D cells in TileCal there are three families of modules; ones instrumented with BASF tiles only, another with PSM tiles and a third with mixed types. We show below that the above-mentioned effect of light collection reduction as a function of tile depth is tile polystyrene type independent. The evidence for this is shown in Fig. B.25 where we present the distribution of the ratio R(O/I) of the tile response to Cs source passing through holes at the outer radius to response at the

[3]The statistics of Fig. B.23(a) is from multiple runs on the EB modules exposed to test beam. The statistics of Fig. B.24(a) is a subset of the B-cells in a single EBC run in ATLAS.

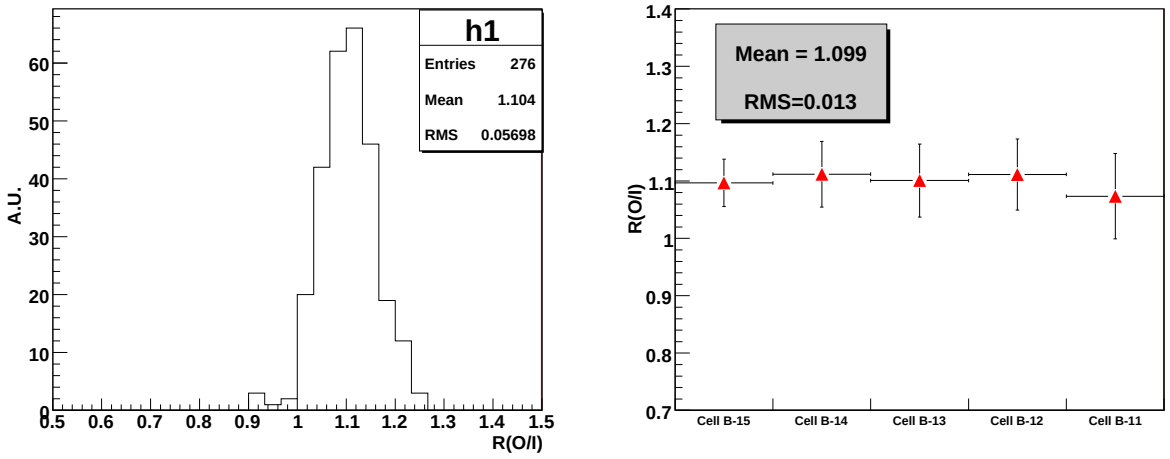

(a) (b)

Figure B.24: (a) The distribution of the ratio of the tile row 7 responses to Cs for its passage through the outer radius hole to that for the inner radius hole. (b) The same ratio for all the B cells' tile row 7 vs the cell position. The sample is a fraction of the EBC modules.

inner radius. The upper plot of Fig. B.25 shows the ratio R(O/I) for modules instrumented exclusively with PSM tiles, whereas the lower plot shows the R(O/I) ratio only for modules only with BASF tiles. For the measured values of the R(O/I) distribution for PSM modules is $Mean = 1.1$ with $RMS = 4.5\%$ and for BASF modules we measured $Mean = 1.107$ with $RMS = 5.4\%$. Hence, within RMS uncertainties, we report the same values for both polystyrene cases.

B.4 Conclusions

The ^{137}Cs system is the main tool used to equalize the response from all of the TileCal cells via setting the PMT HV in an iterative procedure. The absolute energy scale or the pC/GeV conversion scale was determined with electrons and muons impinging the calorimeter at the centre of tiles at $\theta = 20°$ and $90°$ [107]. This created the necessity for us to study and take into consideration possible differences of the TileCal cell response to real particles versus the ^{137}Cs γ-source, since it was reported that the ^{137}Cs weights, obtained with the amplitude method, in BC and D cells were underestimated by 2.5% and $\sim 8.8\%$ respectively for the barrel and 0.9% and 5.5% for the EB [107].

In this Appendix we presented the reason for this, which is the difference in response between particles ($e^{\pm}$, $\mu^{\pm}$) and ^{137}Cs γ-source, which grows larger for larger tile sizes. The previously observed decrease in the e/Cs and μ/Cs ratios as a function of the tile size (1 to 11) is attributed to the light collection decrease

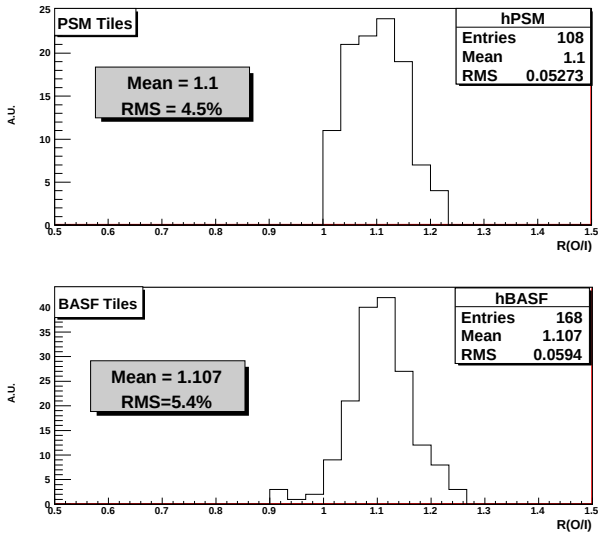

Figure B.25: The distribution of the ratio of the tile size 7 responses to ^{137}Cs at its passage through the outer radius hole over the inner radius hole for modules with tiles made from PSM (top) and BASF scintillator (bottom).

from the outer to the inner radius sides of the tiles. This decrease, as extracted by several independent ^{137}Cs and ^{90}Sr measurements is shown in Table B.1.

The level of decrease that would be consistent with the undercalibration of BC and D cells mentioned above is 1.5% to 2% per cm in the radial direction of the ATLAS detector. The ideal sample, needed to precisely extract the extra correction factors for the BC and D cells would be fine muon radial scans between the source passage holes. Unfortunately, such testbeam data samples are not available. Our investigation showed that there is no dependence on the fiber attenuation or the type of polystyrene used in tile production. The light collection reduction effect is due to the trapezoidal shape of the tile and the fact that the tile radial depth changes with longitudinal layer. Our results indicate the need for additional corrections to the electromagnetic scale factor in BC and D cells as summarized in Tables AA, BB and reported in [107].

Table B.1: Summary of the light collection reduction measurements along tile radius.

Source	Sample	Reference Figure	Measurement (% per cm)	Uncert.
^{137}Cs scans in the pit and TB, outer/inner radius response ratio	Tile 7, $\sim$ 200 B-cells	B.23(a), B.24(a)	0.9 %	11 %
^{137}Cs scans of individual tiles, outer/inner radius response ratio	All sizes, 30 tiles	B.21(b)	0.8 %	15%
^{90}Sr individual tile scans	Tile 11, 3 tiles	B.16(b), B.17(b), B.18(b)	1.5 % to 2.2 %	30%-40%
^{90}Sr individual tile scans	1 tile per size	B.8	1 % to 2 %	13%
^{137}Cs outer radius hole over ^{90}Sr(surface average) ratio	All sizes, 30 tiles	B.21(a)	2 % to 4 %	38%

Appendix C

TileCal Energy Leakage Correction

Energy Leakage from Tile Row to Tile Row for ^{137}Cs γ-source Passage in TileCal Modules

The response of a cell is determined as the mean of individual tile response amplitudes over the time interval corresponding to cell limits (see Fig. C.1(a))

$$I = I_{left} + I_{center} + I_{right} \tag{C.1}$$

A typical picture of a cell response as a function of γ-source position in the Cesium tube is depicted in Fig. C.2. From top to bottom one can see the response of the A cell tile row 3 to 1. One can note that the response of tile row 3 is $\sim 25\%$ less than ones from tile rows 2 and 3. This is due to the fact that the energy leakage from tile row 3 to adjacent tile row 4 belongs to B cells and hence is not registered by the A cell PMTs. When the ^{137}Cs γ-source passes through the tile row, the radiation energy is uniformly distributed around the source path in a cylindrical shape (see Fig. C.1(b)). This causes an energy leakage from the actual tile row into the adjacent row. Therefore, in order to have a good quantitative estimate of the light collection reduction along the tile depth one needs to develop a model for accurate estimation of tile to tile energy leakage.

The main assumptions of the *Energy Leakage Model* are:

- The energy transfers across the boundary between any pair of tile rows is the same
- Light collection depends only on:
  - Geometry of the tile (the trapezoidal shape). Hence, we introduce light collection coefficients R_I and R_O, which describe the tile geometrical features when ^{137}Cs γ-source passes through tile inner and tile outer radius holes, respectively.
  - Depth of the tile.

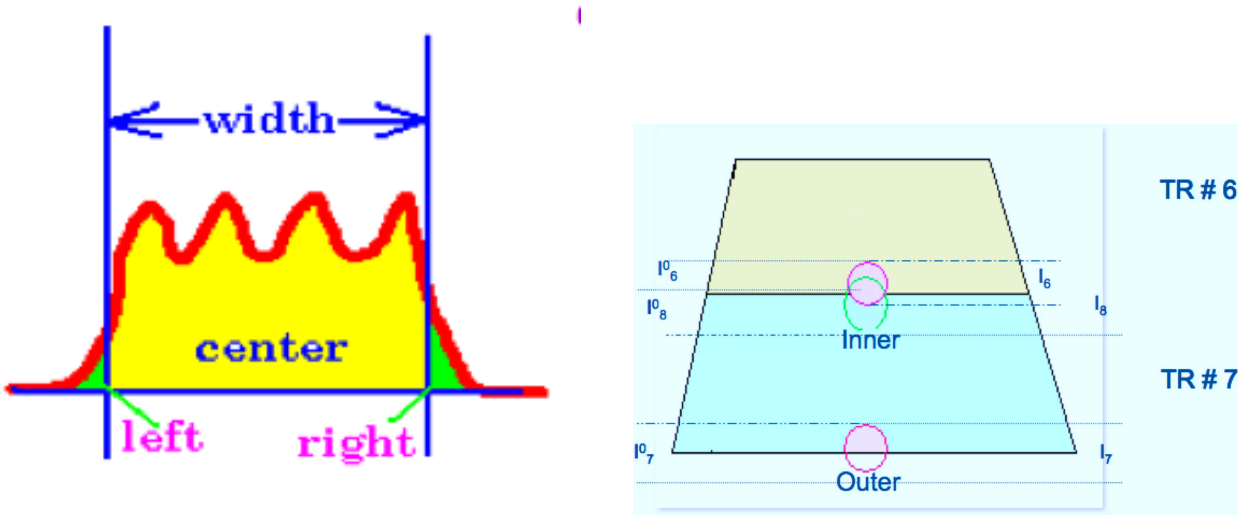

(a) (b)

Figure C.1: (a) Sketch of quantitative measurement of tile light collection to ^{137}Cs γ-source. (b) Two adjacent tiles in the radial direction.

  - Energy deposited in the cell.

- Light collection does not depend on
  - Tile width
  - Read out fiber length (discussed in section 2.1.3)
  - Tile material, i.e. tile sensitivity or the ability for energy-to-light conversion.

Notation

E_0 energy deposit into tiles by ^{137}Cs γ-source

ΔE energy transfer across the tile boundary

S optical sensitivity of tile material

R_I light collection geometrical coefficient at the tile inner radius edge

R_O light collection geometrical coefficient at the tile outer radius edge

I_N measured response of a cell when the ^{137}Cs γ-source passes through tube N

I_N^0 pure response of a cell (excluding the energy leakage component) when the ^{137}Cs γ-source passes through tube N

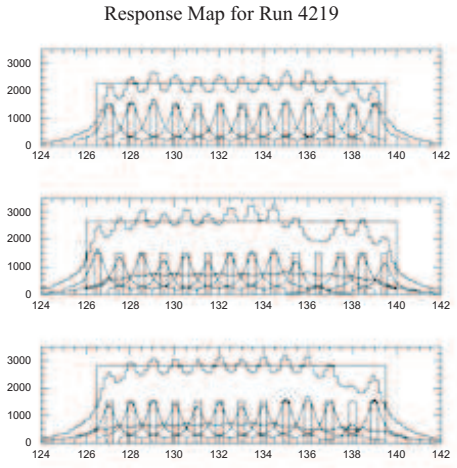

Figure C.2: Typical response to ^{137}Cs γ-source vs position inside a cell with the individual tile amplitudes unfolded.

Hence, based on the assumptions described above the generic expression for cell response will be:

$$I = E \times S \times R \tag{C.2}$$

This enables us to write the equations of energy balance when ^{137}Cs γ-source passes through cesium tubes 6,7,8.

$$I_6^0 = (E_0 - \Delta E) \times R_O = I_6 - \Delta \times R_I \tag{C.3}$$

$$I_8^0 = (E_0 - \Delta E) \times R_I = I_8 - \Delta \times R_O \tag{C.4}$$

$$I_7^0 = (E_0 - \Delta E) \times R_O = I_7 \tag{C.5}$$

We define the inverse of the light collection reduction ratio along the tile depth as:

$$1/R(O/I) = I_7^0/I_8^0 = (E_0 - \Delta E) \times R_O/(E_0 - \Delta E) \times R_I \tag{C.6}$$

Hence,

$$R(O/I) = R_O/R_I \tag{C.7}$$

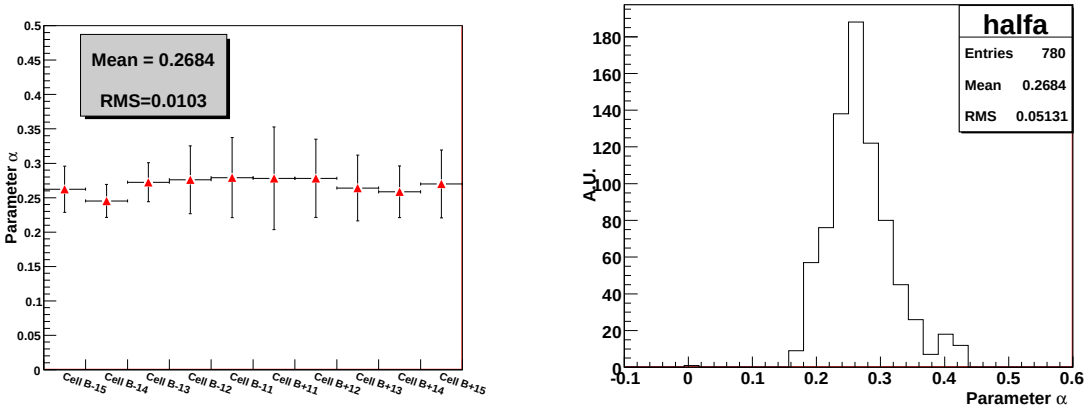

(a) (b)

Figure C.3: (a) Leakage parameter between tile rows vs. B cell position in the Extended Barrel. (b) Leakage parameter from the EB modules calibrated at the testbeam

Upon some simple algebraic manipulations, one obtains:

$$(1/R)^2 - (I_8/I_7) \times (1/R) + (I_6 - I_7)/I_7 = 0 \tag{C.8}$$

The term $\alpha \equiv (I_6 - I_7)/I_7$ is the so-called leakage parameter which describes the ratio of the light collected in tile row 7 with ^{137}Cs γ-source traveling in tube 6, to the case with the ^{137}Cs γ-source traversing the module in tube 7.

The term $\beta \equiv I_8/I_7$ is the light collection reduction ratio in the no-leakage scenario. Both parameters α and β are determined by the optical and geometrical properties of tiles in row 6 and 7. Since we assumed that those properties are similar, we expect that the experimentally measured values of those parameters should converge to some mean value. The distribution of the α-parameter per EB cell is presented in Fig C.3(a), with measured $Mean = 0.268$ and $RMS = 0.051$.

The data was collected during the test beam period 2001/2004. The mean values are well fitted with a horizontal line demonstrating that the α-parameter values measured in various cells are statistically compatible with each other, and hence can be combined. Fig. C.3(b) depicts all measured values of the α-parameter with fitted offset value $p_0 = 0.263 \pm 0.013$. The mean of the latter distribution and the horizontal fit offset are in good agreement within the RMS uncertainties, suggesting validation of the Leakage Model under consideration.

Another validation test is a comparison of the $R(O/I)$ value distribution for the cases of free and fixed (α= 0.268 determined from Fig. C.3(b)) α-parameter values (see Fig. C.4(a) and Fig. C.4(b) respectively).

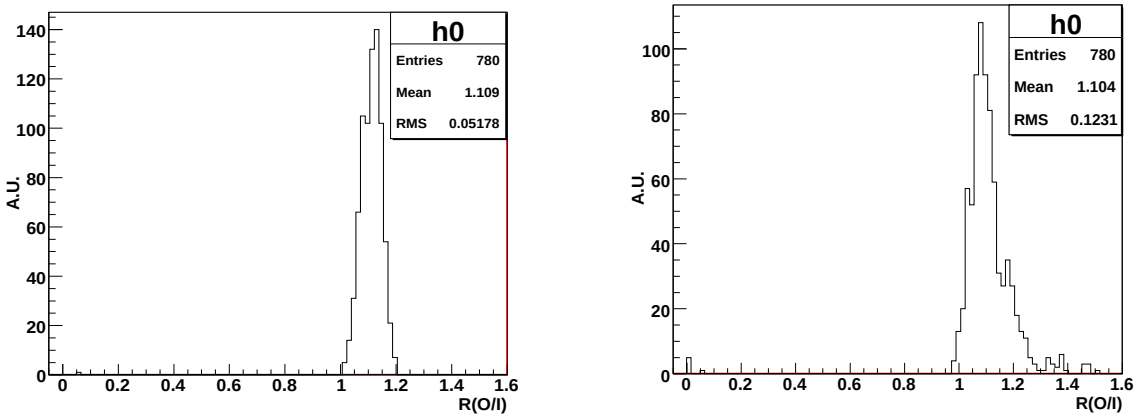

(a) (b)

Figure C.4: The distribution of R(O/I) responses to ^{137}Cs γ-source with the leakage parameter fixed (a) and free (b).

Appendix D

List of MC Samples

ID	Description	Matrix Element	Parton Shower	cross section [pb]	k-factor
5200	$t\bar{t}$ No full hadr. (e, μ, τ)	MC@NLO	Herwig	79.988	1.117
8340	tchan $\rightarrow e$	MC@NLO	Herwig	7.12	1
8341	tchan $\rightarrow \mu$	MC@NLO	Herwig	7.12	1
8342	tchan $\rightarrow \tau$	MC@NLO	Herwig	7.10	1
8343	schan $\rightarrow e$	MC@NLO	Herwig	0.47	1
8344	schan $\rightarrow \mu$	MC@NLO	Herwig	0.47	1
8345	schan $\rightarrow \tau$	MC@NLO	Herwig	0.47	1
8346	$Wt \rightarrow$ inclusive	MC@NLO	Herwig	14.59	1

Table D.1: Top Monte-Carlo samples.

ID	Description	Matrix Element	Parton Shower	cross section [pb]	k-factor
7680	Wenu Np0	Alpgen	Herwig	6921.60	1.20
7681	Wenu Np1	Alpgen	Herwig	1304.30	1.20
7682	Wenu Np2	Alpgen	Herwig	378.29	1.20
7683	Wenu Np3	Alpgen	Herwig	101.43	1.20
7684	Wenu Np4	Alpgen	Herwig	25.87	1.20
7685	Wenu Np5	Alpgen	Herwig	7.00	1.20
7690	Wmunu Np0	Alpgen	Herwig	6919.60	1.20
7691	Wmunu Np1	Alpgen	Herwig	1304.20	1.20
7692	Wmunu Np2	Alpgen	Herwig	377.83	1.20
7693	Wmunu Np3	Alpgen	Herwig	101.88	1.20
7694	Wmunu Np4	Alpgen	Herwig	25.75	1.20
7695	Wmunu Np5	Alpgen	Herwig	6.92	1.20
7700	Wtaunu Np0	Alpgen	Herwig	6918.60	1.20
7701	Wtaunu Np1	Alpgen	Herwig	1303.20	1.20
7702	Wtaunu Np2	Alpgen	Herwig	378.18	1.20
7703	Wtaunu Np3	Alpgen	Herwig	101.51	1.20
7704	Wtaunu Np4	Alpgen	Herwig	25.64	1.20
7705	Wtaunu Np5	Alpgen	Herwig	7.04	1.20

Table D.2: W+jets samples.

ID	Description	Matrix Element	Parton Shower	cross section [pb]	k-factor
7650	Zee Np0	Alpgen	Herwig	668.32	1.25
7651	Zee Np1	Alpgen	Herwig	134.36	1.25
7652	Zee Np2	Alpgen	Herwig	40.54	1.25
7653	Zee Np3	Alpgen	Herwig	11.16	1.25
7654	Zee Np4	Alpgen	Herwig	2.88	1.25
7655	Zee Np5	Alpgen	Herwig	0.83	1.25
7660	Zmumu Np0	Alpgen	Herwig	668.68	1.25
7661	Zmumu Np1	Alpgen	Herwig	134.14	1.25
7662	Zmumu Np2	Alpgen	Herwig	40.33	1.25
7663	Zmumu Np3	Alpgen	Herwig	11.19	1.25
7664	Zmumu Np4	Alpgen	Herwig	2.75	1.25
7665	Zmumu Np5	Alpgen	Herwig	0.77	1.25
7670	Ztautau Np0	Alpgen	Herwig	668.40	1.25
7671	Ztautau Np1	Alpgen	Herwig	134.81	1.25
7672	Ztautau Np2	Alpgen	Herwig	40.36	1.25
7673	Ztautau Np3	Alpgen	Herwig	11.25	1.25
7674	Ztautau Np4	Alpgen	Herwig	2.79	1.25
7675	Ztautau Np5	Alpgen	Herwig	0.77	1.25

Table D.3: Z+jets/Drell-Yan samples with phase space cuts $m_{l^+l^-} > 40$ GeV.

ID	Description	Matrix Element	Parton Shower	cross section [pb]	k-factor
116250	Zee Np0	Alpgen	Herwig	3055.20	1.25
116251	Zee Np1	Alpgen	Herwig	84.92	1.25
116252	Zee Np2	Alpgen	Herwig	41.40	1.25
116253	Zee Np3	Alpgen	Herwig	8.38	1.25
116254	Zee Np4	Alpgen	Herwig	1.85	1.25
116255	Zee Np5	Alpgen	Herwig	0.46	1.25
116260	Zmumu Np0	Alpgen	Herwig	3054.90	1.25
116261	Zmumu Np1	Alpgen	Herwig	84.87	1.25
116262	Zmumu Np2	Alpgen	Herwig	41.45	1.25
116263	Zmumu Np3	Alpgen	Herwig	8.38	1.25
116264	Zmumu Np4	Alpgen	Herwig	1.85	1.25
116265	Zmumu Np5	Alpgen	Herwig	0.46	1.25
116270	Ztautau Np0	Alpgen	Herwig	3055.10	1.25
116271	Ztautau Np1	Alpgen	Herwig	84.93	1.25
116272	Ztautau Np2	Alpgen	Herwig	41.47	1.25
116273	Ztautau Np3	Alpgen	Herwig	8.36	1.25
116274	Ztautau Np4	Alpgen	Herwig	1.85	1.25
116275	Ztautau Np5	Alpgen	Herwig	0.46	1.25

Table D.4: Low mass Z+jets/Drell-Yan samples with 10 GeV $< m_{l^+l^-} <$ 40 GeV.

ID	Description	Matrix Element	Parton Shower	cross section [pb]	k-factor
7280	WbbNp0	Alpgen	Herwig	47.32	1.20
7281	WbbNp1	Alpgen	Herwig	35.77	1.20
7282	WbbNp2	Alpgen	Herwig	17.34	1.20
7283	WbbNp3	Alpgen	Herwig	6.63	1.20

Table D.5: W+bb samples.

ID	Description	Matrix Element	Parton Shower	cross section [pb]	k-factor
9300	Z+bb Np0	Alpgen	Herwig	6.57	1.25
9301	Z+bb Np1	Alpgen	Herwig	2.48	1.25
9302	Z+bb Np2	Alpgen	Herwig	0.89	1.25
9303	Z+bb Np3	Alpgen	Herwig	0.39	1.25
9305	Z+bb Np0	Alpgen	Herwig	6.56	1.25
9306	Z+bb Np1	Alpgen	Herwig	2.47	1.25
9307	Z+bb Np2	Alpgen	Herwig	0.89	1.25
9308	Z+bb Np3	Alpgen	Herwig	0.39	1.25
9310	Z+bb Np0	Alpgen	Herwig	6.57	1.25
9311	Z+bb Np1	Alpgen	Herwig	2.49	1.25
9312	Z+bb Np2	Alpgen	Herwig	0.89	1.25
9313	Z+bb Np3	Alpgen	Herwig	0.39	1.25

Table D.6: Z+bb samples.

ID	Description	Matrix Element	Parton Shower	cross section [pb]	k-factor
7100	WW + 0j, both $W \to l\nu$	Alpgen	Herwig	2.0950	1.26
7101	WW + 1j, both $W \to l\nu$	Alpgen	Herwig	0.9962	1.26
7102	WW + 2j, both $W \to l\nu$	Alpgen	Herwig	0.4547	1.26
7103	WW + 3j, both $W \to l\nu$	Alpgen	Herwig	0.1758	1.26
7104	WZ + 0j, $W \to$ inclusive , $Z \to ll$	Alpgen	Herwig	0.6718	1.28
7102	WW + 2j, both $W \to l\nu$	Alpgen	Herwig	0.4138	1.28
7106	WZ + 2j, $W \to$ inclusive , $Z \to ll$	Alpgen	Herwig	0.2249	1.28
7107	WZ + 3j, $W \to$ inclusive , $Z \to ll$	Alpgen	Herwig	0.0950	1.28
7108	ZZ + 0j, $Z \to$ inclusive , $Z \to ll$	Alpgen	Herwig	0.5086	1.30
7109	ZZ + 1j, $Z \to$ inclusive , $Z \to ll$	Alpgen	Herwig	0.2342	1.30
7110	ZZ + 2j, $Z \to$ inclusive , $Z \to ll$	Alpgen	Herwig	0.0886	1.30
7111	ZZ + 3j, $Z \to$ inclusive , $Z \to ll$	Alpgen	Herwig	0.0314	1.30

Table D.7: Diboson samples.

ID	Description	Matrix Element	Parton Shower	cross section [pb]	k-factor
5205	$t\bar{t}$	AcerMC	Pythia	58.23	1.53
5860	$t\bar{t}$	POWHEG	Herwig	79.171	1.129
5861	$t\bar{t}$	POWHEG	Pythia	79.171	1.129
117255	$t\bar{t}$ ISR min	AcerMC	Pythia	58.23	1.53
117256	$t\bar{t}$ ISR max	AcerMC	Pythia	58.23	1.53
117257	$t\bar{t}$ FSR min	AcerMC	Pythia	58.23	1.53
117258	$t\bar{t}$ FSR max	AcerMC	Pythia	58.23	1.53

Table D.8: Systematic generator and ISR/FSR samples.

References

[1] K. Nakamura et. al. Particle data group. *Journal of Physics G*, 37(7A):596–607, July 2010.

[2] *The CERN LHC, Accelerator and Experiments*. CERN, 2009.

[3] J.J. Aubert et al. Experimental observation of heavy particle j. *Physical Review Letters*, 33(23):1404–1406, 1974.

[4] J.E. Augustin et al. Discovery of a narrow resonance in e^+e^- annihilation. *Physical Review Letters*, 33(23):1406–1408, 1974.

[5] G.S. Abrams et al. Discovery of a second narrow resonance in e^+e^- annihilation. *Physical Review Letters*, 33(24):1453–1455, 1974.

[6] M.L. Perl et al. Evidence for anomalous lepton production in e^+e^- annihilation. *Physical Review Letters*, 35(22):1489–1492, 1975.

[7] S.W. Herb et al. Observation of a dimuon resonance at 9.5 gev in 400-gev proton-nucleus collisions. *Phys. Rev. Lett.*, 39:252–255, Aug 1977.

[8] F.Abe et al. (CDF Collaboration). Observation of top quark production in $p\bar{p}$ collisions with the collider detector at fermilab. *Phys. Rev. Lett.*, 74(2632), 1995.

[9] S.Abashi et al. (D0 Collaboration). Observation of the top quark. *Phys. Rev. Lett*, 74(2632), 1995.

[10] K. Kodama et al. (DONUT Collaboration (2001). Observation of tau neutrino interactions. *Physics Letters B*, 504(3), 2001.

[11] Chris Quigg. *Gauge Theories of the Strong, Weak, and Electromagnetic Interactions*. Addison-Wesley Publishing Company, 1983.

[12] Siegfried Bethke. The 2009 World Average of alpha(s). *Eur.Phys.J.*, C64:689–703, 2009.

[13] UA1 Collaboration. Experimental observation of isolated large transverse energy electrons with associated missing energy in $\sqrt{s} = 540$ gev. *Phys. Lett. B.*, B122(1):103–116, Feb 1983.

[14] UA2 Collaboration. Observation of single isolated electrons of high transverse momentum in events with missing transverse energy at the cern anti-p p collider. *Phys. Lett. B.*, B122(1):476–485, 1983.

[15] CDF Collaboration. Measurement of the top pair production cross section in the dilepton decay channel in $p\bar{p}$ collisions at $\sqrt{s} = 1.96$ tev. *Phys. Rev.*, D(052002), 2010.

[16] D0 Collaboration. Combination of $t\bar{t}$ cross section measurements and constraints on the mass of the top quark and its decays into charged higgs bosons. *Phys. Rev.*, D 80(071102(R)), 2009.

[17] ATLAS Collaboration. Measurement of the top quark pair production cross section in pp collisions at view the mathml source in dilepton final states with atlas. *Physics Letters B*, B707(459), 2012.

[18] CMS Collaboration. Measurement of the $t\bar{t}$ production cross section and the top quark mass in the dilepton channel in pp collisions at $\sqrt{s} = 7$ tev. *JHEP*, 1107(049), 2011.

[19] Hitoshi Murayama. Physics beyond the standard model and dark matter. arXiv:0704.2276v1.

[20] F. Gianotti. Update on the standard model higgs searches in *atlas*. http://indico.cern.ch/getFile.py/access?contribId=0&resId=1&materialId=slides&confId=164890, June 2011.

[21] G. Tonelli. Update on the standard model higgs searches in *cms*. http://indico.cern.ch/getFile.py/access?contribId=1&resId=0&materialId=slides&confId=164890.

[22] *Combined CDF and D0 Search for Standard Model Higgs Boson Production with up to 10* fb^{-1} *of Data*. FERMILAB-CONF-12-065-E, 2012.

[23] http://www.fnal.gov/pub/today/archive_2012/today12-02-23_HiggsResultReadMore.html.

[24] F. Maltoni R. Frederix. Top pair invariant mass distribution: a window on new physics. *JHEP*, 0901:047, 2009.

[25] C.T. Hill. *Phys. Lett.*, B 266(419), 1991.

[26] C.T. Hill. *Phys. Lett.*, B 345(483), 1995.

[27] C.T. Hill. *Phys. Rev.*, D 49(4454), 1994.

[28] S.J. Parke R.M. Harris, C.T. Hill. arXiv:hep-ph:9911288.

[29] C.T. Hill B.A. Dobrescu. *Phys. Rev Lett.*, 81(2634), 1998.

[30] R.S.Chivukula et al. *Phys. Rev.*, D 65(075003), 2002.

[31] H.J. He et al. *Phys. Rev.*, D 65(055006), 2002.

[32] A. G. Cohen N. Arkani-Hamed and H. Georgi. Electroweak symmetry breaking from dimensional deconstruction. *JHEP*, 0208(020), 2002.

[33] A. G. Cohen et al. N. Arkani-Hamed. The minimal moose for a little higgs. *JHEP*, 0208(021), 2002.

[34] A. G. Cohen et al. N. Arkani-Hamed. The littlest higgs. *JHEP*, 0207(034), 2002.

[35] W. Skiba I. Low and D. Smith. Little higgses from an antisymmetric condensate. *Phys. Rev.*, D 66(072001), 2002.

[36] T. Han et. al. Phenomenology of the little higgs model. *Phys. Rev.*, D 67(095004), 2003.

[37] G. Azuelos et al. Exploring little higgs models with atlas at the lhc. *Eur. Phys. J.*, C 39S2(13), 2005.

[38] M. Schmaltz and D. Tucker-Smith. Little higgs review. *Ann. Rev. Nucl. Part. Sci.*, 2005.

[39] S. Dimopoulos N. Arkani-Hamed and G. R. Dvali. The hierarchy problem and new dimensions at a millimeter. *Phys. Lett*, B 429(263), 1998.

[40] G. Antchev, P. Aspell, I. Atanassov, V. Avati, J. Baechler, et al. First measurement of the total proton-proton cross section at the LHC energy of $\sqrt{s}$ =7 TeV. *Europhys.Lett.*, 96:21002, 2011.

[41] A. Martin F. Halzen. *Quarks and Leptons*, chapter 4.2. Wiley and Sons, 1984.

[42] F. Maltoni R. Frederix. Top pair invariant mass distribution: a window on new physics. Technical report, Center for Particle Physics and Phenomenology, 2010.

[43] M. Cacciari et. al. *JHEP*, 09(127), 2008.

[44] R. Vogt N. Kidonakis. *Phys. Rev.*, D 78(074005), 2008.

[45] P. Uwer S. Moch. *Phys. Rev.*, D 78(034003), 2008.

[46] P. Uwer S. Moch. *Nucl. Phys.*, B 183(75), 2008.

[47] *Combination of CDF top quark pair production cross section measurements with up to 4.6* fb^{-1}., number CDF Note 9913, Oct 2009.

[48] D0 Collaboration. Measurement of the production cross section using dilepton events in collisions. *Physics Letters B*, 704(5):403 – 410, 2011.

[49] S. Myers. *The LEP Collider. From design to approval and Commissioning.* CERN, 1991.

[50] ATLAS Collaboration. Luminosity determination in pp collisions at sqrt(s) = 7 tev using the atlas detector at the lhc. *Eur. Phys. J.*, C71, 2011.

[51] T.J. Ypma. Historical development of the newton raphson method. *SIAM Rev.*, 37(4):531–551, 1995.

[52] ATLAS Collaboration. Luminosity determination in pp collisions at sqrt(s) = 7 tev using the atlas detector in 2011. *ATLAS-CONF-20110-011*, 2011.

[53] Catani Kraus Kuhn Webber. Ckkw matching scheme. arXiv:hep-ph/0109231.

[54] M.L. Mangano. Mlm matching scheme. arXiv:hep-ph/0602031.

[55] S. Agostinelli et al. Geant4 - a simulation toolkit. *Nucl. Instr. and Meth.*, A506:250, 2003.

[56] Twiki page: Atlas Production Group.
`https://twiki.cern.ch/twiki/bin/view/AtlasProtected/AtlasProductionGroup`.

[57] T. Sjostrand and S. Mrenna and P.Z. Skands. Pythia 6.4 physics and manual. *JHEP*, 05:026, 2006.

[58] S. Frixione and B.R. Webber. Matching nlo qcd computations and parton shower simulations. *JHEP*, 0206:029, 2002.

[59] P. M. Nadolsky et al. Implications of CTEQ global analysis for collider observables. *Phys. Rev.*, D78:013004, 2008.

[60] G. Corcella et al. Herwig 6: An event generator for hadron emission reactions with interfering gluons (including supersymmetric processes). *JHEP*, 0101:010, 2001.

[61] J. M. Butterworth, Jeffrey R. Forshaw, and M. H. Seymour. Multiparton interactions in photoproduction at HERA. *Z. Phys.*, C72:637–646, 1996.

[62] The ATLAS Collaboration. First tuning of herwig/jimmy to atlas data. ATL-PHYS-PUB-2010-014, 2010.

[63] M. Aliev et al. HATHOR: HAdronic Top and Heavy quarks crOss section calculatoR. *Comput. Phys. Commun.*, 182:1034–1046, 2011.

[64] S. Frixione, P. Nason and C. Oleari. Matching nlo qcd computations with parton shower simulations: the powheg method. *JHEP*, 0711:070, 2007.

[65] Simone Alioli, Paolo Nason, Carlo Oleari, and Emanuele Re. NLO single-top production matched with shower in POWHEG: s- and t-channel contributions. *JHEP*, 09:111, 2009.

[66] B.P. Kersevan and E. Richter-Wąs. The monte carlo event generator acermc version 2.0 with interfaces to pythia 6.2 and herwig 6.5. *arXiv:hep-ph/0405247*, 2004.

[67] The ATLAS Collaboration. ATL-COM-PHYS-2010-695, 2010.

[68] J.T. Childers *et al.* Performance of the electron and photon trigger in p-p collisions at sqrt(s) = 7 tev. ATL-COM-DAQ-2011-008.

[69] The e/gamma combined performance group. Electron performance in the atlas experiment. ATL-COM-PHYS-2010-208.

[70] The e/gamma combined performance group. Electron efficiency measurements using atlas 2010 data at sqrt(s) = 7 tev and https://twiki.cern.ch/twiki/bin/view/atlasprotected/efficiency measurements. ATL-COM-PHYS-2011-322.

[71] See: https://twiki.cern.ch/twiki/bin/view/atlasprotected/topelectronsftoolrelease16.

[72] M. Aoki et. al. The measurement of $t\bar{t}$ cross section in the dilepton decay channel with cut-and-count methods at 7 tev with $\mathcal{L} = 698$ pb^{-1}. ATLAS Internal Note.

[73] M. Agustoni *et al.* Electron energy scale in-situ calibration and performance. ATL-COM-PHYS-2011-263 (2011).

[74] Gerhard X. Ritter and Joseph N. Wilson. *Handbook of computer vision algorithms in image algebra*. CRC Press, Boca Raton, FL, 1996.

[75] Twiki page: Guidelines for Analyses of 2011 Data for EPS. https://twiki.cern.ch/twiki/bin/view/AtlasProtected/MCPAnalysisGuidelinesEPS2011.

[76] N. Benekos *et al.* Lepton trigger and identification for the Winter 2011 top quark analyses. ATL-COM-PHYS-2011-123.

[77] MuComb inefficiencies in MC10b. https://indico.cern.ch/getFile.py/access?contribId=3&resId=0 &materialId=slides&confId=129115.

[78] K. Nakamura *et al.* (Particle Data Group). The Review of Particle Physics. J. Phys. G 37, 075021 (2010).

[79] J. E. Gaiser. *Charmonium Spectroscopy from Radiative Decays of the J/Psi and Psi-Prime*. PhD thesis, SLAC, 1982.

[80] M. Cacciari and G. P. Salam. Dispelling the n^3 myth for the kt jet-finder. *Physics Letters B*, 641(1):57 – 61, 2006.

[81] M. Cacciari, G. P. Salam, and G. Soyez. The anti-kt jet clustering algorithm. *JHEP*, 04:063, 2008.

[82] B. Butler and A. Schwartzman. Track-jet reconstruction and performance. Technical Report ATL-PHYS-INT-2010-040, CERN, Geneva, July 2010.

[83] The ATLAS Collaboration. Jet energy resolution and reconstruction efficiencies from in-situ techniques with the atlas detector using proton-proton collisions at a center of mass energy sqrts = 7 tev. Technical Report ATLAS-CONF-2010-054, CERN, Geneva, July 2010.

[84] Romeo, G. and Schwartzman, A. and Piegaia, R, and Carli, T. and Teuscher, R. Jet energy resolution from in-situ techniques with the atlas detector using proton-proton collisions at a center of mass energy $\sqrt{s} = 7$ tev. Technical Report ATL-COM-PHYS-2011-240, CERN, Geneva, Mar 2011.

[85] Jet energy scale and its systematic uncertainty in proton-proton collisions at $\sqrt{s} = 7$ tev in atlas 2010 data. *ATLAS-CONF-2011-032*, 2011.

[86] A Canepa, D Cinca, S Farrell, H Garitaonandia Elejabarrieta, U Grundler, K Johns, V Kaushik, H Khandanya, X Lei, JR Lessard, T Liss, I Nugent, H Okawa, D Pallin, A Taffard, B Toggerson, and M Watson. Missing transverse energy for top physics analyses with early atlas data at *sqrts*=7 tev. Technical Report ATL-COM-PHYS-2010-821, CERN, Geneva, Oct 2010. Supporting document for top paper.

[87] Tool for met uncertainties. *https : //twiki.cern.ch/twiki/bin/view/AtlasProtected/ TopETmissLiaison_EPS#Tool_for_MET_Uncertainties*, June 2011.

[88] M Antonelli, D Cavalli, E Dobson, N Ilic, K Lie, C Pizio, S Resconi, R Simoniello, M Simonyan, T Sumida, M Testa, R Teuscher, V Tsiskaridze, I Vichou, I Vivarelli, and A Yurkewicz. Reconstruction and calibration of missing transverse energy and performance in z and w events in atlas proton-proton collisions at 7 tev. Technical Report ATLAS-COM-CONF-2011-035, CERN, Geneva, Feb 2011.

[89] Fakemetestimator. *https : //twiki.cern.ch/twiki/bin/view/AtlasProtected/FakeMetEstimator*, June 2011.

[90] ATLAS Collaboration. Atlantis start-up guide. Technical Report CERN, 2006.

[91] M. Mangano, Understanding the Standard Model, as a bridge to the discovery of new phenomena at the LHC, CERN-PH-TH-2008-019, arXiv:0802.0026 [hep-ph].

[92] John M. Campbell and R.Keith Ellis. Next-to-leading order corrections to W^+ 2 jet and Z^+ 2 jet production at hadron colliders. *Phys.Rev.*, D65:113007, 2002.

[93] John M. Campbell, R. Keith Ellis, and Francesco Tramontano. Single top production and decay at next-to-leading order. *Phys. Rev.*, D70:094012, 2004.

[94] Nikolaos Kidonakis. Single top quark production cross section at hadron colliders. *PoS*, DIS2010:196, 2010.

[95] J Butterworth, E Dobson, U Klein, B Mellado Garcia, T Nunnemann, J Qian, D Rebuzzi, and R Tanaka. Single boson and diboson production cross sections in pp collisions at $\sqrt{s} = 7$ TeV. Technical Report ATL-COM-PHYS-2010-695, Aug 2010.

[96] P. Nason, A new method for combining NLO QCD with shower Monte Carlo algorithms, JHEP 11546 (2004) 040.
S. Frixione, P. Nason, and C. Oleari, Matching NLO QCD computations with Parton Shower simulations: the POWHEG method , JHEP **11** (2007) 070.
S. Frixione, P. Nason, and G. Ridolfi, A Positive-Weight Next-to-Leading-Order Monte Carlo for Heavy Flavour Hadroproduction, JHEP **09** (2007) 126.

[97] B. P. Kersevan and E. Richter-Was, The Monte Carlo event generator AcerMC version 2.0 with561 interfaces to PYTHIA 6.2 and HERWIG 6.5, arXiv:hep-ph/0405247.

[98] The ATLAS Collaboration, Expected Performance of the ATLAS Experiment: Detector, Trigger and Physics, CERN-OPEN-2008-020, pages 874–878.

[99] Martin:2009iq, A. D. Martin, W. J. Stirling, R. S. Thorne, and G. Watt, *Parton distributions for the LHC*, Eur. Phys. J. **C63** (2009) 189–285.

[100] R. D. Ball, et al., *A first unbiased global NLO determination of parton distributions and their uncertainties*, Nucl. Phys. **B838** (2010) 136–206.

[101] Update on the jet energy scale systematic uncertainty for jets produced in proton-proton collisions at $\sqrt{s} = 7$ tev measured with the atlas detector. Technical Report ATLAS-CONF-2011-007, CERN, Geneva, Feb 2011.

[102] Wouter Verkerke and David P. Kirkby. The RooFit toolkit for data modeling. *arXiv:ph/0306116*, 2003.

[103] Moneta, L. and Belasco, K. and Cranmer, K. and Kreiss, S. and Lazzaro, A. and Piparo, D. and Schott, G. and Verkerke, W. and Wolf, M. The RooStats Project. Sep 2010. in the proceedings of ACAT 2010, Jaipur, India (2010).

[104] K Cranmer, D B Ta, A Loginov, Y Okumura, J F Arguin, K Hanagaki, M Hirose, W Verkerke, E Shabalina, T Poghosyan, and U Husemann. Measurement of the top quark pair production cross-section using a statistical combination of dilepton and semileptonic final states. Technical Report ATL-COM-PHYS-2011-186, CERN, Geneva, Feb 2011.

[105] ATLAS Collaboration. Measurement of the cross section for top-quark pair production in pp collisions at $\sqrt{s} = 7$ tev with the atlas detector using final states with two high-pt leptons. 2012. arXiv:hep-ph/1202.4892.

[106] ATLAS Collaboration. Measurement of the top quark pair production cross-section based on a statistical combination of measurements of dilepton and single-lepton final states at $\sqrt{s} = 7$ tev with the atlas detector. *ATLAS Conference Note*, (ATLAS-CONF-2011-108), Aug 2011.

[107] Anderson K. J. Calibration of atlas tile calorimeter at the electromagnetic scale. *ATL-TILE-COM-2008-016*, 2008.

[108] S. Errede et al. The effect of the tile light collection reduction along radius on the atlas tile calorimeter uniformity. Technical Report ATL-TILECAL-PUB-2009-005, CERN Public Note, 2008.

[109] P. Amaral et al. Optical masks for the scintillator plates of the atlas tile calorimeter. *ATL-COM-TILECAL-2008-011*, 2008.

[110] A. Abdallah et al. The production and qualification of scintillator tiles for the atlas hadronic calorimeter. *ATL-TILECAL-PUB-2007-010 (ATL-COM-TILECAL-2007-026)*, 2007.

[111] E.Starchenko et al. Cesium monitoring system for atlas tile hadron calorimeter. *NIM A 494 (2002) 381-384, TILECAL-2002-003*, 2002.

[112] E.Starchenko A. Zenine. Geometrical aspects of the tile response to *cs* source. *http://indico.cern.ch/getFile.py/access?contribId=29*, TileCal Week Oct 2001.

[113] A. Gomes et al. Cell geometry and fiber lengths of barrel and extended barrel modules. *ATL-TILECAL-2002-011*, 2002.

[114] J. Abdallah et al. The optical instrumentation of the atlas tile calorimeter. *ATL-TILECAL-PUB-2008-005 ; ATL-COM-TILECAL-2007-025*, 2008.